InSAR measurements of volcano deformation on the Central American Volcanic Arc

Susanna Kathryn Ebmeier

Thesis submitted to the University of Oxford
for the degree of Doctor of Philosophy
in
Geology and Mineralogy

Department of Earth Sciences
University of Oxford

Summer, 2012

Supervised by Juliet Biggs, Tamsin Mather and Don Grainger

Declaration

The contents of this thesis are all my own work, except where otherwise stated. The views and opinions expressed herein are mine and not necessarily those of any other person or body unless so attributed.

Citation: Ebmeier, S. K. (2012), InSAR measurements of volcano deformation on the Cnetral American Volcanic Arc, D.Phil. thesis, University of Oxford, Department of Earth Sciences, Oxford, UK.

This thesis has been typeset using LaTeX 2ε, released under the LaTeX Project Public License (LPPL), and references were compiled using BibTeX. Some of the figures were produced using the open source Generic Mapping Tools (GMT) software, released under the GNU General Public License. Interferometric SAR processing was performed using ROI_PAC, released through Open Channel Foundation, copyright 2002–2008 Caltech/Jet Propulsion Laboratory.

Printed in the United Kingdom.

Abstract

InSAR measurement of volcano deformation on the Central American Volcanic Arc

Susanna K. Ebmeier

Summer, 2012

Satellite measurements of volcano deformation have the potential to illuminate a wide range of volcanic processes and have provided us with the first opportunity to investigate volcano deformation as an arc-scale process. This thesis presents the results of an Interferometric Synthetic Aperture Radar (InSAR) survey of the Central American Volcanic Arc between 2007 and 2010.

My measurements confirm a statistically significant absence of magmatic deformation in Central America relative to other well-studied volcanic arcs. I estimate a minimum detection threshold for deformation at 20 of the arc's 26 active volcanoes using time series analysis of interferometric phase. I find that the majority (∼80%) of literature measurements of volcano deformation made at other arcs would have been possible with the average magnitude of noise in Central American volcanoes. The absence of measurable magmatic deformation in Central America may therefore be due to factors that limit the geodetic expression of magma movement, including the deep pooling of basalts and high parental melt volatile content. The quantification of measurement uncertainty also allows me to use the lack of deformation at specific erupting volcanoes to make order of magnitude estimations of the minimum depth for magma storage that would not result in measurable deformation.

I present measurements and interpretation of non-magmatic deformation associated with edifice development at two Central American volcanoes: Arenal, Costa Rica and Santiaguito, Guatemala. At Arenal, I measure apparently steady slip (∼7 cm/yr) on the volcano's western flanks, which I attribute to gravity-driven slip on the boundary between lavas emplaced of the past 50 years and older tephras and paleosols. At Santiaguito, I demonstrate the measurement of large-scale (∼10-200 m) topographic change from a small set of large baseline interferograms. Measurements of post-2000 lava fields allow me to estimate extrusion rate, map changes to flow morphology make simultaneous measurements of lava flow thickness and subsidence rate.

Extended Abstract

InSAR measurement of volcano deformation on the Central American Volcanic Arc

Susanna K. Ebmeier

Summer, 2012

Deformation data derived from Interferometric Synthetic Aperture Radar (InSAR) provide us with information about a range of volcanic processes, from pre-eruptive inflation to slow, gravity-driven edifice failure. Since the first InSAR volcano deformation measurements were made in the mid-nineties, over 94 deforming volcanoes have been measured word-wide (Chapter 1). The majority of these measurements capture shallow (<5 km) magma movement, mostly not obviously associated with an eruption. Volcano deformation events as measured with InSAR do not appear to be spread evenly around the world, but vary between different tectonic settings, and even between different volcanic arcs.

This thesis presents an analysis and interpretation of L-band InSAR deformation measurements in the Central American Volcanic Arc between 2007-2010. Central America presents a particularly interesting, if challenging, target for an InSAR study due both to the high spatial concentration of volcanic activity and to the diversity in the eruptive character of its volcanoes. However, Central America is a challenging environment for making InSAR measurements, resulting in particularly high measurement artefacts and associated uncertainties. This is primarily due to the high magnitude and variability of tropospheric water vapour in the tropics and to rapid phase decorrelation caused by dense vegetation.

I quantify the effects of some of the factors that limit InSAR measurement in Central America in Chapter 2. Radar path delays due to stratified water vapour in Central America are among the highest to have been measured worldwide and can generally be distinguished from potential deformation using their temporal characteristics and relationship to topography. I find that variability in phase over Central American volcanoes is proportional to volcano edifice height

with a gradient of about ∼2 cm/yr.

InSAR measurement may also be prevented by both high phase decorrelation rates and poor radar penetration of vegetation. The L-band data presented in this thesis is much more successful in penetrating tropical vegetation than more widely available C-band data, or higher spatial resolution X-band data. Phase decorrelation is still relatively rapid, however, with the longest interferograms spanning around 18 months or less. I use a simple coherence model to test the relationship between vegetation type and temporal decorrelation and found no relationship with Normalised Difference Vegetation Index (NDVI), but some systematic variation with land-use type. Decorrelation rates are higher (with a lower standard deviation) for tropical rainforest than for cultivated land.

Data for 20 of the 26 volcanoes in Central America that have been historically active are coherent enough to allow measurement. The most striking result of this thesis is that my measurements show no magmatic deformation at any of these active volcanoes. I do however, make measurements of non-magmatic deformation associated with edifice instability and lava flow subsidence at Arenal, Costa Rica and Santiaguito, Guatemala.

Instead of focusing entirely on those volcanoes that are deforming I estimate the uncertainty for InSAR measurements at each volcano from time series of phase over summit areas (Chapter 3). This allows me to place thresholds on the rate at which each volcano would have to deform in order to be measurable. These thresholds provide a context for each 'null' result, and allow me to use the lack of deformation at particular active volcanoes to make inferences about volcanic processes. For example, the lack of deformation accompanying small explosions at Telica, San Cristóbal and Poás suggest either that any magma volume change during or after eruption took place at a minimum depth of ∼2 km or that shallow volume change was accommodated by magma compressibility rather than deformation.

Similarly, I use the threshold values for deformation to test the limits of where magma could be accumulating beneath persistently active volcanoes without producing measurable deformation. I use literature measurements of degassing flux and magma sulphur content as estimated from melt inclusions to estimate minimum volume change and thus the minimum depth at which magma could be accumulating in a single reservoir. The lack of significant deformation at Pacaya and Masaya volcanoes make it unlikely that there are points of localised accumulation of degassed magma in the shallow elastic crust beneath them (in agreement with gravity measurements at Masaya). This suggests that magma a) returns to depths below our limits of geodetic detection and/or b) is dispersed through the crust in multiple smaller intrusions.

The systematic approach to reporting 'null' results presented in Chapter 3 also provides a framework for comparison of InSAR results in different tectonic settings. I find no evidence of magmatic deformation in Central America above an average rate of around 2.4 cm/yr. This threshold is significantly lower than the majority of InSAR measurements of deformation in other parts of the world. If the deformation events that have been measured with InSAR were distributed evenly around all of the historically active volcanoes in the world, then the probability of observing no deformation at all in Central America would be about 1 %.

Several distinctive characteristics of the Central American Volcanic Arc may act to reduce the potential of magma movement to produce measurable surface deformation. Around half of the arc's eruptive products are basaltic, thought to ascend rapidly during eruption from where they pool at the base of the crust, beyond the depth at which we expect to be able to detect magma accumulation with InSAR. High volatile contents in Central American parental melts may in some circumstances lead to high gas fraction and therefore highly compressible magmas at shallow depths.

Our measurements of steady deformation on the western flanks of Volcán Arenal provide the first evidence of large-scale edifice movement at this volcano (Chapter 4). Arenal's western flanks have been plated by lava flows semi-continuously since the volcano's reactivation in 1968, increasing both the volcano's height and its asymmetry. Motion is apparently steady (average speed of ∼7 cm/yr) and generally down-slope (but steeper than the slope of the volcano itself, at an angle of ∼55° below the horizontal on the volcano's lower flanks). Subsidence is confined to a section of the volcano's western flanks suggesting a shallow source, within the edifice of the volcano itself. I attribute the rapid, high angle deformation at Arenal to slow gravity-driven slip, although it seems probable that lava subsidence also makes some contribution. The boundary between post-1968 eruption lavas and the paleosols and older eruptive products below is a potential location for a sliding plane, although it may be even shallower than this.

My measurements from Santiaguito (Chapter 5) demonstrate the measurement of topographic change from sets of interferograms, an approach that has the potential to be a useful tool for volcanologists. I successfully retrieved extrusion rate, flow morphologies and subsidence from measurements of dacitic lavas extruded at Santiaguito since 2000. Extrusion rate at Santiaguito between 2000 and 2009 was 0.43 ± 0.06 m^3/s, close to mean lava dome extrusion since 1922. Over this time, dacitic lavas from El Caliente dome followed a channel established during

eruptions that started in 2000. The thickest and youngest parts of the lava flows were subsiding at a rate of roughly 6 cm/yr in 2009-10.

Measurement of large topographic change with sets of interferograms is particularly well-suited to large changes in topography that would result in decorrelation and therefore be impossible to measure with DInSAR, especially when such events are followed by a period of scatterer stability (e.g. volcano quiescence). Synthetic tests suggest that a minimum of 5 interferograms (atmospheric noise of maximum standard deviation 6 mm and baselines with mean = 0 m, standard deviation = 250 m) are needed to be sure of capturing uniform topographic change of magnitude $\geq$ 25 m. InSAR measurements of topographic change will be most useful where other methods are limited, for example, by frequent cloud cover.

This thesis demonstrates the retrieval of volcanologically useful information from relatively small sets of interferograms with high levels of atmospheric noise. Measurements at Arenal have improved our understanding of edifice stability and associated hazard at Arenal in spite of coherence being confined almost entirely to fresh lava flows. The measurement of extrusion rate I was able to make at Santiaguito illustrates how phase contributions commonly treated as noise in InSAR processing can be used to find parameters crucial to modeling the eruptive behaviour of many volcanoes. Analysis of ‘null’ results, from volcanoes that were erupting but not deforming, has allowed me to draw some order of magnitude conclusions about the nature of the magmatic plumbing beneath them. Finally, the quantification of uncertainty in InSAR measurements of volcano deformation has also allowed me to make a meaningful comparison of the incidence and global distribution of volcano deformation as measured with InSAR.

Acknowledgements

Many thanks to my supervisors Juliet Biggs and Tamsin Mather for their support and advice. I particularly appreciate the encouragement they have both given me to write up and to present my work. Thanks to Juliet also for putting me up on many occasions over the past four years, both in Miami and more recently in Bristol.

Many thanks also to Don Grainger, Andy Sayer, Elisa Carboni and the Earth Observation Data Group in the department of Atmospheric, Oceanic and Planetary Physics, University of Oxford, where I have been working periodically (on a project not ultimately included in this thesis) during the course of my PhD. I found the time spent working in AOPP interesting and stimulating and I look forward to returning to it very soon.

I have visited and worked at the Rosentiel School of Marine and Atmospheric Science, University of Miami on two occasions in 2009 and 2010. In the first month I spent in Miami I was helped greatly with various computing and processing difficulties by Batuhan Osmanoglu and Scot Baker. Thanks also to Tim Dixon and Falk Amelung for useful conversations about my work.

I was lucky to have the opportunity to visit Arenal, Costa Rica with a group from Georgia Institute of Technology in March 2010. This trip helped me develop a much better understanding of the volcano's structure and to use my InSAR measurements to assist in the placement of campaign GPS stations. I thank Andy Newman (Georgia Tech.), Marino Protti (OVSICORI-UNA) and Rodolfo van der Laat (OVSICORI-UNA) for many useful conversations.

I would like to acknowledge the friendship and support of officemates in the Department of Earth Sciences: they have made me enjoy and look forward to coming in to work.

My PhD was supported by the Natural Environmental Research Council through the National Centre for Earth Observation (NCEO), of which the Centre for the Observation and Modeling of Earthquakes, Volcanoes and Tectonics (COMET+) is a part. All ALOS data were acquired through the WInSAR programme at the University of Miami. The ASTER data are

distributed by the Land Processes Distributed Active Archive Center (LP DAAC), located at the U.S. Geological Survey (USGS) Earth Resources Observation and Science (EROS) Center. Radarsat data were supplied through the University of Miami's Centre for Southeastern Tropical Remote Sensing. TerraSAR-X data were acquired through a NERC small grant to Juliet Biggs and Geoff Wadge (University of Reading).

Juliet Biggs and Tamsin Mather have provided comments and advice on all the chapters in this thesis during their development. Geoff Wadge provided the pre-2000 DEMs used in Chapter 4 and made helpful comments on the manuscripts that make up Chapters 4 and 5 before their publication, as did Falk Amelung. Thanks to John Elliott for useful conversations about inversion and statistics that contributed to the development of Chapter 5, and for proof reading. The papers upon which Chapters 2, 3, 4 and 5 are based were improved following reviews by Matt Pritchard, Manoochehr Shirzaei, Yosuke Aoki and four anonymous reviewers.

For my family: LAE, KPE, SJE and JRE with love and thanks.

And in memory of my grandfather,
Thomas Galloway Muir
who would have been one of the few to read this.

Contents

List of Figures

List of Tables

Chapter 1

Introduction

> Deformation data derived from Interferometric synthetic aperture radar (InSAR) have the capacity to illuminate a range of volcanic processes (Section 1.1). Since the mid-nineties InSAR (Section 1.2) has allowed the measurement of deformation at over 90 volcanoes worldwide (Section 1.3) and increased the scope and potential of geodesy as a tool for volcanologists. This thesis presents an analysis of InSAR data along the Central American Volcanic Arc (CAVA), which has one of the highest densities of active volcanoes in the world. Central America presents a particularly interesting, if challenging, target for an InSAR study due both to the high spatial concentration of volcanic activity and to the diversity in the eruptive style of its volcanoes (Section 1.4).

Volcanoes channel a flux of energy and matter from the Earth's interior to its surface. They play a crucial role in determining the distribution of the Earth's islands and continents, its climate and its capacity for sustaining life. Much of the earth's crust itself is built up from erupted lavas and intruded magma, while elements recycled from the mantle at mid ocean ridges (e.g. *Elderfield and Schultz*, 1996) and volcanic arcs (e.g. *Plank and Langmuir*, 1993) are important to the composition the oceans and atmosphere.

Almost 10% of the world's population lives within 100 km of a volcano that has been active since historical records began (*Small and Naumann*, 2001). Volcanoes present a hazard to the populations surrounding them, both from the eruption of lavas, pyroclastic flows and ash, but also due to events triggered by eruption or magma movement (e.g. lahars, degassing crises or jökulhlaups), or from the structural instability of the volcano's edifice itself. Volcanic activity also has major economic impacts, for example through the effects of ash on agriculture and aviation.

One of the driving aims of volcanology is to understand the behaviour of volcanoes well enough to predict their eruptions. This requires an understanding of both the slow, long-term processes that determine how magmatic plumbing develops beneath a volcano (e.g. *Dzurisin*, 2003), and the rapid, short-lived changes that precede eruptions (e.g. *Sparks et al.*, 2012). Measurements of the deformation of the earth's surface can capture magma movement on both scales.

1.1 Volcano Deformation

Volcano deformation can provide important evidence about the depth, ascent rate and storage conditions of magma. Deformation is also an important precursor to some types of volcanic eruption (*Dzurisin*, 2003). Geodetic data are independent, and often complementary to petrological and geochemical studies.

Ground-based methods of measuring surface movement at volcanoes have included tilt meters, leveling using high precision instruments (e.g. electronic distance meters or laser ranging) and strain meter measurements in boreholes (*Dzurisin*, 2003). More recently, Global Positioning System (GPS) measurements have allowed three dimensional deformation fields to be monitored continuously (e.g. *Owen et al.*, 2000). Interferometric Synthetic Aperture Radar (Section 1.2) has been used to measure volcano deformation since the mid-nineties (*Massonnet and Feigl*, 1995), and has improved the spatial resolution of deformation measurements in some parts of the world by at least an order of magnitude, having a typical pixel resolution of the order of $\sim$20 m, compared to the handful of ground-based instruments it is commonly practical to install. Other approaches to measurement of volcano growth and deformation include ground based radar and LiDAR instruments (e.g. *Wadge et al.*, 2005; *Fornaciai et al.*, 2010).

Deformation is expected to precede and accompany most volcanic eruptions (*Sparks et al.*, 2012). The magnitude and duration of any such deformation depends on the volume of magma on the move, but also the depth, ascent rate and magma composition (particularly gas and crystal fraction). Co-eruptive deformation typically has a smoothly varying spatial pattern, with magnitude decreasing away from the site of eruption (*Dvorak and Dzurisin*, 1997), and is commonly well approximated by a simple point source. Close to an eruptive vent, however, behaviour may be brittle, resulting in chaotic patterns of deformation that are much harder to interpret.

Surface deformation fields can be inverted to find a best fit source depth and rate of volume change. This is commonly achieved using an analytical source model, the simplest and most commonly used of which is a point source in an elastic half-space (*Mogi*, 1958). Although such a model does not account for surface topography, inhomogeneities in the crust or allow finite source geometries, it has been found to fit well to deformation patterns at many volcanoes. The introduction of further complexity is only warranted if data a) include at least two components of displacement (i.e. both vertical and horizontal information) and b) are of high spatial resolution. Other commonly used analytical sources include those for a pressurised ellipsoid (*Davis*, 1986; *Yang et al.*, 1988), penny-shaped crack (*Fialko et al.*, 2001a) and uniform rectangular dislocation (*Okada*, 1985), used to model dyke opening.

Where data are dense, a potentially more informative approach is finite element modeling (FEM), which does not require assumptions about source geometry *a priori* (e.g. *Dieterich and Decker*, 1975; *Lu et al.*, 2005a; *Hautmann et al.*, 2009). This has the advantage over analytical approaches of allowing irregular geometries and non-elastic behaviour, although this requires accurate and detailed knowledge of the thermal and mechanical structure of the crust that is rarely available. *Masterlark* (2007)'s comparison of an analytical forward model (*Mogi*, 1958) to the results of FEM inversion found that analytical solutions were relatively stable with respect to variations in topography and layered variations in elastic properties, but were very sensitive to lateral variations in elastic behaviour and particularly the presence of any weak materials at shallow depths.

1.2 Interferometric Synthetic Aperture Radar

InSAR uses satellite radar images to make relative measurements of ground movement with a precision of millimetres to centimetres. Since its first use for scientific purposes in the early 1990's InSAR has provided new insight into a range of phenomena including, but not limited to, deformation caused by the earthquake cycle, urban subsidence associated with ground water withdrawal, ice-sheet and glacier movement and magma movement beneath volcanoes (examples discussed by *Massonnet and Feigl* (1998) and *Pritchard* (2006)). Detailed reviews of SAR and InSAR processing methods and approaches are provided by *Massonnet and Feigl* (1998), *Hanssen* (2001), *Bürgmann et al.* (2000) and *Simons and Rosen* (2007).

Chirped microwave pulses emitted from a moving satellite are returned from the earth's surface and recorded at the satellite antenna as a set of complex numbers. Synthetic Aperture Radar (SAR) improves upon the resolution of conventional radar (of the order of 5-10 km) by focusing the raw radar echoes to achieve resolutions of the order of 20 m (spatial resolution for SAR instruments mentioned in this thesis are presented in Table 2.5, Chapter 2). A point on the earth's surface can be identified uniquely by the intersection of circles of equal range from the radar antenna, and hyperbolas mapping equal Doppler shift due to the relative motion of the satellite to the ground. Range (cross-track) position is found by sorting each pulse emitted by the satellite according to two way travel time to the Earth's surface, while azimuth (along-track) position is determined from Doppler frequency shift (described in detail by *Burton et al.*, 2000). Range resolution depends on pulse length, and is improved in SAR instruments by using a chirped pulse, that can be post-processed to produce a shorter effective pulse length and therefore higher range resolution ('range compression'). Azimuth resolution is inversely proportional to satellite antenna length, and is improved by combining information from several consecutive pulses to simulate a larger effective antenna length (*Massonnet and Feigl*, 1998; *Bürgmann et al.*, 2000; *Simons and Rosen*, 2007; *Hanssen*, 2001). SAR data are acquired from side-looking geometry to avoid ambiguities between points on the left and right side of the satellite with the same travel time and Doppler shift, so the resulting radar images are distorted relative to ground coordinates (illustrations of radar geometry are included in Section 2.3).

A SAR image is a 2D map of amplitude and phase. Amplitude captures the radar reflectivity, while phase contains contributions from changes at the earth's surface, as well as a term proportional to range. Interferograms are constructed by finding phase difference between two SAR images aligned with the precision of a fraction of a pixel. The phase changes recorded in an interferogram are caused by changes to satellite viewing geometry (satellite position and relative rotation of target between acquisitions, $\Delta\Phi_{spatial}$), instrument thermal noise ($\Delta\Phi_{thermal}$), radar path through the atmosphere ($\Delta\Phi_{atm}$) and back-scatter from the ground surface. Changes at the earths surface capable of introducing phase shifts to an interferogram include deformation ($\Delta\Phi_{def}$), systematic changes to dielectric properties (e.g. due to moisture or thermal expansion/contraction, $\Delta\Phi_{ground}$) and changes to scattering properties within a pixel ($\Delta\Phi_{pixel}$). As this last is the combination of radiation reflected or scattered from numerous objects, it has the appearance of random noise and cannot be predicted in practice. Thus, the total phase change $\Delta\Phi$ is given by the sum of these components:

$$\Delta\Phi = \Delta\Phi_{spatial} + \Delta\Phi_{thermal} + \Delta\Phi_{atm} + \Delta\Phi_{def} + \Delta\Phi_{ground} + \Delta\Phi_{pixel} \tag{1.1}$$

Interferometric measurement of surface deformation ($\Delta\Phi_{def}$) is possible either when other sources of phase shift are constant over large areas, or are relatively small. If surface scatterer properties change rapidly as viewed by the satellite, phase will decorrelate, making phase incoherent and deformation measurement impossible (phase coherence is discussed further in Section 2.4).

For processing, the phase contribution due to changes in satellite position $\Delta\Phi_{spatial}$ is generally separated into a purely geometric component that treats the Earth's surface as a smooth ellipsoid ($\Delta\Phi_{orbit}$), and a topographic component ($\Delta\Phi_{topo}$). $\Delta\Phi_{orbit}$ can be corrected using a linear or quadratic empirical fit, while correction of $\Delta\Phi_{topo}$ requires an accurate digital elevation model (DEM). However, phase artefacts proportional to any difference between the DEM and true topography dominate interferograms for which satellite separation is large (discussed further in Section 2.2 and Chapter 5). Of the remaining terms that contribute to interferogram phase ($\Delta\Phi_{thermal}$, $\Delta\Phi_{ground}$, $\Delta\Phi_{atm}$), the retardation effect of water vapour on radar ($\Delta\Phi_{atm}$) is by far the most significant (see Section 2.1).

Interferogram phase is converted from *modulo 2π* fringes to continuous phase values by unwrapping. The phase gradient is integrated across pixels from a seed point, the displacement of which is set to zero. Unwrapping is possible only across areas that are continuously coherent, so that any unconnected patches of coherent data must be bridged manually by estimating the phase difference. Unwrapped phase data is converted into a map of displacement by multiplying by a factor of $\frac{\lambda}{4\pi}$, where λ is radar wavelength.

1.3 InSAR for Volcano Deformation

InSAR has changed the scope and goals of volcano geodesy over the past decade. Surface displacements are known for every coherent and unwrapped pixel in an InSAR image, while the spatial resolution of GPS or tilt meter data depends on the logistics of field campaigns or funds for installing permanent stations and is therefore limited by practical considerations. One remarkable outcome of InSAR surveys was the discovery of deep (12–25 km) magma accumulation in the Central Andes (*Pritchard and Simons*, 2004a). Prior to this, geodetic measurements of magma movement below depths of ∼6 km were rare, and limited to large calderas (e.g. Yellowstone, Long Valley, *Dvorak and Dzurisin*, 1997). However, the comparatively low temporal resolution of InSAR make it less well suited for measuring short-lived near-vent processes (e.g. *Mastin et al.*, 2008; *Lyons et al.*, 2012) than tilt meter, continuous GPS or even broadband seismometers.

The use of InSAR to observe volcano deformation has allowed measurement and initial hazard assessments in regions that are isolated, inaccessible or otherwise too dangerous for ground-based measurements to be made (e.g. Kiska, Aleutian islands (*Lu et al.*, 2002a) or Nyiragongo, Democratic Republic of Congo (*Wauthier et al.*, 2009). Satellite geodesy has increased the scale of volcano deformation surveys, allowing similar data across a whole volcanic region to be compared and informing the planning and choice of targets for field campaigns (e.g. Uturuncu, Bolivia (*Pritchard and Simons*, 2004a) or Alutu, Ethiopia, (*Biggs et al.*, 2011)). Regional-scale surveys (e.g. *Pritchard and Simons*, 2004a; *Fournier et al.*, 2010; *Philibosian and Simons*,

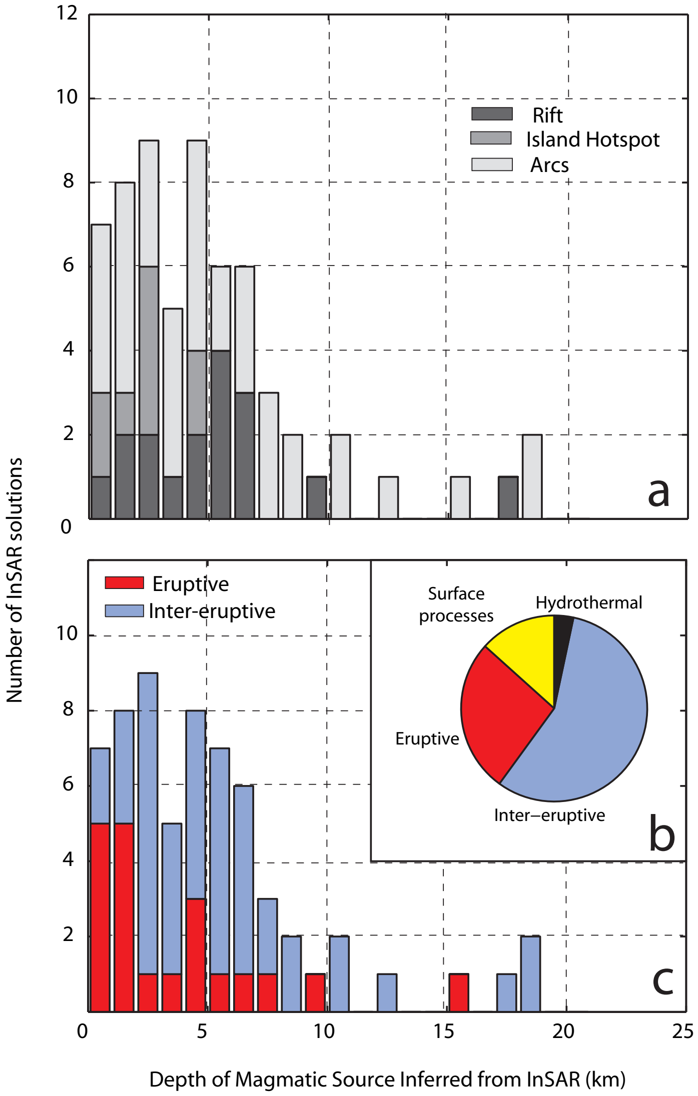

Figure 1.1: a) Histogram of global InSAR data, sorted by depth of inferred magmatic source and separated into measurements made at rifts (dark), island hotspots (grey) and arcs (pale). b) Pie chart showing the percentage of InSAR volcano deformation measurements attributed to inter-eruptive, co-eruptive, hydrothermal or edifice related ('Surface') processes. 'Co-eruptive' events were those clearly associated with a specific eruption, while 'inter-eruptive' refers to deformation where there is not (yet) any clear relationship to an eruption. 'Surface' processes include a range of types of deformation including gravitational spreading, volcano-related fault slip and flow-deposit subsidence. c) Histogram of global InSAR data, sorted by depth of inferred magmatic source and separated according to whether deformation was classed as 'co-eruptive' or 'inter-eruptive'. The literature data from which these figures are constructed is presented in Tables 1.1-1.3 .

2011) have also detected magma movement at volcanoes that otherwise appear to be quiescent (e.g. Paka, Suswa, Menengai on the East African Rift, *Biggs et al.* (2009c)) and at locations not obviously associated with a particular volcanic edifice (e.g. deformation at 'Lazufre' and Hualca Hualca, Central Andes, (*Pritchard and Simons*, 2004a)). The development of global, high resolution satellite data, (especially where it has been made freely available) is particularly important for developing countries where volcano observation is commonly less well funded.

Table 1.1: Summary of global literature on InSAR volcano deformation: co-eruptive and post-eruptive deformation. Events marked '^{a}' are pre-eruptive, '^{b}' indicates a post-eruptive event

Volcano	**Eruption** *date, VEI*	**max. rate** *cm/yr*	**model**	**depth** *km*	**Δvolume** *m^3*	**Reference**
ALEUTIANS/ALASKA						
Seguam	1992-93 VEI 2	10	point source array	0.5-5.5	-	*Masterlark and Lu* (2004)
Okmok	1997 VEI 3	2-10	Mogi	3.5	$-4.7\pm0.5\times10^7$	*Lu and Dzurisin* (2010b)
	2008 VEI 4	17-20	Mogi	3.5	$3.7\text{-}5.2\times10^7$	*Lu and Dzurisin* (2010b)
Makushin	1995 VEI 1	7	Mogi	7	2.2×10^7	*Lu et al.* (2002b)
SUMATRA/JAVA						
Krakatau	2007-08 VEI 2	4^a, 6,-9 ^{b}	dyke	0.4	1.05-	*Agustan et al.* (2012)
Slamet	2009 VEI 1	$3^{a?}$	Mogi	0.8-1.5	$3\text{-}5\times10^5$	*Philibosian and Simons* (2011)
Sinabung	2010 VEI 2	$4.7^{a?}$	Mogi	0.7	-	*Chaussard and Amelung* (2011)
Kerinci	2009 VEI 1	$6.4^{a?}$	Mogi	1.6	-	*Chaussard and Amelung* (2011)
ANDES						
Galeras	2008 VEI 3	-3	Mogi	2	6.5×10^5	*Parks et al.* (2011)
Lascar	1995 VEI 2	-1.7 (summit)	Mogi	0.18	2×10^5	*Pavez et al.* (2006)
Llaima	2003, VEI 2	-10^b	Mogi	4-12	$-10\text{-}46\times10^{6\ b}$	*Bathke et al.* (2011)
	2007-08 VEI 3	8^a	Mogi	4-12	$6\text{-}20\times10^{5\ a}$	
Chaitén	2008 VEI 4	-22	dyke	15.9	$3\text{-}10\times10^7$	*Fournier et al.* (2010)
MEXICO/ANTILLES						
Colima	97-11 dome growth	-1.5 (summit)	Mogi	2.5	0.23×10^6	*Pinel et al.* (2011)
Soufrière Hills	99-00 dome growth	2-3 (summit), 1-2 (farfield)	point source	6	-	*Wadge et al.* (2006)
ITALY						
Etna	1995 VEI 3	?	Yang, fault	4.8		e.g. *Lundgren et al.* (2003)
AFRICA						

Continued on next page

Table 1.1 – continued from previous page

Volcano	**Eruption**	**max. rate**	**model**	**depth**	**Δvolume**	**Reference**
	date, VEI	*cm/yr*		*km*	m^3	
Ol Doinyo Lengai	2007 rifting	<40	dyke, mogi, fault	4, 5.6, 3.6	-	*Biggs et al.* (2009a)
Nyamulagira	2002 VEI 2?	28	two dykes	0, 3	-	*Wauthier et al.* (2012)
Nyiragongo	2002 VEI 2?	15	dyke	1-3?	-	*Wauthier et al.* (2009)
ICELAND						
Eyjafjallaj okull	2010 VEI 4	-	sill	4.5-4.7	$13\text{-}15\times10^6$	*Sigmundsson et al.* (2010)
Hekla	2000 VEI 3	-	Mogi	14-20	$4\text{-}8\ \times10^4$	*Ofeigsson et al.* (2011)
Gjalp/Bardarbunga	-	-	dyke	6-2.5	-	*Pagli et al.* (2007)
ISLANDS						
Fogo	1995 VEI 2	10	dyke	2	-	*Amelung and Day* (2002)
Cerro Azul	1998 VEI 1	-15	Mogi	5	-	*Amelung et al.* (2000a)
Fernandina	1995 VEI 2	90	dyke	3	-	*Amelung et al.* (2000a)
Piton de la Fournaise	1998 VEI 1	50	dyke (open 60 cm)	<1	-	*Sigmundsson et al.* (1999)
	2003 VEI 1	30	dyke	<1	-	*Froger et al.* (2004)
Kilauea	dyke intrusion, 1999	∼10	dyke	5	3.3×10^6	*Cervelli et al.* (2002)

InSAR has now (as of 2012) been used to detect and measure deformation at over 94 volcanoes worldwide (e.g. *Fournier et al.*, 2010) and Tables 1.1-1.3). Almost half of all measurements are of volcanoes in continental and island arcs, roughly a third are from rifts (Iceland and East Africa) and a handful of deformation measurements (all <5 km depth) have been made at island hotspots (Figure 1.1). For small islands, the maximum depth that can be measured geodetically is limited by the diameter of the island. Deformation with source depth below ~ 10 km are primarily found at arcs, the exception being measurements of deep magmatic intrusion in Iceland, e.g. *Jakobsdóttir et al.* (2009) and *Hooper et al.* (2011).

More than half of literature measurements were not obviously associated with a particular eruption ('inter-eruptive'), while around a quarter of the deformation events occurred either during an eruption, or as a clear consequence of it (e.g. Okmok, Chaiten, *Lu and Dzurisin*, 2010b; *Fournier et al.*, 2010). This over-simplified distinction may be useful where it separates rapid co-eruptive deflation and post-eruptive re-inflation events from the more gradual accumulation of magma in the crust, allowing their depths and distributions to be compared (Table 1.1). However, the distinction between 'inter-eruptive' and 'co-eruptive' deformation is not always clear. For example, the intrusion of sills at between 4.5-6.6 km depth beneath Eyjafjallajökull in 1994 (*Pedersen and Sigmundsson*, 2004) in 1994 and 1999 (*Pedersen and Sigmundsson*, 2006) preceded the larger intrusions of 2010 that eventually resulted in eruption (*Sigmundsson et al.*, 2010). At Tunguruhua, Ecuador, InSAR measurements showed uplift equivalent to a volume of 1.2×10^6m^3 (*Biggs et al.*, 2009b) during eruption in 2008. This material has not yet been erupted and may simply result in internal growth of the edifice.

The growing number of InSAR measurements of non-magmatic volcanic processes include the compaction of flow deposits (*Stevens et al.*, 2001a; *Matthews et al.*, 2003; *Fournier et al.*, 2010; *Wade et al.*, 2006) and gravitational spreading (*Lanari et al.*, 2002; *Schirzaei et al.*, 2011). Measurements of lava subsidence were often incidental to the InSAR studies that focused on magmatic deformation, e.g. on the Galapagos Islands (*Amelung et al.*, 2000a), or at Okmok (*Lu and Dzurisin*, 2010b). However, InSAR has also provided new insight into the relative importance of thermal contraction and clast repacking to lava subsidence (*Stevens et al.*, 2001a), and to the strength of fractured pumice flow deposits (*Whelley et al.*, 2012). Measurements of the rheological properties of fresh volcanic deposits are important for understanding the stability of a volcanic edifice.

Table 1.2: Summary of global literature on InSAR volcano deformation not clearly associated with a particular eruption

Volcano	**max. rate** cm/yr	**source depth** km	**Reference(s)**
ALEUTIANS			
Kiska	-5	1	*Lu et al.* (2002a)
Akutan	60	0.4-3.6	*Lu et al.* (2004)
Tanaga	3	?	*Lu* (2007)
Korovin(Atka)	2	?	*Lu* (2007)
Westdahl	3.5	8.7	*Lu et al.* (2000)
Fisher Caldera	-3	1.6-3.5	*Mann and Freymueller* (2003)
Veniaminof	1	8	*Lu* (2007)
Aniakchak	-13	4	*Kwoun et al.* (2006)
Peulik	17	6.6	*Lu et al.* (2002b)
New Trident	4	0.8-2	*Lu et al.* (1997)
KAMCHATKA			
Uzon	15	4	*Lundgren and Lu* (2006)
SUMATRA, JAVA, P.N.G			
Sulu	100	-	*Wicks et al.* (2007)
Talakmau	-4.3	7.4	*Chaussard and Amelung* (2011)
Agung	8.7	2.6	*Chaussard and Amelung* (2011)
Lawu	4.1	2.1	*Chaussard and Amelung* (2011)
Lamongan	6.7	4	*Philibosian and Simons* (2011)
ANDES			
Antisana	2	-	*Mothes et al.* (2008)
Tunguruhua	24	0.55	*Biggs et al.* (2010)
Hualca Hualca	2	8-18	*Pritchard and Simons* (2004a)
Ticsani	8	?	*Riddick et al.* (2008)
Uturuncu	2	12-25	*Pritchard and Simons* (2004a)
Cerro Overo	1	?	*Riddick et al.* (2008)
Lastarria	2.5	7-15	*Froger et al.* (2007)
Lazufre	3	5-13	*Pritchard and Simons* (2004a)
Cerro Blanco	-1.5	5-10	*Pritchard and Simons* (2004b)
Laguna del Maule	18.5	5	*Fournier et al.* (2010)
Copahue	-2	3.4-5.6	*Fournier et al.* (2010)
Cerro Hudson	5,-2	5	*Fournier et al.* (2010)
Cordon Caulle	20	3.8-6.9	*Fournier et al.* (2010)
CASCADES/USA			
Three Sisters	3 to 5	6.5+/-2.5	*Dzurisin et al.* (2006)
Medicine Lake	1	5-6	*Poland et al.* (2006)
Yellowstone	-2	11	*Wicks et al.* (2006)

Continued on next page

Table 1.2 – continued from previous page

Volcano	**max. rate** cm/yr	**source depth** km	**Reference(s)**
Socorro	0.2	19	*Finnegan and Pritchard* (2009)
EUROPE			
Campi Flegrei	3	2.5-3	*Lundgren et al.* (2001)
Nisyros	10	5	*Sykioti et al.* (2003)
Santorini	10	4.5	*Papageorgiou et al.* (2012)
NEW ZEALAND			
Taupo	-20	-	*Hole et al.* (2007)
EAST AFRICA			
Gada' Ale	-12	0.2-0.8	*Amelung et al.* (2000b)
Dabbahu	800	2-9	*Wright et al.* (2006)
Haledebi	-	2.7-8.8	*Biggs et al.* (2009c)
Alutu	(-)3-5 and 10	2.5	*Biggs et al.* (2009c)
Corbetti	-3	3.3-7.8	*Biggs et al.* (2009c)
Menengai	-1	5.2	*Biggs et al.* (2009b)
Longonot	3.3	6.2	*Biggs et al.* (2009b)
Suswa	-1.5	1.9 km	*Biggs et al.* (2009b)
Paka	25	6.3	*Biggs et al.* (2009b)
Harrat Lunayyir	14600	-	*Gomez* (2009)
ICELAND			
Hengil		7	*Feigl et al.* (2000)
Eyjafjallj okull		4.5	*Sigmundsson et al.* (2010)
Hekla	0.5	14-18	*Ofeigsson et al.* (2011)
Krafla	-	21	*de Zeeuw-van Dalfsen et al.* (2004)
Theistareykir	3	8.5	*Metzger et al.* (2012)
Upptyppingar	3	14-22	*Hooper et al.* (2011)
Askja	4	3.2-3.8	*de Zeeuw-van Dalfsen et al.* (2012)
ISLANDS			
Teneguia	-0.4	-	*Perlock et al.* (2008)
Mauna Loa	5	4.7	*Amelung et al.* (2007)
Wolf	0.3	2-3	*Amelung et al.* (2000a)
Darwin	3	2-3	*Amelung et al.* (2000a)
Alcedo	-40	2.2	*Hooper et al.* (2007)
Sierra Negra	90,3	2.3-2.9	*Amelung et al.* (2000a)

Table 1.3: InSAR global literature on measurements of flow deposit subsidence and edifice deformation.

Volcano	**Max. rate** (cm/yr)	**Description**	**Reference(s)**
Unzen	-12	pyroclastic flow compaction	*Matthews et al.* (2003)
Tolbachik	-3	lava subsidence	*Pritchard and Simons* (2004a)
Reventador	-	lava compaction	*Mothes et al.* (2008)
Lascar	-1,2	fracturing and subsidence of pumice flow deposits	*Whelley et al.* (2012)
Lonquimay	-2	lava subsidence	*Fournier et al.* (2010)
Llaima	-11	eruption-related landslip?	*Fournier et al.* (2010)
Paricutin	-4	contraction of lavas	*Fournier et al.* (2010)
Arenal	-7	slow sector subsidence	*Ebmeier et al.* (2010)
Santiaguito	<-6	lava subsidence	*Ebmeier et al.* (2012)
Vesuvius	-10	edifice spreading	*Lanari et al.* (2002)
Damavand	-0.5	edifice spreading	*Schirzaei et al.* (2011)
Seguam	-	thermoelastic contraction of lava	*Masterlark and Lu* (2004)
Okmok	-3	thermoelastic contraction of lavas and viscoelastic relaxation of caldera floor due to loading	*Lu and Dzurisin* (2010b)
Soufrière Hills	-1.2-1.5	contraction and settling	*Wadge et al.* (2006)
Fernandina	-	lava flow subsidence	*Amelung et al.* (2000a)
Sierra Negra	-3.3	lava flow subsidence	*Amelung et al.* (2000a)
Cerro Azul	-	lava flow subsidence	*Amelung et al.* (2000a)
Etna	>0.07	lava flow subsidence	*Stevens et al.* (2001a)
Etna	0.4-1.2	flank instability	*Froger et al.* (2001)
Hekla	-1.4	lava flow loading	*Grapenthin et al.* (2010)
Krapla	-0.7	lava subsidence	*Sigmundsson et al.* (1997)

1.4 The Central American Volcanic Arc

The Central American Volcanic Arc is made up of over 75 Holocene volcanoes, of which 26 are historically active. There is a notable correlation between high population density and recent volcanism in Central America, with population density actually decreasing with radial distance from both Holocene and historically active volcanoes (*Small and Naumann*, 2001). This has been attributed to better soil quality at higher elevations in the tropics, due both to the lower temperature and to a frequently renewed ash supply.

The main volcanic front stretches over 1100 km from Guatemala's border with Mexico, through El Salvador and Nicaragua to central Costa Rica. It originates in the rapid, high angle subduction of the Cocos plate beneath the Caribbean plate (up to 75 mm/yr beneath Costa Rica) (*Syracuse and Abers*, 2006). Volcanoes are spaced closely together (average ∼25 km) (*Carr*, 1984), and are distributed along linear segments ∼100-300 km in length and separated by right-stepping offsets. Segmentation has been attributed both to transverse breaks in the subducting slab (*Stoiber and Carr*, 1973) and to block rotation in the overriding plate (*Burkart and Self*, 1985).

Figure 1.2: Population density map of Central America with Holocene volcanoes marked as crosses, and historically active volcanoes marked as circles. This figure is reproduced from *Small and Naumann* (2001).

1.4.1 Magma Compositions and storage

Compositions of historically active Central American volcanoes range from basaltic to dacitic, with basalts being as least as common as andesites (*Carr*, 1984). With the exception of the Masaya caldera system in Nicaragua, there is not thought to be large-scale shallow storage of basaltic magma in Central America. Basaltic bulk composition analyses suggest magma chamber depths that correlate with Moho position, suggesting that magma pools at the sharp density contrast at the base of the overriding crust (*Carr*, 1984). The most dense and mafic basalts in Central America therefore ascend in Nicaragua, where the crust is thinnest (30 km, relative to 45 km in Costa Rica) and are trapped by low density layers in the shallow crust, forming shallow intrusions (*Carr*, 1984). Other recently erupted basaltic material in Central America has ascended directly from depth, without significant periods of storage, although it seems likely that small volumes of basaltic material are present beneath recently active volcanoes such as Cerro Negro (*La Femina et al.*, 2004) and Izalco (*Carr*, 1981d).

Andesite compositions at many Central American volcanoes show evidence for fractionation across multiple depths and pressures (e.g. *Martin* (1981); *Carr* (1981a); *Alvarado et al.* (2006)).

Figure 1.3: a) Map showing the spatial distribution of ascending ALOS data - the primary dataset presented in this thesis. Black boxes show the track locations and extent of our data and triangles show volcano locations. b) Descending ALOS data used to complement ascending data where possible. c) Map showing the locations of some of Central America's historically active volcanoes.

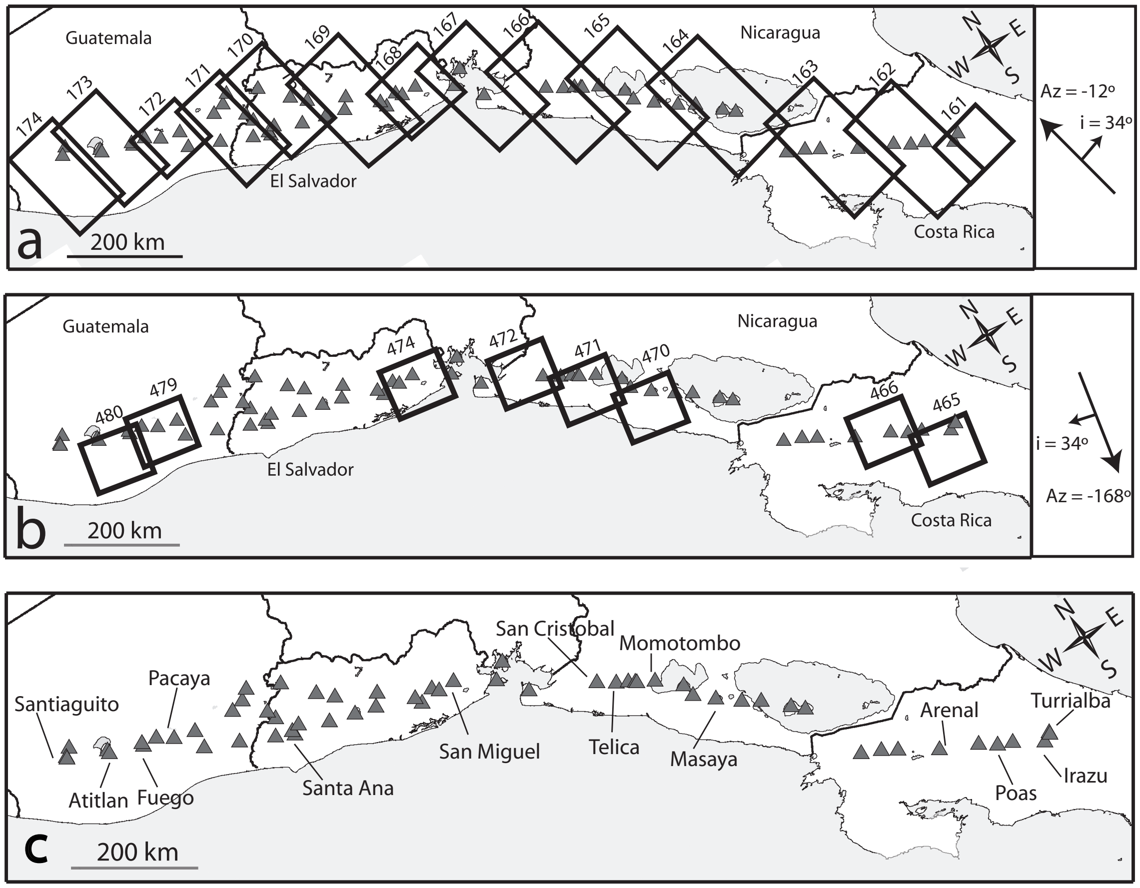

Carr (1981c) infer from the variety of fractionation styles at volcanoes in El Salvador that individual magma bodies are small and easily erupted. For most Central American volcanoes, we know little about the depths or geometries of regions of magma storage. Literature concerning the plumbing of historically active volcanoes in Central America is summarised in Tables 1.4-1.7.

1.4.2 Tectonic setting

Deformation along the active volcanic arc is characterised both by significant arc-parallel motion and by regions of extension (Figures 1.4, 1.5 and 1.6).

Central American kinematics are dominated by the escape of the fore-arc sliver to the northwest, accommodated by a zone of deformation along the volcanic arc (*LaFemina et al.*, 2009; *Turner et al.*, 2007; *Corti et al.*, 2005). This arc-parallel motion has been attributed both to the oblique convergence of the Cocos and Caribbean plates since 7-9 Ma (*DeMets*, 2001; *Morrell et al.*, 2012), and more recently to the continuation of movement initiated by the collision of

Figure 1.4: Figure reproduced from *DeMets* (2001) showing the volcanotectonic setting of the Central American Volcanic Arc. Strike-slip earthquake focal mechanisms are shown along with compressional axes for shallow thrust earthquakes 1962-2001. Plate velocities are relative to the Caribbean plate (*DeMets*, 2001)

the Cocos Ridge with the Caribbean plate in Costa Rica 0.5-5 Ma (*LaFemina et al.*, 2009). It seems probable that both factors play some role in driving fore-arc motion. Convergence in Central America is ~10° anticlockwise of trench-normal, and *DeMets* (2001) estimates the trench parallel component of this motion to be up to 14 mm/yr relative to the Caribbean plate in Guatemala and Nicaragua. However, GPS measurements of high fore-arc motion in El Salvador (13–17mm/yr), where obliquity in convergence is lower than in neighbouring Guatemala and Nicaragua, has been taken to imply that the fore-arc is being pushed from the southeast (*Correa-Mora et al.*, 2009; *Alvarado et al.*, 2011). The lack of a well-defined trench-parallel strike-slip fault (e.g. as exists in Sumatra) is also indicative of an immature system and in keeping with a recent onset of arc-parallel motion (*LaFemina et al.*, 2009).

Segments of the Guatemala, El Salvadoran and Nicaraguan volcanic arcs are also under extension. East-west extension is caused by the slower westward movement of the Caribbean plate relative to the North American plate (10-15 mm/yr less, *Phipps Morgan et al.*, 2008). This difference in relative Caribbean and North American plate motions is mostly, but not entirely, accommodated by sinistral shear in the Motagua shear zone and movement on the fast, well developed Jocotan and Motagua faults, e.g. *Burkart and Self* (1985).

Strike-slip and extensional deformation vary in their relative importance along the arc, and result in different types of faulting and structural features. Arc parallel shear is expressed by dextral, strike-slip faults in Guatemala and El Salvador (Figure 1.4). In Guatemala, strike-slip and extensional deformation seem to have formed separate structures, with shear taking place across the arc, and extension localised in rift zones (*Phipps Morgan et al.*, 2008). The

Figure 1.5: Tectonic setting of the Central American Volcanic Arc. Beachballs show Harvard CMT solutions for earthquakes greater than magnitude 5.

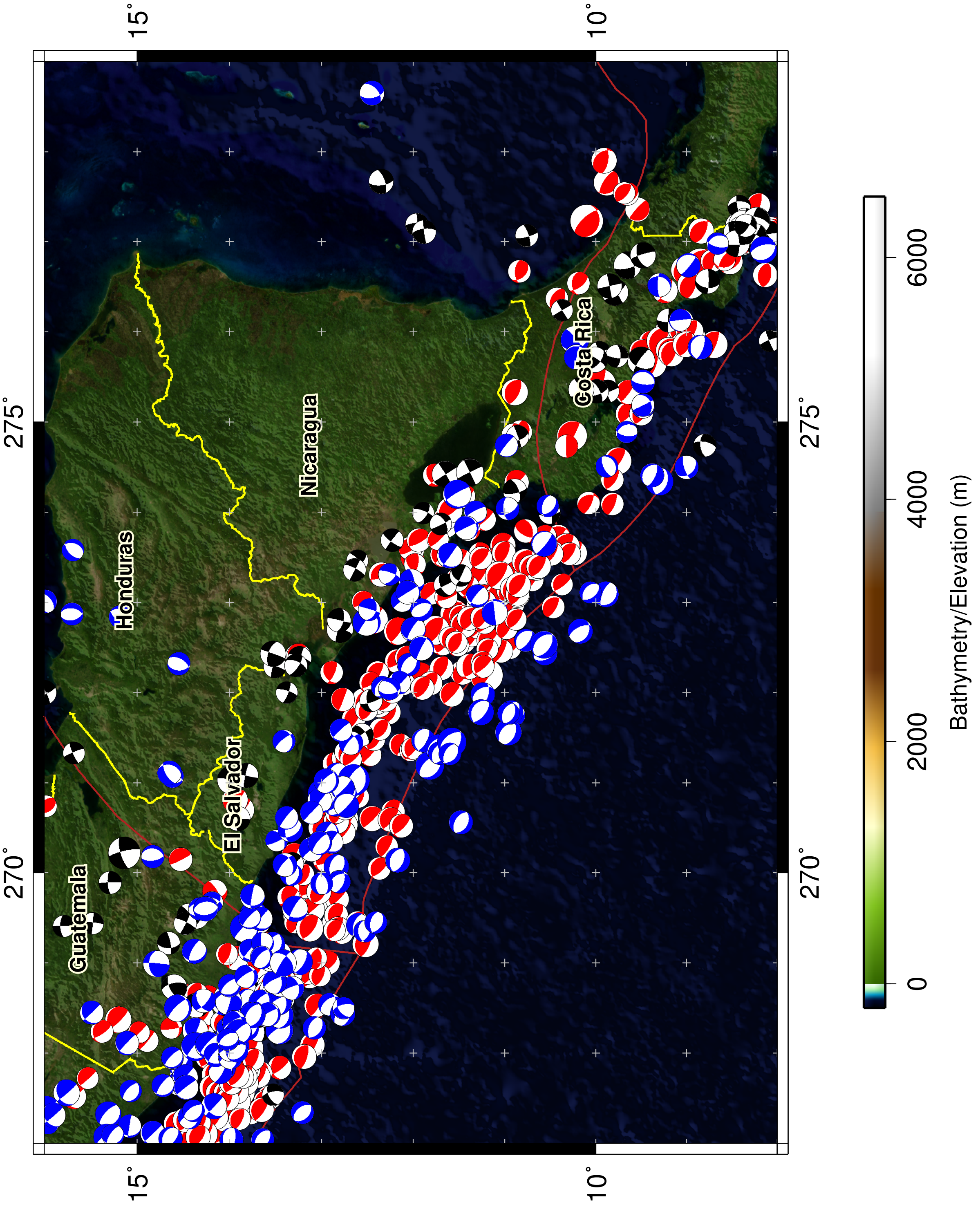

anticlockwise rotation of blocks in Southern Guatemala and El Salvador has been associated both with large extensional basins and the north-south orientation of pairs of composite volcanoes (*Burkart and Self*, 1985).

Arc-normal extension is thought to be most significant in Nicaragua, with long term extension considered to lie between 5 and 10 mm/yr, and expected to be associated with a large

Figure 1.6: Figure from *LaFemina et al.* (2009) showing GPS derived vector fields for Nicaragua and Costa Rica relative to the Caribbean plate. Large black arrows show relative rate and azimuth between the Cocos and Caribbean plates (*DeMets*, 2001)

intrusive magma flux, 1-2 orders of magnitude larger than recent extrusive volcanism (*Phipps Morgan et al.*, 2008). Even here, however, most recent seismicity can be attributed to strike slip faulting. Trench parallel strike-slip faults are poorly developed in Nicaragua, and high-rate oblique convergence may be accommodated by bookshelf faulting involving displacement along NE trending sinistral faults (*La Femina et al.*, 2002). *La Femina et al.* (2002) propose that these arc normal faults may have developed due to the trench-ward migration of the Nicaraguan active arc (50 km over 10 Ma, *Syracuse and Abers*, 2006).

In Costa Rica, fore-arc strain is accommodated on northwest and northeast trending strike slip and oblique slip conjugate faults, while the trailing end of the fore-arc sliver causes some extension (*Lewis et al.*, 2008). Trench parallel motion is present in Northern Costa Rica, but absent south of the Cocos ridge collision zone (and south of the active arc), where convergence is trench normal *LaFemina et al.* (2009).

There is some evidence to suggest that the kinematics of the Central American Volcanic Arc are still evolving, potentially as a result of collision of Cocos Ridge with Costa Rica <3 Ma (*Morrell et al.*, 2012). *Acocella and Funiciello* (2010)'s comparisons of measurements of arc and slab motions for 15 arc segements imply that slab-arc geometry in Central America may be out of equilibrium. Compared to other subduction zones, the Central American Arc was found to have a remarkably high extension rate relative to the trench normal component of subduction, with the only other outlier being Kamchatka (*Acocella and Funiciello*, 2010).

Table 1.4: Summary of published data concerning magma storage for historically active volcanoes in the Central American Volcanic Arc: Guatemala

Volcano	**Dominant composition**	**Volume**[a] **(km ^{3})**	**t**[b] **(km)**	**Last eruption and current eruptive character**	**Magma storage**	**Key references**
Santa María/ Santiaguito	dacitic lava dome complex	18/ 2	50	Plinian eruption of Santa María in 1902 (VEI 6(?)). Persistent dome building at Santiaguito since 1922	No petrological evidence for shallow magma storage, 1902 magma thought to have risen rapidly from reservoir at the base of the crust. Fractionation of Santiaguito dacites occurs during slow ascent	*Rose* (1972b); *Harris et al.* (2004)
Almolonga	andesitic stratovolcano (dacitic Cerro Quemado dome complex historically active)	5	~50	last eruption 1818	Cerro Quemado lavas originate in mixing of mafic and silicic material	*Michael Conway* (1992)
Atitlán	large composite cone (silicic)	33	~55	Last eruption 1853	Discontinuous trend of geochemical reversals indicates development of a series of small zoned magma bodies	*Woodruff et al.* (1979); *Newhall* (1987)
Acatenango	basaltic-andesitic stratovolcano (paired)	62	47	Last eruption 1972.		*Halsor and Rose* (1988)
Fuego	basaltic stratovolcano (paired)	73	47	Entered current phase of explosive activity in 2002. Variable explosive activity from VEI 2 to Strombolian, pyroclastic flows, lava flows.	petrological evidence indicates magma development at two depths: a) a shallow dyke system (2-8 km, >0.1 km^3) too narrow for convection and b) a large, deep chamber (8-16 km, >1 km^3), where closed system fractionation takes place. Fractionation by crystal redistribution during ascent in 1974 eruption.	*Martin* (1981); *Chesner and Rose* (1984); *Harris and Anderson* (1984); *Roggensack* (2001); *Lyons et al.* (2009)
Pacaya	basaltic complex volcano	17	45	periods of effusive eruption, with intermittent explosive episodes (Strombolian and Vulcanian)	magma 100-200m below surface in conduit, gravity anomaly modeled as 70-180m in radius from gravity data, large scale convection at shallow levels	*Eggers* (1983); *Conway et al.* (1992); *Rodríguez et al.* (2004); *Bardintzeff and Deniel* (1992)

[a] Edifice volumes are from *Carr et al.* (2003)

[b] Crustal thicknesses (**t**) are estimated from CRUST 2.0 (*Laske et al.*)

Table 1.5: Summary of published data concerning magma storage for historically active volcanoes in Central American Volcanic Arc: El Salvador

Volcano	**dominant composition**	**Volume**[a] **(km ^{3})**	**t**[b] **(km)**	**Last eruption and current eruptive character**	**Magma storage**	**Key references**
Santa Ana	andesitic-trachyandesitic (rhyolitic eruptions from NE flank in historical times)	220	38	VEI 3 eruption 2005, since then fumerolic activity and degassing	Two large chambers (bimodal lava silica contents), convecting graded magma chamber (negative Bouguer anomaly 3-7 km), overlain by highly developed hydrothermal system.	*Carr* (1981a,c); *Rodríguez et al.* (2004)
Izalco	basaltic-andesite stratovolcano (parasitic cone of Santa Ana)	2	38	nearly continuous Strombolian activity since first eruption in 1770. Last effusive activity in 1966.	Graded magma chamber, distinct (deeper) source from Santa Ana.	*Carr* (1981a,c)
San Salvador	basaltic-andesitic stratovolcano	68	35	VEI 3, 1917. infrequent explosive eruptions in historical times	Long lasting, stable reservoir with open-system fractionation.	*Carr* (1981c); *Fairbrothers et al.* (1978)
Ilopango	caldera, dacitic-rhyolitic	29	35	Last eruption 1880. Dome growth in caldera lake.	Historical eruptions were triggered by mafic intrusion into crystallising dacites. Large volumes of erupted dacites thought to be generated rapidly.	*Richer et al.* (2004); *Kutterolf et al.* (2008); *Garrison et al.* (2012)
San Miguel	basaltic-andesitic stratovolcano	68	35	Minor Strombolian since last lava flows in 1867. VEI 1 2002	Evidence for shallow magma storage (2-10 km), and shallowing of magma chamber over time as cone grew, drainage of shallow chamber thought to be responsible for the collapse of the summit region	*Carr* (1981c); *Chesner et al.* (2004)
Conchagüita	basaltic-andesitic stratovolcano	1	∼32	Last eruption 1892	-	-

[a] Edifice volumes are from *Carr et al.* (2003)

[b] Crustal thicknesses (**t**) are estimated from CRUST 2.0 (*Laske et al.*)

Table 1.6: Summary of published data concerning magma storage for historically active volcanoes in Central American Volcanic Arc: Nicaragua

Volcano	dominant composition	Volume[a] (km ^{3})	t[b] (km)	Last eruption and current eruptive character	Magma storage	Key references
Cosigüina	andesitic composite volcano	33	~35	Last eruption 1859	-	*Self et al.* (1989)
San Cristóbal	andesitic stratovolcano	65	35	Frequent minor explosive eruptions (VEI 1 and 2), most recent in 2010	High number of very shallow microseismic earthquakes and subsidence of crater floor in the 1970-1980s suggests shallow magma.	*Hazlett* (1987); *McNutt and Harlow* (1983); *Wood* (1974); *Gemmell* (1987)
Telica	basaltic-andesitic stratovolcano	28	34	Frequent minor explosive eruptions (VEI 1), most recent in 2008.	Magma reservoir at least 600 m down below active crater (from subsidence rate), not exceeding 500 m in diameter. Potentially an older, larger shallow storage region below 1.5 km. Eruption in 1997 preceded by seismic event at 6 km depth.	*Roche et al.* (2001); *Gemmell* (1987); *Locke et al.* (2003)
Cerro Negro	basaltic cinder cones	1	34	Born in 1850, frequent explosive eruption since that time (VEI 2 and 3), most recently in 1999.	Magma rose from at least 6km depth very during 1992 eruption	*Roggensack et al.* (1997); *McKnight and Williams* (1997); *La Femina et al.* (2004); *Carr* (1987); *Rose et al.* (1973)
Las Pilas	basaltic-andesite complex	12	34	Last eruption 1954, small phreatic explosions.	-	-
Momotombo	basaltic-andesite stratovolcano	18	34	Last confirmed eruption 1905, before that minor explosive eruptions were frequent (VEI 1 and 2).	Magma present few hundred metres below crater (thermal anomalies, fumerole temperatures, magnetotellurics)	*Gemmell* (1987); *Quisefit et al.* (1989); *Frische et al.* (2006); *Oppenheimer* (1993); *Benhamou et al.* (1988)
Masaya	basaltic shield volcano	168	34	Frequently active in historical times, high flux degassing, lava flows, occasional minor explosive eruptions (VEI 1 and 2)	interconnected, magma filled chambers extend from surface down to about 500m, below which is a larger magma reservoir	*Williams-Jones* (2003); *Burton et al.* (2000); *Rymer et al.* (1998); *Métaxian et al.* (1997) *and many others*
Concepción	basaltic-dacitic stratovolcano	19	~35	Last eruption 2011, currently active	Recent activity have been stored for a short time at relatively shallow depths	*Borgia and van Wyk de Vries* (2003a)

[a] Edifice volumes are from *Carr et al.* (2003)

[b] Crustal thicknesses (**t**) are estimated from CRUST 2.0 (*Laske et al.*)

Table 1.7: Summary of published data concerning magma storage for historically active volcanoes in the Central American Volcanic Arc : Costa Rica

Volcano	Dominant composition	Volume[a] (km ^{3})	t[b] (km)	Last eruption and current eruptive character	Magma storage	Key references
Rincón de la Vieja	basaltic-dacitic complex volcano	201	~36	VEI 2, 1998. phreatic eruptions, lahars and minor explosions	Shallow magma stored below active crater, at least 2 km. Possibly evidence for 4 pipes full of solidified andesite around summit area.	*Tassi et al.* (2005); *Kempter* (1996, 2000)
Miravalles	andesitic stratovolcano	132		Last eruption 1946, geothermal fields exploited for power.	-	-
Arenal	andesitic stratovolcano	13	37	Almost continuous since 1968, minor explosions, lava flows, occasional pyroclastic flows	12–14 km chamber drained during (and since) 1968 eruption, lava compositions are increasingly mafic.	*Reagan et al.* (1987); *Ryder et al.* (2006); *Lesage et al.* (2006); *Streck et al.* (2005); *Wade et al.* (2006)
Poás	basaltic-dacitic stratovolcano	168	41	Small phreatic eruptions 2009-2010, several VEI 1 central vent eruptions 2006-2010.	Solidified andesite magma in top of conduit, becoming molten below about 500 m (not a chamber).	*Rymer and Brown* (1987); *Rymer* (2000); *Prosser and Carr* (1987); *Thorpe et al.* (1981); *Fournier et al.* (2004); *Oppenheimer* (1992)
Turrialba	basaltic-dacitic stratovolcano	290	45	Phreatic eruption Jan 2010, previously VEI 3 1866	Hypocentral earthquake determinations from 2001-2002, 2005 and 2007 at depth 4-6 km	*Martini et al.* (2010); *Tassi et al.* (2009); *Reagan et al.* (2006); *Husen et al.* (2003)
Irazu	basaltic-dacitic complex	227	45	VEI 2 1994. Explosive eruptions from central and flanks vents, phreatic eruptions. Lava dome extrusion in the 1960s	Complicated plumbing, small magma chambers (trace element heterogenieties), one near surface to allow batch mixing over short timescales before eruptions. Two magma pipes with solidified andesite plugs, possibly with a molten material in pipe below 1km depth.	*Alvarado et al.* (2006); *Clark et al.* (1998); *Boyce and Hervig* (2009)

[a] Edifice volumes are from *Carr et al.* (2003)

[b] Crustal thicknesses (**t**) are estimated from CRUST 2.0 (*Laske et al.*)

1.5 Thesis structure

The rest of this thesis are organised as follows:

Chapter 2 is adapted from *Ebmeier et al.* (in press) and describes some of the technical difficulties of applying InSAR methods to a volcanic arc in the tropics, illustrated with examples from Central America. Particular attention is paid to the two most significant obstacles to the application of InSAR in the tropics: stratified water vapour and phase decorrelation due to dense vegetation.

Chapter 3 describes the results of an arc-scale survey of deformation in Central America. I discuss the significance and implications of the lack of magmatic deformation observed in Central America in terms of regional tectonics. I also investigate the implications of the lack of measurable deformation during eruptions of varying character between 2007-2010.

Chapter 4 is an expanded version of *Ebmeier et al.* (2010), and describes slow slip on the western flank of Arenal Volcano, Guatemala. Analysis of this signal suggests that it is shallow, gravity driven and limited to relatively young lava flows.

Chapter 5 describes a novel approach for measuring large-scale topographic change (and consequently effusion rate) at a volcano. This is applied to Santiaguito volcano, Guatemala, where lava thickness and subsidence rate are retrieved simultaneously. This work is published in *Ebmeier et al.* (2012).

Chapter 6 summarises the work outlined above and describes its context in recent volcano geodesy.

1.6 Related references:

Ebmeier, S. K., J. Biggs, T. A. Mather, G. Wadge, and F. Amelung (2010), Steady down-slope movement on the western flank of Arenal volcano, Costa Rica, **Geochemistry, Geophysics, Geosystems**, 11, Q12,004 14PP, doi:10.1029/2010GC003263.

Ebmeier, S. K., J. Biggs, T. A. Mather, J. R. Elliott, G. Wadge, and F. Amelung (2012), Measuring large topographic change with InSAR: Lava thicknesses, extrusion rate and subsidence rate at Santiaguito volcano, Guatemala, **Earth and Planetary Science Letters**, 335-336,216225, doi:10.1016/j.epsl.2012.04.027

Ebmeier, S. K., J. Biggs, and T. A. Mather. Applicability of InSAR to tropical volcanoes: insights from Central America, **Geological Society of London Special Publication**, **accepted June 2012**

Ebmeier, S. K., J. Biggs, and T. A. Mather. The apparent lack of deformation on the Central American Volcanic Arc, **in revision with JGR 14th December 2012.**

Chapter 2

The application of InSAR to volcanoes in the tropics

adapted from Ebmeier, S. K., J. Biggs, and T. A. Mather. *Applicability of InSAR to tropical volcanoes: insights from Central America*, Geological Society of London Special Publication, **accepted June 2012**

The global distribution of InSAR measurements of volcano deformation is currently spatially uneven (see Chapter 1). This is due, in part, to the differences in radar returns from different types of land surface. The majority of radar satellites have operated at C-band, $= 5.6$ cm, which is known to be affected by vegetation cover. This is a particular problem in the tropics where dense, rapidly growing evergreen vegetation is especially prevalent and causes a high rate of change in surface scatterer properties and therefore rapid decorrelation. This has presented significant obstacles for some C-band studies of volcano deformation in the tropics (*Zebker et al.*, 2000; *Stevens and Wadge*, 2004; *Pinel et al.*, 2011). In recent years this problem has been addressed to some extent with the launch of the Japanese satellite, ALOS, in 2006, which operates at L-band ($\lambda = 23$ cm) wavelengths. L-band radar penetrates dense vegetation better and allows a greater fraction of radar returns from more stable scatterers on the ground surface. ALOS data has allowed the first InSAR measurements at many volcanoes in the Caribbean, Northern Andes, Indonesia and Central America (*Fournier et al.*, 2010; *Biggs et al.*, 2009c; *Ebmeier et al.*, 2010; *Parks et al.*, 2011; *Philibosian and Simons*, 2011). Nonetheless, since the C-band archive stretches back to 1993 while ALOS was only launched in 2006, heavily vegetated volcanoes, many of which are in the tropics, have been understudied relative to those in drier regions.

Many of the worlds active volcanoes are in the tropics and have little or no coverage by ground based geodetic measurement (e.g. *Fournier et al.*, 2011a), so that InSAR observations may be the only available method for assessing and monitoring their geodetic activity and the related volcanic hazard. Quantifying the applicability of InSAR to tropical volcanoes is therefore important from both hazard mitigation and satellite design perspectives.

In this chapter I discuss the factors that affect the measurement of volcano deformation in the tropics using InSAR, drawing on examples from my L-band survey of the Central American Volcanic Arc (CAVA) between 2007 and 2010. Some of these factors apply globally (e.g. Digital Elevation Model (DEM) quality) while others (water vapour variations, vegetation) are of particular concern at tropical volcanoes.

I start by discussing the most significant issue, namely stratification and the variability in tropospheric water vapour concentration, which creates artefacts over topographic peaks (Section 2.1). Although such atmospheric artefacts are found at volcanoes across a wide range of latitudes, the significantly greater variability in water vapour concentrations in the tropics make them an extreme case.

I describe artefacts associated with the use of global Digital Elevation Models (DEMs) in Section 2.2 and geometric distortion effects in Section 2.3. Section 2.4 discusses patterns in phase decorrelation rates across the arc and their relationship to vegetation indexes and land use classifications and compare the usefulness and coherence of C-, L- and X- band SAR for a case study volcano, Arenal. The significance of the lack of observations of volcano deformation in Central America in relation to uncertainties in InSAR measurement and to tectonic setting is discussed in Chapter 3.

2.1 Tropospheric water vapour

2.1.1 Water Vapour Characteristics

In order to convert the observed phase changes to measurements of displacement, it is assumed that radar propagates at a constant speed. This would be reasonable for free space, where phase is dependent only on radar wavelength and path length, but introduces errors where there are significant spatial and temporal heterogeneities in the atmosphere. The effective path length actually depends on temperature, pressure and partial pressure of water vapour between satellite and ground surface and is separated into 'wet' and 'hydrostatic' delays, caused by water vapour and hydrostatic pressure respectively (*Bevis et al.*, 1992; *Hanssen*, 2001). Water vapour artefacts in interferograms depend on the difference between atmospheric conditions on the two dates when SAR data were acquired. Variations in water vapour (e.g. 10 cm in equivalent path delay for a 20% change in relative humidity) are expected to produce larger path delays than hydrostatic pressure (*Zebker et al.*, 1997). Nevertheless a 20 mb shift from fine to stormy weather could produce 4 cm equivalent path delay.

The spatial and temporal characteristics of the atmospheric artefacts depends on the distribution of water vapour in the troposphere. Where water vapour is mixed turbulently, it exhibits spatial correlation over length scales typically of the order of 10 km (e.g. *Hanssen*, 2001; *Lohman and Simons*, 2005), shows minimal or no correlation with topography and has typical variability of 1cm (e.g. *Pritchard and Simons*, 2004a). Large, steep volcanoes are commonly associated with both local turbulence on much smaller spatial scales and systematic features in atmospheric mixing caused by high topography (e.g. *Webley et al.*, 2004).

Vertically stratified water vapour in the troposphere results in low magnitude slant range path delays over high topography and higher, more variable paths delays over low topography (e.g. *Pavez et al.*, 2006). The resulting artefacts in an interferogram correlate with topography, and appear as concentric fringes around topographic peaks (Figure 2.1). As we may expect volume change of a sub-edifice magma chamber to produce a similar phase pattern, centred over the volcanic edifice (e.g. as observed at Etna, *Massonnet et al.*, 1995; *Beauducel et al.*, 2000), it is particularly difficult to distinguish between these two effects.

In equatorial zones seasonal variations in water vapour are largely controlled by the north-south migration of the inter-tropical convergence zone (ITCZ), producing some of the greatest variations in water vapour globally. Radar path delays of up to 11 cm, 8 cm and 6 cm have been measured at Mount Cameroon (*Heleno et al.*, 2010), Sakurajima, Japan (*Remy et al.*, 2003), and Soufrière Hills, Montserrat (*Wadge et al.*, 2006) respectively, Table 2.1.

2.1.2 Identification of Atmospheric Artefacts

Characteristic features of atmospheric phase artefacts include (a) a correlation between topography and phase (for stratified water vapour), (b) an association of the signal with particular acquisition dates and (c) either the lack of any dependence on time (turbulent water vapour) or a seasonal dependence (stratified water vapour) of signal magnitude (Figure 2.2). Water vapour artefacts are identified using a combination of these properties, as well as through the use of independent atmospheric data or models (examples from the literature shown in Table 2.1).

A correlation between height of topography and phase in an individual interferogram is indicative of the presence of water vapour, (e.g. Figure 2.3) but is not necessarily diagnostic. The injection or drainage of a body of magma within or just below a volcanic edifice could conceivably create a similar pattern in phase. However, where a number of topographic peaks in the same interferogram show similar phase patterns, they are most likely caused by atmospheric delay.

Analysis of the temporal development of phase through a set of interferograms provides

Figure 2.1: Cartoon illustrating the generation of a topographically correlated phase delay due to variations in concentration of stratified water vapour. Typical values for peak phase delay range from 1-5cm (2cm would indicate a 5% change in relative humidity).

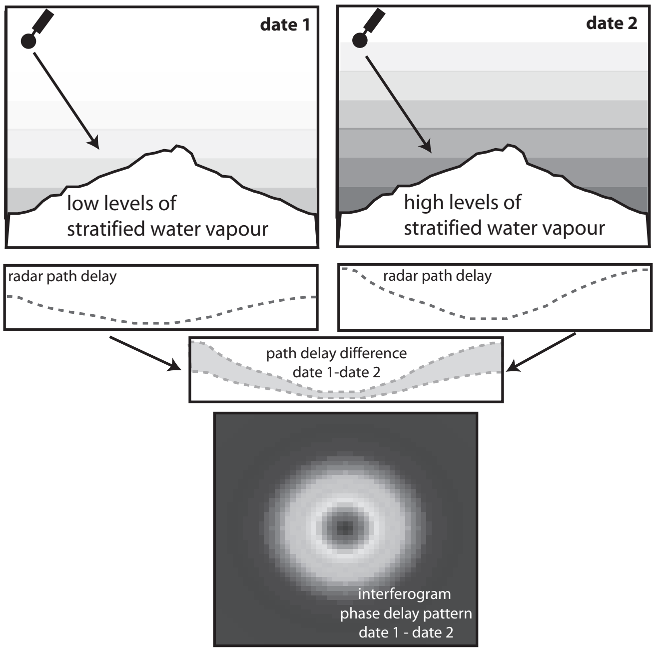

Table 2.1: Selected literature examples of the identification and/or mitigation of water vapour signals over volcanoes.

Volcanic	Maximum magnitude of atmospheric delay (cm)	Volcano height (m)	Explicit means of identification as stratified water vapour	Mitigation method	Reference
Mount Cameroon	11	4095	Phase-elevation correlation and seasonal correlation with MODIS and GPS water vapour measurements	-	*Heleno et al.* (2010)
Sakurajima	8	1117	Phase-elevation correlation	Network adjustment based on phase- elevation relationship	*Remy et al.* (2003)
Soufrière Hills	6	915	Implicit in correction	GPS water vapour correction	*Wadge et al.* (2006)
Popocatépetl	7	5426	Comparison to predicted delay from meteorological model	Correction of unwrapped phase with model delay	*Pinel et al.* (2011)
Colima	17	3850	Comparison to predicted delay from meteorological model	Correction of unwrapped phase with modelled delay	*Pinel et al.* (2011)
Etna	~6	3330	Comparison with atmospheric model	Correction from high resolution atmospheric model	*Wadge et al.* (2002, 2010)
Hualca Hualca	4	5967	Pair-wise logic, time independence	-	*Pritchard and Simons* (2004a)

further evidence to distinguish between atmospheric artefacts and true deformation. The method of ‘pair-wise logic’ (e.g. *Massonnet and Feigl*, 1995) compares pairs of interferograms that have a common date in master and slave positions. If artefacts of a similar magnitude and spatial pattern but opposite sign appear, then the artefact can be associated with the SAR acquisition date held in common. Two examples of such pairs from Momotombo volcano, Nicaragua are shown in Figure 2.4. Although this method had the advantage of simplicity, it is only reliable where atmospheric conditions are relatively stable and unusual phase delays are associated with a small number of acquisition dates.

At the sampling of the satellite repeat intervals, the temporal signal of atmospheric water vapour is expected to be either structureless, with a random variation in phase between relatively constant bounds or to vary with the period of a year as a function of seasonal variations in water vapour (e.g. *Heleno et al.*, 2010). Creating time series of interferometric phase (e.g. *Lundgren et al.*, 2001; *Berardino et al.*, 2002) is a useful tool when dealing with situations where atmospheric effects seem to dominate the majority of interferograms. Long term, steady-rate deformation may be detectable in this way, but reversible deformation (where net deformation over longer timespan interferograms is likely to be zero, as the ground returns to its original position) may be missed.

2.1.3 Water vapour in Central America

We use the characteristic properties described above to identify atmospheric water vapour in the Central American data set. We constructed time series for active volcanoes in Central America using a linear least squares inversion of the phase changes from a network of interferograms (e.g. *Lundgren et al.*, 2001; *Schmidt and Bürgmann*, 2003). Inversion was carried out with a generalised inverse matrix using singular value decomposition and solving for velocities between satellite acquisitions (e.g. *Berardino et al.*, 2002), rather than displacements, to avoid unrealistic discontinuities. This problem is commonly rank deficient where there are subsets of interferograms that do not hold an acquisition in common. We therefore solve for velocity relative to the first date, which we explicitly define as showing no deformation.

InSAR only provides relative measurements, as phase changes are always found relative to a reference point. While for volcanoes it is generally possible to select a reference far away from any deformation source, it is very difficult to avoid the effects of local atmospheric variation. If a reference pixel is selected over an area where atmospheric variation differs to that over the volcano, local differences in atmospheric delay are likely to dominate time series and mask any deformation. We avoid this problem by referencing our interferograms to the average value of phase within an annulus centred on the volcano, thus minimising the impact of atmospheric

Figure 2.2: Flowchart illustrating the process of analysing InSAR phase delays to (a) Phase 1: check the data for quality and (b) Phase 2: distinguish between atmospheric and deformation features. Deformation may or may not be correlated with topography, but perfect correlation is very rare

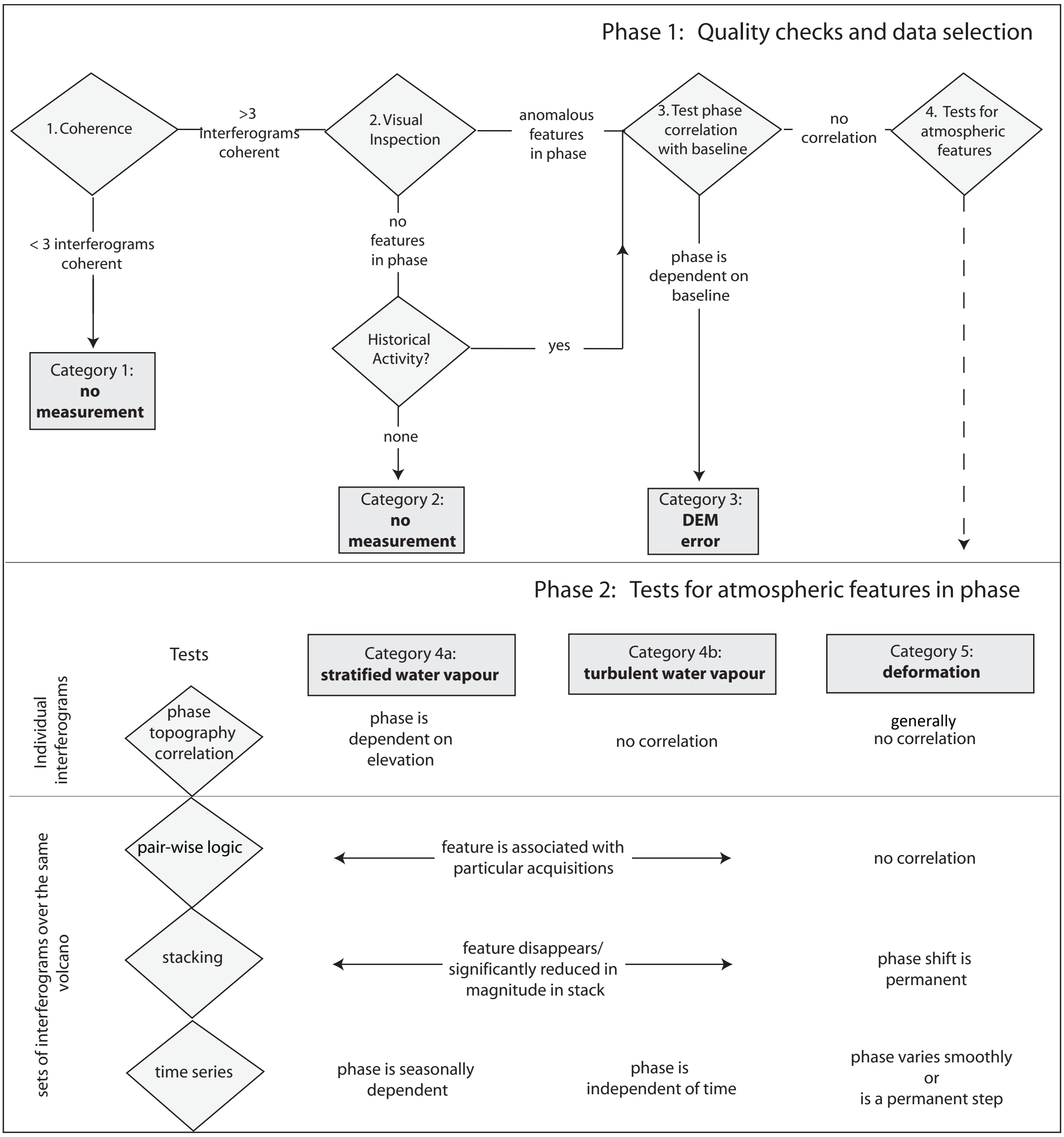

noise in other parts of the interferogram on our time series. Reference annuli typically had inner radii of 2-6 km and outer radii with limits defined by either the edge of the interferogram or (more commonly) the limit of the continuously coherent area. The difference between the mean height of topography within this area and the volcano summit was generally close to the volcano edifice height.

We remove a linear trend from the time series at a point over the volcanos edifice and find the root mean squared variation of the remaining signal. This r.m.s. variation is used as an indicator of the average magnitude of atmospheric delay at each volcano. The residual appears random with no systematic seasonal or similar trend. R.m.s variation shows a linear relationship with the difference in topographic height between the volcanic edifice and the mean height of the reference area (Figure 2.5). Excluding one outlier (Santa Ana, El Salvador) the time series r.m.s. variation increases with a best-fit gradient of 2 centimetres per kilometre height difference (Figure 2.5). The high value at Santa Ana is associated with large topographically correlated phase in one interferogram (Track 171, 9th March 2009 - 9th September 2009) and the removal of this interferogram from the time series reduces r.m.s. variation at Santa Ana to 3.8 cm, well within the normal distribution. There are no similar features in other interferograms for Santa Ana, and the time series is otherwise very similar to that for nearby cinder cone Izalco (just under 5 km South of Santa Ana).

This relationship between volcano edifice height and magnitude of atmospheric phase artefact has implications for the uncertainties on InSAR measurements at different volcanoes. For transient deformation (taking place over a period greater than the satellite repeat time) to be distinguishable from normal atmospheric variation at a volcano of edifice height exceeding 2000 m (e.g. Fuego), it must exceed about 4 cm, while it may be possible to detect much lower magnitude deformation (>1 cm) at low relief volcanoes (e.g. Masaya). Although it is not possible to test this with this dataset, if the interferograms were limited to those from the same season (e.g. winter-winter, or summer-summer), it seems probable that the relationship between topographic height and atmospheric variation would be weaker.

2.1.4 Potential for mitigation of Atmospheric Artefacts

Several methods have been proposed (such as stacking, empirical corrections, external data and models) by which atmospheric artefacts can be reduced or removed (e.g. *Hanssen*, 2001; *Remy et al.*, 2003; *Li et al.*, 2005, 2006; *Wadge et al.*, 2006). In this section, each method is outlined and assessed in terms of its applicability to the volcanoes of Central America.

As turbulent water vapour artefacts are essentially random in time, stacking a set of interferograms together will increase signal to noise ratio. However, the improvement in signal to noise ratio is achieved at a loss of temporal resolution, and is therefore better suited to studying long term than transient volcano deformation events.

Empirical corrections for stratified water vapour can be made on the basis of correlations between phase and topography. This is most robust for very large data sets with high temporal repeatability, so that analysis of phase-topography correlations for a set of interferograms can be used to make adjustments to the network of interferograms (e.g. *Beauducel et al.*, 2000; *Remy et al.*, 2003). Alternatively, where the area of deformation is already well-constrained by other data sources, topographically correlated fringes can also be removed from individual

Figure 2.3: Two interferograms (a and c) of San Miguel, El Salvador sharing a common date and their associated plots of range change against topographic height (b and d) on the edifice.

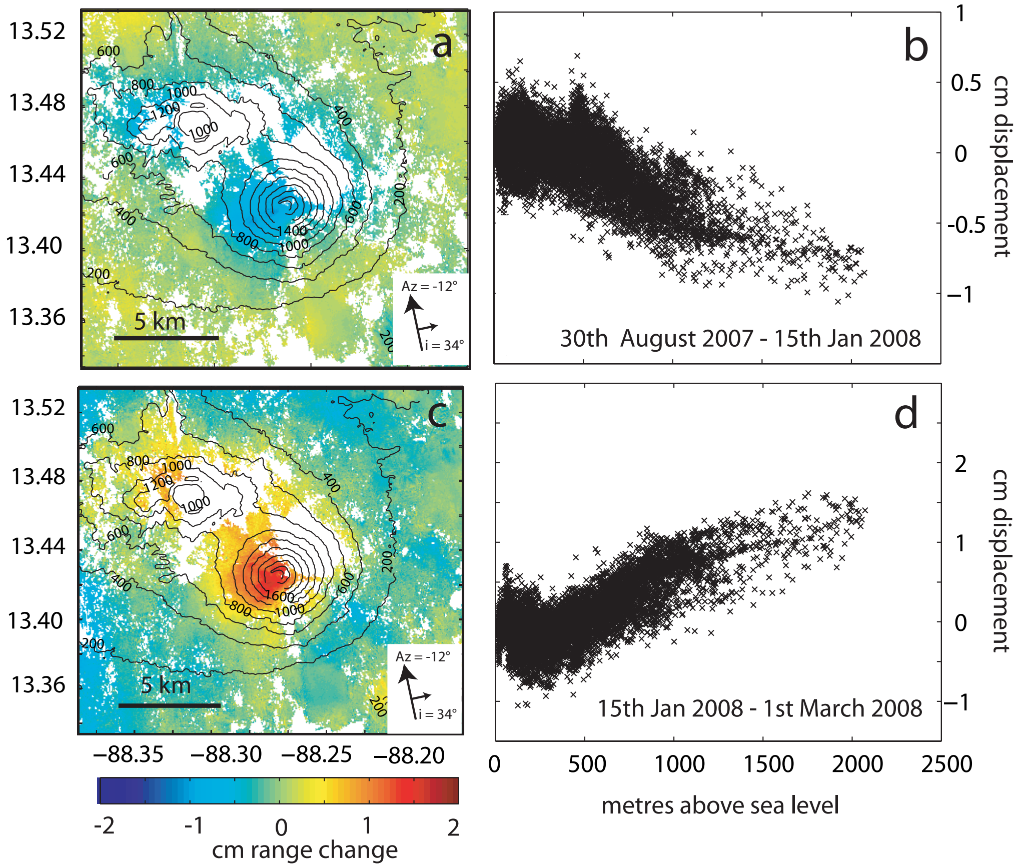

interferograms by solving for a best-fit relationship with topography, sometimes treated as linear (e.g. *Wicks et al.*, 2002), but shown to be better approximated by a non-linear model for steep volcanoes (*Remy et al.*, 2003). Recent studies have used band-pass decomposition (*Lin et al.*, 2010) and wavelet analysis (*Shirzaei and Bürgmann*, 2012) to find the relationships between topography and phase for different components of an interferogram.

Other approaches applied to correcting the effects of water vapour phase delays over volcanoes require direct measurements of water vapour, ideally coincident with SAR acquisitions. These include GPS measurements of water vapour *Wadge et al.* (2002, 2010) or satellite-based measurements (e.g. *Li et al.*, 2005; *Pavez et al.*, 2006). Calculation of phase delay directly from empirical water vapour and hydrostatic pressure values requires a high spatial density (limited for ground based instruments) and high temporal density (limited for satellite instruments) of measurements in order to provide a useful correction. A low density of measurements creates particular difficulties where the water vapour field is highly dynamic, as is commonly the case in the tropics. High resolution weather models have been used successfully to correct for atmospheric water vapour at Etna and over Hawaii (*Webley et al.*, 2004; *Wadge et al.*, 2006; *Foster* *et al.*, 2006) but so far have only been applied over limited areas, where local atmospheric physics is well understood.

In the absence of high densities of ground-based atmospheric measurements for calibration and an understanding of the dynamic weather systems around individual volcanoes, regional InSAR surveys of volcano deformation such as this are generally unsuitable for correction of atmospheric artefacts. Meteorological reanalysis data (e.g. *Jolivet et al.*, 2011; *Fournier et al.*, 2011b) has been used to removed atmospheric contributions on a regional scale, but the low spatial resolution of weather data available makes this approach more suitable for retrieving longer wavelength interseismic deformation than the deformation of volcanoes. Empirical atmospheric corrections from an assumed relationship with topography are likely to introduce artefacts or to remove elements of any deformation signal masked by it. Therefore, I did not attempt to remove water vapour variations from any of the Central American data.

Figure 2.4: a) North-South LOS range-change transects through a pair of interferograms from Momotombo volcano, Nicaragua. The fact that these lines are very close to being mirror images shows that the largest contribution to phase is associated with the date held in common and reflects an atmospheric artefact. Lines of the same shade hold an acquisition date in common. b) Scatter plot of phase from interferogram where common date is the master against (-1) phase from interferogram where common date is slave.

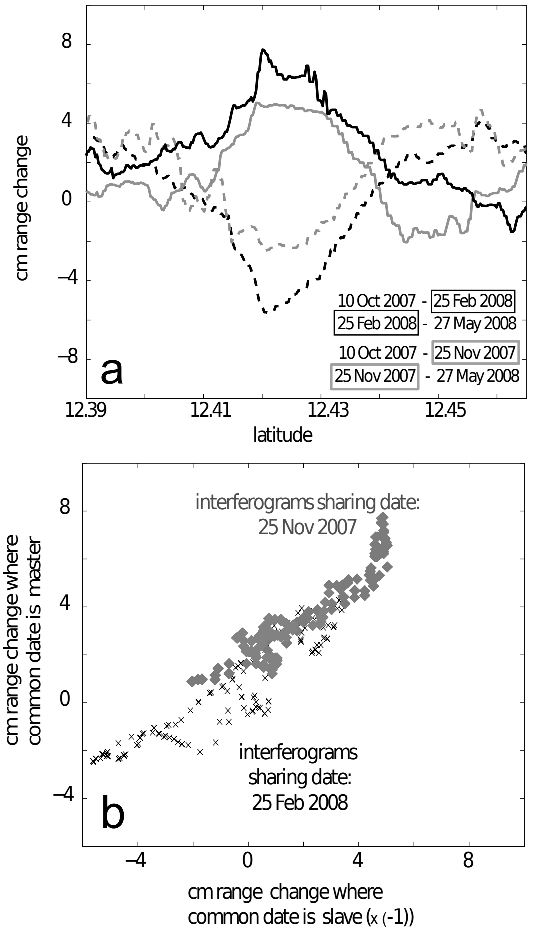

2.2 Limitations of Global DEMs and mitigation

Digital Elevation models (DEMs) are used to correct for the change in path length associated with the change in satellite position between acquisitions. Errors (δz) or gaps in the DEM propagate into the interferogram, creating phase shifts ($\Delta\phi$ topo), which are proportional to the satellite perpendicular baseline (B_{perp}), and inversely proportional to radar wavelength (λ), incidence angle (θ_i) and range of satellite from the ground (r) (e.g. *Rodriguez and Martin*, 1992; *Zebker and Villasensor*, 1992).

$$\delta\phi_{\text{topo}} = \frac{4\pi \mathrm{B}_{\text{perp}}}{\mathrm{r}\lambda\sin\theta_i}\delta\mathrm{z} \tag{2.1}$$

Such topographic phase changes can be identified by examining the relationship between phase ($\Delta\phi$) and perpendicular baseline (B_{perp}) for a set of interferograms and can be the result of a change in topography (Δz) since the DEM data were acquired, e.g. fresh lava flows emplaced since DEMs acquisition (*Ebmeier et al.*, 2012), or an error in the DEM itself (Figure 2.6b and c). For the same perpendicular baselines, topographic artefacts would be greater for C-band than L-band data but in practice the baselines for ALOS are generally much larger than for Envisat, and will produce greater topographic errors.

Over much of the world the only DEMs available for InSAR processing are global data sets derived from satellite data such as NASA's Shuttle Radar Topography Mission 90 m DEM (SRTM) and the Advanced Spaceborne Thermal Emission and Reflection Radiometer (ASTER GDEM). The SRTM DEMs (*Rosen et al.*, 2001) was acquired from single pass Interferometric Synthetic Aperture Radar (SAR) instrument on an 11 day shuttle mission in February 2000. Errors in height from SRTM data are made up of uniformly distributed, small systematic errors due to shuttle motion ($>$ 2 m) and spatially variable medium to short wavelength errors, particularly over steep topography (2-10 m) (*Rodriguez et al.*, 2006). These errors are larger and more common both at lower latitudes, where fewer data were collected, and over high topographic relief, where geometric decorrelation in phase (see Section 2.4) has most impact (*Rodriguez et al.*, 2006). The volcanic arc in Central America falls into both of these categories, and can be expected to have errors of the order of 10 m, which correspond to artefacts of magnitude 0.5-2 cm for ALOS interferograms (typical baselines 500-2000 m).

The ASTER GDEM (*Reuter et al.*, 2009) was constructed from Aster band-3 near infrared imagery. DEMs are produced from the 10 year archive of stereo pairs of ASTER images, cloud-covered areas are masked out and the DEMs are stacked; the final ASTER GDEM records the best-fit topography for the non-cloudy images. The average root mean squared error in GDEM heights is 18-29 m (*Reuter et al.*, 2009). Largest uncertainties are expected to be in areas of frequent cloud cover where the DEM was constructed from small numbers of ASTER stereopairs (e.g. Pacaya, Figure 2.6a and b).

The SRTM DEM was interpolated to a resolution of 30 m and used in InSAR processing for the majority of volcanoes in Central America. For a few volcanoes where there were issues with the SRTM data or there has been significant topographic change since 2000, results were also compared to interferograms corrected using ASTER GDEM. Despite gaps in the SRTM DEM around some volcano summits (e.g. Momotombo, Nicaragua, Figure 2.6 c), the interpolated version was accurate enough to allow us to process interferograms without introducing artefacts into the phase. However, the GDEM was found to introduce artefacts, presumably due to the low number of cloud-free images. With enough interferograms and a large enough range of baselines, it is possible to use Equation 2.1 to calculate errors in topographic height with an

Figure 2.5: a) Time series of phase over the edifice of San Miguel, El Salvador (summit 2130 m a.s.l.) and b) Las Pilas, Nicaragua (1088 m a.s.l.). Error bars show the standard deviation of 100 Monte Carlo repetitions of the inversion with randomly generated, non-spatially correlated noise of amplitude 1 cm added to each interferogram. c) Plot of root mean square variation in detrended time series for active volcanoes as a function of the height different between volcano summit area and the average topographic height of the reference annulus. The thick solid line shows the line of best-fit, the dashed line shows 95% confidence envelope for the mean and thinner solid line on part c) and dots on parts a) and b) show 95% confidence envelope for any individual point.

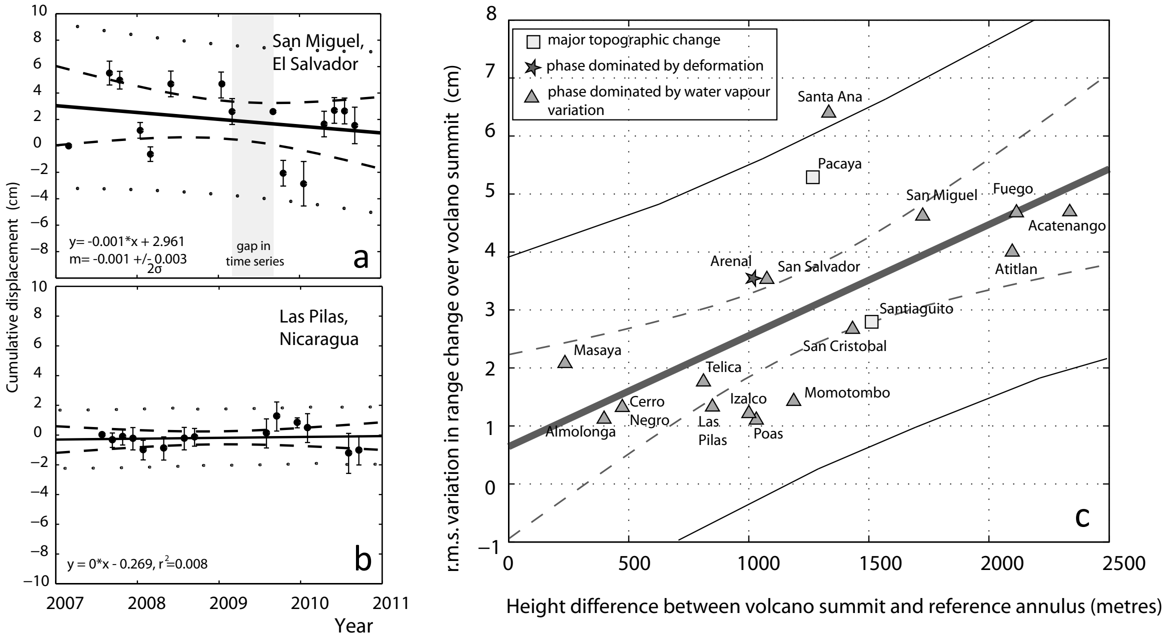

accuracy sufficient to correct any errors in the DEMs (see Chapter 4).

Both SRTM and GDEM have very low spatial resolutions (90 m and 30 m) compared with new X-band SAR data (3 m), such as that from TerraSAR-X (TSX). This new data will be most useful over small areas where deformation is known to be taking place and a high resolution local DEM can be acquired.

Figure 2.6: a) The number of ASTER images used to determine topographic height over Pacaya volcano, Guatemala at each pixel. Data is not used when the ground is obscured by cloud or by the volcanic plume. b) Map of DEM error calculated from topographic phase changes in a set of interferograms corrected using the ASTER GDEM. c) Data gap near the summit of Momotombo, Nicaragua, SRTM 90 DEM. Similar features are found in both SRTM and GDEM. Interpolation of such gaps generally do not result in DEM errors in interferograms.

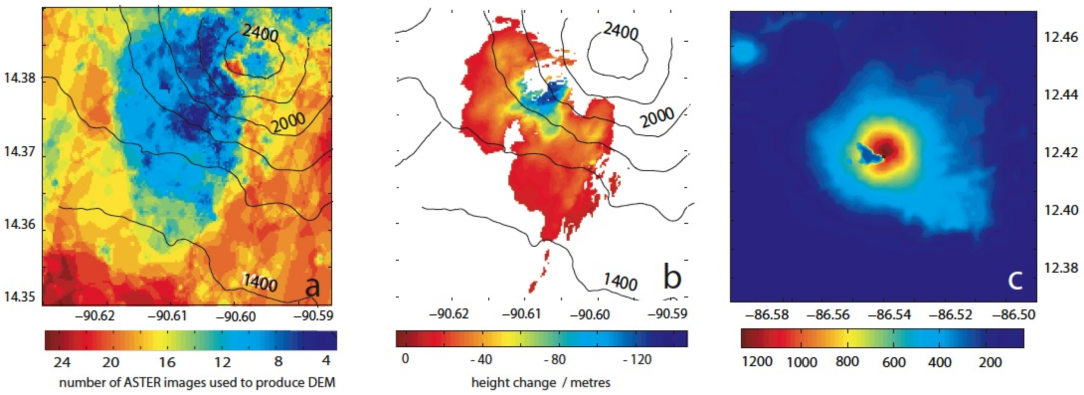

2.3 Geometric Distortion and Optimal Acquisition strategy

Radar satellites produce images in range and azimuth coordinate systems, which due to the effects of topography, may be distorted in comparison with ground based coordinate systems (e.g. Figure 2.7 a-b). Interferograms are reprojected into latitude and longitude (geocoded) using a DEM (e.g. Figure 2.7 c-d). The extent of the geometric distortions depend on radar look angle and the steepness of topography and can cause problems for measurements at steep-sided stratovolcanoes (e.g. Atitlan, Guatemala).

Where the slope is steep, but the angle is less than the satellite look angle, the side of a volcano facing the satellite becomes foreshortened - the geocoded pixel size is smaller on the far side of volcano than the near side. For slope angles exceeding the satellite look angle, returns from the top of the slope will arrive before those at the bottom (layover, Figure 2.7 g) and parts of the far side of the volcano will not produce a radar return (shadowing). At some of the steepest volcano summits in Central America we observe a layover and shadow effects (e.g. Fuego or Atitlan, Guatemala). In this case there can be no correction and data for that section of the volcano cannot be used. Foreshortening and layover will also have an effect on coherence as the radar potentially samples a much greater area of the ground, effectively increasing the pixel ‘size’ (See Figure 2.7 f).

To ensure that there is good resolution on all parts of steep volcanic edifices, it is necessary to have images from both ascending and descending paths. Many deformation signals are isolated to only one part of a volcanic edifice : for example, an earlier survey of Central American volcanoes

Figure 2.7: a) Example of amplitude image of Atitlan and Toliman volcanoes in ascending radar geometry b) Amplitude image of Atitlan and Toliman in descending radar geometry. c) Ascending amplitude image reprojected into latitude and longitude showing foreshortening of the western slope. d) Descending amplitude image in latitude and longitude showing foreshortening of the eastern slope. e,f,g) Cartoons showing the conditions that lead to foreshortening, layover and shadow, when volcano slopes exceed the satellite look angle. The satellite is moving into the page in each instance, arrow shows satellite line of sight, dotted lines indicate points of apparently equal distance from the satellite.

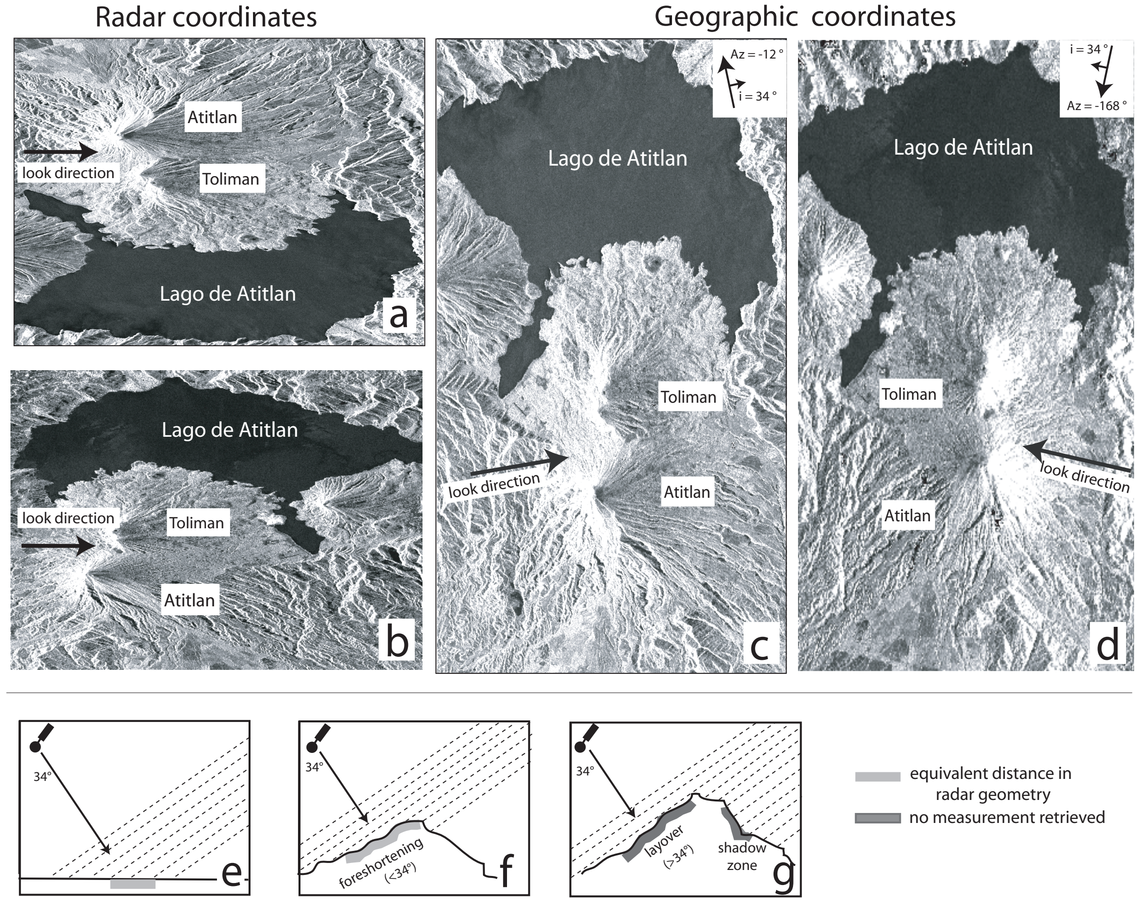

(*Fournier et al.*, 2010) missed asymmetrical gravity-driven deformation at Arenal, Costa Rica (discussed in Chapter 4), as only ascending images were examined. Furthermore, since InSAR only measures displacement along the satellite line of sight, any motion perpendicular to this vector will not be detected, so images from both look directions are required to determine the direction of the vector displacement.

2.4 Interferometric Coherence

The coherence of a pixel is usually described in terms of interferometric correlation ($|\hat{\lambda}|$), which is defined for each pixel using the complex values for both images (y_1 and y_2) across a square of at least 3x3 pixels (Equation 2.2). A value of 1 indicates identical phase for all pixels. When interferometric coherence tends to 0, each pixel response is independent (*Seymour and Cumming*, 1994; *Hanssen*, 2001).

$$|\hat{\lambda}| = \frac{|\sum_{n=1}^{9} y_1^{(n)} y_2^{*(n)}|}{\sqrt{\sum_{n=1}^{9} |y_1^{(n)}|^2 \sum_{n=1}^{9} |y_2^{(n)}|^2}} \tag{2.2}$$

Interferometric decorrelation is caused by changes in satellite position (geometric decorrelation), instrument properties (thermal decorrelation) and in surface scatterer characteristics (temporal decorrelation) (*Zebker and Villasensor*, 1992).

Geometric decorrelation occurs where the radar wavelength is less than the difference in path length between radar returns from opposite sides of a pixel, and is most pronounced at large baselines.

Temporal decorrelation is caused by scatterers within a pixel moving or changing their reflective properties. For satellite incidence angles of less than 45, InSAR is more sensitive to vertical than horizontal changes to scatters, so that surfaces where volume scattering is significant (e.g. forests, dense vegetation) are expected to decorrelate more rapidly with time (*Zebker and Villasensor*, 1992). Precipitation, wind and ecological processes have all been observed to contribute to temporal deccorelation (*Ahmed et al.*, 2011).

2.4.1 Coherence in Central America

The poor radar penetration of dense tropical vegetation using widely used SAR instruments (e.g. ERS, ASAR, ENVISAT) has been the primary factor limiting InSAR measurements in the tropics. The effect of vegetation on InSAR is dependent on wavelength, with L-band radar ($\lambda =$ 23 cm) maintaining coherence much better than C-band ($\lambda = 5.6$ cm). The relative coherence between two interferograms showing the same part of the ground will depend on numerous factors in addition to SAR wavelength, including time spanned, perpendicular baseline, differences between surface scatterers and different rates of instrument related decorrelation (e.g. *Hanssen*, 2001; *Zebker and Villasensor*, 1992). As interferometric correlation (γ) is estimated from phase values for a set of neighbouring pixels (Equation 2.2), pixel dimensions are also important. In addition, choices made during InSAR processing, such as spatial wavelength of filtering and degree of multilooking (reduction of spatial resolution with the aim of increasing the size of a coherent area) will also affect our estimations of correlation. Due to the nature of the estimator used to examine interferometric correlation (Equation 2.2), areas that are entirely incoherent will still produce an apparent coherence value. I therefore use empirically derived threshold coherence when comparing the coherence of interferograms processed to different number of looks in Section 2.4.2.

I use the data from our arc-scale survey to examine patterns of interferometric coherence in Central America. As this is all L-band ALOS data, processed in the same manner, comparison

Figure 2.8: Mean coherence for the whole Central American data set plotted as a function of (a) time in days and b) perpendicular baseline. Each point represents the mean value of coherence for a 0.1 × 0.1 degree box in an interferogram. The choice of resolution captures regional scale differences in vegetation and land use. Mean values are marked with circles on (a) and (b), and best-fit exponential functions are shown by dashed lines. (c) and (d) show box and whisker plots of the percentage of pixels with correlation above 0.15 as a function of time and perpendicular baseline, respectively. The limits of the boxes are the 25th and 75th percentile, while the central black line shows the position of the median. Minimum and maximum values are shown by the extent of the black line.

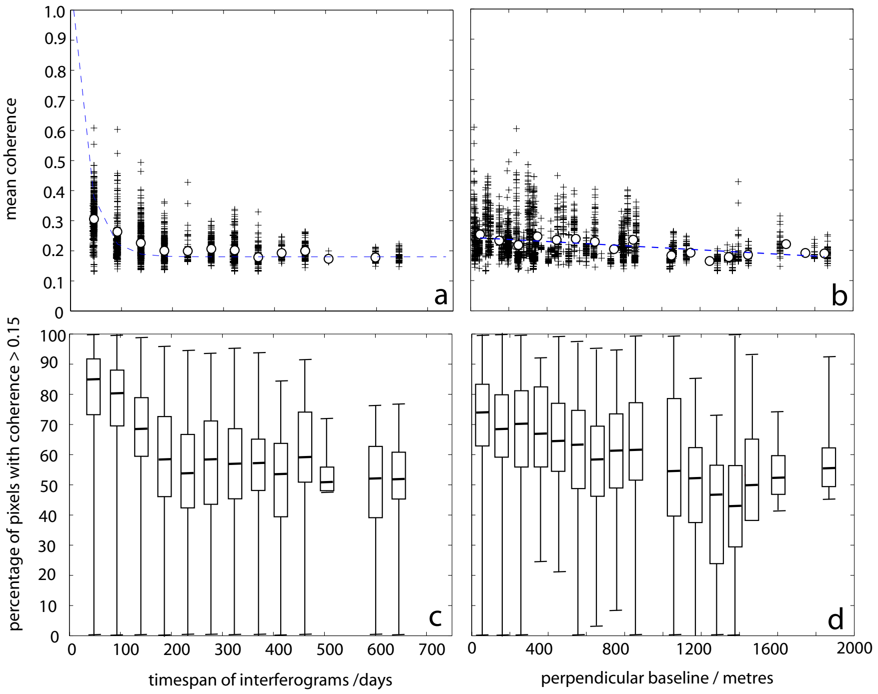

between coherence as a function of time and spatial baseline for different areas can be made directly. Of the 26 active volcanoes in the arc, L-band data for just 3 (Concepcion, Irazu and Turrialba) were too incoherent to make any measurement of deformation at all. However, measurements are restricted at other volcanoes by high rates of decorrelation, which meant that only short temporal baseline interferograms could be constructed. Making the distinction between water vapour signals and deformation often requires enough interferograms to examine the temporal development of the phase, so this hampers our analysis. It also imposes spatial limitations on our measurements. At Arenal (Chapter 4, Section 2.5), for example, coherence is limited to the stable surfaces of young lava flows. This confined our measurement to a 2.5 km^2 region on the western side of the volcano, making the measurement of any longer wavelength deformation impossible. The summits of volcanoes with continuous or semi-continuous explosive activity, such as Santiaguito, Fuego, Pacaya (Guatemala) or Arenal (Costa Rica) were also consistently incoherent.

Figure 2.9: Schematic examples of our simple coherence model for average coherence across track 172 in Guatemala (a) and 166 in Nicaragua (b) (as shown in Figure 1a). These show model predictions as a function of time only for percentage coherence above a threshold value of 0.15. Black dashed lines show exponential time dependence, finer dashed line shows our approximation of seasonal dependence and solid lines show the combined model. c) Plot illustrating the fit between average percentage coherence ¿ 0.15 for all our data at a resolution of 0.1 degrees and model predictions for the same value. d) Map of root mean squared error in model predictions across Central America, using the same resolution as for Figure 11.

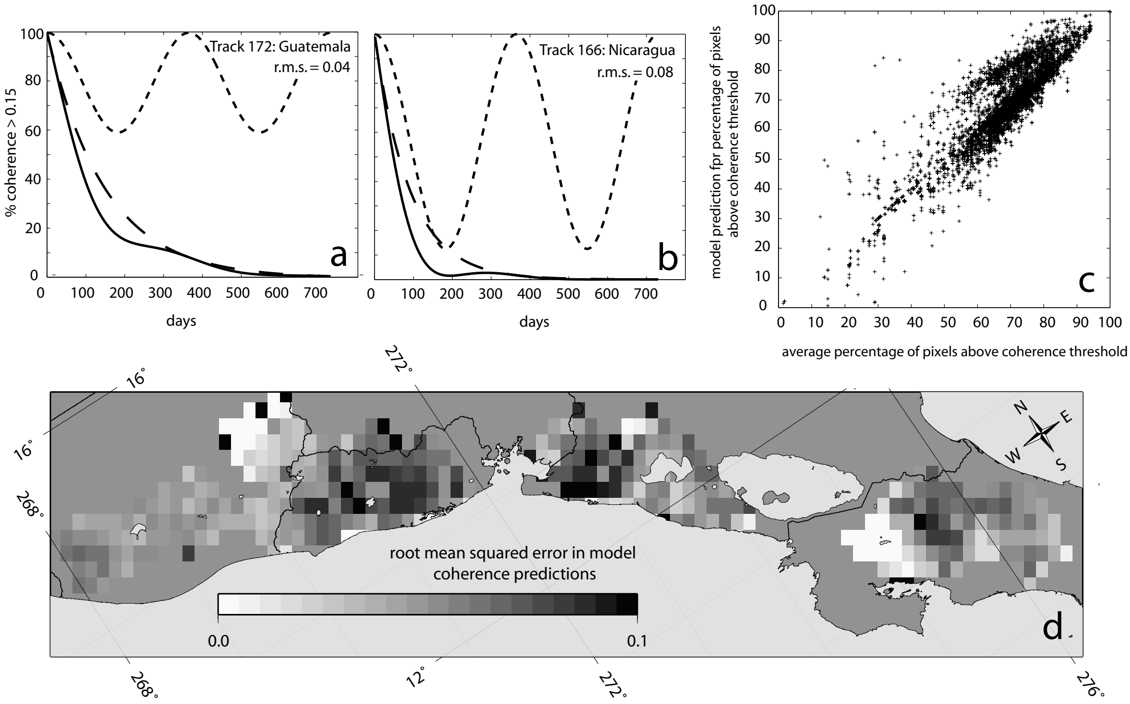

We investigate the relative importance of the contributions of geometric and temporal decorrelation to patterns of coherence across Central America. Unlike the many analytical models for coherence used to measure for example, stem volume or tree heights, (e.g. *Balzter*, 2001; *Santoro et al.*, 2002), we do not aim to extract information about ecological processes from InSAR coherence , but to predict where InSAR measurements at volcanoes are likely to be useful and where they are most likely to be limited by rapid decorrelation. Temporal decorrelation is generally caused by volcanic activity, slope instability or sometimes very rapid changes in vegetation cover (e.g. rapidly developing kill zones at Pos and Turrialba (*Martini et al.*, 2010)) close to the volcano's summit. The lower flanks of volcanoes in Central America, however, are commonly either covered by rainforest or are intensively cultivated. It is on the lower slopes and surrounding area that we expect to observe any deformation associated with deeper magmatic processes, so understanding the relationship between vegetation cover and decorrelation is useful for understanding limitations on volcano deformation measurement.

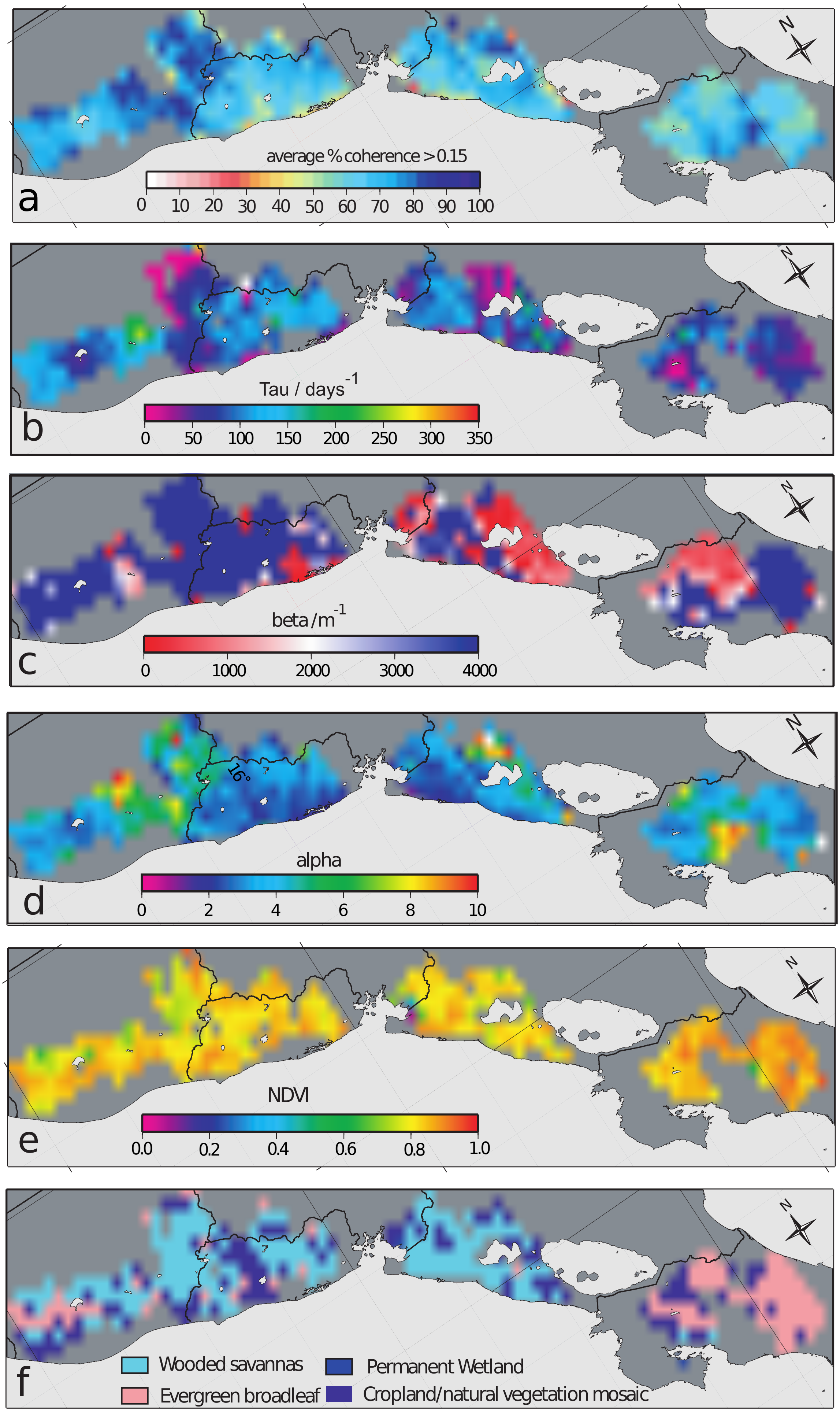
N
a
average % coherence > 0.15
0 10 20 30 40 50 60 70 80 90 100
b
Tau / days-1
0 50 100 150 200 250 300 350
c
beta / m-1
0 1000 2000 3000 4000
d
16°
alpha
0 2 4 6 8 10
e
NDVI
0.0 0.2 0.4 0.6 0.8 1.0
f
Wooded savannas
Evergreen broadleaf
Permanent Wetland
Cropland/natural vegetation mosaic

2.4.2 Coherence Model

Mean coherence for the complete Central American ALOS data (Figure 2.8, data sampled into 0.1 × 0.1 degree boxes) shows a dependence on both time-span of interferogram and perpendicular baseline. After about 200 days mean coherence has decayed exponentially to a value of about 0.18, compared to a value of 0.3 for interferograms covering the shortest possible time-span (46 days). The difference between coherence in the lowest and highest baseline interval is less significant, falling from 0.26 to 0.19.

Mean coherence is not particularly useful as an indicator of whether volcanic edifices will be coherent, as they make up a relatively small proportion of a scene by area, and are commonly not representative of the rest of an interferogram. Fresh, young lavas, for example, decorrelate slowly, whereas scattering properties of explosive products alter rapidly, especially when deposited on steep slopes. It is considered possible to use interferometric data where its coherence is above about 0.15, the value used as the threshold for unwrapping routines (e.g. branchcut algorithm, *Goldstein et al.*, 1988). The percentage of pixels above this threshold coherence and the mean coherence are related, but not directly proportional, as coherences are not normally distributed about the mean value (Figure 2.8, c and d). The relationships between percentage coherence above 0.15 and time or baseline are therefore not as clear as for mean coherence, but more likely to yield information useful for our purpose of investigating volcano deformation.

We model percentage coherence > 0.15 (C) as the product of exponential decay functions describing coherence in terms of time in years (t), perpendicular baseline separation (B_{perp}) and a parameter describing seasonal dependence (α). For simplicity, we neglect the effects of some instrument dependent parameters also associated with decorrelation (rotation of satellite look angle, thermal decorrelation, as discussed by *Zebker and Villasensor*, 1992; *Hanssen*, 2001). Our choice of exponential decay functions to describe temporal and geometric decorrelation is informed by analytical expressions (e.g. temporal decorrelation, Zebker and Villasensor [1992]) and examination of the coherence-temporal baseline relationship and coherence-spatial baseline relationship for our complete dataset (Figure 2.8).

Figure 2.10 *(preceding page)*: a) Map of mean percentage of pixels with correlation > 0.15 per box. This figure simply shows the mean values for our input data set and makes no distinction for temporal or spatial baseline. b) Map of Central America showing parameter τ , describing relative rate of decorrelation as a function of time (lower values = faster decorrelation). c) Parameter β, describing relative rate of decorrelation as a function of baseline. Where the colour scale is saturated, β values are very high (exceeding 10,000), indicating that coherence is not strongly dependent on baseline. d) Parameter describes the strength of any seasonal dependence of decorrelation (lower values = greater seasonal effect). e) Normalised Difference Vegetation Index (NDVI) from MODIS level 3 'atmosphere' product at 1 degree resolution, re-sampled to same resolution as our calculations of τ. f) Land use map from MODIS level 3 'land' product, resampled to 0.1 0.1 degree resolution. Land use is classified according to the International Geosphere-Biosphere Programme (IGBP) index.

Figure 2.11: Histograms showing distribution of values for IGBP classifications (a) 'Evergreen Broadleaf', (b) 'Woody Savanna' and (c) 'Cropland/natural vegetation mosaic' environments. (d), (e) and (f) show distributions of alpha. Dotted lines show the mean value.

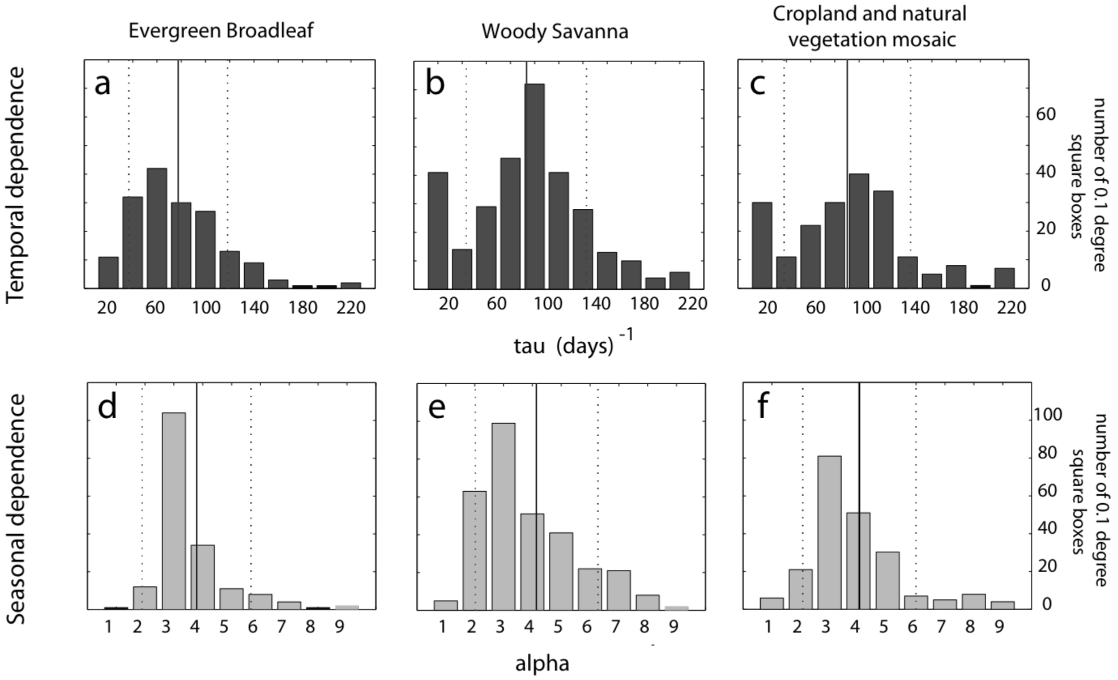

$$C = 1 + \frac{1}{\alpha}(e^{\frac{-|B_{perp}|}{\beta}} e^{\frac{-t}{\tau}} \cos 2\pi \mathrm{t} - 1) \tag{2.3}$$

The parameters β and τ reflect the dependence of coherence on B_{perp} and time spanned by the interferogram respectively. We use non-linear inversion, where the difference between model predicted values and our coherence data were minimised using a least-squares method, to find the values of β , τ and α that best fit the data. We checked that our results for these parameters were global, rather than local solutions, by varying the starting values for each parameter used in the least squares method and confirming that our solutions were not affected.

The parameter α is added to the expression to allow for a seasonal difference in coherence and controls the amplitude of a cosine function with the period of a year, which moderates the shape of the exponential expressions (Figure 2.9a and b). This additional parameter was found to significantly improve the fit of our model to the coherence data (for example, reducing the residual in fit by about 20% in northern Nicaragua, Track 166). A low α value indicates that coherence has a strong seasonal dependence.

Two examples, expressed as a function of time, are shown in Figure 2.9a and b. The best fit solution for Track 172 (Figure 2.9a) in Central Guatemala, shows slower decorrelation as a function of time and a lesser seasonal dependence than data from Track 166 (Figure 2.9b) in Northern Nicaragua (τ = 150 and α= 4.9, relative to 90 and 2.3). Predicted coherence above

Figure 2.12: Graph showing predicted decorrelation as a function of time for ‘Evergreen broadleaf’ (mostly rainforest) and ‘Cropland/Natural vegetation mosaic’ land uses.

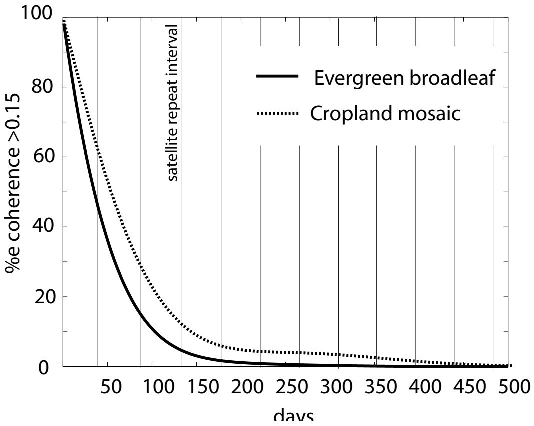

the threshold value is calculated from our best-fit values for τ, β and α for 0.1 x 0.1 degree boxes across Central America and shown plotted against actual coherence on Figure 10c. The spatial distribution of the root mean squared misfit between predicted and measured percentage of pixels above threshold coherence is shown in Figure 2.9d.

The distribution of values of τ, β and α across Central America is spatially noisy (Figure 2.10 b, c and d) but the temporal dependence parameters (τ and α) show some trends, which are discussed in Section 2.4.3. Beta (β), however, takes very high values across the majority of Central America (>10,000), showing that geometric factors are largely of lesser significance than time dependent processes (the colour scale in Figure 2.10 c is saturated). The remaining, lower values of β, are typically of the order of 1000-3000 m^{-1}, show no correlation with topographic height and are mostly isolated to two tracks with some particularly large baseline interferograms (Tracks 165 and 162).

2.4.3 Coherence and land use

Our arc-scale analysis of coherence data shows that time-dependent processes, most likely associated with vegetation growth, dominate decorrelation rates (e.g. *Fransson et al.*, 2001; *Liu et al.*, 2001; *Ahmed et al.*, 2011). We might therefore expect Normalised Difference Vegetation Index (NDVI) to be a useful predictor for interferometric coherence. Correlations between NDVI and coherence have been observed in data from other parts of the world (e.g. Hawaii and in north-western China *Rosen et al.*, 1996; *Liu et al.*, 2010), with higher NDVI being associated with poor coherence. In Central America, however, there is no systematic relationship between NDVI and either τ or α (Figures 2.10 b, d, e). NDVI varies very little across Central America (although it takes slightly higher values in Costa Rica than further north) because vegetation index is similar for both rainforest and cultivated land. Comparison of NDVI with a MODIS land-cover map using International Geosphere-Biosphere Programme (IGBP) classifications shows no clear relationship between type of land cover and NDVI (Figure 2.10 e and f).

The temporal parameter τ, and to some extent, our seasonal parameter show distinct distributions for areas of different IGBP land used classification (Figure 2.11). For 'Evergreen broadleaf,' dominated by tropical rainforest and cloud forests in Central America, τ has a left skewed distribution with a mode interval of 50-70 days-1 (Figure 2.11a). The less densely vegetated land, 'Cropland/vegetation' and 'Woody savanna', decorrelate less quickly (modes of 90 - 110 days^{-1}, Figure 2.11b-c). These classifications are likely to include more developed landscapes, including agricultural areas where surface scatterers are regularly altered due to human activity (e.g. ploughing, harvesting). We attribute the high number of pixels showing very low values for τ in these categories to be caused by human interference with the landscape.

Our parameter describing the seasonal dependence of coherence, α, has a modal value of 2.5 across all landcover classifications, suggesting some seasonal trends in coherence across the whole area of study (Figure 2.11 d-f). The distribution in values is slightly more left-skewed in the 'Evergreen broadleaf' land-cover category than where vegetation was less dense, a feature we attribute to seasonal agricultural practices increasing the numbers of low values for alpha. Seasonal effects are smallest over high topography in Guatemala, Costa Rica and Northwest of Lake Managua in Nicaragua and largest in the coastal regions of El Salvador and Nicaragua. We see a very small range of values for alpha in areas dominated by rainforest ('Evergreen Broadleaf,' Figure 2.10 d), and much greater seasonal variation where land use category suggests some degree of cultivation (Figure 2.11 e and f).

We use the IGBP land use classifications to make coarse predictions of decorrelation rate for different land types. On average, we expect rainforest environments to decorrelate faster than cropland (Figure 2.12), with the largest differences between the two environments in the shortest possible interferograms (46 and 92 days for ALOS). However, this simple approach will not capture the detailed spatial patterns of coherence seen in Figure 2.10a. The IBGP classifications 'cropland/vegetation mosaic' and 'woody savanna' in particular, deviate from a normal or skewed normal distribution of the temporal decorrelation parameter, τ (Figure 2.11b and c). There are significant parts of Central America where these environments decorrelate much more quickly than the average, as shown by the peaks at low values for τ on Figure 2.11b and c.

Table 2.2: SAR satellite instrument parameters referred to in text

Instrument	Period Operational	Wavelength (cm)	Repeat interval (days)	Typical look angle (degrees)	Range resolution (m)	Azimuth resolution (m)
ERS-1/2(ESA)	1992-2000/1995-2011	5.66(C-band)	35	~23	10	5
ALOS(JAXA)	2006-2011	23.6(L-band)	46	10-51	9-30	10
RadarSat-1/2(CSA)	1995/2007-	5.66(C-band)	24	20-49	25	25
TerraSAR-X(DLR)	2008-	3.12(X-band)	11	20-45	2-3	3
SENTINEL(ESA)	poss. from 2013?	5.66(C-band)	12	20-46	5	5

2.5 Comparison of SAR wavelength

Data from four different satellite instruments (ERS, RadarSat, ALOS and TSX - see Table 2.5) were used to make measurements at Arenal volcano, Costa Rica, which is known to be deforming (see Chapter 4). To make a meaningful comparison of coherence between these different platforms we estimate a threshold value for interferometric correlation, below which we do not expect data to be useful. For this we use the average value for a section of the interferogram over Lake Arenal, which will always be incoherent. As reflected and backscattered radiation from the lake surface will be completely incoherent, any value below this threshold shows that data are unusable. The actual value of this threshold will depend on a combination of the factors listed above, but the percentage of pixels above threshold coherence will show the proportion of data that may yield useful interferometric deformation measurements. The percentage of pixels above the given threshold value are shown in Figure 2.13 and are plotted with respect to temporal and spatial baseline in Figure 2.14.

Phase correlation in the area around Arenal is among the lowest in Central America, with high phase correlation exclusively over the young lava around the volcano in the majority of interferograms. As expected, due to its longer wavelength, L-band data produces the greatest proportion of pixels over the coherence threshold, followed by the TSX interferogram, which has a smaller pixel size. All the TSX interferograms constructed showed significantly better coherence than ERS or RadarSat interferograms of equivalent temporal length. The proportion of pixels above threshold coherence were generally slightly higher in the RadarSat than in the few ERS interferograms and this is likely due to shorter perpendicular baselines (Figure 2.13 b).

Although L-band data produces the greatest proportion of coherent pixels, over extremely stable surfaces such as lava flows, we find that RadarSat data maintains coherence for up to 600 days (Figure 2.14 a). C-band data are useful for measuring the deformation of small, stable areas. To date only L-band data has been demonstrated to be suitable for surveying arcs as a

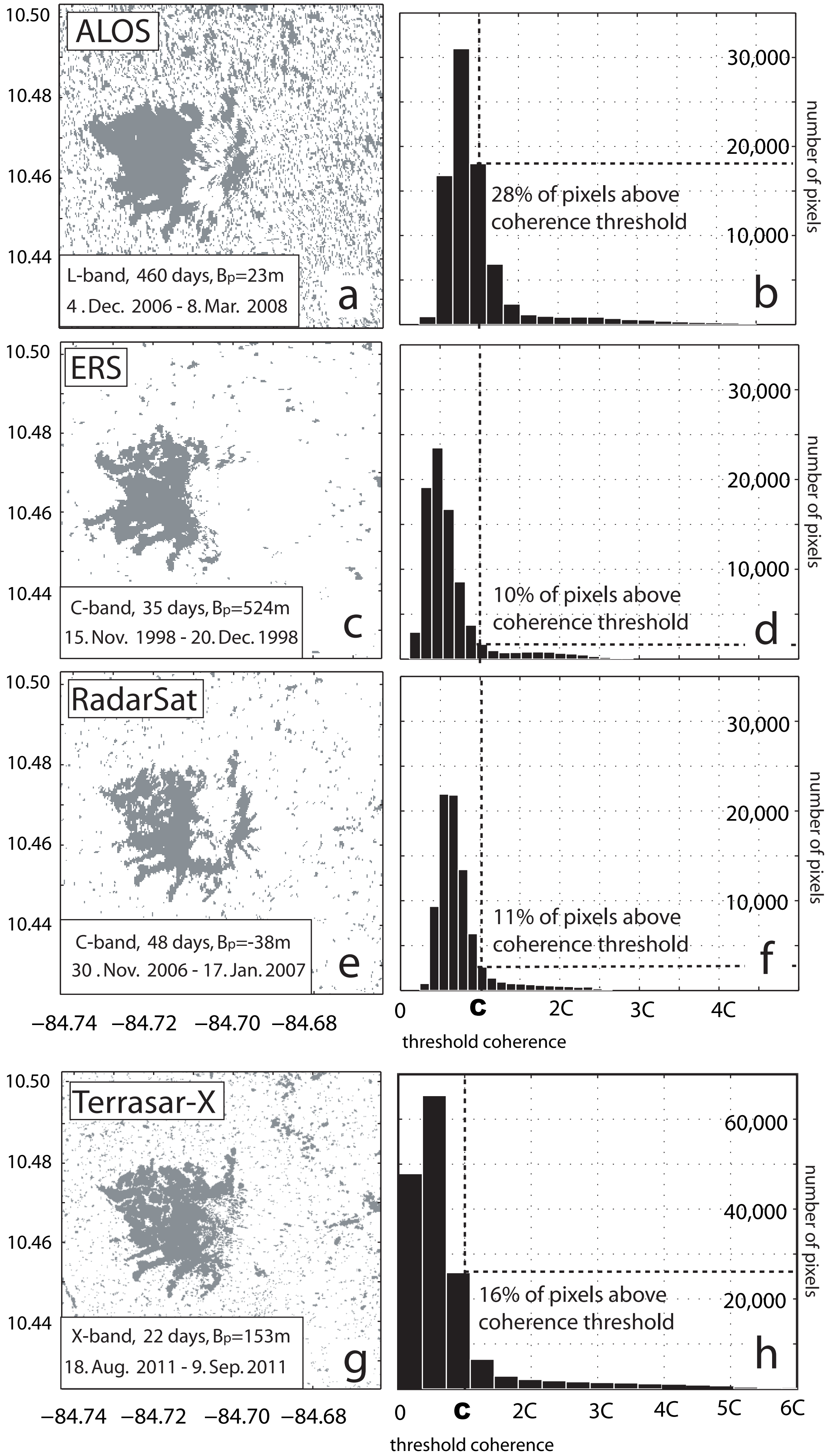
ALOS
L-band, 460 days, Bp=23m
4 . Dec. 2006 - 8. Mar. 2008
a
28% of pixels above coherence threshold
b
ERS
C-band, 35 days, Bp=524m
15. Nov. 1998 - 20. Dec. 1998
c
10% of pixels above coherence threshold
d
RadarSat
C-band, 48 days, Bp=-38m
30 . Nov. 2006 - 17. Jan. 2007
e
11% of pixels above coherence threshold
f
Terrasar-X
X-band, 22 days, Bp=153m
18. Aug. 2011 - 9. Sep. 2011
g
16% of pixels above coherence threshold
h
10.50
10.48
10.46
10.44
−84.74 −84.72 −84.70 −84.68
10,000
20,000
30,000
40,000
60,000
number of pixels
0
C
2C
3C
4C
5C
6C
threshold coherence

whole in the tropics (e.g. *Philibosian and Simons*, 2011). High-resolution, short repeat time X-band InSAR may prove useful for individual volcanoes but is currently prohibitively expensive for large scale mapping. The upcoming European Space Agency instrument, Sentinel (Table 2.5), will be C-band but have a higher spatial resolution, shorter repeat time and tighter orbital tube than ERS and RadarSat. We therefore expect this new data to be much more useful than earlier C-band instruments, although it seems unlikely that it will be as suitable for regional-scale surveys in the way that the ALOS L-band data is. These results agree with expectations (e.g. *Rosen et al.*, 1996), but this is the first time that coherence has been quantified for such a large dataset.

Figure 2.13 ***(preceding page)*****:** Maps showing pixels above (grey) and below (white) the threshold coherence around Arenal for (a) ALOS , (c) ERS, (e) RadarSat and (g) Terrasar-X interferograms. Threshold values were found from the mean correlation value over part of Lake Arenal and were 0.18, 0.3, 0.35 and 0.1 respectively. Corresponding histograms show the distribution of pixels about this value. The boundary between data above and below the coherence threshold value is marked with a dotted line. Note the different scales on the x- and y-axes for the TSX data. The data points corresponding to each of the interferograms shown here are marked on Figure 15 by black boxes.

Figure 2.14: Percentage of pixels above threshold coherence calculated for our complete data set at Volcan Arenal, Costa Rica, shown as a function of (a) time span and (b) magnitude of perpendicular baseline. The interferograms shown in Figure 14 are indicated by black boxes.

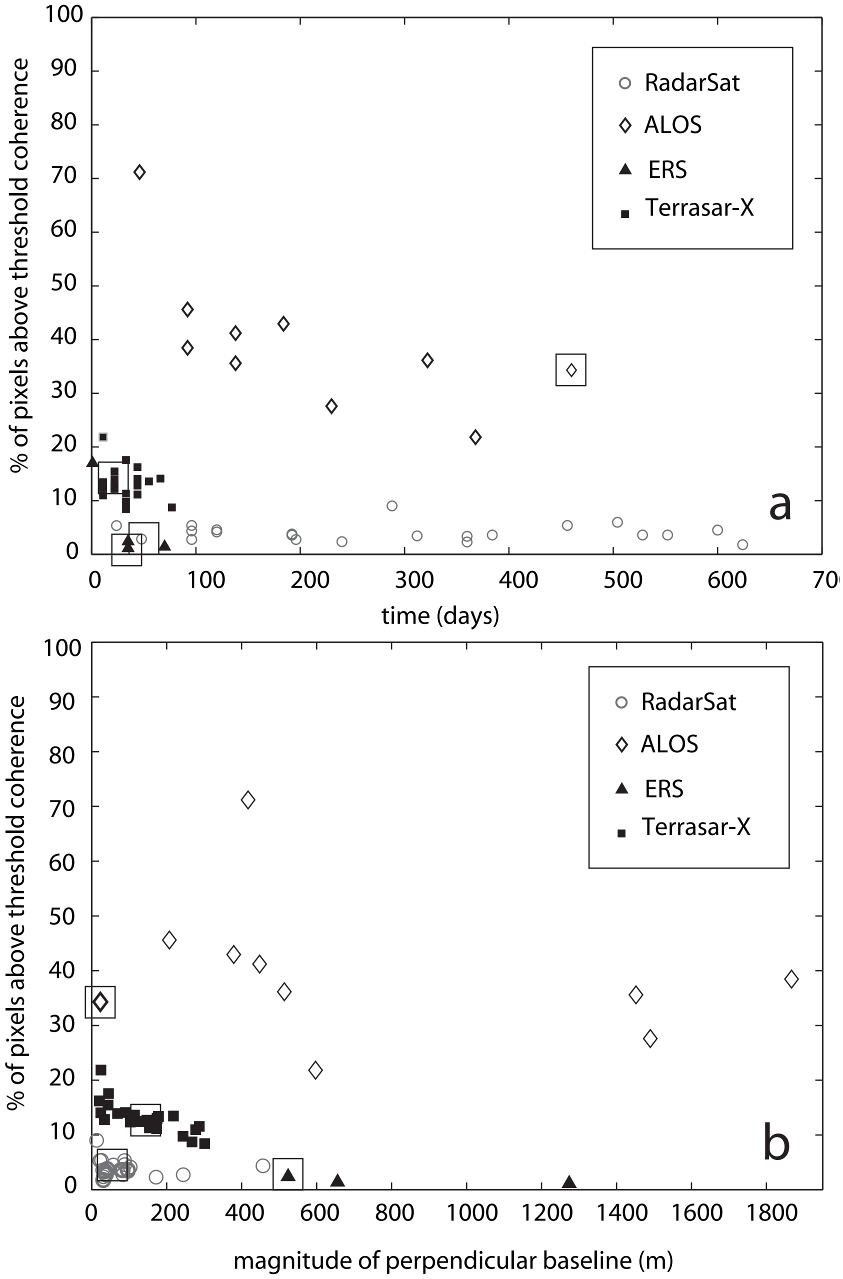

2.6 Summary

Our analysis of data from Central America demonstrates factors that determine the usefulness of InSAR at volcanoes both within the tropics and worldwide. In summary, water vapour artefacts and poor coherence are the greatest challenges to making successful InSAR measurements at volcanoes. This means that the characteristics of volcanoes worldwide that inhibit measurement of deformation with InSAR include (1) vegetation cover that leaves little of the ground exposed (e.g. rainforest), (2) persistent activity, (3) steep slopes and (4) large contrasts in topography. Thus, young stratovolcanoes present particularly difficult targets for measurement with InSAR. Recent activity can, however, present some advantages for InSAR as young lavas and explosive deposits present more stable scattering surfaces for InSAR than older, densely vegetated slopes.

Two of the most important limiting factors for measuring volcano deformation with InSAR, water vapour artefacts and vegetation-related loss of coherence, are particularly significant in the tropics. Root mean squared variations in path delay due to stratified water vapour changes reached as much as 6.4, 5.3 and 4.8 cm at Santa Ana, Pacaya and Fuego, respectively (Figure 2.5). This variability in path delay over a volcano is proportional to its edifice height (gradient = 2cm/km height). Although the presence of water vapour artefacts does not prevent InSAR phase measurements from being made, it may mask deformation signals, complicating interpretation at volcanoes with high relief. Furthermore, very steep slopes can lead to layover and foreshortening in the radar geometry (Figure 2.7). One satellite look angle is not necessarily sufficient to be sure of detecting deformation.

In Central America, the lower slopes of most volcanoes as well as the surrounding areas are vegetated to some extent. The degree to which this affects InSAR measurement depends on the type and density of vegetation and has implications for the measurement of deeper magmatic movement. In general, decorrelation rates are greater in the southern arc than in the north, although there is considerable variability (Figure 2.10a). Although there is no relationship with NDVI, coherence varies systematically with land use type, such that decorrelation rates are higher, and standard deviation lower, for tropical rainforest than for cultivated land (Figure 2.11).

Our comparison of L-, C- and X-band in one of the least coherent parts of Central America demonstrates the importance of having L-band data for measuring volcano deformation in the tropics (Figures 2.13 and 2.14). The application of C-band data of varying spatial resolutions is limited to small, stable areas. X-band radar shows potential for penetrating vegetation to allow measurements over a larger spatial area, but only over short (< 100 day) time periods. We expect Sentinel data to perform better than ERS or RadarSat data due both to its shorter proposed repeat time and higher spatial resolution. It is unlikely, however, to allow measurements over as large regions as L-band data in tropical areas.

Chapter 3

On the lack of InSAR measurements of deformation on the CAVA

This chapter includes a work submitted for review: Ebmeier, S. K., J. Biggs, and T. A. Mather, *On the apparent lack of InSAR measurements of deformation on the Central American Volcanic Arc,* revision submitted to Journal of Geophysical Research - Solid Earth, December 2012.

3.1 Arc-scale InSAR Surveys

The development of satellite based Interferometric Synthetic Aperture Radar (InSAR) has allowed volcano deformation to be measured at a continental scale (e.g. *Pritchard and Simons*, 2004a; *Fournier et al.*, 2010; *Philibosian and Simons*, 2011, see Tables 1.1 and 1.2). InSAR uses the difference in phase between two time-separated radar images to measure small displacements of the earth's surface at a precision of up to a few millimetres (comprehensive reviews of InSAR techniques are given by *Massonnet and Feigl* (1998) and *Bürgmann et al.* (2000)).

Deformation has now been detected with InSAR at over 94 volcanoes worldwide, with marked differences between the number of observations of deformation at different volcanic arcs (*Fournier et al.*, 2010), not obviously related to the number of historically active volcanoes. This disparity may be the consequence of both differences in the applicability of InSAR measurement under different environmental conditions and differences in magmatic processes. The extraction of information about deformation from differential phase requires the identification of phase shifts from other sources, including variations in tropospheric water vapour, differences in satellite viewing geometry and scattering properties of the earth's surface.

Environmental conditions that affect InSAR measurement vary systematically between different parts of the world. In Central America, several contributors to interferometric phase are of especially high magnitude (Chapter 2). For example, tropospheric water vapour has both higher magnitude and greater variability in the tropics than in equatorial zones (e.g. *Heleno et al.*, 2010). Dense, rapidly growing vegetation also limits use of InSAR measurements.

In this paper we describe the results of an InSAR survey of the Central American Volcanic Arc (CAVA), using the first significant set of radar data capable of penetrating tropical vegetation (2007-2010). In order to understand the significance of our measurements, we produce time series of the phase around 20 historically active volcanoes and calculate a minimum radar detectable rate for deformation at each (Section 3.2.1). We discuss the implications of the lack of measurable deformation at volcanoes that erupted during our survey (Sections 3.4.1 and 3.4.2). Comparison of minimum detection rates with the magnitudes of deformation measured by InSAR at other well-studied volcanic arcs (Kamchatka, Aleutians/Alaska, Cascades, Mexico, Andes, Italy, Greece, Sumatra/Java) suggests that the apparent lack of deformation in Central America is not primarily the result of measurement artefacts (Section 3.5). In Section 3.5.1, we discuss some of the factors that may limit the geodetic expression of shallow magma movement in Central America.

3.2 Systematic Survey of Central America

We used the first significant set of radar data capable of penetrating tropical vegetation (L-band, ALOS PALSAR) to search for volcano deformation in Central America between 2007 and 2010. Earlier InSAR surveys of Central America did not detect any volcano deformation, but were limited in scope by the poor coherence of C-band data (*Zebker et al.*, 2000), and the limited quantity of L-band data analysed in broader survey mode (*Fournier et al.*, 2010).

We were able to construct an average of ∼15 ascending interferograms for each historically active volcano and supplemented this with descending data where possible. The Repeat Orbit Processing software (ROI_PAC) (*Rosen et al.*, 2004) was used to construct interferograms, which were unwrapped using a branch-cut algorithm (*Goldstein et al.*, 1988). Topographic correction was carried out using NASA's Shuttle Radar Topography Mission 90 m digital elevation model, interpolated and re-sampled to a spacing of 30 m.

Interferograms showing all Central American volcanoes were examined visually for anomalous phase patterns, while phase around historically active volcanoes was scrutinised in more detail (our systematic approach is set out as a flowchart in Chapter 2). Results were considered inconclusive where fewer than three interferograms were coherent over the volcano's edifice, so that phase changes due to deformation and atmospheric water vapour could not be distinguished.

Table 3.1: Survey results for active volcanoes in Central America. Number of interferograms refers to the number processed and used during any stage of analysis, the numbers used in time series generation were sometimes lower due to variable coherence and difficulties in unwrapping.

Volcano	Track/Frame	# of ifgms	Activity during survey	Detection threshold cm/yr	Survey result
Santiaguito	174/280	17	weak-moderate explosions, ash plumes ($\leq$ 5 km), short pyroclastic flows, block and ash avalanches, lava flows, lahars	1.6	lava subsidence[1]
Almolonga	174/280	17	none (geothermal field)	0.8	no deformation
Atitlan	173/280 480/3330	17	none	4.2	no deformation
Acatenango	173/280 480/3330	11	none	5.1	no deformation
Fuego	173/280 480/3330	11	intermittent moderate strombolian, pyroclastic flows, lava flows, ash plumes ($\leq$ 6 km)	5.1	no deformation
Pacaya	172/270 479/3330	24	multiple semi-continuous lava flows and intermittent strombolian activity, ash and fumerolic plumes ($\leq$ 1 km)	3.0	no deformation
Santa Ana	171/260	15	lahars, intense fumerolic activity about crater lake	6.2	no deformation
Izalco	171/260	15	none	1.0	no deformation
San Salvador	170/250 474/3350	20	none	1.7	no deformation
Ilopango		0	none	-	inconclusive: poor coherence
San Miguel	168/250 474/3350	20	elevated seismicity, fumerolic	2.4	no deformation
Cosigüina	167/240-250	14	none	2.2	no deformation
Conchagüita	167/240-250	14	none	2.6	no deformation
San Cristòbal	166/230-240 472/3370	36	VEI 1 (8.11.07, 22.06.08, 21.11.08) and VEI 2 (6.9.09). Ash plumes ($\leq$ 9 km)	2.7	no deformation
Telica	166/230-240 471/3370	36	VEI 1 (28.10.08,5.7.08) small phreatic explosions, ash plumes ($\leq$ 2 km), minor ash explosions, incandescence in crater	1.8	no deformation
Cerro Negro	166/230-240 471/3370	36	none	1.4	no deformation
Las Pilas	166/230-240 471/3370	36	none	1.4	no deformation
Masaya	165/220-230 470/3380	20	lava lake, VEI 1 (18.6.08), intermittent ash eruptions, phreatomagmatic eruption, steam and ash plumes	1.3	subsidence within ring fault[2]
Momotombo	165/230 166/230 471/3370	49	fumerolic/geothermal	0.6	no deformation
Concepciòn	164/200	20	VEI 1 (9.2.07, 30.6.08, 11.12.09) and VEI 2 (24.11.07) explosions, gas and ash plumes ($\leq$ 1 km)	-	inconclusive: poor coherence
Rincon de la Vieja	164 220-230	11	low level fumerolic and seismic activity	-	inconclusive: poor coherence
Miravalles	164 220-230	11	none	-	inconclusive: poor coherence
Arenal	163/190 466/3410 467/3410	12	small explosions, occasional pyroclastics	1.2	flank slip[3]
Poàs	162/190 466/3410	18	VEI 1 (13.1.08, 12.1.09 and from 11.2009), phreatic explosions, fumerolic activity, landslides	0.9	no deformation
Irazu	161/180 465/3420	15	minor fumerolic	-	inconclusive: poor coherence
Turrialba	161/180 465/3420	15	increase in degassing and seismic activity preceded a VEI 2 eruption (5.1.10-24.7.10)	-	inconclusive: poor coherence

[1] *Ebmeier et al.* (2012), [2] *Caravantes et al.* (in prep), [3] *Ebmeier et al.* (2010)

At volcanoes where we had sufficient numbers of coherent interferograms we examined the relationship between phase and perpendicular baseline separation to test for artefacts introduced by errors in the digital elevation model used in processing. We then used pair-wise logic (e.g. *Massonnet and Feigl*, 1995), stacking (e.g. *Pritchard and Simons*, 2004a) and time series (e.g.

Lundgren et al., 2001; *Berardino et al.*, 2002) to examine the temporal and spatial properties of phase and to distinguish between atmospheric delays and deformation.

Time series were constructed using a least squares approach (e.g. *Lundgren et al.*, 2001), where the minimum constraint was applied to velocity rather than displacement (e.g. *Berardino et al.*, 2002). It was explicitly assumed that the velocity was zero before the first acquisition date, so that our time series show displacements relative to this date (see Figure 3.2). Time series show line-of-sight radar delay for the coherent area surrounding the volcano's summit, found relative to the average delay for an annulus centred on the volcano with radii chosen to encompass as large a continuously coherent area as possible without including topographic features associated with the volcano being studied (average inner radius 5-6 km). Referencing to the average of an area rather than an individual pixel minimises the impact of atmospheric variation at a reference point, so that time series reflect just the differences between path delay over the volcano itself relative to the rest of the interferogram. Uncertainties in the time series were found using a Monte Carlo approach, where randomly generated atmospheric noise of mean amplitude 1 cm was added before inversion, neglecting the effects of spatial correlation. Error bars on Figure 3.2 therefore reflect primarily how well each acquisition date is linked to the rest of the network. Gaps in the time series where it was not possible to link independent groups of interferograms are shown in Figure 3.2 as grey bars.

3.2.1 Systematic approach to deformation reporting

Most InSAR papers publish details of deformation signals but do not comment on volcanoes where no deformation was observed. To make a meaningful comparison between volcanic arcs it is vital to distinguish between volcanoes with good quality data but that were not deforming, and those at which data quality were too poor for any measurement to be made. We therefore conduct a systematic survey of all volcanoes in the region, defining the limits of detectability at each.

The duration of a deformation event measurable with InSAR is limited by the spacing of radar acquisition dates, while its magnitude is limited by the contributions of other sources of phase change and the total length of the period of observation. In Central America, the greatest contributions to differential phase come from variations in stratified water vapour (Chapter 2).

The temporal resolution of our data (46 days at best) is low enough that we do not expect to observe 'recoverable' deformation, where the ground deforms and then returns to its original position (e.g. *Watson et al.*, 2000; *Dzurisin*, 2003). It includes large gaps (up to almost 18 months for Track 173, Figure 3.2) and is generally irregularly spaced through time. We therefore limit ourselves to the consideration of deformation causing 'permanent' change to the earth's surface.

Deformation can be identified in a single interferogram if it either a) significantly exceeds the magnitude of atmospheric noise (δ) or b) is spatially distinctive from atmospheric phase features. Where deformation results in permanent change to the ground, signal to noise ratio can be improved by ‘stacking’ interferograms together. A stack of N independent interferograms is expected to have $\sqrt{N}\times$ the noise than any individual image ($\delta_{stack} = \delta_{ifgm}\sqrt{N}$).

We use the root mean squared variation of our detrended time series (e.g. Figure 3.2) as an approximation of the typical magnitude of atmospheric noise in an interferogram or sum of consecutive interferograms (where the atmospheric contributions of dates appearing in consecutive interferograms cancel out). This value reflects the variance in radar path delay over the volcano summit relative to the rest of each interferogram, and thus captures the atmospheric variability important to our measurements better than an average of maximum variances for full interferograms. Minimum detection rate for each volcano is then $(\delta_{ifgm}\sqrt{N})$/t, where N is the number of independent chains of interferograms and t is the total time spanned by all of the interferograms used (e.g. *Biggs et al.*, 2007).

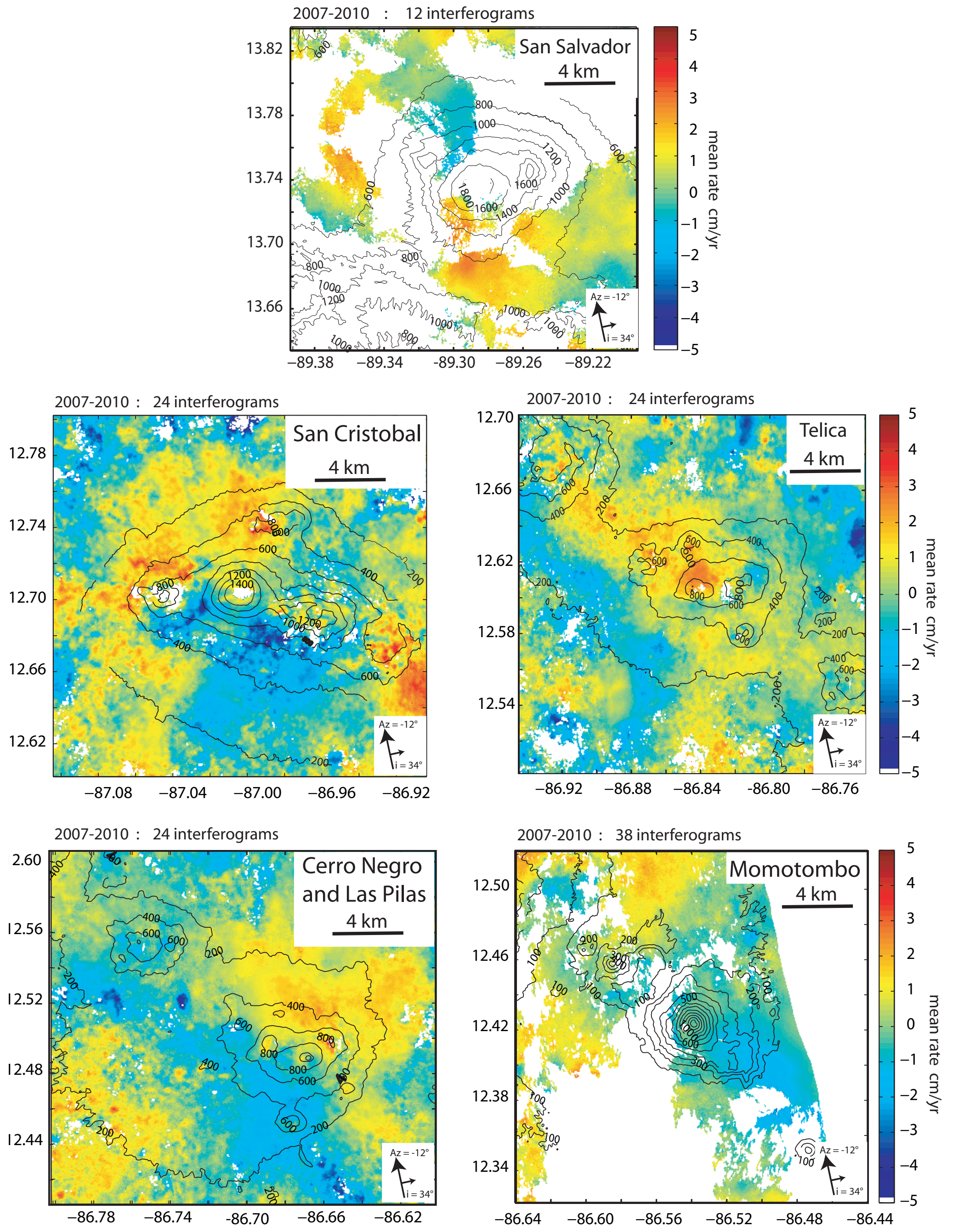

Figure 3.1: Examples of stacked data from El Salvador (San Salvador) and Nicaragua (San Cristòbal, Telica, Cerro Negro, Las Pilas and Momotombo), showing the extent of interferometric coherence and levels of atmospheric noise. Further examples of stacks and individual interferograms from the ALOS Central American data set are presented in Chapter 2.

3.3 Results

Of the 26 historically active volcanoes in Central America we were able to make measurements at 20 (77%)(Table 3.1). Interferograms covering the remaining 6 (Ilopango, Concepciòn, Rincon de la Vieja, Miravalles, Irazù, Turrialba) are dominated by incoherence.

We observed two volcanoes in the CAVA deforming as a result of loading processes: steady, downslope movement of young lavas at Arenal, Costa Rica between 2005 and 2009 (*Ebmeier et al.*, 2010) and the subsidence of young lavas at Santiaguito lava dome in 2009-2010 (*Ebmeier et al.*, 2012). We also detected a region of slow subsidence at Masaya, Nicaragua, confined to an area identified through ground-based geophysical surveys to be inside a ring fault system (*Caravantes et al.*, in prep).

A selection of time series constructed from ascending data for the summit areas of historically active volcanoes are presented in Figure 3.2 (somes examples of stacks of interferograms from Nicaragua are presented in Figure 3.1, and several individual interferograms from this dataset are shown in Chapter 2). At volcanoes where data were coherent, we examined time series to distinguish between characteristics typical of water vapour, and those potentially caused by deformation. Some volcanoes (e.g. Santa Ana, Figure 3.2 g) show jumps associated with individual dates within the time series. Although conceivable that this is a rapid, reversible displacement, it is much more likely to be caused by anomalous levels of water vapour on that particular acquisition date. A lack of systematic temporal structure in time series (e.g Figure 3.2 j, k, l) is also indicative of varying levels of water vapour.

The similarities between the time series showing Atitlan, Fuego and Acatenango (Figure 3.2 c,d and e) and, to a lesser extent Izalco and Santa Ana (Figure 3.2f and g) are indicative of stratified water vapour. A correlation between phase delay (water vapour concentration) and topographic height commonly leads to volcanoes of similar edifice height showing similar radar path delays. It also leads to a correlation between time series variation and edifice height (discussed further in Chapter 2).

Our estimations of detection thresholds presented in Table 3.1, and Table 3.2) vary between 0.6 cm/yr (at Momotombo, Nicaragua) and 6.2 cm/yr (at Santa Ana, El Salvador), with an average value of 2.4 cm/yr. High thresholds for detection are associated with low numbers of interferograms (shorter total time covered by data) and with the high magnitudes of stratified water vapour artefacts over the larger volcanic edifices (e.g. at Atitlan, Acatenango, Fuego and Santa Ana).

There were few reports of deformation at any of Central America's volcanoes during our period of observation (2007-2010), with the notable exception of a potential inflation (2007) and subsequent deflation (early 2008) at Turrialba, Costa Rica, associated with the development of new fumerolic vents (e.g. *Martini et al.*, 2010; *Smithsonian Institution*, 2008a). As our InSAR data were almost entirely incoherent in the area surrounding Turrialba, this did not allow us to refine our estimations of detection threshold. Broadband seismometers have been used to measure cycles of recoverable, near-vent deformation at Fuego (tilt begins $\sim$ 25 minutes before explosion, *Lyons et al.* (2012)) and Santiaguito (eruptive cycle of $\sim$ 1 hr, *Sanderson et al.*

(2010)) at both temporal resolution higher and magnitudes lower than those recoverable from our InSAR data.

Previous ground based measurements of deformation in Central America seem predominantly to have captured low-magnitude, spatially limited signals. For example, one dry-tilt instrument 1 km South of Poás' crater has shown a general trend of subsidence since measurements began in 1989 (∼ 6 rad/year, *Smithsonian Institution* (1993a)), but electronic distance meter (EDM) measurements made across the volcano summit have not detected significant changes (e.g. *Smithsonian Institution*, 1993b, 2000). Similarly, levelling measurements across Irazú's crater area captured a period of expansion in 1991-1992 (horizontal expansion rate of 1.3 cm/yr, *Smithsonian Institution* (2008b)). Repeat elevation measurements at gravity stations in Masaya caldera between October 1994 and September 2001 record variations in height of average standard deviation 3.6 cm/yr (*Williams-Jones*, 2003). However, these measurements show no systematic trends consistent with large scale inflation or deflation, so that any volcano deformation they do capture is likely to be short-lived or spatially localised and therefore very difficult to isolate in a noisy InSAR dataset. In contrast, *Eggers* (1983) measured deflation of up to 20cm at Pacaya, Guatemala, in 1979-80, magnitudes that would have been well above our InSAR detection limits.

Of the 20 historically active volcanoes in Central America where InSAR measurement was possible, we demonstrate that 10 (∼50%) did not deform permanently above a rate of 2 cm/yr and 16 did not deform above a rate of 5 cm/yr (∼80%) between 2007 and 2010. No evidence of deformation associated with magma movement was found.

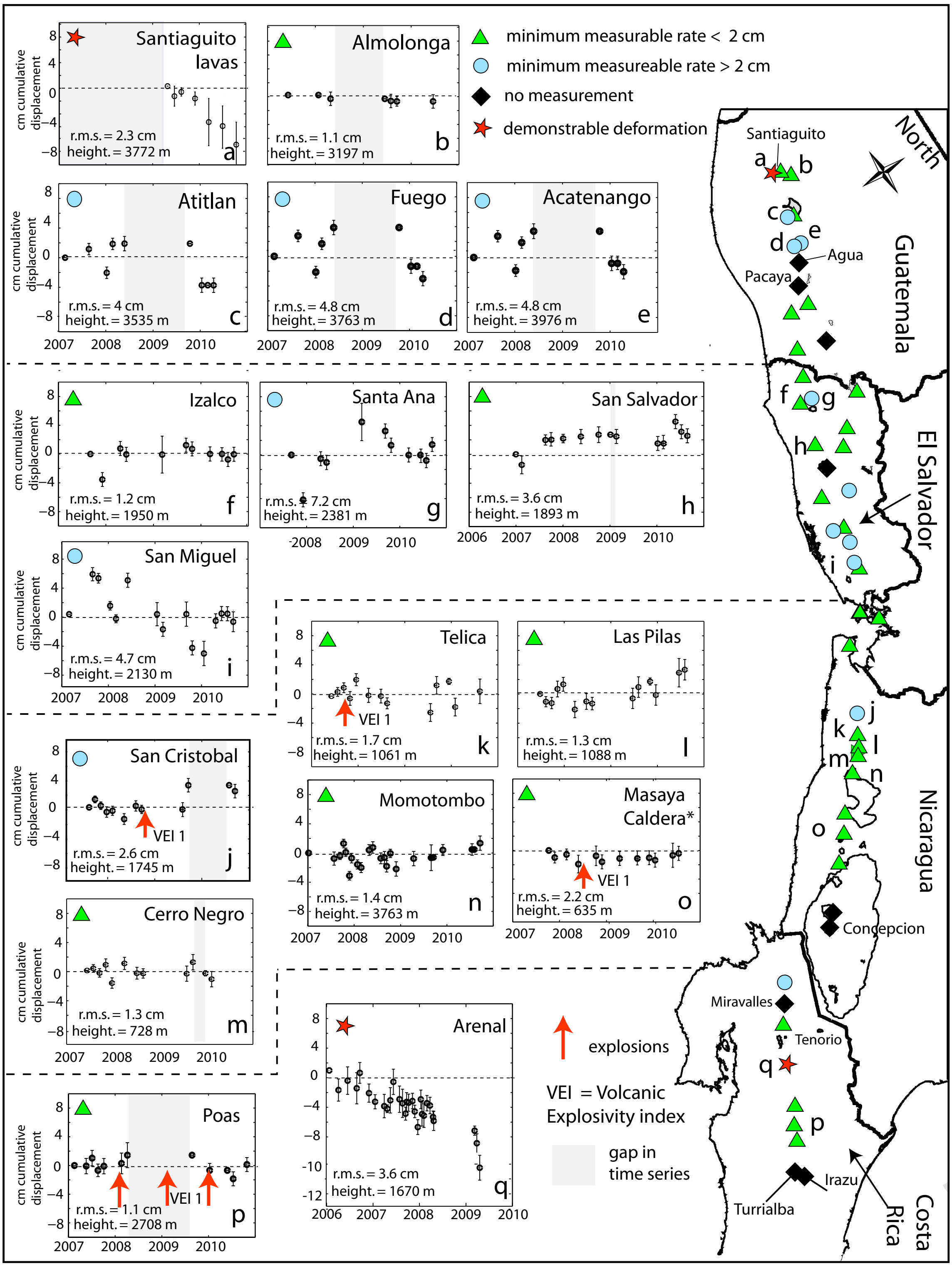

Figure 3.2: Summary of survey results from Central American volcanoes. Time series (a-q) are shown for the average path delay over summit regions of historically active volcanoes. The time series for Masaya (∗) shows the average for inside Masaya Caldera, rather than the region within the ring fault, as described in *Caravantes et al.* (in prep). The time series shown for the Santiaguito lavas was constructed after the removal of a component of phase caused by major topographic change (*Ebmeier et al.*, 2012), while that for Arenal includes C-band RadarSat data that allows us to extend the time series back into 2005 (*Ebmeier et al.*, 2010). The activity of these volcanoes during the period of InSAR survey is described in Table 3.1. Explosive eruptions are marked on the time series by red arrows, and gaps in the time series are shown as grey boxes.

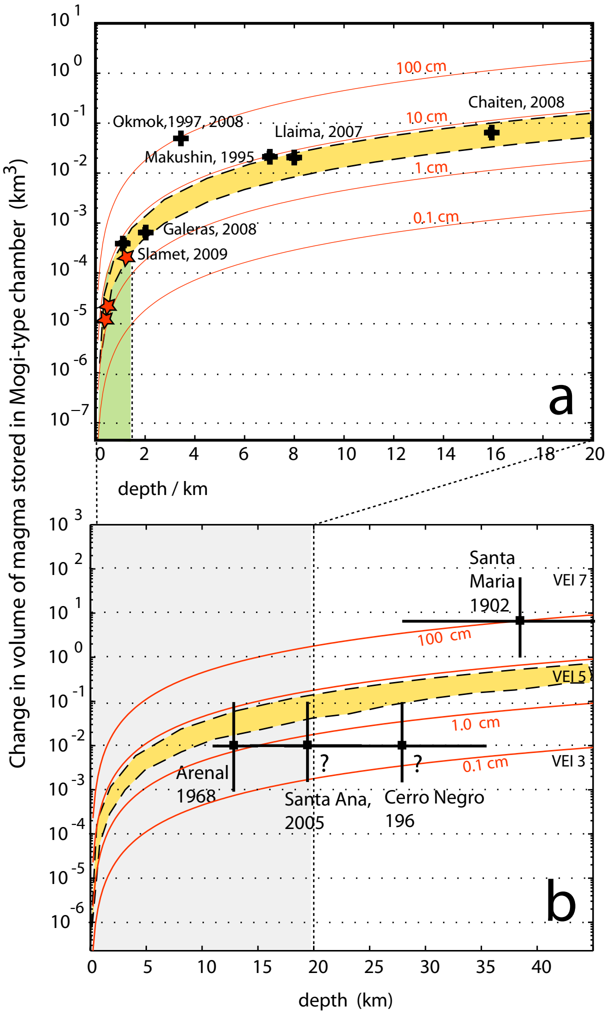

Figure 3.3: Plots illustrating the relationship between depths, volume changes and deformation for explosive eruptions in the literature. Red contours show equal magnitude surface deformation for a simplified Mogi model. The orange bars show the range of minimum deformation magnitudes (found from threshold rates, Table 3.1, and longest interferogram timespan) for explosive eruptions during this survey. a) Literature examples of volcanoes where magma depth and volume change has been estimated from InSAR data (black crosses) Estimated position of explosions in CAVA (2007-2010) are indicated by red stars and associated range of minimum depths is shown by the green box. References are in Table 1.1. b) Large historical eruptions in Central America plotted to show their relative size (we use VEI index ± 1 as a rough indicator of erupted volume) and presumed depth of reservoir. Magma storage is thought to take place at 12-14 km at Arenal (*Pertermann and Lundstrom*, 2006), 'lower crustal' depths for Cerro Negro and Santa Marìa (*Rose*, 1972b; *La Femina et al.*, 2004) and at 'mid crustal' depth at Santa Ana *Carr* (1981a)).

3.4 Comparison to eruptive record

In total, 14 of the 26 historically active volcanoes in Central America exhibited some level of activity between 2007-2010, including periods of lava effusion (e.g. Pacaya), strombolian activity (e.g. Fuego, Arenal), high flux degassing (e.g. Masaya) and fumerolic activity (e.g. Santa Ana, San Miguel). Five volcanoes had minor explosive eruptions during the period of our observations (San Cristòbal, Telica, Masaya, Concepciòn and Poàs, marked on Figure 3.2). A summary of activity from 2007-2010 is outlined in Table 3.1.

Lack of co-eruptive deformation is under-reported in the InSAR literature, but a summary of explosive events where no deformation was measured is presented in Table 3.3, and includes eruptions of similar and higher explosive index than those that occurred during our survey.

3.4.1 Explosive Eruptions

The mechanism by which an explosive eruption is driven determines the character of deformation, if in fact any deformation occurs. For example, rapid cycles of inflation and deflation can be driven by conduit pressurisation building up beneath a crystallised plug before explosion (e.g. Montserrat, deformation period 6–18 hrs, *Voight et al.* (1999)). Even more rapid deformation cycles are associated with the growth of bubbles and ascent of mafic magma in an open conduit (e.g. Stromboli, deformation period $\sim$ 250 seconds, *Genco and Ripepe* (2010)). In Central America, explosions at Fuego (*Lyons et al.*, 2012) and Santiaguito (*Sanderson et al.*, 2010) are associated with conduit pressurisation processes and deformation beyond the temporal resolution of ALOS data used in this study (satellite repeat time 46 days).

Minor explosions associated with the clearing of a blockage in a dominantly open system are also unlikely to result in high magnitude deformation. Explosions at Masaya have previously been attributed to such 'vent-clearing' processes (e.g. 23^{rd} April 2001, VEI 1, *Williams-Jones*, 2003) and the event during our measurement period (18^{th} June 2008, VEI 1, *Smithsonian Institution*, 2009) is expected to have been similar in character. Phreatic eruptions at Poàs in 2008 and 2009 are also likely to have been associated with vent-clearing. Recent deployment of continuous GPS at Telica allowed measurement during a series of ash explosions in May 2011 and showed little deformation (*Witter et al.*, 2011). The non-juvenile composition of the ash from these explosions combined with the lack of deformation suggests that this eruption was amagmatic. If the eruptions at Telica and San Cristobal during 2007 and 2008 were similar in character to this eruption, then it seems likely that there was no significant coeruptive deformation at these volcanoes during our InSAR survey.

The majority of coeruptive deformation events measured with InSAR to date have captured

Table 3.2: Estimated limits to our deformation measurements at active Central American volcanoes. Values for linear regression gradient and R^2 are included only where an interconnected network of interferograms can be constructed spanning all or most of ther period between 2007 and 2010. Our estimations of r.m.s. of detrended time series however, include approximations of variability even where time series have extensive or numerous gaps. The uncertainties in our minimum rates for these volcanoes will be greater than for those for which an interconnected network of interferograms can be constructed.

Volcano	# independent images in stack[a]	time spanned (days)[b]	gradient (cm/yr)[c]	R^2 [c]	r.m.s of detrended time series (cm)[c]	Noise, stack[d] (cm)	Detection threshold[e] (cm/yr)
Santa Maria	3	920	-2.5	0.91	2.3	3.9	1.6
Almolonga	3	920	-	-	1.1	1.9	0.8
Atitlan	3	598	-	-	4.0	6.9	4.2
Acatenango	3	598	-	-	4.8	8.3	5.1
Fuego	3	598	-	-	4.8	8.3	5.1
Pacaya	2	920	-1.2	0.35	5.3	7.5	3.0
Santa Ana	3	736	-0.3	0.1	7.2	12.5	6.2
Izalco	3	736	-0.1	0.2	1.2	2.1	1.0
San Salvador	5	1702	0.7	0.5	3.6	8.0	1.7
San Miguel	2	1012	-0.4	0.1	4.7	6.6	2.4
Conchaguita	3	828					
Cosiguina	3	828					
San Cristobal	4	598	0.7	0.6	2.6	4.5	2.7
Telica	4	598	0.4	0.4	1.7	2.9	1.8
Cerro Negro	4	598	-0.3	0.3	1.3	2.3	1.4
Las Pilas	4	598	0	0.01	1.3	2.3	1.4
Momotombo	5	2070	-0.36	0.24	1.4	3.1	0.6
Masaya	2	874	0.1	0.02	2.2	3.1	1.3
Arenal	3	1852	-6.0	0.86	3.6	6.2	1.2
Poas	3	782	-	-	1.1	1.9	0.9

[a] The number of subsets of interferograms that do not share a common acquisition date (chains)

[b] The sum of the length in days of all the independent chains.

[c] Gradient and R^2 are from linear regression of time series of path delay around the volcano summit area, as illustrated in Figure 1.

[d] The expected magnitude of noise in the stack, calculated from the product of the noise expected for individual interferograms (r.m.s. variation from time series) and the increase in noise expected from adding together all chains (square root of the number of. independent chains).

[e] Expected magnitude of noise in the stack divided by total time in all chains.

the accumulation, emptying and/or recharge of a chamber, most commonly at depths above 5 km, and almost all above 10 km depth (Tables 1.1 and 1.2). Many examples of deformation accompanying dyke intrusion (Table 1.1), and a few instances of conduit processes or summit caldera subsidence (e.g. at Lascar and Colima, *Pavez et al.*, 2006; *Pinel et al.*, 2011) have also been captured by InSAR measurement.

A comparison of the explosive eruptions covered by our survey (Table 3.1) and some examples of those from the global literature that have produced measurable coeruptive deformation (Table 1.1) from the global literature are presented in Figure 3.3a. We limit comparison to coeruptive deformation associated with an explosive event where approximation as a point source was considered reasonable. An orange bar shows the range of deformation detection limits found for erupting Central American volcanoes in this study. The estimated position of the Central American explosions in depth-volume space are show on Figure 3.3a as a green box, based on the assumption that any associated volume change did not exceed 10^{-5} km^3. Even if explosions at San Cristóbal, Poàs and Telica (2007-2009) were associated with the deflation and subsequent recharge of shallow chambers, differing from the 2011 Telica eruption described above, the volume changes would have been the among the lowest measured with InSAR (e.g., Llaima and Slamet, *Bathke et al.*, 2011; *Philibosian and Simons*, 2011).

Although eruptions between 2007 and 2010 did not result in permanent deformation above the level of atmospheric noise, historical eruptions in Central America have been significantly larger. Figure 3.3c shows 20^{th} century eruptions of explosivity index VEI 3 and greater. Of these larger eruptions, we expect the 1902 eruption of Santa Marìa to have produced high magnitude surface deformation (>10 cm), and Arenal's 1968 eruption to have resulted in deformation of the order of a few centimetres, high enough to potentially be detectable with this study's measurement limits.

3.4.2 Persistent Activity

Persistently active volcanoes show evidence of significant surface activity (e.g. degassing, fumerole fields, high surface temperatures) over extended periods of time, without a large associated extrusive flux (*Francis et al.*, 1993). Central American volcanoes where mass flux estimated from SO_2 degassing flux and melt inclusion sulphur content exceed effusion rate by two or three orders of magnitude include Masaya, Pacaya and Telica. Such processes are thought to be maintained through the convective overturning of magma within a network of conduits, where buoyant magma loses volatiles and heat to the atmosphere (or overlying hydrothermal system) and sinks to accumulate in the shallow to mid-depth crust (e.g. as described by *Locke et al.*, 2003). The rise and fall of magma level in a rigid conduit takes place on a timescale of weeks to months (days for Strombolian activity) and is not accompanied by deformation for mafic systems where magma is of a low enough viscosity not to couple to conduit walls. Observations of such processes have been made from micro-gravity measurements at Telica, Poas and Masaya, and have captured changes in conduit magma level (*Rymer et al.*, 1995; *Williams-Jones*, 2003; *Locke et al.*, 2003) apparently unaccompanied by large-scale deformation. The accumulation of degassed magma is therefore the only component of typical 'open' system behaviour expected to produce deformation.

Francis et al. (1993) suggest that the accumulation of degassed magma may result in endogenous growth due to localised emplacement into and beneath a volcano's edifice, a process

Table 3.3: Observations of a lack of co-eruptive deformation reported in the literature. As a lack of deformation is rarely reported, we expect these literature examples to represent a minimum number of cases of a lack of co-eruptive deformation

Volcano	Eruption start date(s)[1]	Magnitude [1] [2]
Lascar[a]	19.04.1993	VEI 4
Irruputuncu[a]	1.09.2003	VEI 2
Aracar[a]	26.11.95	VEI 2
Ojos del Salado[a]	14.11.1993	VEI 1 (uncertain)
Nevados de Chillàn[b]	29.08.03	VEI 1
Villarica[b]	25.05.03, 5.08.2004	VEI 1
Llaima[b]	9.04.03, 26.5.2007	VEI 2
Popocatepetl[c]	03.1996	VEI 3
Pacaya[c]	1995-1996	Strombolian
San Cristòbal[d]	8.11.2007, 06.2008	VEI 1
	6.09.2009, 9.06.2010	VEI 2
Telica[d]	28.10.2007, 5.07.2008	VEI 1
Masaya[d]	16.06.2008	VEI 1
Concepciòn[d]	9.02.2007, 30.07.2008, 11.12.2009	VEI 1
	24.11.2007	VEI 2
Poàs[d]	13.01.2008, 12.01.2009, 09.2009	VEI 1
Shishaldin[e]	13.03.1999	VEI 3
Pavlof[e]	11.09.1996 (?)	VEI 2
Cleveland[e]	2.2.2001 (?)	VEI 3
Korovin[e]	8.5.1998	VEI 3
Sakura-jima[c]	1995-1996	VEI 2
Fogo[f]	2.4.1995	VEI 2
Piton de la Fournaise[g]	8.3.1998	VEI 1
Semeru[h]	various, 2007-2009	ash, pyroclastics
Raung[h]	26.7.07, 12.06.08	VEI 2
Shiveluch[i] [3]	1997-1999	VEI 2-3
Kliuchevskoi[i] [3]	2001-2002	VEI 2
Bezymianny[i] [3]	1992-2002	VEI 2-3 (frequent)

[1] as recorded in the Smithsonian database, accessible here: http://www.volcano.si.edu/index.cfm

[2] Volcanic Explosivity index is used where appropriate, otherwise a description of the type of activity is provided

[3] Potential range of dates and eruption magnitudes are shown, as eruptions where measurements were possible are not specified.

[a] *Pritchard and Simons* (2004a), [b] *Fournier et al.* (2010), [c] *Zebker et al.* (2000), [d] this work, [e] *Moran et al.* (2006),
[f] *Amelung and Day* (2002), [g] *Sigmundsson et al.* (1999),[h] *Philibosian and Simons* (2011), [i] *Pritchard and Simons* (2004c)

Table 3.4: Selected persistently active volcanoes in Central America, where activity is characterised by open system activity. Estimations of volume flux assume a magma density of 2.8 kgm^{-3}. We use the highest values of sulphur content we could find in the literature.

Volcano	Extrusion rate m^{3}yr^{-1}	SO_2 flux [a] t/day	S content of melt incl ppm	mass flux kg/yr	volume flux m^{3}yr^{-1}
Pacaya	5.3×10^{6} [e]	1540 ± 370	1680[c]	$2\pm0.4\times10^{11}$	$5\pm0.1\times10^{8}$
Telica	very low	280 ± 240	2408[b]	$2\pm1\times10^{10}$	$8\pm6\times10^{6}$
Masaya	7×10^{4} [f]	800 ± 590	385[b,d]	$4\pm2\times10^{11}$	$1\pm0.9\times10^{8}$

[a] 1997-2004 mean SO_2 flux as in *Mather et al.* (2006). Uncertainties are one standard deviation in contributing measurements

[b] *Sadofsky et al.* (2008), [c] the highest of the values found by *Walker et al.* (2003)

[d] *Stoiber et al.* (1986) found 320 ppm S in melt inclusions in scoria from 1981. This is very low for a basalt (e.g. *Wallace* (2005)), and is therefore probably not representative of parental melt composition. Volume flux at Masaya may therefore be a factor of ~3 lower than our estimates (see Figure 3.4).

[e] 1961-2001, *Durst* (2008)

[f] since 1524, *Stoiber et al.* (1986). Extrusive flux over the past two decades has been much lower than this.

that should be detectable as deformation. It has also been suggested that magma may return to cumulate complexes at greater depths (e.g. *Locke et al.*, 2003) or be recycled in an active reservoir (*Harris et al.*, 1999). In Central America, gravity measurements have not uncovered shallow magma accumulation at Masaya or Poás, although small increases in gravity at Telica between 1994-2000 indicate an accumulation of material at depths below several hundred metres (*Locke et al.*, 2003).

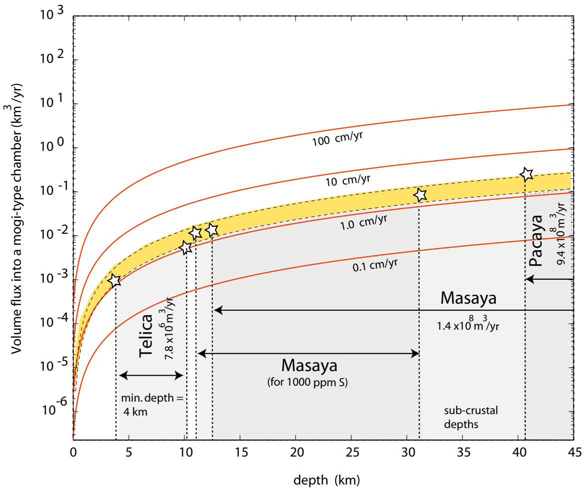

Figure 3.4: Estimations of the depths below which degassed magma could be accumulating in a reservoir that can be reasonably approximated as a point source without causing measurable surface deformation. The range of threshold detection rates for Telica, Pacaya and Masaya is indicated by the orange bar bounded by dashed lines, and peak surface deformation contours are shown in red (as for Figure 3.3). Estimated volume fluxes are derived from average SO_2 emission fluxes (1997-2003) and the sulphur content of melt inclusions (calculations are presented in Table 3.4). The range between upper and lower bounds on volumes treated as one standard deviation of the SO_2 flux measurements made between 1997 and 2003, is indicated by a grey box for each volcano to give an indication of uncertainty. A lower potential volume flux for Masaya, estimated for sulphur content of 1000 ppm is included as melt inclusion measurements of sulphur content at Masaya are very low and may not reflect parental melt compositions.

Measurements of surface deformation will be more sensitive to localised accumulation than to dispersed intrusion. We use our InSAR measurements to make an order of magnitude estimation of the depth below which localised magma accumulation could be taking place without causing measurable deformation. We estimate mass flux of degassing magma at three persistently active volcanoes from average degassing flux (Q_{SO_2}) and estimations of melt sulphur content (ΔC_S), as described by *Kazahaya et al.* (1994). This is converted to a volume change (ΔV) using an assumed magma density (ρ_m) of 2800 kgm^{-3} as follows:

$$\Delta V = \left[\frac{M_S Q_{SO_2}}{M_{SO_2} \Delta C_S \rho_m} - Q_{eff} \right] \qquad (3.1)$$

where Q_{SO_2} is average degassing flux of SO_2 (*Mather et al.*, 2006), M_S and M_{SO_2} are the molecular masses of S and SO_2 and Q_{eff} is the volcano effusion flux (as presented in Table

3.4). We estimate ΔC_S, the decrease in magma sulphur content expressed as a mass fraction, from melt inclusion analyses (*Walker et al.*, 2003; *Sadofsky et al.*, 2008). We choose the highest measured value for magma sulphur content (closest to parental melt concentration) in each case, and assume complete degassing. The mass and volume fluxes presented in Table 3.4 may therefore be underestimates. Our estimation of SO_2 mass flux at Masaya (4×10^{11}kg/yr) is of the same order of magnitude as *Stoiber et al.* (1986)'s estimate of mass flux for 1980-1982, 1.9×10^{11}kg/yr, which assumes that 75% of the magma's sulphur content is lost during degassing.

We use our estimated volume fluxes in conjunction with our threshhold detection rates, (V_r) for Masaya, Pacaya and Telica (1.3 cm/y, 3 cm/yr and 1.8 cm/yr, respectively) to make order of magnitude estimates of minimum accumulation depth using an elastic half-space point source model (Figure 3.4). Minimum depth would then be approximately:

$$d_{min}^2 = \frac{(1-\nu)}{\pi V_r}\left[\frac{M_S Q_{SO_2}}{M_{SO_2}\Delta C_S \rho_m} - Q_{eff}\right], \tag{3.2}$$

The uncertainties in this approach are very high, so that our estimations of minimum depth are only meaningful if treated as an order of magnitude estimation. For example, we assume that the SO_2 fluxes used to estimate magma mass flux (Q_{SO_2}) during our observation period (2007–2010) were similar to the average of measurements made over the period between 1997 and 2003 (*Mather et al.*, 2006). We use the standard deviation in measurements contributing to the 1997-2003 mean to approximate temporal variability in SO_2 flux and show the effect of one standard deviations difference on our estimations of minimum depth in Figure 3.4. The uncertainty in magma sulphur content (ΔC_S) is also expected to be high, as melt inclusion measurements may not reflect parental melt content (e.g. compare estimations of depths for Masaya published S content and 1000 ppm, Figure 3).

Our order of magnitude estimations suggest that there is no localised magma accumulation above depths of ~4 km at Telica, and none above the lower crust and base of crust at Pacaya or Masaya, respectively. This makes the unrealistic assumption of elastic behaviour down to the base of the crust, so true minimum detection depths are expected to be shallower than this.

Our results, in common with gravity data (*Locke et al.*, 2003), suggests that there is no shallow, localised accumulation of magma at persistently active volcanoes in Central America. Degassed magma is therefore likely to be a) returning to great depth, and/or b) dispersed through the mid-lower crust in a large number of individually small intrusions so that volume changes are too small to result in surface deformation. The greater the area over which degassed magma is distributed, the lower the rates of any resultant surface deformation.

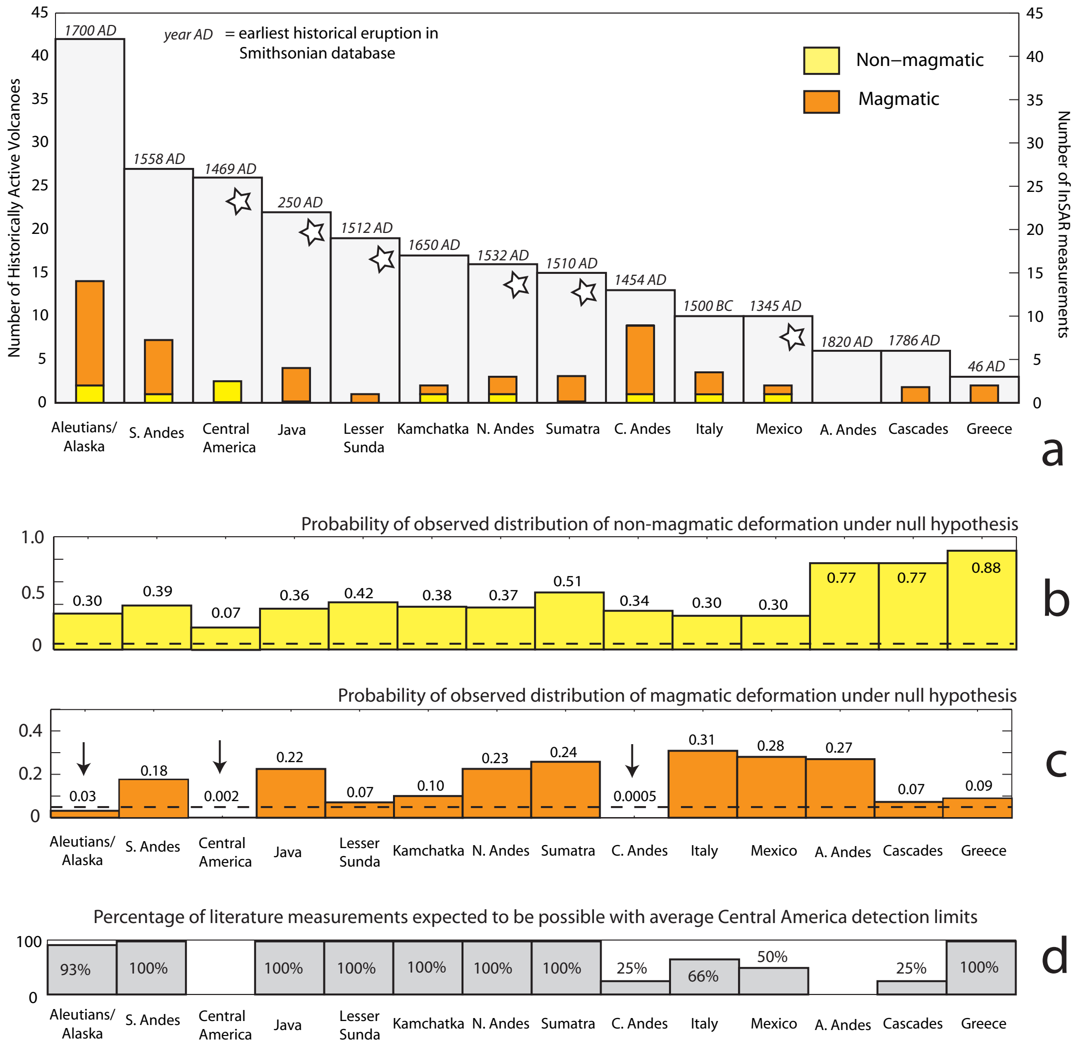

Figure 3.5: a) Literature InSAR measurements of volcano deformation at 14 of the world's best geodetically studied volcanic arcs, presented in decreasing order of the number of historically active volcanoes. The date of the first historical eruption recorded in the Smithsonian database is marked in italics at the top of each bar, and bears no obvious relationship to the number of historical eruptions recorded. The number of measurements of non-magmatic deformation is shown in yellow and magmatic deformation is shown in orange. White stars mark arcs where survey-type studies have been made just with ALOS data and therefore have the same temporal coverage. b) Probabilities of the observed numbers of non-magmatic deformation events occurring at each arc if deformation measurements were evenly spread around the world's historically active volcanoes (Fisher exact test of independence). The 95% confidence interval is shown as a dotted line. c) Probabilities of the observed numbers of magmatic deformation events occurring at each arc if deformation measurements were evenly spread around the world's historically active volcanoes. Arcs where deviation from the expected number of deformation events are statistically significant (at the 95% level) are marked with an arrow. d) The percentage of measurements for each arc that exceed the average level of atmospheric noise at Central American volcanoes (see Table 3.5).

3.5 Comparison to other volcanic arcs

We compare our results to literature measurements of deformation at other volcanic arcs (Figure 3.5a), separating observations into magmatic and non-magmatic processes (including loading effects and the deformation of flow deposits). Any statistical comparison that relies on examining the temporal distribution of InSAR deformation measurements is problematic, because observation periods are not commonly reported in the literature, especially where no deformation was measured. We therefore test the statistical significance of the lack of deformation observed in Central America with respect to the distribution of deformation at historically active volcanoes at other volcanic arcs. Our null hypothesis is that all historically active volcanoes are equally likely to deform in a manner measurable with InSAR. We use Fisher's exact test of independence (*Fisher*, 1922) to examine the probability that each arc in Table 3.5 is part of the global set of InSAR measurements. For our purposes, an exact test is favourable over criteria that rely on the sample distribution approximately matching a theoretical distribution (e.g. Pearson's χ^2 test) due to the small sample size (P-values set out in Table 3.6).

We do not reject our null hypothesis for non-magmatic deformation (Figure 3.5b), as this is distributed relatively evenly between active volcanoes. The probabilities of the observed distributions of magmatic deformation arising randomly, however, are considerably lower, and we find statistically significant (at the 95% level) deviations in the numbers of measurements of deformation in Central America, the Central Andes and Aleutian Islands (Figure 3.5c). In both the Central Andes and Aleutians the number of observations of deformation exceed the number expected per historically active volcano, while in Central America they are significantly lower than expected. If deformation measurements were distributed evenly across the world's historically active volcanoes, the probability of none of Central America's 26 historically active volcanoes deforming in a manner measurable using InSAR would be <0.01.

An obvious concern given the different time periods of observations is that temporal sampling might control the number of measurements of volcano deformation at different arcs. We do not think that this is the case, because arcs with exactly the same temporal coverage of InSAR measurements show a range in number of deformation measurements. Specifically, the recent availability of L-band data (since 2007) has allowed the first InSAR surveys of volcano deformation to be made for Java, Lesser Sunda, Sumatra, the Northern Andes and Central America (marked with a star on Figure 3.5), with the number of measurements of volcano deformation being 4, 1, 3, 3 and 0, respectively (*Philibosian and Simons*, 2011; *Fournier et al.*, 2010; *Biggs et al.*, 2009b; *Chaussard and Amelung*, 2011). For these arcs with data only since 2007, only Central America shows any statistically significant undersampling for magmatic deformation.

This result indicates a systematic difference in the occurrence of deformation measurable with InSAR on the CAVA, relative to other well-studied arcs. We investigate whether this difference is likely to be due to particular difficulties in making InSAR measurements by comparing literature deformation measurements to the average minimum measurable rate for Central America (2.4 cm/yr, Table 3.5 and Table 3.2). This allows us to make estimates of the approximate percentage of deformation measurements that would have been possible with similarly high levels of atmospheric noise to Central America (Figure 3.54). Although the large majority of literature measurements would have been possible (~80 %), a slightly lower percentage of magmatic deformation events (73%) exceed our average minimum detection rate than non-magmatic events (86%). If we repeat the Fisher tests of independence including just those deformation events that would have been observable in Central America, the probability of no historically active volcanoes deforming in Central America is even lower than that shown in Figure 3.5b, with a P-value still less than 0.01.

We find a statistically significant difference in the number of measurements of magmatic deformation made in Central America relative to other parts of the world. As ~80 % of literature measurements exceed the average minimum detectable rate for Central America, this may imply some difference in the average character of magma storage.

3.5.1 Limiting factors for surface deformation

The factors that control the geodetic expression of magma movement at an individual volcano are numerous and complex. Magma flux, composition, storage depth, storage geometry, and the existence of an open conduit are all important. Although there may be general commonalities in these factors for volcanoes in the same regional setting, local conditions may be equally significant (e.g. chamber geometry may be affected by local stress fields). Factors affecting the occurrence of deformation may also vary along the length of a volcanic arc. In Central America, the existence of systematic along-strike variation in geochemistry and tectonic parameters are well-established (*Patino et al.*, 2000; *Carr et al.*, 2003; *Bolge et al.*, 2009). We therefore limit ourselves to suggesting factors applicable across all or most of the CAVA that may have the potential to contribute to low geodetic expression of magma movement.

The CAVA has a high proportion of basalts to andesites (*Carr*, 1984) relative to continental arcs, so that more magma rises directly from the base of the crust without a period of crustal storage. The large density contrast at the base of the Central American crust (thickness = ~25–45 km) is thought to trap basalts at depths well below those for which volume changes are commonly detected geodetically (e.g. Figure 3.3). Volume changes would have to be both localised and exceed volumes on the order of 10^7–10^9 m^3 to produce deformation of the order of 1 cm magnitude. Basalts are thought to ascend rapidly from depth during eruption (e.g. at Fuego, Guatemala or Cerro Negro, Nicaragua), with the only exception being around Masaya in Nicaragua where thinner crust allows the ascent of denser, more mafic material that becomes trapped by less dense layers in the shallow crust (*Walker et al.*, 1993). As basalts are at least as common as andesites in Central America, this means that a large proportion of volcanic activity

Table 3.5: Arc-scale comparison of InSAR-measured deformation. Bracketed, bold numbers indicate the number of measurements that would have been possible with Central American limits applied. References that describe large-scale surveys are included in the table, information regarding individual volcanoes is summarised in Tables 1.1 and 1.2

Volcanic Arc	temporal coverage	# volcanoes	# historically active	# InSAR measurements			% > threshold
				magmatic	non-magmatic	total	
Kamchatka [1]	1992-2003	77	17	1(**1**)	1(**1**)	2(**2**)	100%
Alaska/Aleutians [2]	1992-2010?	91	42	12(**10**)	2(**2**)	14(**12**)	93%
Cascades [3]	~1992-2001	64	6	2(**1**)	0	2(**1**)	50%
Mexico [4]	1990s, 2007-2010	43	10	1(**0**)	1(**1**)	2(**1**)	50%
Central America [5]	2007-2010	**72**	**26**	**0**	**3**	**3**	-
Northern Andes [6]	2006-2010	35	16	2(**2**)	1(**1**)	3(**3**)	100%
Central Andes [7]	1992-2010	69	13	8(**2**)	1(**0**)	9(**2**)	25%
Southern Andes [8]	2002-2008	63	27	6(**6**)	1(**1**)	7(**7**)	100%
Austral Andes [9]	1996-1999	7	6	0	0	0	-
Italy [10]	~1992-2000	15	10	2(**1**)	1(**1**)	3(**2**)	66%
Greece [11]	1995-2000, 2010-11	6	3	2(**2**)	0	2(**2**)	100%
Sumatra [12]	2007-2010	32	15	3(**3**)	0	3(**3**)	100%
Java [13]	2007-2010	39	22	4(**4**)	0	4(**4**)	100%
Lesser Sunda [14]	2007-2010	28	19	1(1)	0	1(1)	100%
% observable in Central America:				73%	86%	78%	

[1] *Pritchard and Simons* (2004b); *Lundgren and Lu* (2006)
[2] *Lu* (2007); *Lu and Freymueller* (1998); *Lu et al.* (2002a, 2003b); *Lu and Dzurisin* (2010a); *Moran et al.* (2006)
[3] *Dzurisin et al.* (2006); *Poland et al.*, 2006)
[4] *Fournier et al.* (2010); *Pinel et al.* (2011)
[5] this work and *Ebmeier et al.* (2010, 2012); *Caravantes et al.* (in prep)
[6] *Mothes et al.* (2008); *Biggs et al.* (2010); *Parks et al.* (2011)
[7] *Pritchard and Simons* (2004a); *Fournier et al.* (2010); *Sparks et al.* (2008); *Pavez et al.* (2006); *Froger et al.* (2007)
[8] *Pritchard and Simons* (2004b); *Fournier et al.* (2010); *Bathke et al.* (2011)
[9] *Pritchard and Simons* (2004b); *Fournier et al.* (2010), [10] *Lundgren et al.* (2001); *Lanari et al.* (2002)
[11] *Sykioti et al.* (2003); *Papageorgiou et al.* (2012), [12] *Chaussard and Amelung* (2011)
[13] *Philibosian and Simons* (2011), [14] *Agustan et al.* (2012); *Chaussard and Amelung* (2011)

is not expected to involve any stage of storage in the shallow crust.

The compressibility of bubble-rich magma can accommodate some or even all of the volume change associated with a magmatic intrusion, so that large intrusions can result in low magnitude surface deformation (e.g. *Johnson et al.*, 2000; *Mastin et al.*, 2009). This effect is most significant for pressure changes involving evolved, gas-rich magma at shallow depths (e.g. *Mastin et al.*, 2008). Conditions that affect the compressibility of a shallow magma include its temperature, time of residence in the crust (and therefore crystal content), parental melt content and the degree of degassing, i.e. remaining exsolved gas content. In the absence of a

Table 3.6: Probabilities of observing the number of deformation events found at 14 volcanic arcs (as in Figure 3.5) according to a Fisher's exact test with the null hypothesis that deformation is evenly distributed around the world. Each arc was compared to the rest of the global literature separately. Data for which the deviation from the null hypothesis is significant (i.e. distribution of deforming volcanoes is not spatially random) are underlined.

Volcanic Arc	**Non-magmatic deformation**	**Magmatic deformation**
Aleutians/Alaska	0.333	$\underline{0.032}$
Southern Andes	0.397	0.175
Central America	0.198	$\underline{0.003}$
Java	0.4012	0.225
Lesser Sunda	0.4570	0.071
Kamchatka	0.367	0.100
Northern Andes	0.359	0.225
Sumatra	0.542	0.258
Central Andes	0.326	$\underline{0.0005}$
Italy	0.280	0.308
Mexico	0.280	0.280
Austral Andes	0.787	0.270
Cascades	0.787	0.073
Greece	0.888	0.090

Table 3.7: Summary of physical characteristics of tectonic parameters for selected well-studied segments of volcanic arcs. These arc segments do not correspond directly to the arcs shown in Figure 3.5, but do give an indication of nearby tectonic parameters. Extension is considered to be positive and compression negative.

Volcanic Arc	Convergence rate[1] (trench normal)	Extension/ Compression[1]	Arc-parallel slip[1]	volume extrusion rate per 100km[1]	modelled H_2O Flux at 100 km[2]	average surface heat flux[3]
	mm/yr	mm/yr	mm/yr	km^{3}yr^{-1}	TgMa^{-1}m^{-1}	mWm^{-2}
Kamchatka	74	10 ± 5	5 ± 3	$3 \pm 0.9\times10^{-3}$	25	84
East Aleutians	65	-5 ± 5	0 ± 1	$0.2 \pm 0.07\times10^{-3}$	19	-
Alaska (Katmai)	58	-1 ± 1	0 ± 1	$0.26 \pm 0.05\times10^{-3}$	15.2	77
Cascades	24	2 ± 1	0 ± 1	$0.95 \pm 0.04\times10^{-3}$	1.9	80
Mexico	51	0.4 ± 0.04	0.14 ± 0.01	$0.14 \pm 0.04\times10^{-3}$	6.1	111
Central America	73	8^{*} and $4^{\S}$ ± 2	11 ± 2	$3.1 \pm 0.8\times10^{-3}$	17-21	82
Andes (Southern)	75	-1 ± 1	10 ± 8	$1.3 \pm 0.4\times10^{-3}$	16	79
Sumatra	41	0 ± 2	23 ± 2	$6.6 \pm 2\times10^{-3}$	10-12	66

[1] *Acocella and Funiciello* (2010)

[2] (*van Keken et al.*, 2011), fixing slab-overriding plate coupling depth at 80 km and including contributions from serpentenisation (based on thermal models of *Syracuse et al.* (2010))

[3] *Zellmer* (2008)

N.B. In Central America, extension has both arc-parallel (*) and arc-normal (§) components

Figure 3.6: a) Illustration of parameter space for the ratio of peak LOS deformation (spatially averaged) for a vertically elongated ellipsoid (*Yang et al.*, 1988) and spherical source of equal volume and centre depth for the same pressure change (0.5 Pa). Major axis length directly describes the degree of vertical elongation because minor axis length was held constant at 1 km. Dotted line indicates the edge of the region for which Yang's finite approximation for an ellipsoid in an elastic half space is expected to be accurate, approximated as where the semi-major axis is less than 0.4×depth (e.g. *Segall*, 2010, pg 224) b) Example peak satellite line-of-sight (LOS) displacements for ellipsoid and sphere of the same volume at centre depth 8 km, where the ellipsoid is elongated by a factor of 4. LOS is as for the majority of ascending ALOS data used in this study, and refers to an incidence angle of ~34°.

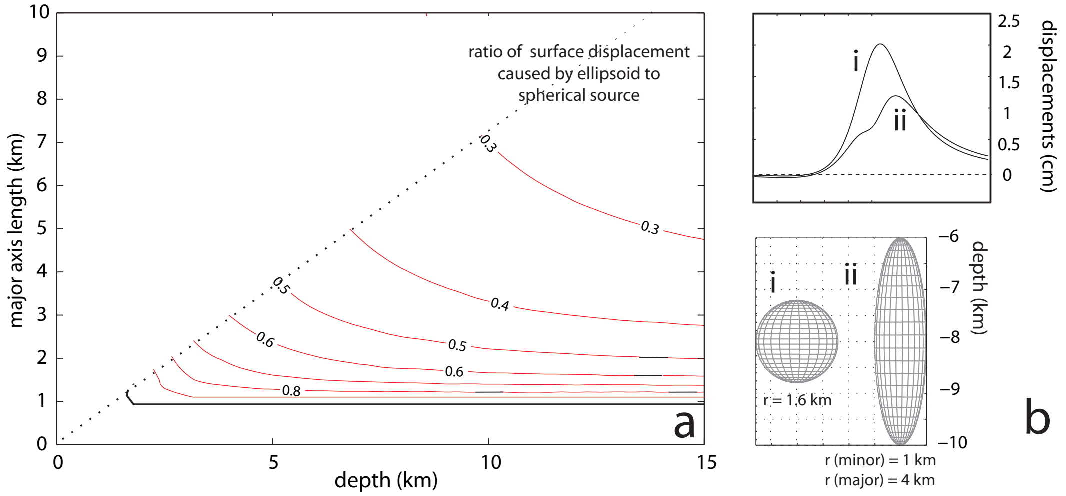

detailed knowledge of all of these conditions, the problem of magma compressibility in Central America is underconstrained. However, if exsolved gas content at shallow depths correlates with parental melt volatile content, perhaps where little to no degassing has taken place, then the distinctively high water contents inferred for Central American parental melts (*Wallace*, 2005; *Sadofsky et al.*, 2008) may result in particularly high magma compressibility.

Vertically elongated magma reservoirs, thought to be common beneath stratovolcanoes, produce lower magnitude surface deformation than spherical reservoirs for the same depth and pressure change. We expect magma reservoirs beneath a number of Central American volcanoes to be vertically elongated (e.g. evidence from polybaric fractionation at San Miguel, El Salvador (*Carr*, 1981b), narrow reservoir radius at Telica, Nicaragua (*Roche et al.*, 2001)). For example, comparison of a vertically elongated ellipsoid (*Yang et al.* (1988), major axis = 4 km, minor axis = 1 km) to a sphere of the same volume and with the same centre depth and pressure change (8 km and 0.5 MPa, respectively) suggests that maximum surface deformation for the ellipsoid is only ~40 % that of the sphere (Figure 3.6). We expect vertically elongated magma storage to be favoured in transtensional or extensional stress fields. Regional stress in the CAVA is dominated by dextral shear associated with the movement of the fore-arc sliver to the northwest (*Correa-Mora et al.*, 2009; *LaFemina et al.*, 2009; *Alvarado et al.*, 2011), and by east-west extension accommodated by north-south trending normal faults. Many magmatic centres in Central

America are located in extensional zones (e.g. *Burkart and Self*, 1985).

The relevance and relative importance of these three factors could be estimated for Central America, given a more complete knowledge of magma storage conditions, including stalling depths, magma reservoir geometries, residence times in the crust, and the exsolved gas content of shallow magma reservoirs. In combination with deformation measurement, such data has the potential to promote the development of a more systematic understanding of the relationship between magmatic intrusion and crustal deformation.

3.6 Conclusions

We examine L-band InSAR data (2007–2010) for the Central American arc and are able to make measurements at 20 out of 26 historically active volcanoes. We use stacking and time series analysis to distinguish between potential deformation and water vapour artefacts in interferograms and estimate threshold deformation detection rates using time series for the historically active volcanoes (Section 3.2). We find no evidence of magmatic deformation in Central America between 2007 and 2010.

The lack of deformation accompanying explosions at Telica, San Cristóbal and Poás is unsurprising for such minor eruptions, presumably associated with very small, if any, chamber volume change (Section 3.4.1). Recent high degassing fluxes and the lack of deformation at Pacaya and Masaya volcanoes suggest there are no points of localised accumulation of degassed magma at shallow depths (<10 km) in the elastic crust beneath them. This suggests that magma a) returns to depths below our limits of geodetic detection and/or b) is dispersed through the crust in multiple smaller intrusions (Section 3.4.2).

Our quantification of detection thresholds for InSAR at Central American volcanoes confirmed a lack of magmatic deformation, found to be statistically significant in relation to the distribution of literature magmatic deformation measurements with respect to historically active volcanoes. In spite of high levels of stratified atmospheric water vapour and resulting high threshold for detection (average rate 2.4 cm/yr), we expect the majority of volcano deformation rates measured with InSAR in other parts of the world to have been possible under Central American environmental conditions (Section 3.5).

We suggest several factors that have the potential to limit magnitudes of surface deformation associated with volcanic activity in Central America (Section 3.5.1). These include deep magma storage and rapid ascent, the potential impact of high parental melt water content on shallow magma compressibility and the influence of vertically elongated magma reservoir geometries. Such factors may act in isolation or combination to result in reduced magnitudes of surface deformation in Central America relative to other volcanic arcs.

Chapter 4

Steady downslope deformation at Arenal, Costa Rica

adapted from Ebmeier, S. K., J. Biggs, T. A. Mather, G. Wadge, and F. Amelung (2010), *Steady downslope movement on the western flank of Arenal volcano, Costa Rica*, Geochemistry, Geophysics, Geosystems, 11, Q12,004 14PP, doi:10.1029/2010GC003263.

The deformation of a volcano is caused by both volcanic activity and mechanical processes associated with the building and settling of an edifice. Volcano deformation is most commonly measured with the aim of illuminating magmatic processes. However, measurements of deformation also capture surface processes, such as the subsidence of fresh eruptive products (e.g. *Stevens et al.*, 2001a) and spreading of the edifice (e.g. *Lundgren et al.*, 2004). Volcanoes are built of poorly consolidated rock at rates greatly exceeding those of erosion, making them inherently unstable. At many active and dormant volcanoes, edifice instabilities present a significant hazard to surrounding populations, from localised rockfalls to massive sector collapses (*Ward and Day*, 2003). The dangers associated with an unstable edifice are most extreme where the removal of an overburden could cause rapid decompression of a magma body and trigger an eruption. The best chance of identifying regions of instability on a volcano comes from understanding and monitoring the deformation of its edifice.

In this chapter I use interferometric data to measure the deformation of Arenal's edifice over four years between late 2005 and mid 2009. The rate of motion was found from time series analysis, and components of motion were resolved from imagery with different look angles. Different scenarios for the origin of the deformation of Arenal's western flanks are then considered and tested against information deduced from analysis of the results from interferometry and existing structural, geophysical, volcanological and petrological information.

4.1 Volcán Arenal

Volcán Arenal is Costa Rica's most active volcano, and has been almost continuously erupting for ~40 years. Arenal was dormant for several centuries before its reactivation in July 1968, when a lateral blast and subsequent vulcanian eruption killed 78 people and destroyed two nearby villages. An area of around 15 km^2 was severely damaged during three days of blast eruptions and a further 230 km^2 experienced significant ash fall (*Alvarado et al.*, 2006). The eruption blast opened up a radial fissure running west from the summit, feeding three explosion craters (A, B, C - Figure 4.1b and c). Crater D, at the then summit of the volcano, has remained inactive through the current phase of activity. Since this initial eruption, activity at Arenal has shifted through several phases, with a general trend of decreasing effusion rate (2 m^{3}s^{-1} in 1968 to 0.086 m^{3}s^{-1} between 2000 and 2004, *Wadge et al.* (2006)). In 1973, during a brief pause in activity, lava effusion shifted from the lowest of the new explosion craters (A) to the highest (C), which has been active ever since. Today, activity at Arenal is dominated by occasional, short lava flows and intermittent low level explosions, with only 4-6% of Arenal's total output being pyroclastic flows (*Wadge et al.*, 2006) which currently present the biggest hazard to the population around Arenal.

Today at least 7000 people live within a 6 km radius of Arenal, mostly in the town of La Fortuna, where most of the population is to some extent dependent on volcano and hotspring related tourism for their livelihood. Lake Arenal, which extends to within 4 km of Arenal's western flank, was created in 1979 by the building of the Sangregado Dam, which supplies a high proportion of Costa Rica's hydroelectricity (Figure 4.1).

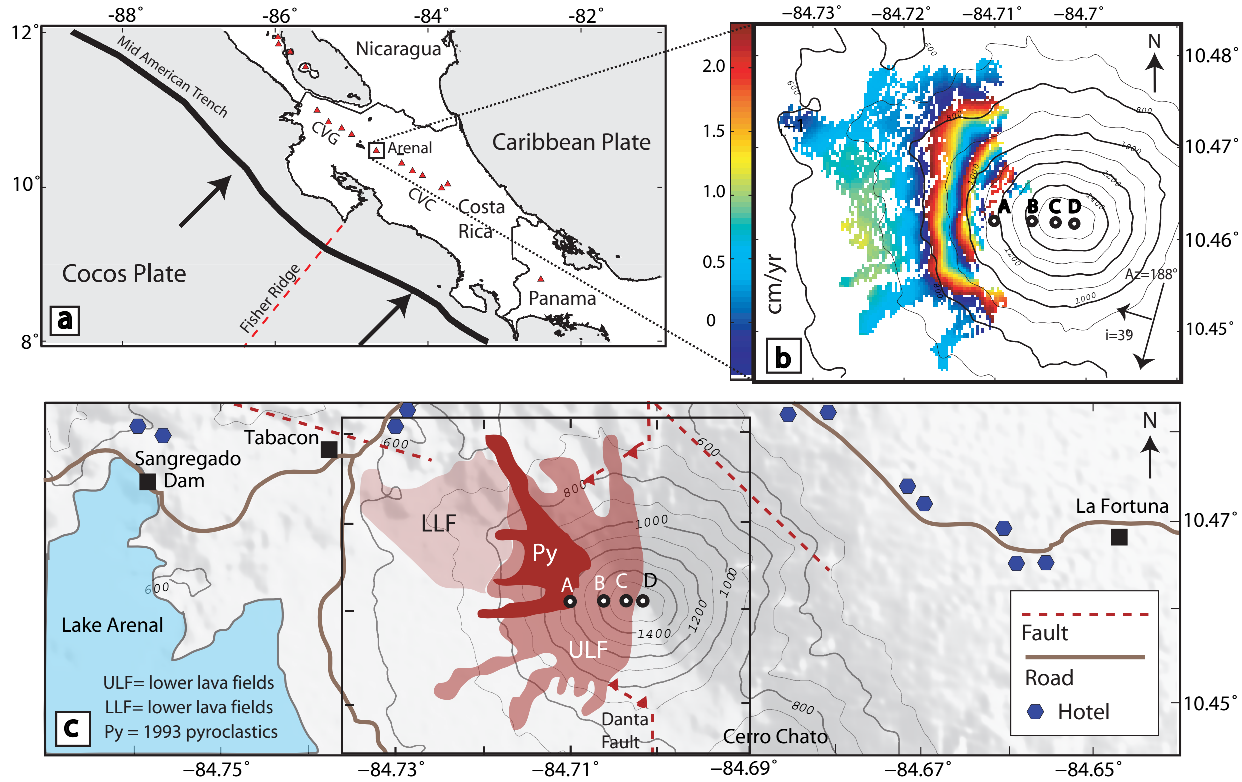

Figure 4.1: a.) Map showing the location of volcanoes in Costa Rica b.) Average LOS deformation rate in cm/yr for descending Radarsat interferograms 2005-2008. This figure is wrapped so that one complete transition through the colour scale represents 2.56 cm deformation. c) Schematic map showing the extent of the post 1968 lavas (after *Wadge et al.* (2006) and *Alvarado et al.* (2006)) and the locations of towns, hotels and significant infrastructure. Craters A-D are repesented by open circles. LLF = lower lava fields (1968-1973), ULF = upper lava fields (1974-2005). Pyroclastic flow (Py) deposits are from 1993. Active faults (younger than 4 ka) are marked by red dashed lines, including the Danta fault. *Alvarado et al.* (2006) infer the presence and location of the thrust fault shown here from pre-1968 aerial photography. The box used for inset (b) and in subsequent figures is outlined on (c).

4.2 Interferometric Data

Interferograms were constructed from two sets of satellite data: ALOS (mid 2007-2009) and Radarsat (late 2005-2008). A significant number of interferograms produced; ~75% of the Radarsat and ~30% of the available ALOS were incoherent over Arenal and were discarded. 40 interferograms that were phase coherent over at least parts of the volcano's edifice remained, and were used in analysis (Table 4.1).

The interferograms show a consistent pattern of fringes on Arenal's western flanks for the whole time between December 2005 and April 2009 (Figure 4.2). All of the longer period interferograms (Figure 4.2 a, c, e, g) show a remarkably similar, sharp-cornered subsidence signal, increasing in rate towards the volcano summit. Short time period interferograms (Figure 4.2 b, d, f, h) exhibit greater variation in signal shape, with peak subsidence appearing on different parts of the volcano on different dates, suggesting that the net motion captured in the long-time period interferograms actually represents the cumulative motion of many smaller units.

Table 4.1: Coherent ALOS (look angle: 34°, heading 192°descending and 348° ascending) and RadarSat (look angle 39°, heading 188°) interferograms.

Instrument Track, Direction	Master Date (yymmdd)	Slave Date (yymmdd)	B_{perp} (metres)
ALOS 467, descending	070922	071107	-444
	070922	090327	-748
	071107	090327	357
ALOS 466,descending	080121	080422	-123
	080121	090310	-640
	080121	090425	-849
	080422	090310	-517
	080422	090425	-725
	090310	090425	-208
ALOS 163,ascending	070306	070906	379
	070306	080122	513
	080908	081024	413
RadarSat descending	051229	060404	-457
	051229	070117	81
	051229	070517	-7
	060122	071008	31
	060615	070610	-172
	061130	070117	-38
	070117	070517	-88
	070117	070728	82
	070117	080112	-97
	070330	070423	22
	070821	080417	31
	070914	080324	-41
	071008	080417	244
	071125	080229	83
	070330	080205	35
	070423	080205	13
	070610	070914	-26
	070821	071219	103
	060404	071125	58
	060919	070330	96
	060919	080229	-29
	060826	080229	75
	060826	071125	-87
	071125	071219	-390
	080112	080205	-132
	080112	080324	249
	070610	080324	-67
	080112	080205	-132

This shows that although the average pattern of deformation is relatively constant between 2006 and 2009, the instantaneous rate of motion varied with space and time across Arenal's edifice (Figure 4.5).

4.2.1 Patterns of Coherence

Steep, unstable slopes, large baseline separations, dense vegetation and frequent eruption all contribute to phase decorrelation at Arenal (The relative importance of various factors contributing to decorrelation in Central America are discussed in Chapter 2). Coherence is therefore limited to parts of the western slopes of the volcano, roughly defined by the edges of the post-1968 lavas, but stopping short of the summit (Figure 4.2).

The response of L- (λ = 23 cm) and C-band (λ =5.6 cm) radar to vegetation is markedly different, with L-band having been demonstrated to have better coherence in highly vegetated regions than C-band (e.g. *Fournier et al.*, 2011a). This is illustrated by the difference between Radarsat (C-band) and ALOS (L-band) interferograms of Arenal (Figure 4.2). Variations in coherence are associated with changes in the lava surface stability. The best coherence is on young lava fields, which generally have exceptional scatter stability (*Lu and Freymueller*, 1998). In all but the shortest time period interferograms (Figure 2 (f, h)), coherence breaks down above an elevation of about 1100 m. Below this height the surface is grown through with low lying vegetation and is sufficiently stable for drainage channels of height ∼10-30 m to be established. Above this height, slopes are much less stable, with no drainage channels and semi-continuous rockfalls as a consequence of the high rate of break up of steep lava fronts near the summit. However, a few short-period ALOS interferograms (Figure 4.2 (f, h)) show that subsidence does not extend all the way up to Crater C, but reaches its peak value between 1200-1440 m elevation.

The lack of coherence on Arenal's eastern slopes is attributed to a combination of denser, more mature vegetation right up to the summit and loose, rockfall prone material. Furthermore, the eastern side of the volcano is roughly perpendicular to the radar look direction for descending acquisitions, (which constitute 92% of interferograms used) and is therefore foreshortened in radar geometry. We do not extrapolate our observations onto the eastern flank because none of the observed fringes, the volcano structure or young flows are radially symmetric. The signal we observe is limited to young (<40 years) lava flows, while material east of the summit is predominantly older and cannot be assumed to be deforming in the same way.

4.2.2 Topographic Artefacts

A concern in the interpretation of the Arenal dataset was the possibilty that any apparent deformation signal could be an artefact caused by the difference between the DEM used in processing and actual topography. This could be either because of uncertainty in the SRTM data used to construct the DEM, or because the volcano's surface has changed significantly since 2000, when the SRTM data were acquired (*Rosen et al.*, 2001).

The first possibility is relatively easy to discount, since the uncertainty in SRTM data in Costa Rica is expected to be ∼5-7 m (*Rodriguez et al.*, 2006). For the Arenal interferograms (Table 4.2), the greatest risk of DEM errors contaminating any deformation signal will be for those C-band interferograms of longest baseline separation, but the altitude of ambiguity for even the longest of these is still many times the expected error in the SRTM data.

Table 4.2: Range of perpendicular baselines (B_{perp}) and heights of ambiguity (h_a) for C-band and L-band interferograms of Arenal (metres)
.

	ALOS		RadarSat	
	Min	Max	Min	Max
B_{perp}	123	849	7	457
h_a	675	98	2898	62

The second option, of there being significant topographic change since the DEM data was collected, was tested by examining the relationship between perpendicular baseline separation and magnitude of apparent deformation. An artefact in phase change caused by a DEM error is expected to be proportional to baseline seperation (e.g. *Hooper et al.*, 2004), so the lack of correlation between the two properties in the Arenal data (Figure 4.3) suggests that the phase shift at Arenal represents a genuine ground movement. This is reasonable as the lava emplaced since 2000 has not extended beyond the incoherent zone around Arenal's summit. Between 2000 and 2004 a maximum thickness of around 40 m of lava was emplaced, but never extended any further downslope than Crater A (*Wadge et al.*, 2006). Between 2005 and 2010 lava effusion rates have been even lower. We conclude that the SRTM data are an accurate reflection of Arenal's current topography in coherent areas, and that the phase signal represents real deformation and not a DEM error.

Artefacts caused by topographically correlated variations in water vapour (*Wadge et al.*, 2002) are identifiable from their association with particular acquisition dates and their tendency to change sign depending on whether the image is used as the master or slave. The fact that apparent deformation is consistent in sign and approximate rate in all interferograms allows the possibility of a significant stratified water vapour effect to be disregarded.

4.2.3 Components of Motion

InSAR measures displacement along a single line of sight. Multiple measurements from different look angles can be combined to resolve this into a full 3D deformation field (e.g. *Wright et al.*, 2004). In practice, interferograms can be produced from SAR data from ascending and descending orbits, providing only 2 independent constraints on a 3 dimensional problem. Resolving components of motion therefore requires an external source of information or an assumption (*Fialko et al.*, 2001b, e.g.). The assumption was therefore made that N-S motion was negligible, allowing us to resolve the volcano's deformation field into a 2D plane with axes running vertically and E-W (e.g. *Biggs et al.*, 2009b).

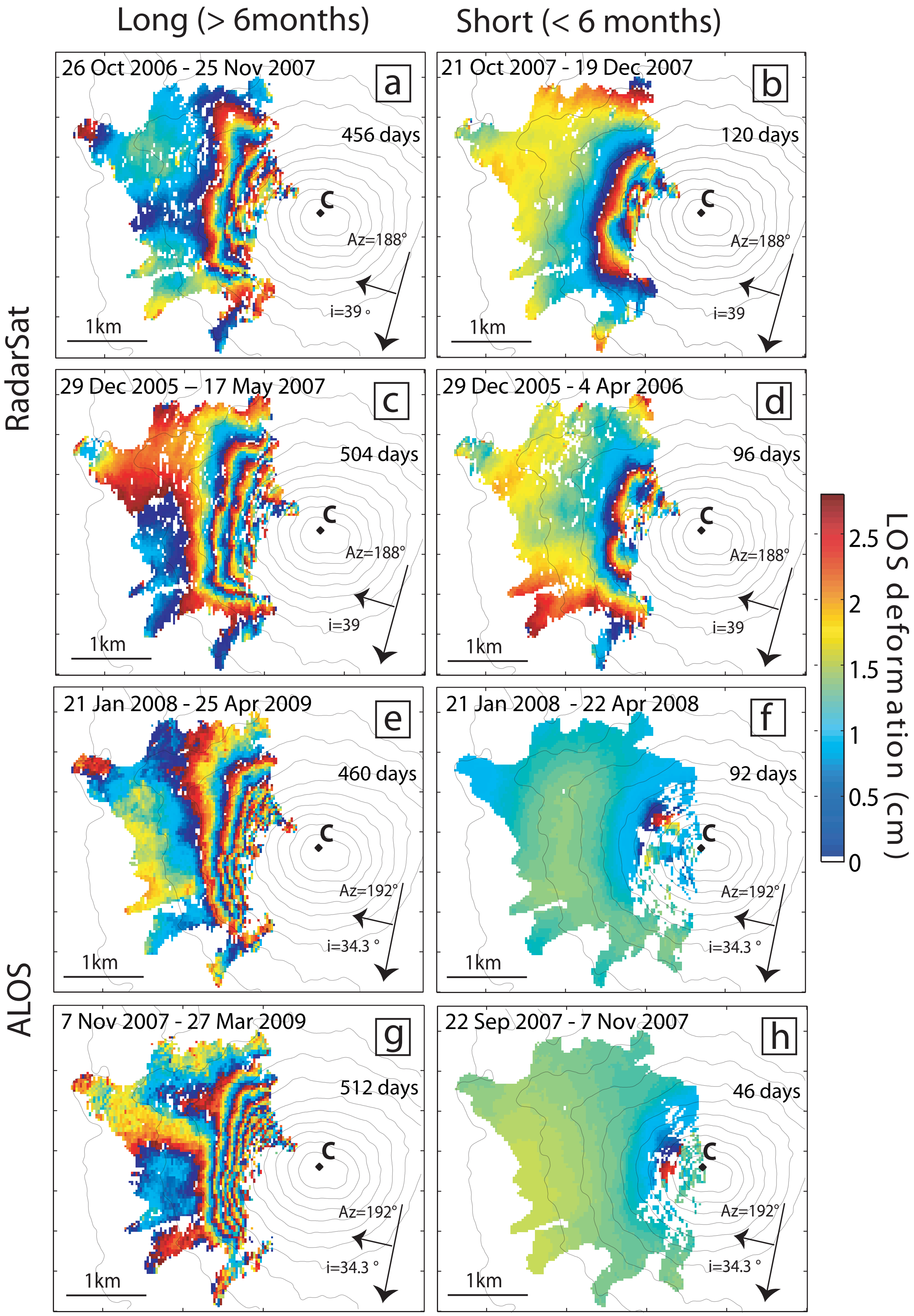
Long (> 6months)
Short (< 6 months)
RadarSat
ALOS
26 Oct 2006 - 25 Nov 2007
a
456 days
21 Oct 2007 - 19 Dec 2007
b
120 days
29 Dec 2005 – 17 May 2007
c
504 days
29 Dec 2005 - 4 Apr 2006
d
96 days
21 Jan 2008 - 25 Apr 2009
e
460 days
21 Jan 2008 - 22 Apr 2008
f
92 days
7 Nov 2007 - 27 Mar 2009
g
512 days
22 Sep 2007 - 7 Nov 2007
h
46 days
C
Az=188°
i=39
Az=192°
i=34.3 °
1km
LOS deformation (cm)
2.5
2
1.5
1
0.5
0

This assumption is reasonable since ascending and descending satellites look from close to due east and west respectively, and will therefore only capture a minor component of N-S motion (the N component of the line of sight unit vector is -0.1). A pair of ascending and descending interferograms (Figure 4.4) were converted to rate before the inversion, since their time spans were not coincident. The lack of deformation signal in the ascending interferogram suggest that their LOS vertical and horizontal components of motion cancel each other out and are therefore likely to be of similar magnitude. Vertical and east-west components of motion were then resolved pixel by pixel from the LOS displacements of the two interferograms, and used to calculate the total magnitude and angle of motion. The limited number of ascending interferograms mean that angle of motion could only be found for September 2007 - January 2008. The LOS displacement rates,patterns and magnitude of the interferograms used in the inversion were typical of the rest of the dataset. For the descending data this meant that the rate fell within the error bounds of the mean value found from a time series constructed from the complete dataset. This allows us some confidence that the components of motion calculated are representative.

The angle of deformation obtained from the inversion of different lines of sight allows us to refine our picture of slope movement at Arenal. The downward and westward components of motion are of similar magnitude, with the upper slopes moving at angle of ~50° below the horizontal. There is a sharp boundary (Figure 4.4) between this shallow downwards and westwards motion of around 12 cm/yr and the steeper, lower magnitude motion at the base of Arenal's slopes. This change in angle and rate of motion is level with the zone where the volcano slopes becomes shallower, but is still a notable boundary if the angle of motion is normalised for the slope gradient, as in Figure 4.4.

4.2.4 Time series

The temporal distribution of interferograms over Arenal is controlled by the distribution of ALOS and Radarsat acquisitions, baseline separations and the rate of decorrelation at different radar wavelengths. The interferograms used in the analysis at Arenal (Table 4.1) are therefore unevenly distributed, making any temporal variations in subsidence rate very difficult to detect directly from the interferograms.

Figure 4.2 ***(preceding page)*:** Sample Radarsat (a-d) and ALOS (e-h) interferograms showing typical deformation signals for time periods greater than 6 months (a, c, e, g) and less than 6 months (b, d, f, h). All interferograms are wrapped to C-band and projected over topographic contours as for Figure 1b. The active summit crater is marked C, as for Figure 1. Azimuth (Az) and incidence angles (i) are indicated for each interferogram.

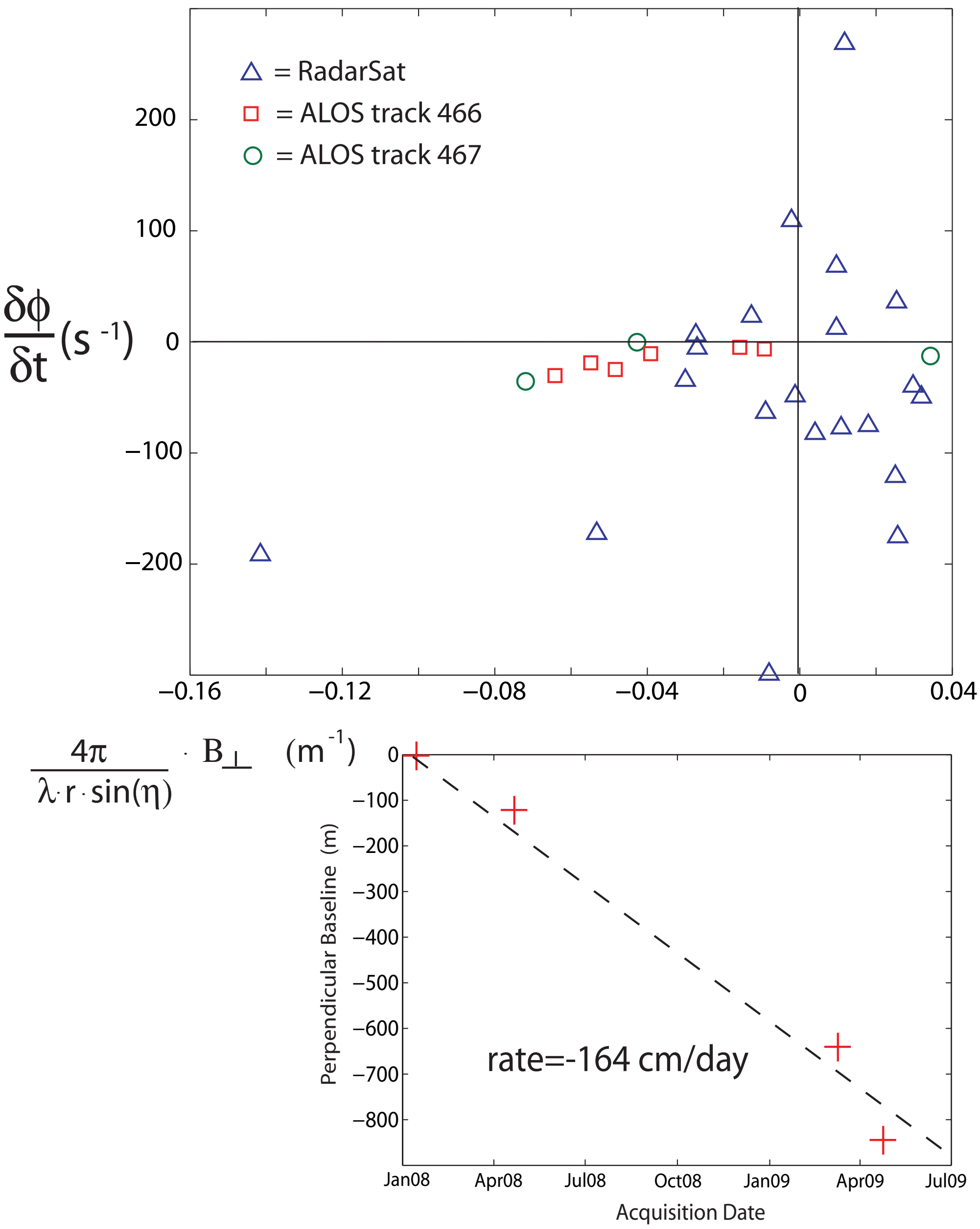

Figure 4.3: a) Rate of change in phase plotted as a function of a parameter combining radar wavelength, range, incidence angle and perpendicular baseline. $\frac{\delta\phi}{\delta t}$ is plotted rather than $\delta\phi$ in order to check for systematic relationships between baseline and time. b) Plot of cumulative baseline for each acquisition date from track 466 found from least square inversion of baseline separation for all interferograms.

A time series can generally be constructed for a network of interferograms by using a linear least-squares inversion of the displacements for each interferogram to find the incremental displacements between acquisition dates (*Berardino et al.* (2002); *Schmidt and Bürgmann* (2003), described in detail in Chapter 1). Inversion was carried out using a generalized inverse (the Moore-Penrose pseudoinverse) matrix, found from singular value decomposition and unrealistic discontinuities are avoided by fitting the minimum constraint to velocity over a time interval rather than displacement (*Berardino et al.*, 2002). Interferograms over Arenal were constructed

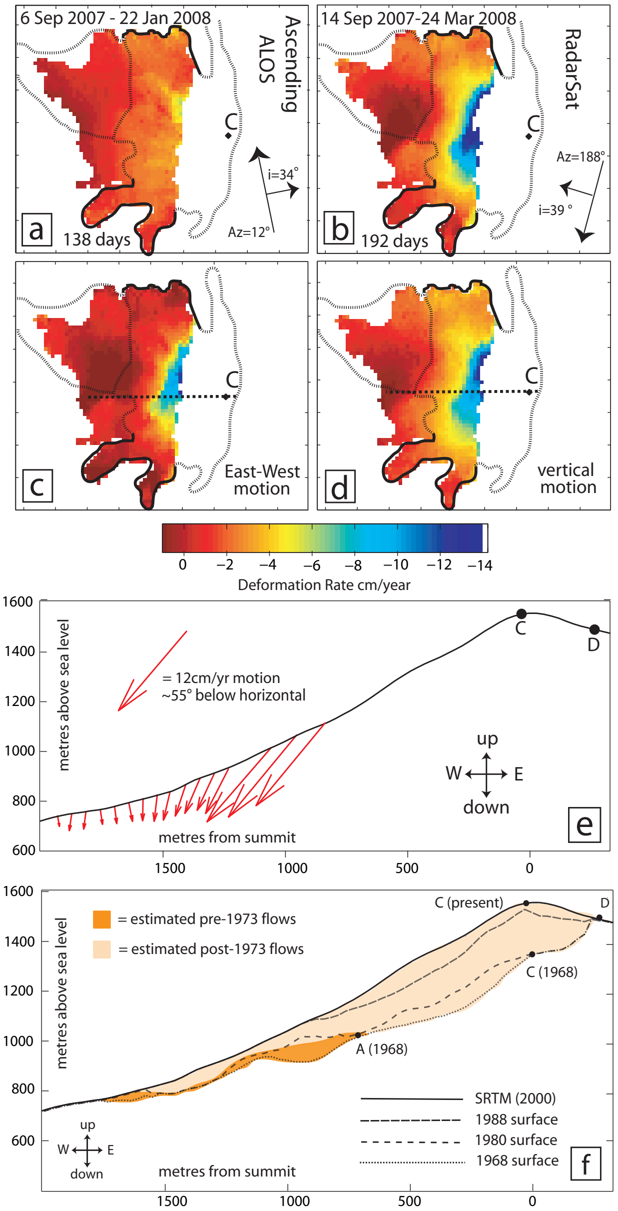

Figure 4.4: a) Ascending ALOS and b) descending Radarsat interferograms used to find best-fit components of motion in 2 dimensions. c) East-West and d) vertical components of motion resolved using the assumption that North-South motion was negligible. Negative rates represent westwards and downwards motion. The dotted line represents the trace of profiles e and f. e) The total magnitude and angle of motion shown as vectors on a transect through Arenal's summit, so that the arrow length is proportional to the rate. Due to limited coherence, the average value of an area at the western edge of the lava fields was used as a reference point assumed to experience no deformation. f) Cross section of Arenal's post-1968 deposits as estimated using the lava isopach maps constructed by *Wadge et al.* (2006). The boundary between pre-1973 (from Crater A) and post-1973 lavas is estimated from the profiles for which topographic data was available.

using four different satellite tracks and therefore make up four independent groups. The three interferograms from ALOS ascending data are of poor coherence and were not used in the time series construction, leaving three independent groups of dates (Table 4.1, Figure 4.5).

We created links between isolated groups of acquisitions from different tracks by assuming that the displacement between acquisition dates less than 8 days aparts was negligible. For a typical deformation rate (6 cm/year), 8 days of motion would produce at most a millimeter of displacement. This was seen to improve the reliability of our velocity solutions in tests using synthetic data.

We use a Monte Carlo inversion to estimate errors on the time series, which are likely to include random atmospheric noise in the original interferograms, topographic correlations in water vapour and orbital ramps. The Arenal lava fields make up the only coherent part of most of the interferograms used, so the last two sources cannot be entirely eliminated by inspection of the far-field. We simulate atmospheric noise by adding an element of normally distributed random noise to every pixel in every interferogram. The noise had a mean amplitude of 1cm (e.g. *Pritchard and Simons*, 2004a), but the effects of spatial correlation were neglected (discussed further in Chapter 1). We repeated the procedure 100 times to find the distribution of uncertainty in the resulting velocities. This uncertainty reflects the strength of links to the rest of the network for each acquisition date and is not evenly distributed across the acquisition dates. The errors between adjacent acquisitions are typically 1-4 cm and cumulative errors on rate are 2-5 cm/yr.

Time series from Arenal show a steady average rate of motion for the whole period of 2005-2009, with best fit rates of between $\sim$ 6 and 8 cm/yr found from least squares inversion. In Figure 4.5 d we show a representative time series from the centre of the western flank (location marked on 4.5 a). In a few locations there are sharp changes in rate of motion (e.g. the start of 2008, Figure 4.5 f), suggesting that parts of Arenal's slopes may be moving as discrete blocks. However, these variations lie within the bounds of uncertainty, so it is not possible to determine conclusively whether motion is spatially and temporally discontinuous or uniform and constant.

4.2.5 Comparison of InSAR results with Electronic Distance Meter Measurements

The magnitude and direction of movement observed with InSAR is supported by electronic distance meter measurements made by OVSICORI-UNA since 2008 on 5 locations on Arenal's western flank. These show a shortening between a control station at the base of the volcano and 4 reflectors at different distances due east up the flanks. The highest of these ($\sim$890 m and $\sim$840 m asl) allow measurement of a contraction rate of $\sim$6 cm/yr in the E-W direction, a value that corresponds well with those found from the InSAR components of motion at an equivalent height. The limits of this contraction also match well to the remote sensing data, as reflectors below about 780 m asl do not appear to be getting closer to the reference station. This east-west contraction has been interpreted to be a consequence of spreading caused by substrate relaxation (*Alvarado et al.* (2010) and pers. comm. Rodolfo van der Laat, 2010).

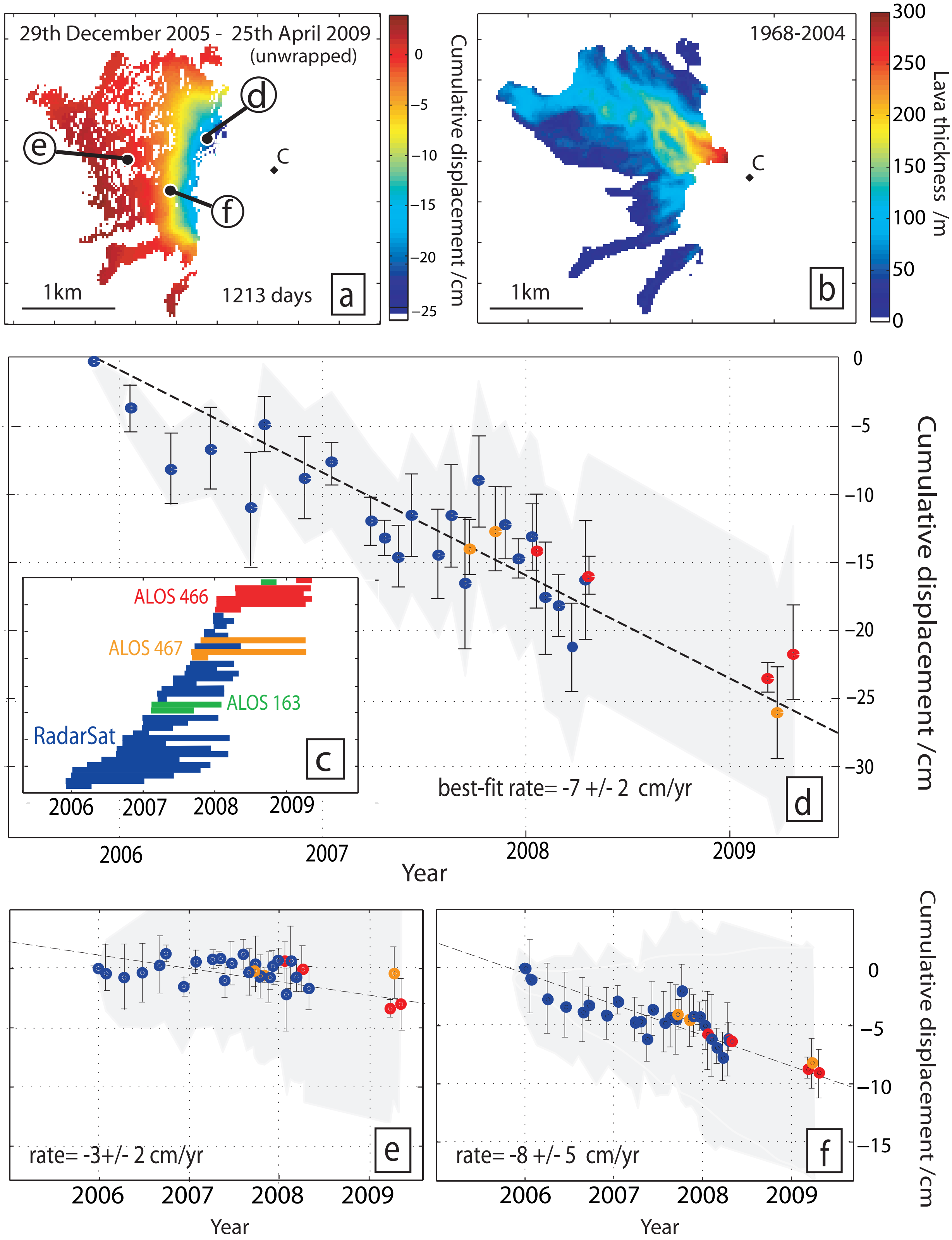

Figure 4.5: a) Map of cumulative displacement (cm) between the first and last acquisition dates used in time series (29th December 2005 - 25th April 2009). The location of time series d,e, and f are marked. b) Thickness of lavas emplaced between 1968 and 2004, after *Wadge et al.* (2006). c) Temporal distribution of interferograms used in analysis. d) Cumulative displacement (cm) for a representative point high on Arenal's flanks. Uncertainties are found from Monte Carlo inversion for the displacement at each acquisition date relative to the last are shown as error bars, while the uncertainty in cumulative displacement is shown in pale gray. e) Cumulative displacement from further down the flank, showing lower rate of slip than d. f) Time series of cumulative displacement indicative of block-like motion, showing a significant change in slip rate at the start of 2008.

4.3 Interpretation of ALOS and RadarSat data

A range of processes associated both with magmatic activity or structral instabilities can cause deformation of a volcano's edifice. At Arenal, conceivable origins for a subsidence signal include (1) magmatic deflation (e.g. Okmok *Lu et al.*, 2005c), (2) the thermal and mechanical contraction of post-1968 lava fields (e.g. Etna *Stevens et al.*, 2001a) and (3) gravitationally-driven creep (e.g. Mombacho *van Wyk de Vries and Francis*, 1997), possibly exacerbated by sub-edifice fault movement (as predicted by the models of *Lagmay et al.* (2000) and observed at Etna *Lundgren et al.* (2004). The following sections consider the plausibilities of each of these explanations with respect to our InSAR measurements and other independent observations from the literature.

4.3.1 Magmatic Deflation

Magma withdrawal is typically modeled using a decreasing pressure source beneath the volcano. Point pressure source forward models (*Mogi*, 1958) were used to test the limits that the observed pattern and shape of deformation impose on source location (Figure 4.6). The depth of magma chamber was held constant for a range of values from ∼20 km - 0.2 km, while change in volume was varied systematically. For depths below 1.7km, modeled deformation cannot be limited to the edifice and fringe spacing is too large unless change in volume exceeded $5 \times 10^8 \mathrm{m}^3$. Our best-fit model places a point source at a depth of 1.2km and volume change of $0.5 \times 10^6 \mathrm{m}^3$, although shallower sources and lower volumes can produce similar results. However, a point surce model is incapable of reflecting the distinctive, 'square' deformation patterns seen in the interferograms.

The generally accepted model for Arenal's plumbing is of a magma chamber in the mid to lower crust, receiving a continuous flux of mantle material (*Reagan et al.*, 1987; *Streck et al.*, 2005). Phase equilibria place the depth at which magma pools at ∼12-14 km. Magmatic deflation at these depths would produce a broader, more symmetrical signal with a more diffuse fringe pattern than we observe (e.g. *Pritchard and Simons*, 2004a). For sub-edifice depths (2-14 km), the modeled deformation is longer wavelength than that observed and cannot match the observed fringe spacing unless a massive volume change ($> 5 \times 10^8 \mathrm{m}^3$) is introduced. In order to match both fringe spacing and signal extent a Mogi source must be at depths shallower than ∼1.2 km, well within the height of the edifice (1.7 km). Studies of both the petrology (*Ryder et al.*, 2006) and shallow conduit seismicity (*Lesage et al.*, 2006) are both consistent with a near steady-state open magmatic system with a deep source and show no evidence of magma storage within 1 km of the summit, as would be required to cause the observed deformation. The lack of evidence for the presence of any significant volume of magma stored in Arenal's edifice allow

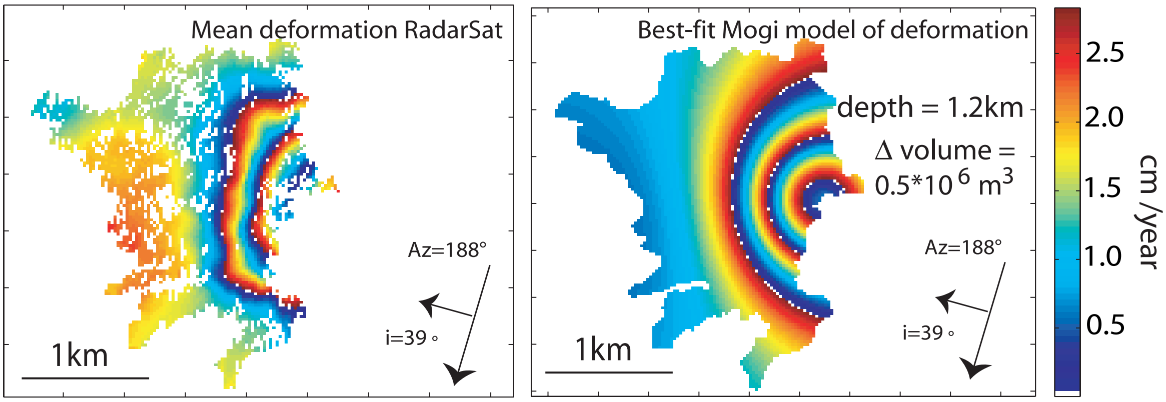

Figure 4.6: Comparison of mean rate of deformation (cm/yr) for all the Radarsat data and the best-fit Mogi model, projected into the same LOS deformation as the RadarSat data.

us to discount magmatic deflation as the cause of the deformation.

4.3.2 Lava Subsidence

Lava subsidence is caused by a combination of thermoelastic contraction and the repacking of irregular clasts during cooling. While mechanical contraction is thought to be a function only of lava thickness and time for a compositionally uniform flow (*Stevens et al.*, 2001b), thermoelastic contraction rate is dependent on both lava thickness and distance from the edge of the lava body (*Peck*, 1978). InSAR observations of lava contraction at Etna show subsidence ~10 years after emplacement (*Stevens et al.*, 2001a,b), while at Okmok (Aleutian Islands), lava subsidence of ~ 1.5 cm/yr has been measured on a flow over 35 years old (*Lu et al.*, 2005c). We therefore expect some deformation due to lava contraction at Arenal, where lavas are 0-42 years old.

Typically, lava subsidence is characterised by fringes that end at the edge of young flows and peak subsidence coinciding with the thickest point in the lava field (e.g. *Pritchard and Simons*, 2004a; *Lu et al.*, 2005c). Given the limited coherence over Arenal, the information on the angle of deformation provided by the resolved components of motion gives the best evidence against thermal contraction as the primary cause of deformation. Maximum contraction of lava flows is expected to occur perpendicular to the lava surface, so that motion would be predominantly downwards, with a small component of motion towards the volcano (ie. eastward on the western flank), in contrast to the high rate of westwards motion resloved from our interferometric data. Clast repacking could be expected to act in a downslope direction but is unlikely to account for such a high rate. The lower magnitude near-vertical deformation observed at the base of Arenal's slopes (Figure 4.4) could conceivably reflect lava contraction and compaction, but the direction and magnitude of the signal above this height, and especially at heights over 900 m suggests than another process is dominant. Although lava subsidence may well contribute to

Table 4.3: Summary of measurements of subaerial gradual volcano spreading

Volcano	Inferred deformation mechanism	Measurement type	Rate (cm/yr)	Key references
Etna	edifice fault movement	diff. InSAR extension	0.75	*Lundgren et al.* (2004)
Concepción	substrate flow	GPS	0-5 extension	*Borgia and van Wyk de Vries* (2003b)
Colima	edifice compaction	precision levelling and GPS	<7 horizontal	*Murray* (2002)
Vesuvius	substrate flow and faulting	diff. InSAR	0.6	*Borgia et al.* (2005)
Kilauea	basal decollement sliding	trilateration and tilt	6-10 (1983-2000)	*Delaney and Denlinger* (1999)
Arenal	edifice sliding	diff. InSAR	7	this work

the deformation signal at Arenal it cannot be the primary mechanism.

4.3.3 Gravity-driven deformation

Gravity-driven deformation ranges from rapid catastrophic edifice collapse at velocities of tens of m/s (*Ward and Day*, 2003) to gravitational spreading, which typically occurs at rates of millimetres per year (*Lundgren et al.*, 2004). Studies of debris flow deposits (*Duffield et al.*, 1982) and volcano morphology (*Borgia et al.*, 2000) show that such processes are widespread, but observations of the active processes and measurements of rate are sparse. Both rapid and gradual deformation develop as a result of the need to accommodate the increase in weight and volume of a growing volcano. The spatial scale and speed of failure depends on the mechanical properties of the edifice and substrate, the volume and internal structure of the edifice and the presence of external stresses such as those caused by magma intrusion or an earthquake. Slow spreading has been suggested as a precursor to sector collapse at several volcanoes (*van Wyk de Vries and Francis*, 1997).

The direction and shape of deformation at Arenal are matched well by other observations of gravity driven deformation (see references in Table 4.3). Similarly constant rates of motion have also been used to infer that deformation is being driven by a constant load (*Lundgren et al.*, 2004). There is no obvious thrust feature to accomodate this motion at the base of the western slope, but such a feature may be obscured by the presence of drainage channels and rockfall debris. The rate of motion of 7 cm/yr is high compared to other measurements of subaerial gravity-driven motion (Table 1), but within the very broad range of 1-50 cm/yr suggested by *van Wyk de Vries and Francis* (1997) for precursory spreading for flank collapse.

Arenal shows several characteristics associated with shallower edifice failure at other volcanoes, including a layered structure and steep, conical morphology (*Voight*, 2000). Its edifice is constructed from interbedded lavas and tephras, with heterogenieties in structure controlling the location of failure plane. Asymmetry predates Arenal's current phase of eruption, with thinner tephra deposits and longer lava flows on the eastern side (*Borgia et al.*, 1988). Lavas emplaced since 1968 have also significantly altered the shape of Arenal's cone, increasing the load on the western sector of the volcano and the steepness of the slopes as Crater C has become the summit. Lava effusion since 1968 has increased the volume of Arenal's edifice by 4%, with almost all of the new material being on its western side (*Wadge et al.*, 2006). This pattern of emplacement is unusual among stratovolcanoes of similar size and composition and is a result of 40 years of near-continuous eruption.

Although the motion of Arenal's western flank is best explained by a relatively shallow process, we cannot preclude the possibility that the Pliocene-Pleistocene volcanic deposits beneath the volcano are also deforming. Substrate deformation is used to explain some of the highest rates of gravity driven deformation observed at volcanoes (Table 4.3), especially where the substrate is weak. However, the ratio of brittle to ductile layer thickness beneath Arenal appears too high to facilitate basal spreading (*Merle and Borgia*, 1996). The presence of the strike-slip Danta fault below Arenal may also contribute to instability in the edifice, although its rate of motion is not known with enough accuracy to constrain this.

Possible failure planes are at the base of the post-1968 lavas or on the interface between lavas from Crater A (pre-1973) and Crater C (post-1973). The shape and extent of the youngest lava fields have been well constrained by comparison of DEMs from 6 dates between 1968 and 2004 (*Wadge et al.*, 2006), so that we can subtract lava thicknesses from the SRTM DEM (acquired in 2000) to find the approximate level of the pre-1968 surface. Since there was no DEM acquisition between the end of effusion from Crater A and the start from Crater C, the location of this boundary must be estimated (Figure 4.4). The base of the 1968 lavas lies on a layer of tephra from the lateral blast eruption and a loose paleosol surface, giving a sharp contrast in competence. We consider this the most likely sliding plane for a slow slope failure. The total volume of material above this plane is $550 \pm 80 \times 10^6$ m^3 (*Wadge et al.*, 2006), giving a mass of 1.3×10^{12}kg (after *Wadge*, 1983).

4.4 Implications

At least 20 major edifice collapses have occurred in the last 500 years at volcanoes globally (*Voight*, 2000). Sector collapse can be triggered by cryptodome or dike intrusion (*Elsworth and*

Voight, 1995), destabilisation caused by an earthquake (*Lagmay et al.*, 2000) or the inevitable result of long-term slow spreading and core weakening (*van Wyk de Vries and Francis*, 1997). Although Arenal is significantly younger and smaller than other volcanoes that have experienced flank collapse, the unusually high rate of deformation (∼7 cm/yr) suggests that the western flank already has an established plane of failure. A magmatic intrusion, as thought to be responsible for the 1968 blast eruption, or a high magnitude earthquake as may be expected on the subduction zone beneath the Nicoya peninsula (*Protti et al.*, 1994), could conceivably trigger failure on the western flank of Arenal. Although the magma chamber is believed to be in the mid to lower crust (Section 4.1), it is possible that a collapse event could cause sudden decompression of a shallow conduit (*Manconi et al.*, 2009). Arenal's shallow conduits experience a cycle of sealing, over-pressurisation and explosive rupture, with a correlation between volcano-seismic activity and earth tides that implies strong sensitivity of the system to changes in confining pressure or stresses (*Williams-Jones*, 2001). Even a small scale gravitational failure has the potential to trigger an explosive eruption. The relatively constant rate of sliding indicates that Arenal's western flank has been in a steady state during the period of observation, but it is unclear whether this is stabilising or destabilising the slope. Any rapid increase in the rate of sliding may be taken as a precursor to collapse, so monitoring the deformation of Arenal's western slopes is important for detecting an increase in risk to the population around the volcano.

4.5 Summary

The deformation of Volcán Arenal, Costa Rica, was measured using both ALOS and Radarsat interferograms between 2005 and 2009. The good spatial coverage and high resolution of the InSAR data allowed us to measure an unusual volcanic deformation signal that would have been unresolvable with fewer measurement points. This demonstrates InSAR's strength as a tool for observing and analysing complex deformation systems. Arenal's lower western flanks, to which interferogram coherence is limited, are moving downslope at an angle of ∼55° below the horizontal plane and a consistent average speed of about about 7 cm/year. The close fringe spacing and small spatial wavelength of deformation are indicative of a shallow source, which we attribute to slow gravity-driven slip. Our favoured location for the sliding plane is the boundary between post-1968 eruption lavas and the paleosols and older eruptive products below, although it is conceivable that it is even shallower. The instability of Arenal's western slopes is a consequence of the volcano's asymmetric, composite structure and the rapid increase in loading of the western flank since 1968. Other reported observations of gravity-driven deformation are of significantly slower spreading caused by sub-edifice deformation, making Arenal unusual.

Monitoring Arenal is vital for scientific and hazard purposes. Distinguishing between constant and discontinuous block-like motion and establishing depth to sliding plane(s) is important for understanding the deformation mechanism. Any increase in the rate of sliding on Arenal's western flanks may also indicate potential collapse.

Chapter 5

Measurements of topographic change: Santiaguito, Guatemala

adapted from Ebmeier, S. K., J. Biggs, T. A. Mather, J. R. Elliott, G. Wadge, and F. Amelung (2012),*Measuring large topographic change with InSAR: Lava thicknesses, extrusion rate and subsidence rate at Santiaguito volcano, Guatemala*, **Earth and Planetary Science Letters**, 335, 216–225, doi:10.1016/j.epsl.2012.04.027

Lava flows can produce changes in topography on the order of 10s-100s of metres. A knowledge of the resulting volume change provides evidence about the dynamics of an eruption. I demonstrate an approach for using differential InSAR phase delays to estimate height differences between the current topography and a Digital Elevation Model (DEM). This does not require a pre-event SAR image, so it does not rely on interferometric phase remaining coherent during eruption and emplacement. Synthetic tests predict that we can estimate lava thickness of as little as ∼9 m, given a minimum of 5 interferograms with suitably large orbital baseline separations. In the case of continuous motion, such as lava flow subsidence, we invert interferometric phase simultaneously for topographic change and displacement.

I apply this to Santiaguito volcano, Guatemala, and measure increases in lava thickness of up to 140 m between 2000 and 2009, largely associated with activity between 2000 and 2005. Mean extrusion rate between 2000 and 2009 is 0.43 +/- 0.06 m^3/s, which lies within the error bounds of the longer term extrusion rate between 1922-2000. The thickest and youngest parts of the flow deposit were shown to be subsiding at an average rate of ∼-6 cm/yr.

5.1 Introduction

Measurements of lava volume flux at erupting volcanoes are important both as evidence of the processes driving an eruption, and for monitoring the development of young lava flows and associated hazard. The volume flux of lava at a volcano can provide important evidence about source depth or conduit dimensions (*Harris et al.*, 2007), and therefore constrain models of the magma dynamics driving an eruption. Comparison of current time-averaged effusion rates to past rates derived from field measurements can give us insight into long-term trends in volcanic behaviour *Siswowidjoyo et al.* (e.g. 1995) and to distinguish between increasing and decreasing levels of activity within long-duration eruptions (*Wadge*, 1981; *Harris*, 2000). Lava extrusion rate (or effusion rate for less viscous magmas) is also a primary control on the shape, pattern of growth, cooling rate and morphology of a lava field (*Rowland and Walker*, 1990; *Pinkerton and Wilson*, 1994) and is thus a key parameter for predicting the eventual extent and associated hazard.

Interferometric Synthetic Aperture Radar (InSAR) measures the phase change between time separated radar images. Geometric phase contributions are corrected during the construction of interferograms using satellite orbit information and Digital Elevation Models (DEMs) (described in Chapter 2). Where the DEM used in processing differs from the topography at the time when InSAR data is acquired, phase contributions originating in the difference in topography (generally referred to as 'DEM errors'), remain in the interferograms. Since InSAR is most commonly used to measure millimetre- to centimetre-scale deformation, these topographic phase shifts are generally treated as nuisance factors and corrected (e.g. *Berardino et al.*, 2002; *Samsonov et al.*, 2011).

In this chapter I present an application for estimating topographic changes on the order of 10s to 100s of metres, using a set of Interferometric Synthetic Aperture Radar (InSAR) images. I run synthetic tests to determine limitations, uncertainties and data requirements, and measure change in lava thickness, long-term extrusion rate (Section 5.3.2) and flow shape (Section 5.3.3) at Santiaguito volcano, Guatemala, between 2000 and 2009. We also solve simultaneously for lava subsidence during our period of InSAR data acquisitions (Section 5.3.4). Finally, I discuss the usefulness of this method as a tool for volcanologists.

5.1.1 Background: Measurements of lava extrusion rate

Time-averaged lava extrusion rates are commonly estimated using either satellite (e.g. *Harris et al.*, 2011) or ground-based (e.g. *Ryan et al.*, 2010) remote sensing methods since they allow a complete flow-field to be measured simultaneously and can be repeated at long intervals.

In contrast, field measurements capture instantaneous fluxes that may not be representative of overall lava flux and rely on potentially dangerous measurements of mean lava velocity and channel dimensions (e.g. *Calvari*, 2003) and are less suited to long-term extrapolation (discussed in detail by *Wright et al.*, 2001).

Remote sensing measurement of lava flux, both ground- and satellite-based, falls into two categories: 1) thermal methods (e.g. as at Stromboli (*Calvari et al.*, 2010), Kilauea (*Harris et al.*, 1998) or Unzen (*Wooster and Kaneko*, 1998)) and 2) volumetric methods (e.g. at Okmok (*Lu et al.*, 2003a), Etna (*Stevens et al.*, 2001a) or Arenal (*Wade et al.*, 2006)). Thermal methods (discussed in detail by *Harris et al.* (2007)) use heat flux models to calculate lava mass fluxes. This relies on there being a linear relationship between heat flux and lava flow area, a reasonable assumption where flow area is controlled by cooling, but not where it is limited by topographic features (*Harris et al.*, 2007). Volumetric methods involve differencing digital elevation models (DEMs), which can be constructed from topographic maps (e.g. *Wade et al.*, 2006), field measurements (e.g. *Sparks et al.*, 1998), aerial/satellite laser altimetry (e.g. *Garvin*, 1996), ground-based radar (e.g. *Macfarlane et al.*, 2006) or satellite optical/radar data (*Lu et al.*, 2003a). Volumetric estimates of effusion rates will be underestimates where material has been removed by erosion between measurements of topography.

Routinely acquired satellite data can produce a greater temporal frequency of measurements than could be achieved from ground based campaigns. However, two primary limitations apply to the use of satellite data to estimate lava effusion rate: cloud/water vapour cover and acquisition geometry. Infrared imagery (e.g. ASTER/MODIS) cannot be used where the site of interest is cloud covered. *Coppola et al.* (2010)'s comparison of ground and satellite based thermal measurements found that ∼65% of MODIS imagery of Piton de la Fournaise was obscured by clouds and unusable. The construction of DEMs from satellite data generally requires a specifically designed acquisition strategy, such as the ERS1/2 tandem mission. DEMs can be constructed from pairs of radar images only where spatial separation (satellite baseline) is high and temporal separation is low.

5.1.2 Background: Santiaguito lava fields

The Santiaguito lava dome complex (Figure 5.1a) has been growing persistently since 1922 in the explosion crater formed by the 1902 eruption of Santa Maria volcano. Activity since 1922 has consisted of intermittent explosions and ash plumes and the extrusion of dacitic lava flows, forming a dome complex of ∼1.1 km^3 (*Harris et al.*, 2003). Since 1977, activity has been centred on El Caliente vent (Figure 5.1).

The average extrusion rate between 1922 and 1984, as estimated from detailed field mapping,

Figure 5.1: a) Santa Maria volcano and Santiaguito lava dome, Guatemala. Lavas and other eruptive products from the growth of Santiaguito between 1922 and 2006 are marked schematically, after *Escobar et al.* (2008). b) Time series of extrusion rate at Santiaguito between 1920 and 2010. Extrusion rates are from *Harris et al.* (2007); *Rose* (1972a, 1987) and show time-averaged, rather than instantaneous rates.

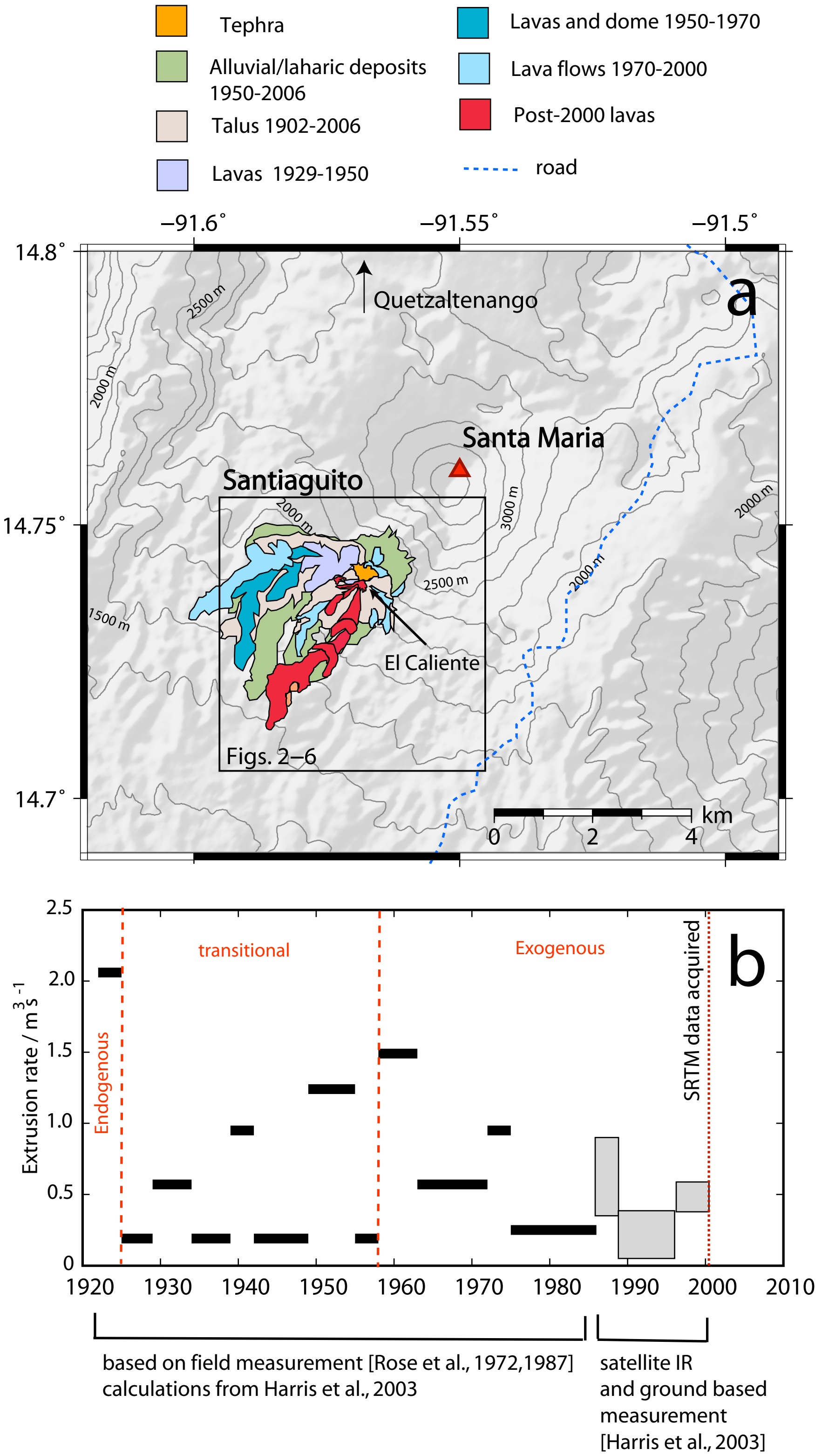

Figure 5.2: Illustration of criteria for identifying DEM artefacts. a) Map of the correlation coefficient squared (R^2) of the correlation coefficient between phase and baseline. b) Map of the lower limit of the 95% confidence interval for correlation coefficient (R). c) Map of the lower limit of gradient of phase with respect to baseline ($\frac{\delta\phi}{B_{perp}} - \sigma_{\frac{\delta\phi}{B_{perp}}}$). d) Example of $\frac{\delta\phi}{B_{perp}}$ relationship where there is a significant difference between the DEM and current topography. e) Example of an area of smaller topographic change where the $\frac{\delta\phi}{B_{perp}}$ relationship is still robust and f) Illustration of relationship between $\delta\phi$ and B_{perp} where there has been no significant topographic change between 2000 and 2007. Locations of d, e and f are indicated on a, b and c.

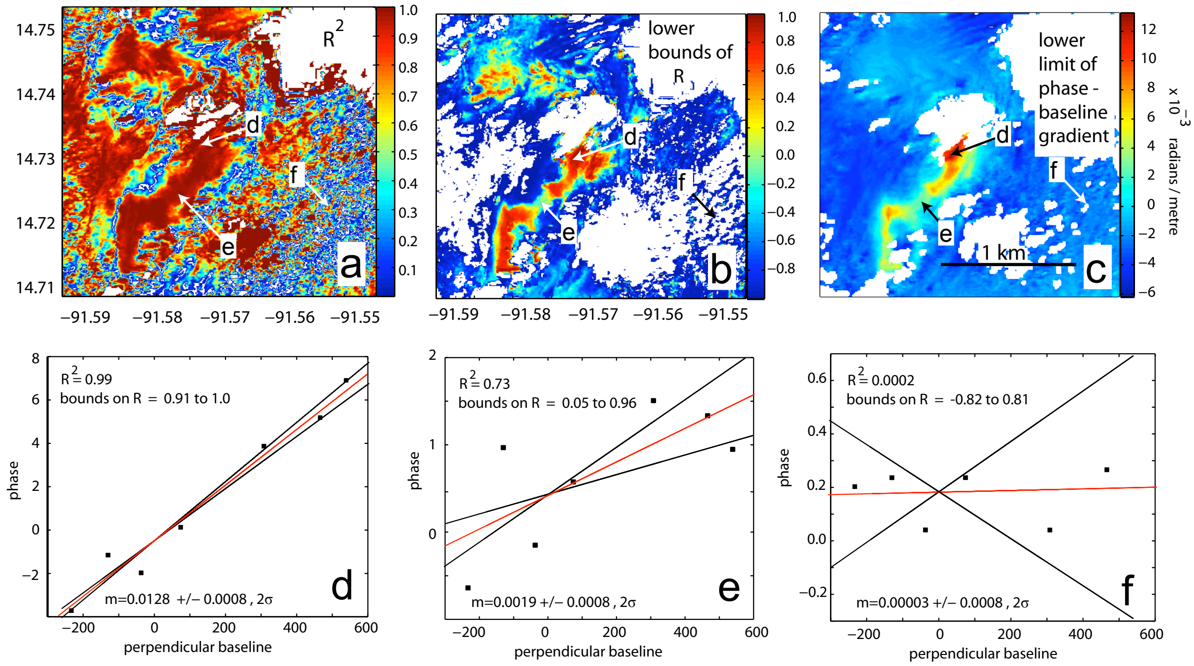

was 0.46 m^3s^{-1} (*Harris et al.*, 2003). *Harris et al.* (2003) made 18 further estimates of extrusion rate at Santiaguito between 1987 and 2000, using thermal satellite imagery. These showed a cyclical pattern in extrusion with a short (3–6 years) burst of high rate extrusion, followed by a longer period (3–11 years) at a lower rate, but with an overall decay in extrusion rate between 1922 and 2000 (Figure 5.1b). Instantaneous extrusion rate increased from 0.6 m^3s^{-1} in 2000 to 1.4 m^3s^{-1} in 2002, the highest measurement of extrusion at Santiaguito since 1963 (these short-lived rates greatly exceed the time averaged values shown in Figure 1b). Such high rates are short-lived and are likely to be missed by time-averaged eruption rate estimates. Activity at Santiaguito has changed from endogenous, where the dome grows by the subsurface accumulation of magma (1922–1929), through a period of transition (1929–1958) to exogenous (1958 onwards) behaviour, where lava is extruded onto the ground surface. Flow length has also increased due to decreasing silica content and consequently lower viscosity (*Harris et al.*, 2003). *Harris et al.* (2003) suggest that these changes are indicative of magma source exhaustion and suggest that a continued decrease in extrusion rate, silica content and increase in duration of low flux periods might indicate that the Santiaguito lava dome eruption is drawing to a close,

but later observations of higher rate extrusion in 2002 (*Harris et al.*, 2004), and more recently in 2011-early 2012 are not in keeping with this interpretation. Santiaguito's most recent period of high extrusion rate activity has produced twin lava flows extending more than 2 km from El Caliente, and were advancing at more than 5 m per day in June 2011 (J.B. Johnson, personal communication, 2012).

5.2 Method

Interferograms include phase contributions from differences in satellite position and resulting viewing geometry. These are generally divided into a 'flat earth' correction ($\delta\phi_{orbit}$), and a correction for the effect of viewing topography from different angle ($\delta\phi_{topo}$). Other contributions come from changes to the distribution of tropospheric water vapour between radar acquisitions ($\delta\phi_{atm}$), changes to scattering properties of the ground ($\delta\phi_{pixel}$) and ground movements ($\delta\phi_{defo}$) (e.g. *Massonnet and Feigl*, 1998).

$$\delta\phi = \delta\phi_{orbit} + \delta\phi_{topo} + \delta\phi_{atm} + \delta\phi_{pixel} + \delta\phi_{defo} \tag{5.1}$$

Phase shifts caused by topography change ($\delta\phi_{topo}$) between the times of DEM and InSAR acquisitions exhibit a characteristic linear relationship with the perpendicular separation of satellite positions (B_{perp}), where the gradient depends primarily on radar wavelength (λ), incidence angle (ν), range of satellite from the ground (r) and vertical change in topography (δz) (e.g. *Rodriguez and Martin*, 1992; *Zebker and Villasensor*, 1992; *Ferretti et al.*, 1999).

$$\delta \mathrm{z} = \frac{\mathrm{r}\lambda \sin\nu}{4\pi B_{perp}} \delta\phi_{topo} \tag{5.2}$$

Thus, where phase change of an individual pixel can be shown to have a systematic relationship to baseline (B_{perp}), we assume that topographic phase contributions, $\delta\phi_{topo}$, dominate the measured phase shift, so the change in topography since the DEM was constructed can be calculated. The first step is to map out the region over which topographic change has taken place using phase-baseline relationships for a set of interferograms (described in detail in Section 5.3.1). The second is then to invert phase data covering that region to retrieve change in topographic height. Where deformation is expected to be negligible, this can be a single inversion. Joint inversion for $\delta\phi_{topo}$ and $\delta\phi_{def}$ is discussed in Section 5.3.4.

Using a set of interferograms, this problem is of the form **d=Gz**, where **d** is a column vector containing the pixel phase shift in each interferogram, **z** is the corresponding change in topographic height and **G** is a design matrix containing the corresponding set of perpendicular baselines and a constant multiplier, $\frac{\mathrm{r}\lambda\sin\nu}{4\pi}$. Baselines estimated for the start and end of each interferogram were interpolated linearly to find the baseline at Santiaguito, and constant values for ν (39.2°) and r (843044 m) are used. This is reasonable as the variation in these two properties is less than a fraction of a percent, and orders of magnitude lower than the uncertainty in our phase measurements expected to be introduced by atmospheric artefacts.

We find topographic change ($\mathbf{z}$) using a weighted linear least squares inversion, carried out pixel by pixel:

$$\mathbf{z} = [\mathbf{G}^T \ \mathbf{W}_\phi{}^{-1}\mathbf{G}]^{-1}\mathbf{G}^T \ \mathbf{W}_\phi{}^{-1}\mathbf{d} \tag{5.3}$$

Each interferogram in the inversion is weighted according to its maximum variance (σ^2_{max}). We use a weighting matrix, $\mathbf{W}_\phi$, with diagonal elements of σ^2_{max} for each interferogram and off-diagonal elements of 0, so that we neglect the effects of covariance in atmospheric noise between interferograms.The uncertainty in $\mathbf{z}$ (σ_z) is then $\left(\frac{r\lambda\sin\nu}{4\pi}\right)^2[\mathbf{G^T W}_\phi{}^{\mathbf{-1}}\mathbf{G}]^{-1}$.

5.3 Application to Santiaguito

Interferograms covering Santiaguito lava dome, Guatemala, were produced from ALOS data between 2009 and 2010 (Track 174, Frame 280, 7 interferograms, from 7 acquisitions, Table 5.1). Interferograms were constructed using the Repeat Orbit Processing software (ROI_PAC) developed at Caltech/JPL (*Rosen et al.*, 2004) with topographic correction made using NASA's Shuttle Radar Topography Mission 90 m Digital Elevation Model (DEM) (*Rosen et al.*, 2001), which was interpolated and resampled to a spacing of 30 m. SRTM data were acquired from single pass Interferometric Synthetic Aperture Radar (SAR) instrument on an 11 day shuttle mission in February 2000 for the specific purpose of producing a global DEM (*Rosen et al.*, 2001). The atmospheric error typical of each interferogram is obtained from a 1D covariance model fit to the auto-covariance function of atmospheric noise in each interferogram (*Hanssen*, 2001; *Wright et al.*, 2004). Maximum standard deviations are in the range 4-7 mm and typical length scales are 13-63 km.

5.3.1 2D lava flow map

We test and apply two criteria for identifying topographic phase shifts at Santiaguito: (1) the lower confidence interval of the Pearson product-moment correlation coefficient (R) between $\delta\phi$ and B_{perp} (*Wonnacott*, 1990) (e.g. Figure 5.2) and (2) the minimum gradient as calculated from

Table 5.1: Interferograms used in analysis of Santiaguito lava flows, all constructed from ALOS L-band data. Baselines are estimated using a simple linear interpolation of orbit data. We expect that an uncertainty of ~5% in Bperp will be insignificant for baseline values above 50 m, and only exceed 10 m in magnitude for baselines below about 40 m. We therefore estimate Bperp only to the nearest metre.

Master date	Slave date	time spanned (days)	estimated B_{perp} over Santiaguito	maximum variance in noise (mm^2	Typical length scale of noise (km)
14th June 2009	30th July 2009	46	-224	31	3.4
14th June 2009	14th Sep. 2009	92	77	34	2.1
30th July 2009	14th Sep. 2009	46	301	32	3.1
14th Sep. 2009	15th Dec. 2009	92	394	19	0.8
15th Dec. 2009	17th Mar. 2010	92	460	43	1.3
17th Mar. 2010	17th June 2010	92	-59	30	1.6
17th June 2010	17th Sep. 2010	92	-25	40	1.6

inversion formal errors, ($\mathbf{z}$-σ_z) (e.g. Figure 5.2c).

Although a strong correlation between $\delta\phi$ and B_{perp} is reflected by a high value for the coefficient of determination (R^2), this may be due either to a topographic phase shift or simply consistently low phase values across all baselines. Using the lower limits of the 95% confidence interval for the correlation coefficient, however, allows us to distinguish between these two cases (compare Figures 5.2a and 5.2b). The boundary where the lower limit of the correlation coefficient falls below 0 (or rises above 0 when considering a decrease in topographic height), captures the extent of a region of topographic change and can be extracted from phase data using a mask. Similarly, where the minimum value for phase-baseline gradient falls below 0, there is no demonstrable relationship between $\delta\phi$ and B_{perp} and therefore no significant topographic change. We find this method (criterion (2)) slightly more useful with the Santiaguito data, as the use of the lower confidence interval for R occasionally returns false positives (as can be seen on Figure 5.2b). There is a good general correlation between the map outline of the ALOS determined thickness changes found here, the field mapping of the lava flows (*Escobar et al.*, 2008) extruded between 2000 and 2006 (Figure 5.3c) and an ASTER image from February 2009 (Figure 5.3b). Santiaguito's topography did not change significantly during the time when SAR data were acquired (2007-2010). The last extrusive period to affect the coherent region at Santiaguito ended in 2005 (*Escobar et al.* (2008) and Smithsonian database) and I assume that topographic changes due to weathering, rockfall and ash deposition are below the sensitivity of my measurements.

It is expected that the spatial resolution of our data to be the same as the DEM used in processing (90 m), and that we can deduce the shape of the deposit from our ($\mathbf{z}$-σ_z) maps to a precision of about two pixels (180 m) around its edges. We are unable to capture the complete lava flow map at Santiaguito due to phase incoherence. Where the scattering properties of the ground change rapidly, the radar phase returned from the ground alters between satellite acquisitions in an unpredictable way so that shifts caused by topographic change or deformation are not retrievable. Incoherence in the area around El Caliente vent is presumably caused by changes in scatterer properties due to minor explosive eruptions and rockfall deposits from dome activity.

5.3.2 Lava volume and effusion rate

We find a maximum lava thickness of $\sim$ 140 m at the closest measurable point to the active vent. Lava thickness decreases with distance from the vent, with some individual flow units clearly identifiable in the structure (Figure 5.3d and 5.4a-e). We estimate flow-field volume by integrating the height increase across all pixels on the surface of the lava flow and find a total increase in volume of 1.20 $\times 10^8$ m^3 between 2000 and 2009. Uncertainty in calculations of volume will depend on the accuracy with which we can resolve the edge of the deposit and estimate the surface area it covers. At Santiaguito, the lava flow perimeter is $\sim$8 km long. If we assume that we can locate the edge of the lava flow to a precision of 2 pixels, each 90 m across , this gives an estimated area error of $\sim$1.4 km^2. In combination with our uncertainties for lava thickness, this gives us a total uncertainty in volume change between 2000 and 2009 of the order of 1×10^7 m^3, or 10%.

The mean rate of change in volume between 2000 and 2009 is therefore 0.43 ± 0.06 m^3/s, very close to the time averaged rate (1922–2000) of 0.44 ±0.01 m^3/s, calculated by *Harris et al.* (2003). Over our area of measurement, this rate actually reflects periods of high rate lava extrusion between 2000 and 2005 and then a lack of significant extrusive activity between 2005 and 2009. We estimate volume flux during this more active period to be 0.78 m^3/s. This is slightly higher than the extrusion rate measured by *Durst* (2006) ($\sim$0.68 m^3/s) using analysis of ASTER DEMs from 2002 and 2005, and is comparable to past periods of high extrusion (*Harris et al.*, 2003).

It is, however, likely to be an underestimate of the total flow rate over this time, as we do not have data for the complete lava flow field from 2000–2009. This is partially due to incoherence, but we are also unable to take account of the volume of any material eroded between 2000 and 2009 (unlike the thermally derived fluxes). *Harris et al.* (2003) suggested that extrusion rates calculated from pre-1980 field measurements underestimate the lava flux at Santiaguito between 1922 and 1987 by 5-25%, from estimations of eroded volumes from a debris fan downstream of the volcano. If the rate presented here is a similar underestimate, then mean extrusion rates could be as high as 0.45-0.54 m^3/s from 2000 to 2009.

Figure 5.3: a) Example of an interferogram showing topographic phase shifts at Santiaguito lava dome, Guatemala (14th June 2009 - 14th September 2009, perpendicular baseline = -233 m.) Azimuth (Az) and incidence angle (~ 39 deg) directions are indicated. b) ASTER multispectral image at 15 metre resolution from 7^{th} February 2009 (Red, green and near infrared bands) with colours inverted and saturation increased, to make lava flows clearer. c) Schematic map of lava flows from El Caliente vent at Santiaguito, after *Escobar et al.* (2008). Flows emplaced after the SRTM data were acquired in 2000 are coloured red. d) Map of lava thicknesses calculated from phase shifts in our complete set of interferograms over Santiaguito.

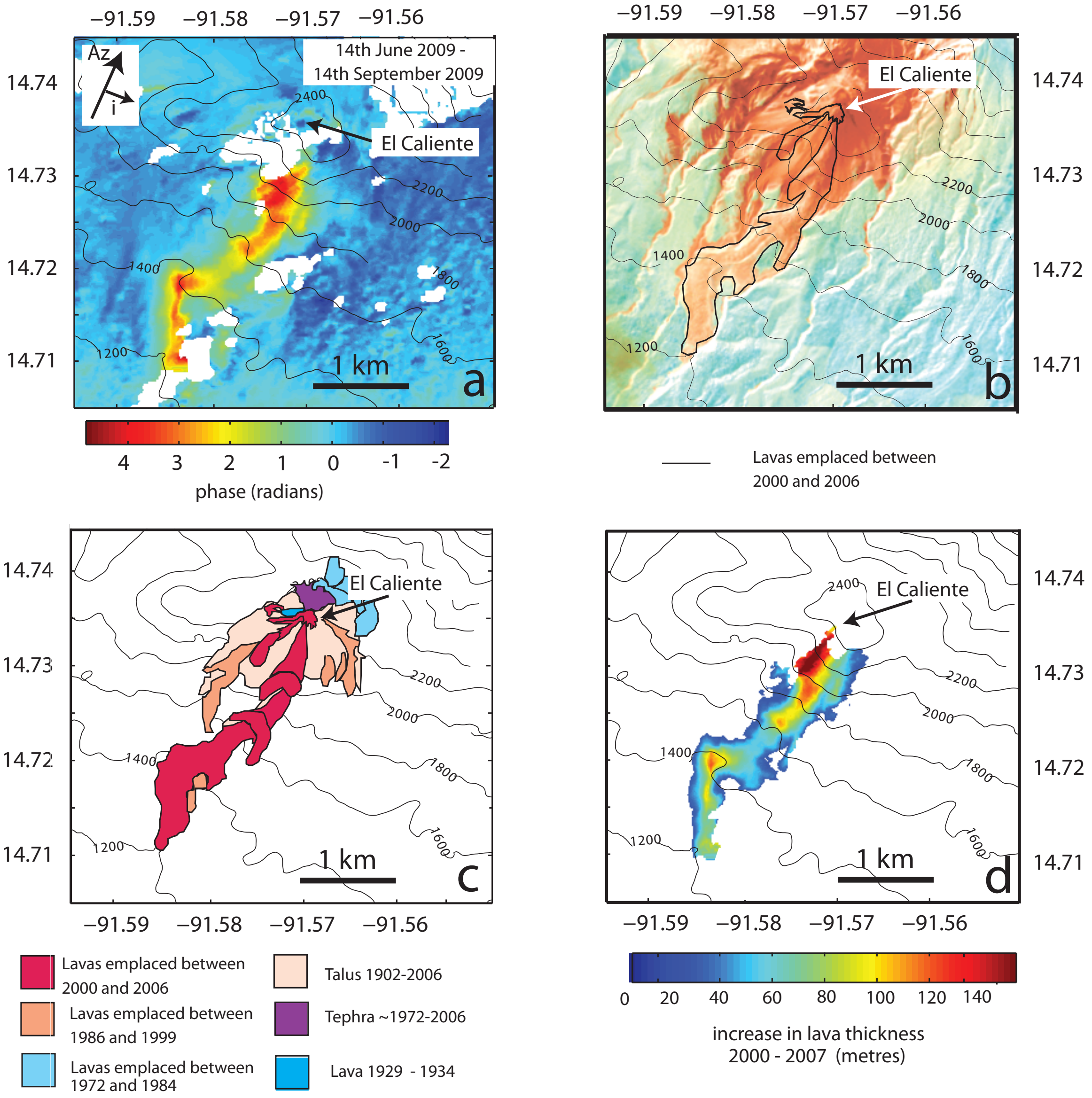

5.3.3 Flow morphology

We are able to examine large-scale lava flow morphology at Santiaguito using profiles through our lava thickness maps superimposed on the original 2000 DEM. The SRTM data were acquired in February 2000 during a period of extrusion that started in July 1999. The morphology of a central channel flanked by levees was already established by this time and appears as a shallow

Figure 5.4: a) Profile along lava flow showing new material over original SRTM surface. b, c, d and e show cross sectional profiles of the lava flow thickness. The SRTM topographic surface is shown by a solid black line, while the young lava is shown in solid grey. Cross section locations are shown on the inset to Figure 5.4a.

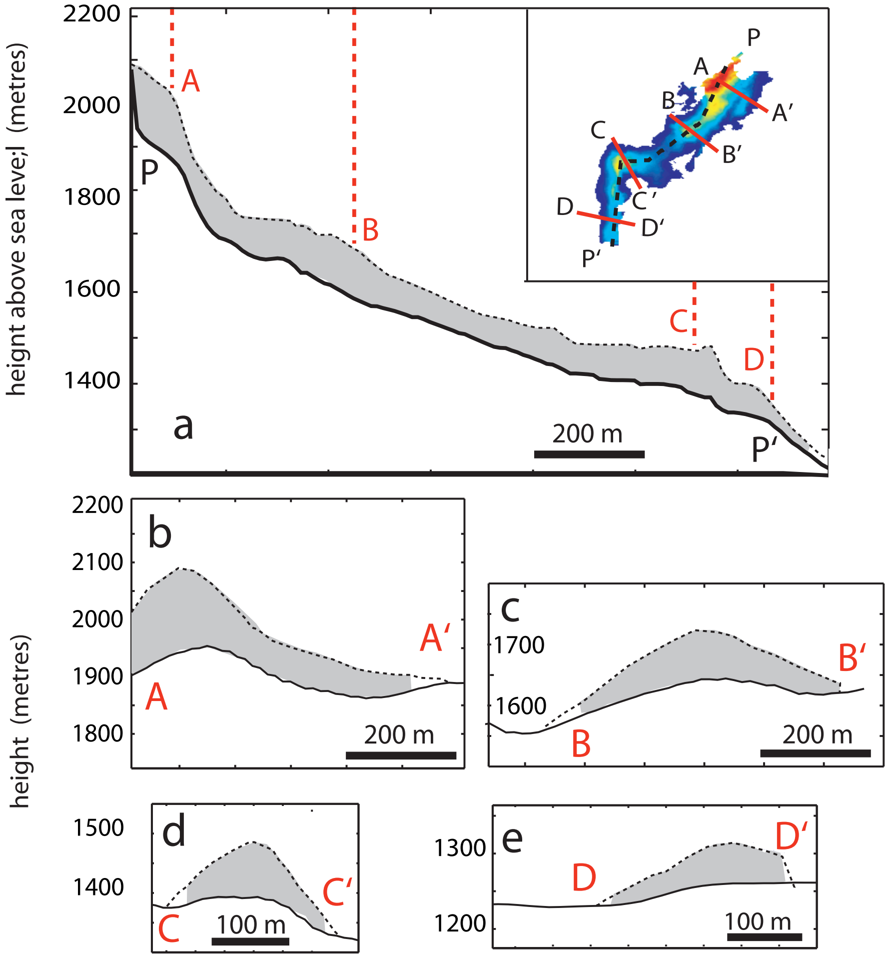

'ridge' in the SRTM DEM (Figure 5.4). Subsequent viscous, dacitic lavas followed this channel in 2001-2002, 2003 and 2004, gradually increasing the height of channel, levees and banks and increasing the lava flow's aspect ratio.

Profiles A, B and C on Figure 5.4 (b-d) cut across part of the lava field identified as 'channelised' by *Harris et al.* (2004) using satellite thermal imagery and synchronised field observations in 2000, 2001 and 2002. We see no evidence of the stable channel and levee structures seen by *Harris et al.* (2003), which are also visible in recent ASTER imagery (Figure 5.3b) in the older parts of the lava flows (Figure 5.3c). This is presumably because the levee width (68 ± 25 m measured in 2002 *Harris et al.*, 2004) is below the resolution of the SRTM DEM (∼90 m, oversampled to 30 m for InSAR processing). Thus the ridges represented by the SRTM data in Figure 5.4 are interpreted as channelised lava flows (as of February 2000) that continued to

Table 5.2: Summary of InSAR measurements of lava subsidence made to date. 'Age' is the interval in years between lava flow emplacement and InSAR measurement of subsidence.

Volcano	**Lava composition**	**Age (years**	**Max. flow thickness (m)**	**Max. subsidence rate (cm/yr)**	**References**
Krafla (1975-1984)	basaltic	17-20	50	0.6	*Sigmundsson et al.* (1997)
Tolbachik (1975-1976)	basaltic	16-28	80	~2	*Pritchard and Simons* (2004c); *Fedotov et al.* (1980)
Okmok (1945-1958)	basaltic	35-38	20-30	~1.5	*Lu et al.* (2005a)
Okmok (1997)	basaltic	0.1	50	83	*Lu et al.* (2005a)
Okmok (1997)	basaltic	3	50	4	*Lu et al.* (2005a)
Colima (1998-1999)	andesitic	3-8	30 (flow fronts)	1.5	*Pinel et al.* (2011); *Navarro-Ochoa et al.* (2002); *Zobin* (2002)
Santiaguito (2004-2005)	dacitic	4-6	120	6	this work
Paricutin (1943-1953)	basaltic-andesite	54-65	>70	4-4.5	*Fournier et al.* (2010)
Reventador (2005)	andesitic	3-4	-	1-2	*Mothes et al.* (2008)
Sierra Negra (1979)	basaltic	13-19	-	3	*Amelung and Day* (2002)
Lonquimay (1988-1989)	andesitic	13-21	55	2	*Fournier et al.* (2010); *Naranjo et al.* (1992)
Nyamuragira (1991-1993)	basaltic	6-11	-	1-4	*Colclough* (2006)
Nyamuragira (1991-1993)	basaltic	13-18	-	0.9	*G. Wadge, pers. comm. 2012*
Nyamuragira (2004)	basaltic	2-5	-	1	*G. Wadge, pers. comm. 2012*
Etna (1983)	basaltic	10-14	55	0.8	*Stevens et al.* (1999)
Etna (1989)	basaltic	3-4	10	3.5	*Briole et al.* (1997)
Etna (1991-1993)	basaltic	1-2	96	25.6	*Briole et al.* (1997)

be used by subsequent flows, though the channel/levee structure is smoothed out in these data. Profile D (Figure 5.4e) is from the zone of dispersed flow and has a lower aspect ratio. The limiting factor for measuring flow morphology from interferogram-derived topographic change is the resolution of the DEM used in interferogram construction.

5.3.4 Lava flow subsidence

Channelised lava may continue to flow as it cools and after its source flux has stopped, resulting in advancement of the flow toe, a fall in the level of lava in the channel, and potentially the sinking or even collapse of any bridging crust across the channel (e.g. *Borgia*, 1983). Such processes are expected to result in deformation soon after flow emplacement of a magnitude too large to detect with differential InSAR (several metres, see Figure 5.10b). As our data covers a period 3-5 years after the most recent flows at Santiaguito were emplaced, we expect our measurements to capture deformation associated with contraction and compaction, rather than flow processes.

After flow has ceased, the subsidence of lava may be caused by thermal contraction (*Peck*, 1978) or by mechanical processes, such as the rearrangement of clasts (*Stevens et al.*, 2001a). Reported InSAR measurements of lava subsidence range in magnitude from 0.8 cm/yr at Etna to ~83 cm/yr at Okmok (Geoff Wadge, pers. comm., 2012) with a few cm/yr being typical. Most lava subsidence measurements to date have been made at basaltic, low viscosity flows (Table 5.2, Figure 5.7). Rates are often constant by the time surfaces become coherent enough to measure using InSAR. We expect lava flows as young as those at Santiaguito to still be subsiding, as InSAR observations of lava flows at Etna and Okmok volcanoes have measured subsidence ~10 and 35 years after emplacement, respectively (*Stevens et al.*, 2001a; *Lu et al.*, 2005b).

I solve simultaneously for change in lava thickness and for deformation, weighting interferograms on the basis of atmospheric noise as described above (Figure 5.5a). I use a similar approach to constructing time series as discussed in Chapters 2 and 4 and take a linear least squares inversion of interferogram phase to find velocities between acquisition dates (e.g. *Berardino et al.*, 2002), using a generalised inverse matrix (Moore-Penrose pseudoinverse) found from singular value decomposition. Velocities are found relative to the first acquisition date, before which it is assumed that there was no ground motion. This allows us to construct subsidence time series (e.g. Figure 5.5e). As the design matrix for such a joint inversion is rank deficient, I use a finite difference approximation of the second differential of the time series as a smoothing constraint. Zero value constraints are used for the first and last dates in the time series. As subsidence is expected to be linear, the smoothing parameter is overweighted (Figure 5.6).

The trade-off between our uncertainties in lava thickness and subsidence rate is investigated using a Monte Carlo approach, where randomly generated, spatially correlated noise (as described in Section 5.2) is added before performing the joint inversion and repeated for 100 perturbed datasets. This showed a positive trade-off between lava thickness and subsidence rate. A conservative approach is therefore taken to estimating uncertainties in lava subsidence. The error in lava thickness from our single inversion (±9 m) will result in phase shifts of between -0.03 and 0.48 radians in the individual Santiaguito interferograms and an apparent subsidence rate of magnitude ± 2 cm/yr. I do not expect to be able to detect subsidence below this rate.

Both joint inversion and correction of phase from single inversion result in similar trends in subsidence rate measurements. We measure the largest subsidence rates (6–10 ± 2 cm/yr in satellite line of sight) at the thickest, youngest part of the flow (Figure 5.5a,b,d,e). In this part of the field the most recent lava flows were only 5 years old (from 2004) at the time our first SAR data acquisition, and total thickness of lava emplaced lies between ~90 and 140 m. Thinner, older parts of the flow show no deformation above a rate of ~ 2 cm/yr, except for an area on the edge of the 2001-2002 flow (Figure 5.5a and b).

The subsidence rate of young lava is expected to depend on its age, thickness, composition and the morphology of the underlying substrate. As measurements across most of the lava field are below the bounds of our expected uncertainty, there is insufficient data to distinguish between these possibilities. However, a plot of lava subsidence against thickness does show some positive correlation, with a higher gradient at thicknesses above about 100 m, where the lava flows are youngest (gradient=0.04cm/yr/m, R^2=0.77, Figure 5.5c). Although the general correlation between these two parameters across the whole lava field may reflect the trade-off between them, this change in gradient suggests a difference in behaviour between the post-2004 and older lavas (Figure 5.5a,b,c,d)]. Similar positive correlations between flow thickness and subsidence rate have been measured for basaltic flows (*Lu et al.*, 2005a; *Stevens et al.*, 2001a). Without a knowledge of flow temperature structure or data allowing us to map the temporal development of subsidence rate, it is not possible to distinguish between subsidence mechanisms. However, in addition to the thermal contraction expected for such a young flow, some degree of clast repacking/gravity-driven compaction seems likely, given the steepness of the slope upon which this flow was extruded (Figure 5.5d).

Although it is expected that highly viscous and thermally insulated flows such as Santiaguito will subside more slowly than less viscous basalts, the rather limited set of global measurements show no evidence of this (Figure 5.7). My subsidence rate at Santiaguito adds to a very small set of observations of lava subsidence at andesitic-dacitic volcanoes (Table 5.2).

Figure 5.5: (a) Map of subsidence rate found from joint inversion. The apparently reduced area of the subsiding flow-field retrieved by joint inversion is a consequence of higher formal errors in lava thickness. (b) Schematic map showing the relative ages of lava flows emplaced after 2000, after *Escobar et al.* (2008) (c) Scatterplot of subsidence rate against lava thickness, showing an apparent linear relationship between increasing lava thickness and subsidence rate. (d) Profile of young lava laid over the original SRTM DEM (as in Figure 3). The size and direction of the arrow shows subsidence rate in satellite line of sight obtained from joint inversion. Inset panel below shows variation in subsidence rate with distance from El Caliente vent. Red dotted lines indicate the range of error in subsidence rate expected from an error in lava thickness of ±9 m. (e) Time series showing cumulative deformation in the satellite line of sight at the thickest part of the lava flow (~ 140 m). Location of time series (e) is marked on d.

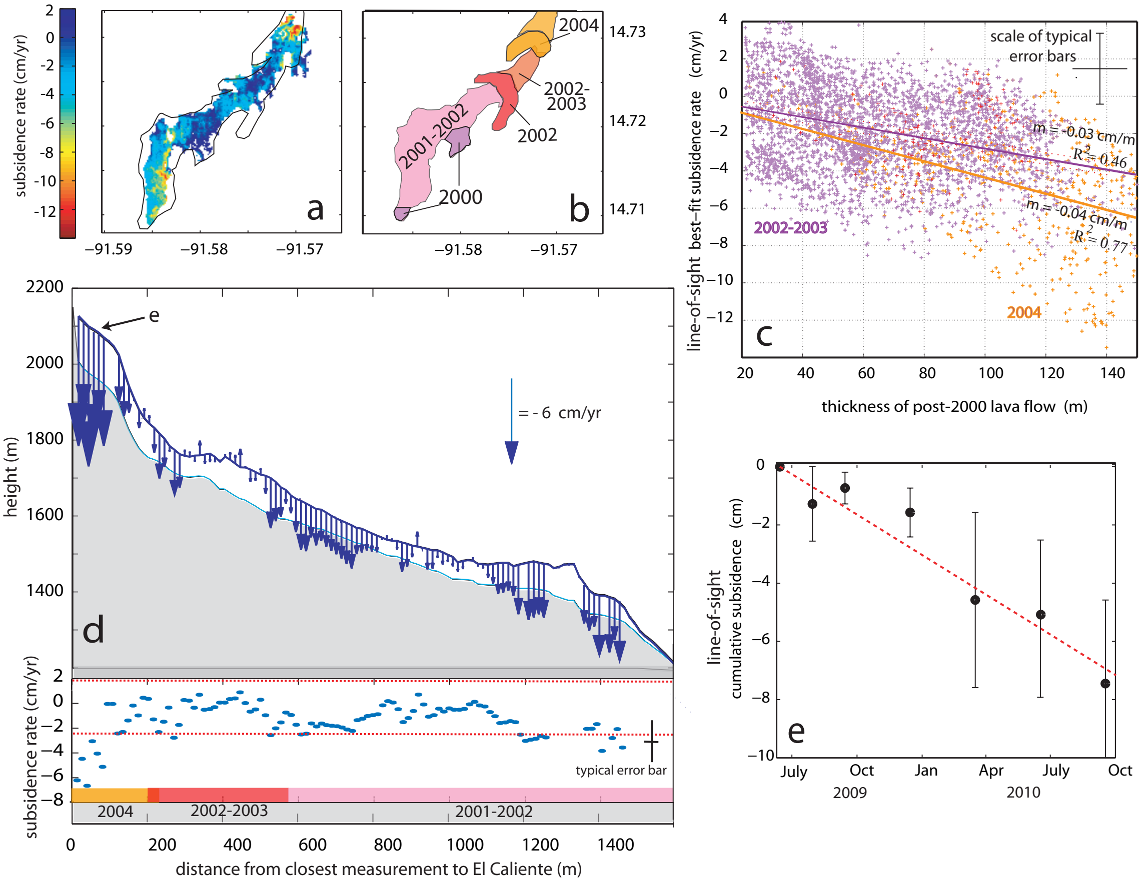

Figure 5.6: We use a smoothing factor κ to constrain joint inversion for topographic change and lava subsidence. Smoothing supplies us with an additional constraint for our inversion, which is otherwise rank deficient. The choice of a low smoothing factor would allow the lava subsidence time series to fluctuate in response to atmospheric phase contributions in individual interferograms. If a very large smoothing coefficient is chosen, we effectively assume that lava subsidence rate is linear. As the r.m.s. variation of this over-damped solution still lies below the variability expected to be caused by atmosphere we choose a high value of smoothing factor ($\kappa = 200$) for the inversions presented here. In practice, this gives us essentially the same result as inverting for a single rate, which would have been a reasonable assumption given the age of the lava flows.

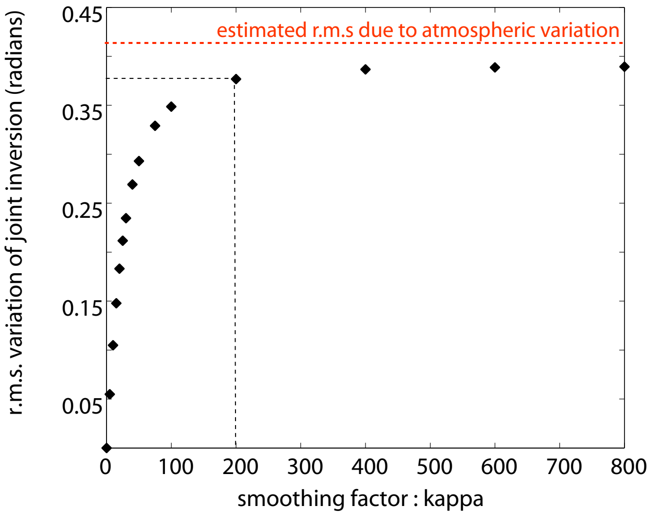

Figure 5.7: Lava subsidence rates normalised by maximum lava thickness (Table 5.2) are shown as a function of the age of the lava at the time of InSAR measurement. Basaltic lavas are shown in blue, andesites in red and our result for the dacitic lava of Santiaguito in black. Numbers in brackets refer to year of lava flow emplacement.

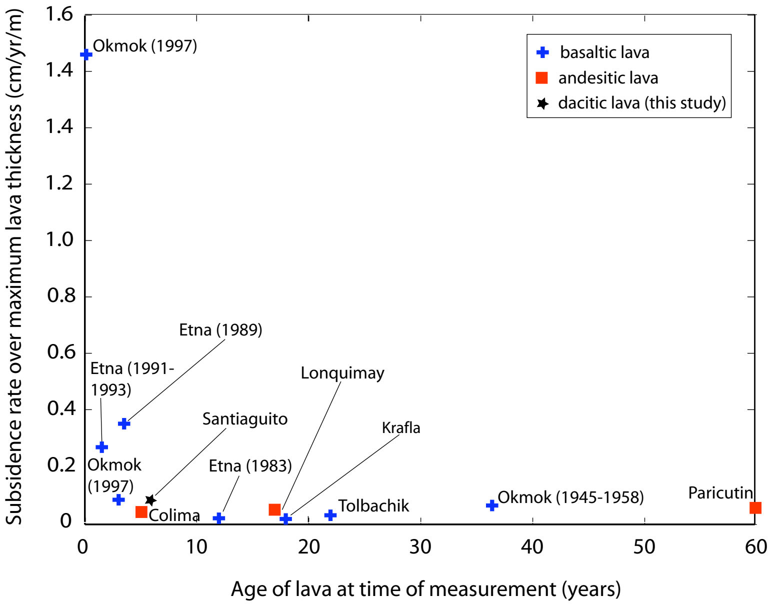

5.4 Discussion

The measurements of lava thicknesses at Santiaguito presented here demonstrate an approach suitable for monitoring extrusion and volume changes at remote or inaccessible volcanoes. They represent the first measurement of volume flux at Santiaguito since extrusion of the 2004–2005 lava flows and the first observation of lava subsidence at this volcano. My measurement of 0.43 ± 0.06 m^3/s between 2000 and 2009 should be treated as a minimum value for extrusion rate. This minimum rate is close to the long term average extrusion rate (1922-2000). Lava extrusion since 2000 has remained cyclical, with periods of high extrusion in 2000-2005 and 2011- early 2012 (J.B. Johnson, personal communication, 2012). There is no evidence in Santiaguito's flux estimates to indicate exhaustion of its magmatic source.

The ability to make combined measurements of lava flow thickness and subsidence rate may be a powerful tool for studying post-emplacement flow deformation. Where lava subsidence is higher rate or more widespread than at Santiaguito, the relationship between these two parameters could allow us to distinguish between thermal and mechanical contraction.The measurement of lava subsidence in addition to lava thickness would also be aided by a larger dataset and therefore longer time series than is available at Santiaguito.

5.4.1 Method Applicability and Synthetic tests

Uncertainties are expected to be introduced to our measurements of height change by (1) errors in the DEM used in processing (∼7 m for SRTM, *Rosen et al.*, 2001), (2) surface displacement (see Section 5.2) and (3) variations in tropospheric water vapour. The effects of (1) will be systematic, while (2) and (3) may be random, increasing the scatter in the $\frac{\delta\phi}{\delta B_{perp}}$ relationship.

For a dataset such as the one at Santiaguito, consisting of 7 interferograms with up to 140 m of height change and atmospheric noise of maximum standard deviation 6 mm, the formal error from inversion to find $\frac{\delta\phi}{B_{perp}}$ is ± 0.0009 radians/m, which corresponds to a mean uncertainty in lava thickness of $\sim \pm$ 9 m.

We generate sets of synthetic interferograms and changes in topography (Figure 5.8) to examine both the variability and distribution of uncertainties and the general limits of application for the methods described in Sections 5.2 and 5.3. We calculate the expected phase changes for synthetic lava fields of variable thickness and shape and add them to sets of randomly generated spatially correlated noise (e.g. *Lohman and Simons*, 2005) of the same means and standard deviations of variance and typical length scale as our interferograms for Santiaguito (Figure 5.8).

Residuals between the input synthetic lava field and the lava thicknesses retrieved were of a magnitude of ∼2 m for lava thicknesses greater than about 25 m (Figure 5.10). For lava thinner

Figure 5.8: Flowchart outlining the construction of sets of synthetic interferograms and tests for the effects of lava thickness and number of interferograms on the retrieval of topographic change.

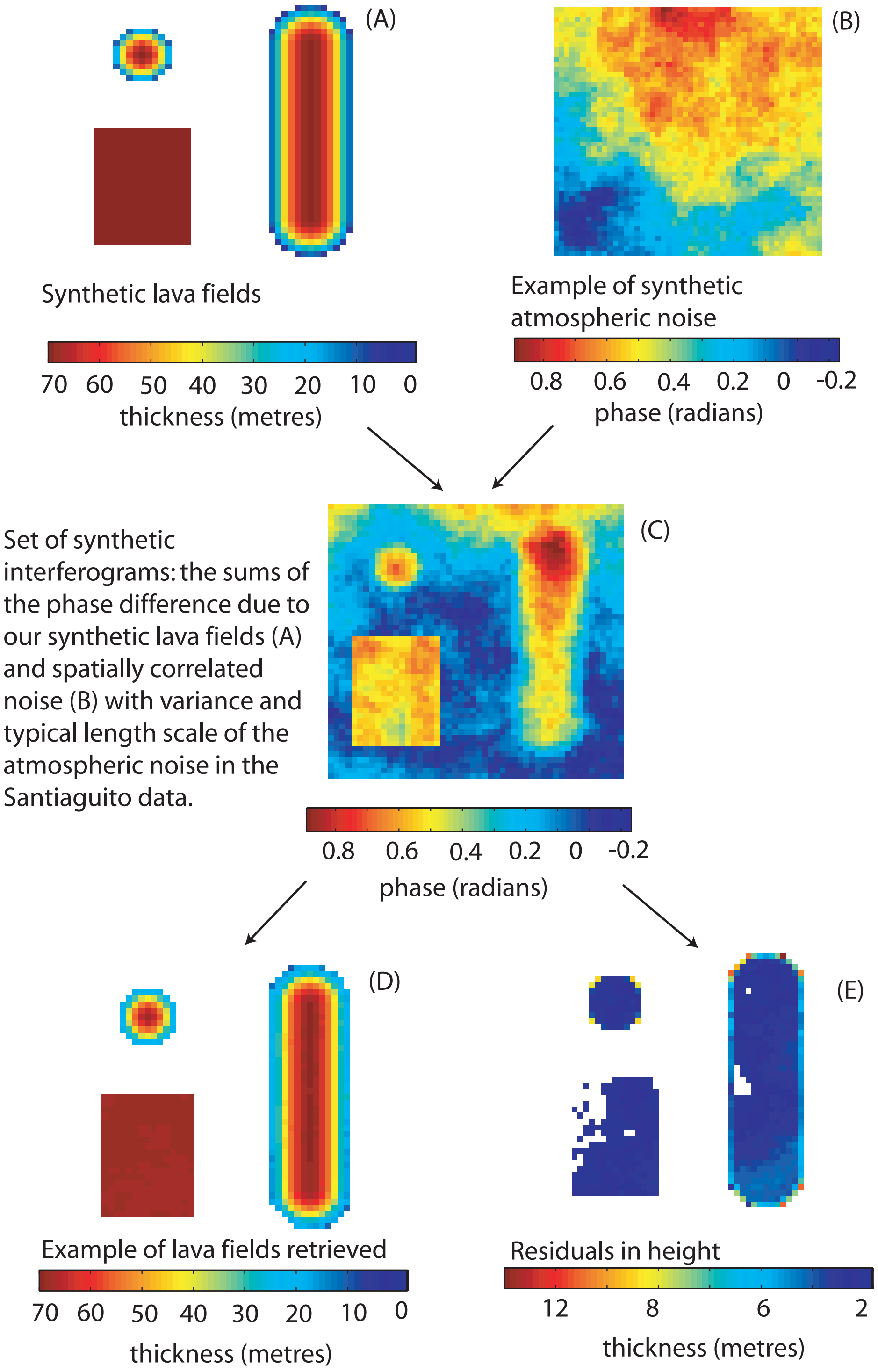

Figure 5.9: Percentage of the lava volume retrieved from synthetic tests as a function of a) lava thickness and b) the number of interferograms. For a) we use a set of interferograms with the same baselines as the Santiaguito data set and for b) we use 500 sets of randomly generated baselines with the same mean and standard deviation as the Santiaguito data. The percentage error in b) is therefore the mean error for all sets of baselines.

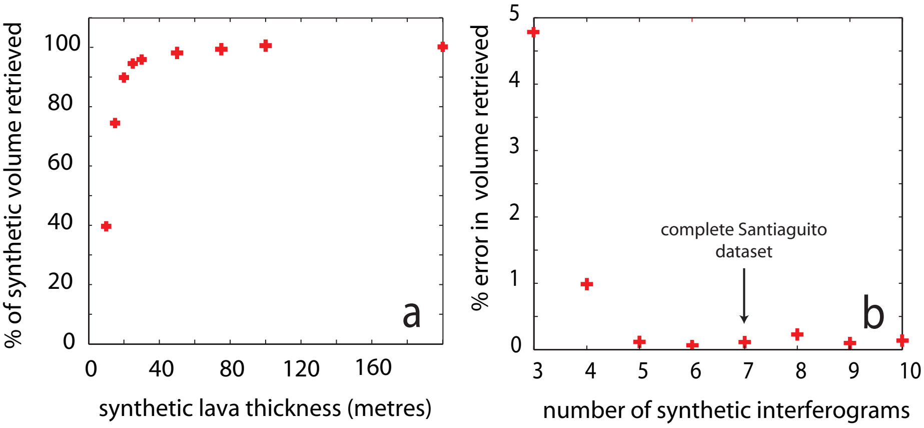

than ~7 m, the residuals exceed lava thickness. We use a Monte Carlo approach to find the mean percentage of the synthetic lava flows retrieved from these sets of synthetic interferograms using the method described above when we vary 1) synthetic lava thickness (100 repetitions) and 2) the number of interferograms used in the inversion (500 repetitions with normally distributed baselines of the same standard deviation, 250 m, as the Santiaguito data). For synthetic lava fields with an average thickness of ≥~30 m, we expect to be able to retrieve close to the complete volume of lava (Figure 5.9a). Our tests suggest that a minimum of 5 interferograms are required to retrieve the complete lava field (Figure 5.9b).

We expect to be able to detect topographic change in excess of ~7 m, given a minimum of 5 interferograms. For change greater than about 25 m, we expect uncertainties to be less than ~8%. This will allow measurement of topographic change about an order of magnitude greater than InSAR deformation measurements, and at the upper end of what is measurable using range or azimuth offsets (*Jonsson et al.*, 2002) (Figure 5.10b).

5.4.2 InSAR for measuring topographic change ≥~ 25 m

I have demonstrated with data from Santiaguito that topographic height change can be extracted from sets of interferograms with sufficient accuracy to be a useful tool for volcanologists. It is well-suited to measuring systems where changes are large, and are followed by a period of quiescence when interferograms can be constructed. This could include periodically extrusive volcanic activity and possibly very thick pyroclastic and lahar deposits. Other potential applications include measuring mass wasting deposits, such as post-earthquake or hurricane

Figure 5.10: (a) Magnitudes of residuals between synthetic lava field in interferograms with similar properties to Santiaguito data and thicknesses retrieved from inversion to find **m**. These values provide an indication of the magnitude of the expected error for any pixel in our lava thickness maps. Expected errors exceed lava thickness below thicknesses of about 7 m. (b) Illustration of range of topographic change measurable relative to other InSAR techniques.

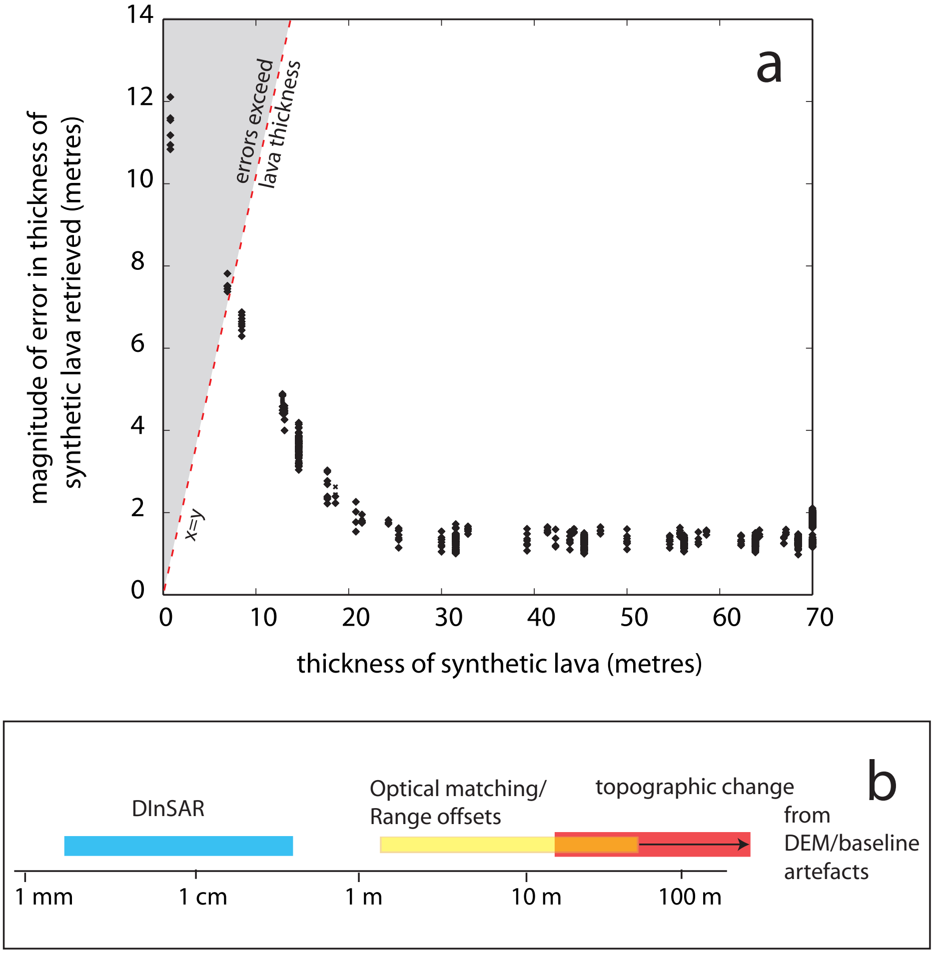

landslides. It will be less useful for targets such as lava domes themselves (rather than lava flows or pyroclastic flow deposits) because the surface changes so often that no coherent signal can be retrieved.

InSAR measurements of topographic change will be most useful where other methods are limited, for example, by frequent cloud cover. The spatial coverage of routinely acquired InSAR data is potentially greater than that available from purpose designed missions for DEM production.

Given a sufficient temporal density of data it should also be possible to construct a time series of topographic change. Measuring a continuous emplacement process is challenging, because the emplacement of fresh material will introduce chaotic phase changes to backscattered radar, making interferograms phase incoherent and unusable. However, if small sets of interferograms can be constructed during quiescent periods, they could be used to find topographic change relative to the acquisition of the DEM used in processing, and allow us to measure variations in time averaged extrusion rate. The time intervals over which this would be possible depends on 1) the number of interferograms needed to make height change measurements and 2) the repeat time of SAR satellite acquisitions. Our tests with synthetic data suggest that a minimum of 5 interferograms (atmospheric noise of maximum standard deviation 6 mm and baselines with mean= 0 m, standard deviation=250 m) are needed to be sure of capturing uniform topographic change of magnitude $\geq$ 25 m. For smaller magnitude change, shorter baselines or a greater variance of atmospheric noise, more will be required. Under ideal conditions, 5 independent interferograms can be first constructed from 10 SAR data acquisitions. This would give a temporal 'bin size' of 460 days for the ALOS data used in this paper (repeat time 46 days), less than 110 days for TerraSar-X data (<11 day repeat) and 120 days for the forthcoming ESA satellite, Sentinel-1 (12 day repeat). Shorter perpendicular baselines (e.g. ±50 as expected for Sentinel-1) will make measurement of topographic change more difficult. For baseline distributions similar to the ALOS data presented here, the primary limiting factors for measuring extrusion rate at long lasting volcanic eruptions will be the relative stability of radar scatterers on the ground surface and any deformation occurring during the period of InSAR measurement.

5.5 Summary

I have shown that topographic change in excess of ~25 m can be measured from interferometric phase delays in a small set of interferograms and demonstrated the usefulness of such information in volcanology. At Santiaguito I measure an extrusion rate of 0.43 ± 0.06 m^3/s between 2000 and 2009, observe the changes in flow morphology over this time, and measure lava subsidence of up to 6 cm/yr on the thickest and youngest parts of the flow. I believe that this approach will be particularly useful for volcanic activity whereby thick lava flows or pyroclastic deposits are emplaced with little warning, as no satellite image prior to emplacement is needed. The ability to measure the change in lava thickness and subsidence simultaneously is also an advantage. This technique may also have important applications for mass wasting events such as landslides.

Chapter 6

Conclusions

This thesis provides examples of how volcanologically useful information can be retrieved from sub-optimal InSAR data. Interferograms from Central America have high magnitudes of atmospheric noise and large regions where decorrelation is rapid. Additionally, the short effective lifetime of JAXA's ALOS instrument (just over 3 years) has reduced the potential for noise reduction via stacking as has been achieved in other parts of the world.

Deformation at Arenal was discovered and measured in spite of the very limited phase coherence in the surrounding region of Costa Rica (coherence was actually limited just to lava flows at Arenal in the majority of interferograms). Even this small region of coherent data (roughly 2 × 5 km) has improved our understanding of edifice stability and associated hazard at Arenal, although interpretation is made more difficult by not being able to measurement any longer wavelength deformation linked to deeper processes. My work on topographic change at Santiaguito has demonstrated that phase contributions commonly treated as noise in InSAR processing can be used to find parameters crucial to modeling the eruptive behaviour of many volcanoes (i.e. extrusion rate).

Further to this, analysis of 'null' results, from volcanoes that were erupting but not deforming, has allowed me to draw order of magnitude conclusions about the nature of the magmatic plumbing beneath them. Finally, quantifying uncertainty in InSAR measurements of volcano deformation has allowed me to make the first meaningful comparison of the incidence and global distribution of volcano deformation as measured with InSAR.

6.1 Thesis summary

I have presented an analysis and interpretation of InSAR deformation measurements in the Central America between 2007-2010. It was possible to construct coherent interferograms that included the majority of Central America's 75 volcanoes, and I was able to make measurements at 20 out of the 26 of the volcanoes that have been historically active.

Central America is a particularly challenging environment for making InSAR measurements. This is primarily due to the high magnitude and variability of tropospheric water vapour in the tropics and to rapid phase decorrelation caused by dense vegetation. In Chapter 2, I quantify the effects of these factors on InSAR measurement in Central America.

Radar path delays due to stratified water vapour in Central America are among the highest to have been measured worldwide (Table 2.1.1). These can generally be distinguished from potential deformation using their temporal characteristics and relationship to topography. I used the root mean squared variability of time series over individual volcanoes as an indication of the uncertainty in path delay and found that this value was proportional to volcano edifice height above the immediate surrounding topography (gradient = 2 cm/km height).

The L-band data presented in this thesis is much more successful in penetrating tropical vegetation than more widely available C-band data. Phase decorrelation is still relatively rapid, however, with the longest interferograms spanning around 18 months or less. I used a simple coherence model to test the relationship between vegetation type and temporal decorrelation and found no relationship with NDVI, but some systematic variation with land-use type. Decorrelation rates are higher (with a lower standard deviation) for tropical rainforest than for cultivated land (Figure 2.11).

Instead of focusing entirely on those volcanoes that were deforming, I estimated the uncertainty for InSAR measurements at each volcano (Chapter 3). This allowed me to place thresholds on the rate at which each volcano would have to deform in order to be measurable. These thresholds provide a context for each ‘null’ result, and allow me to use the lack of deformation at particular active volcanoes to make inferences about volcanic processes. For example, the lack of deformation accompanying small explosions at Telica, San Cristóbal and Poás suggest that any magma volume change during or after eruption took place at a minimum depth of ∼2 km (Section 3.4.1).

Similarly, I use the threshold values for deformation to test the limits of where magma could be accumulating beneath persistently active volcanoes without producing measurable deformation. I use literature measurements of degassing flux and magma sulphur content to estimate minimum volume change and thus the minimum depth at which magma could be accumulating in a single reservoir. The lack of significant deformation at Pacaya and Masaya volcanoes allow us to dismiss the possibility that there are shallow points of localised accumulation of degassed magma in the elastic crust beneath them. This suggests that magma a) returns to depths below our limits of geodetic detection and/or b) is dispersed through the mid to shallow crust in multiple smaller intrusions (Section 3.4.2).

The systematic approach to reporting 'null' results presented in Chapter 3 also provides a framework for comparison of InSAR results in different tectonic settings. We find no evidence of magmatic deformation in Central America above an average rate of around 2.4 cm/yr. This threshold is significantly lower than the majority of InSAR measurements of deformation in other parts of the world (Section 3.5). If the deformation events that have been measured with InSAR were distributed evenly around all of the historically active volcanoes in the world, then the probability of observing no deformation at all in Central America is about 2 %.

Several distinctive characteristics of the Central American Volcanic Arc may act to reduce the potential of magma movement to produce measurable surface deformation. Around half of the arc's eruptive products are basaltic, thought to ascend rapidly during eruption from where they pool at the base of the crust, beyond the depth at which we expect to be able to detect magma accumulation with InSAR. High volatile contents in Central American parental melts may in some circumstances lead to high gas fraction and therefore highly compressible magmas at shallow depths. A tendency for magma reservoirs to be vertically elongated, rather than spherical or sill-like, may also effectively 'dampen' any surface deformation by up to $\sim$ 50%. For example, vertically elongated reservoirs produce smaller magnitude surface deformation than equivalent volume spherical sources, with the effect increasing with depth and degree of elongation.

Our measurements of steady deformation on the western flanks of Volcán Arenal, Costa Rica, provide the first evidence of large-scale edifice movement at this volcano (Chapter 4). Arenal's western flanks have been plated by lava flows semi-continuously since the volcano's reactivation in 1968, increasing both the volcano's height and its asymmetry. Motion is apparently steady (average speed of $\sim$7 cm/yr) and generally down-slope (but steeper than the slope of the volcano itself, at an angle of $\sim$55° below the horizontal on the volcano's lower flanks). Subsidence is limited to a section of the volcano's western flanks suggesting a shallow source, within the edifice of the volcano itself. I attribute the rapid, high angle deformation at Arenal to gravity-driven slip, although it seems probable that lava subsidence also makes some contribution. The boundary between post-1968 eruption lavas and the paleosols and older eruptive products below is a potential location for a sliding plane, although it may be even shallower than this. However, the deformation mechanism at Arenal is still poorly understood and further measurements are required to distinguish between different scenarios (Section 6.2).

The measurement of topographic change (>10 m) from sets of interferograms has the potential to be a useful tool for volcanologists and can allow the measurement of extrusion rate, flow morphologies and joint retrieval of flow deposit thickness and subsidence. My measurements from Santiaguito (Chapter 5) have demonstrated this , as I successfully retrieved all of these properties from a relatively small set of interferograms. Extrusion rate at Santiaguito between 2000 and 2009 was 0.43 ± 0.06 m^3/s, close to mean lava dome extrusion since 1922. Over this time, dacitic lavas from the El Caliente dome followed a channel established during eruptions that started in 2000. The thickest and youngest parts of the lava flows were subsiding at a rate of roughly 6 cm/yr in 2009-10.

Measurement of large topographic change with sets of interferograms is particularly well-suited to large changes in topography that would result in decorrelation and therefore be impossible to measure with DInSAR, especially when such events are followed by a period of scatterer stability (e.g. volcano quiescence). Synthetic tests suggest that a minimum of 5 interferograms (atmospheric noise of maximum standard deviation 6 mm and baselines with mean = 0 m, standard deviation = 250 m) are needed to be sure of capturing uniform topographic change of magnitude $\geq$ 25 m. InSAR measurements of topographic change will be most useful where other methods (e.g. thermal imaging) are limited, for example, by frequent cloud cover.

6.2 Edifice stability at stratovolcanoes

InSAR data have the potential to provide insight into the growth, stability and eventual collapse of volcanoes. Measurements of edifice stability are important both for the assessment of hazards presented by active and dormant volcanoes, and for understanding volcano-related mountain building. Steep, conical volcanoes with a layered internal structure are particularly prone to shallow edifice failure *Voight* (2000).

The slow, gravity-driven subsidence of a volcano's edifice causes volcanoes to spread. The eventual outcome of such spreading can range from a) an increase in the stability of the volcano as its weight spreads over a larger area (*Borgia et al.*, 2000) to b) sudden collapse (*Ward and Day*, 2003). High spreading rates (and a high degree of internal hydrothermal alteration) have been associated with sudden failure (*van Wyk de Vries and Francis*, 1997). A change in the rate of edifice spreading may precede collapse, although this has not yet been measured. InSAR measurement is well-suited to detecting long term changes in rate of spreading due to its regular measurement intervals and potential for future automation. However, its low temporal resolution may not be sufficient to guarantee that any sudden change of rate preceding collapse would be detected.

InSAR measurements also have the potential to address the effect of sub-edifice faults on edifice stability. Although the effect of strike-slip, normal or thrust faulting has been predicted by analogue models (*Lagmay et al.*, 2000) and observed at dormant edifices (e.g. *Watt et al.*, 2009), measurements of the active process have so far been rare, with exception of Etna (*Borgia *et al.*, 1992; *Froger et al.*, 2001).

6.2.1 Deformation mechanism at Arenal

My measurements of gravity driven deformation at Arenal in Chapter 4 (volume = 1×10^{10} m^3) provide a contrasting example to the deformation taking place at the much larger and older Mount Etna (volume = 14×10^{11} m^3). At Etna, radial collapse of the volcano's edifice is taking place in concert with deeper basal spreading associated with magma reservoir dynamics (*Lundgren et al.*, 2004). At Arenal, it has so far only been possible to measure relatively shallow gravity-driven deformation, due to poor coherence away from the recent lava flows. As the magma reservoir below Arenal (12–14 km, *Reagan et al.*, 1987; *Streck et al.*, 2005) is thought to be much deeper than that at Etna (4–5 km, e.g. *Lundgren et al.*, 2001), it is improbable that there is any direct relationship between spreading and magma chamber dynamics at Arenal.

The deformation of Etna's edifice is well established and clearly associated with several well-established faults that demarcate radial rift zones moving outwards at different rates. At Arenal there is no clear relationship to the strike-slip Danta fault that bisects the volcano. If the deformation at Arenal does in fact prove to be caused by slip on a shallow fault plane, it may be considered analogous to the steady movement of the middle to upper flanks of Etna, which are thought to be driven by gravity alone (*Lundgren et al.*, 2004).

Although the InSAR data presented in this thesis are best explained by shallow gravity-driven slip, questions still remain about the mechanism of deformation at Arenal. The absence of a thrust feature at the base of the volcano's western flank, for example, is puzzling. The interferograms presented here are of insufficient temporal resolution and too high noise to be certain of distinguishing between continuous motion of one large block at Arenal, or the motion of many small units. Motion between 2005 and 2009 appears to have been steady, although high levels of atmospheric noise may mask either a long term change in velocity or a 'stop-start' pattern to the deformation.

I hope to address these questions though analysis of higher spatial and temporal resolution TerraSAR-X (TSX) data. However, TSX presents particular challenges for InSAR analysis. The lack of a DEM of resolution close to that of the SAR data (2×3 m at best) prevents the construction of high resolution interferograms. I aim to address this by oversampling the SRTM DEM used for processing L- and C-band data in Chapter 4 and applying the methods discussed in Chapter 5 to correct this DEM. Each additional independent interferogram constructed contributes an iterative improvement to the DEM, which can then be used to remove topographic contributions to phase from the interferograms. Arenal TSX data may also provide a good test case for empirical removal of tropospheric water vapour signal, which, if successful, may reduce noise enough to make any small changes in slip rate apparent in a time series.

6.3 InSAR measurements of topographic change

I have shown in Chapter 5 that topographic change in excess of ~25 m can be measured from interferometric phase delays in a small set of interferograms and demonstrated the usefulness of such information in volcanology. The spatial coverage of routinely acquired InSAR data is greater (and easier to acquire) than that available from purpose designed missions for DEM production. Sets of interferograms constructed during quiescent periods have the potential to increase the effective number of topographic models that can be constructed, allowing higher resolution time series of volcano extrusion. I expect such approaches to be more difficult with the tighter orbital tube proposed for ESA's Sentinel instruments, although it may be possible to obtain lower precision measurements of topographic change from larger sets of interferograms. Higher resolution measurements of topographic change from SAR data may be expected from using the high resolution (2-3 m) TanDEM-X DEMs in conjunction with X-band data, although uncertainty in height measurement will be similarly dependent on satellite baseline separation. Permanent scatterer (PSInSAR) and distributed scatterer (e.g. SqeeSAR) approaches also have potential for generating high resolution DEMs (as well as deformation measurement) in less coherent areas.

The exploitation of the InSAR archive to measure changes in topography depends to some extent on the availability of DEMs for use in processing. Interferograms constructed from data after 2000 can be used in conjunction with NASA's SRTM global DEM to measure changes since that time. Earlier SAR data may be corrected with local DEMs. The ASTER GDEM is not appropriate for use with this method, as it is constructed from infra-red images acquired over a period of up to 10 years and therefore captures an average rather than a 'snapshot' of the earth's topography. A potential target for measurement of topographic change since the SRTM data were acquired in 2000 is Reventador, Ecuador, where lava flows of volumes up to 4×10^7 m^3 have been effused on four occasions since 2000. The use of SAR imagery to find approximate extrusion rate will be most useful for remote, inaccessible, cloud-covered volcanoes where other measurements are not possible. Such targets may include Nyiragongo (DCR) or Montagu Island (South Sandwich Islands), both of which have erupted significant volumes of lava since 2000.

Other potential applications for the method described in Chapter 5 include measurement of rapidly emplaced, thick pyroclastic flows or lahar deposits. It is important to measure any changes that these make to pre-existing topography, as this will have an impact on the path of future flows and associated hazard. Routinely acquired, post-event SAR images may allow rapid initial corrections to be made to DEMs, before the acquisition of new topographic data from aerial or satellite measurements can be arranged.

The large changes in the surface topography of ice sheets after sub-glacial eruptions could also be measured in this manner. Although it is likely to be impossible to construct interferograms that span a sub-glacial eruption due to massive changes to the scattering properties of the ice surface, after the eruption has ended the remaining ice may stabilise sufficiently to allow the construction of post-eruption interferograms.

The measurement of landslide volume from InSAR may provide insight into the ratio between erosion and mountain building, particularly where many instances of large scale land movement are triggered by an external event, such as a hurricane or large earthquake. The quantification of mass wasting associated with such natural disasters is important for determining long-term time averaged erosive flux.

6.4 InSAR's potential as a tool for volcanology

InSAR has made major contributions to our understanding of several volcanic processes, and alerted us to activity at many volcanoes previously thought to be dormant (see Chapter 1). However, the global distribution of InSAR measurements of volcano deformation is uneven, showing no obvious correlation with the number of historically active volcanoes or concurrent volcanic activity (e.g. Chapter 3). The usefulness of InSAR for either research or monitoring purposes depends on a) environmental and instrumental conditions and b) the magnitude and nature of deformation caused by volcanic activity.

6.4.1 Environmental and instrumental limitations

As discussed in Chapter 2, factors that limit InSAR measurement include (1) dense vegetation or periodic snow cover, (2) frequent explosive activity, (3) steep slopes and (4) large contrasts in topography. It is therefore much more difficult to make measurements at young stratovolcanoes than at large shield volcanoes. Further to this, where only a small area around a volcano is coherent (e.g. for small islands, or volcanoes surrounded by rainforest), the type of deformation that is detectable may be limited to shallower processes. Instrumental wavelength also affects the spatial distribution of InSAR deformation measurements, as only L-band data has been shown capable of large scale surveys in tropical regions.

However, environmental and instrumental limitations to InSAR measurement may not always be the limiting factor for where volcano deformation has been observed with InSAR. This is demonstrated in Chapter 3, in which I showed that despite the challenges of making InSAR measurements in the CAVA, the majority of signals seen at other vocanic arcs would nonetheless have been observable under these conditions.

6.4.2 Tectonic setting and volcano deformation

I expect there to be systematic differences in the magnitude of surface deformation at different volcanoes depending on a) the depth at which magma stalls in the crust and b) magma composition. This can be illustrated by a very general comparison between magma storage at continental arcs and rifts.

At continental arcs, the large density contrast at the base of thick crust allows basaltic, water-rich melts to stall, fractionate and interact with melted country rock in deep crustal hot zones (as proposed by *Annen et al.*, 2006). This results in volatile-rich, low viscosity melts that ascend rapidly to the point of water saturation, where crystallisation begins and they stall again in the shallow crust.

The residence of material in the deep crust at continental arcs is unlikely to be detectable geodetically unless it is associated with especially large volume changes (as seen in the Central Andes, Table 1.2). In the shallow crust we are able to measure much smaller volume changes (e.g. Galeras, Tungurahua, Table 1.1).

However, for arc magmas where water contents are high, there is a potential for high bubble fractions above the depth of water saturation, especially for evolved magmas that have been resident in the crust for some time. This results in high magma compressibility, which can accommodate a high proportion of any volume change associated with either a fresh intrusion or loss of material in an eruption, reducing the magnitude of any resulting surface deformation. Whether or not measurable deformation accompanies volume changes in a shallow arc context will therefore depend in part on whether degassing has taken place.

At rifts, however, hot, thin crust and rapid extension allow large volumes of mafic magmas to ascend to shallow depths, where volume changes are close enough to the surface to produce high magnitude, measurable deformation (e.g. dyking events in East Africa and Iceland, volcano inflation/deflation in Kenya and Ethiopia, Tables 1.1–1.3). It should be noted that magma volatile contents in rift settings are low (i.e. <1 wt%), so that even shallow reservoirs are likely to be relatively incompressible.

6.4.3 Deformation Monitoring

The differences in the geodetic expression of volume change for volcanoes in different settings has implications for the use of InSAR for volcano monitoring. This thesis demonstrates that a lack of deformation measured by InSAR cannot necessarily be treated as evidence of a lack of shallow magma, or a lack of volcanic hazard. It is crucial that both the method limitations and the volcanic setting's influence on magmatic plumbing are considered when interpreting InSAR data.

Bibliography

Acocella, V., and F. Funiciello (2010), Kinematic setting and structural control of arc volcanism, *Earth and Planetary Science Letters*, *289*(12), 43 – 53, doi:10.1016/j.epsl.2009.10.027. 1.4.2, 3.7

Agustan, F. Kimata, Y. E. Pamitro, and H. Z. Abidin (2012), Understanding the 2007-2008 eruption of Anak Krakatau Volcano by combining remote sensing technique and seismic data, *International Journal of Applied Earth Observation and Geoinformation*, *14*, 73–82, doi:10.1016/j.jag.2011.08.011. 1.1, 3.5

Ahmed, R., P. Siqueira, S. Hensley, B. Chapman, and K. Bergen (2011), A survey of temporal decorrelation from spaceborne l-band repeat-pass insar, *Remote Sensing of Environment*, *115*(11), 2887 – 2896, doi:10.1016/j.rse.2010.03.017. 2.4, 2.4.3

Alvarado, D., C. DeMets, B. Tikoff, D. Hernndez, T. Wawrzyniec, C. Pullinger, G. Mattioli, H. Turner, M. Rodriguez, and F. Correa-Mora (2011), Forearc motion and deformation between El Salvador and Nicaragua: GPS, seismic, structural, and paleomagnetic observations, *Lithosphere*, *3*(1), 3–21, doi:10.1130/L108.1. 1.4.2, 3.5.1

Alvarado, G. E., M. J. Carr, B. D. Turrin, C. C. Swisher, H.-U. Schmincke, and K. W. Hudnut (2006), Recent volcanic history of Iraz volcano, Costa Rica: Alternation and mixing of two magma batches, and pervasive mixing, *Geological Society of America Special Papers*, *412*, 259–276, doi:10.1130/2006.2412(14). 1.4.1, 1.7

Alvarado, G. E., G. J. Soto, H. Schmincke, L. L. Bolge, and M. Sumita (2006), The 1968 andesitic lateral blast eruption at Arenal volcano, Costa Rica, *Journal of Volcanology and Geothermal Research*, *157*, 9–33, doi:10.1016/j.jvolgeores.2006.03.035. 4.1, 4.1

Alvarado, G. E., S. Carboni, M. Cordero, M. Aviles, and M. Valverde (2010), Stability of the cone and the foundation of Arenal volcano, Costa Rica, *Cities on Volcanoes Abstracts Volume, 2010,Tenerife, Canary Islands*, pp. 31st May – 4th June 2010. 4.2.5

Amelung, F., and S. Day (2002), InSAR observations of the 1995 Fogo, Cape Verde, eruption: Implications for the effects of collapse events upon island volcanoes, *Geophysical Research Letters*, *29*(12), 120,000–1, doi:10.1029/2001GL013760. 1.1, 3.3, 5.2

Amelung, F., S. Jónsson, H. Zebker, and P. Segall (2000a), Widespread uplift and 'trapdoor' faulting on Galápagos volcanoes observed with radar interferometry, *Nature*, *407*, 993–996. 1.1, 1.3, 1.2, 1.3

Amelung, F., C. Oppenheimer, P. Segall, and H. Zebker (2000b), Ground deformation near Gada 'Ale volcano, Afar, observed by radar interferometry, *Geophysical Research Letters*, *27*, 3093–3096, doi:10.1029/2000GL008497. 1.2

Amelung, F., S.-H. Yun, T. R. Walter, P. Segall, and S.-W. Kim (2007), Stress Control of Deep Rift Intrusion at Mauna Loa Volcano, Hawaii, *Science*, *316*, 1026–, doi:10.1126/science.1140035. 1.2

Annen, C., J. D. Blundy, and R. S. J. Sparks (2006), The genesis of intermediate and silicic magmas in deep crustal hot zones, *Journal of Petrology*, *47*, 505–539(35), doi:10.1093/petrology/egi084. 6.4.2

Balzter, H. (2001), Forest mapping and monitoring with interferometric synthetic aperture radar (insar), *Progress in Physical Geography*, *25*(2), 159–177, doi:10.1177/030913330102500201. 2.4.1

Bardintzeff, J.-M., and C. Deniel (1992), Magmatic evolution of Pacaya and Cerro Chiquito volcanological complex, Guatemala, *Bulletin of Volcanology*, *54*, 267–283, doi:10.1007/BF00301482. 1.4

Bathke, H., M. Shirzaei, and W. T. R. (2011), Inflation and deflation at the steep-sided Llaima stratovolcano (Chile) detected by using InSAR, *Geophysical Research Letters*, *38*, L10,304, doi:10.1029/2011GL047168. 1.1, 3.4.1, 3.5

Beauducel, F., P. Briole, and J. Froger (2000), Volcano-wide fringes in ERS synthetic aperture radar interferograms of Etna (1992-1998): Deformation or tropospheric effect?, *Journal of Geophysical Research*, *105*, 16,391–16,402, doi:10.1029/2000JB900095. 2.1.1, 2.1.4

Benhamou, G., P. Allard, J. C. Sabroux, G. Vitter, D. Dajlevic, and A. Creusot (1988), Oxygen fugacity of gases and rocks from Momotombo volcano, Nicaragua: Application to volcanological monitoring, *Journal of Geophysical Research*, *93*, 14,872–14,880, doi:10.1029/JB093iB12p14872. 1.6

Berardino, P., G. Fornaro, R. Lanari, and E. Sansosti (2002), A new algorithm for surface deformation monitoring based on small baseline differential SAR interferograms, *IEEE Transactions on Geoscience and Remote Sensing*, *40*, 2375–2383, doi:10.1109/TGRS.2002.803792. 2.1.2, 2.1.3, 3.2, 4.2.4, 5.1, 5.3.4

Bevis, M., S. Businger, T. A. Herring, C. Rocken, R. A. Anthes, and R. H. Ware (1992), GPS Meteorology: Remote Sensing of Atmospheric Water Vapor Using the Global Positioning System, *Journal of Geophysical Research*, *97*, 15,787–15,801. 2.1.1

Biggs, J., T. Wright, Z. Lu, and B. Parsons (2007), Multi-interferogram method for measuring interseismic deformation: Denali Fault, Alaska, *Geophysical Journal International*, *170*, 1165–1179, doi:10.1111/j.1365-246X.2007.03415.x. 3.2.1

Biggs, J., F. Amelung, N. Gourmelen, T. H. Dixon, and S.-W. Kim (2009a), InSAR observations of 2007 Tanzania rifting episode reveal mixed fault and dyke extension in an immature continental rift, *Geophysical Journal International*, *179*, 549–558, doi:10.1111/j.1365-246X.2009.04262.x. 1.1

Biggs, J., E. Y. Anthony, and C. J. Ebinger (2009b), Multiple inflation and deflation events at Kenyan volcanoes, East African Rift, *Geology*, *37(11)*, 979–982. 1.3, 1.2, 3.5, 4.2.3

Biggs, J., E. Y. Anthony, and C. J. Ebinger (2009c), Multiple inflation and deflation events at Kenyan volcanoes, East African Rift, *AGU Fall Meeting Abstracts*, pp. F4+. 1.3, 1.2, 2

Biggs, J., P. Mothes, M. Ruiz, F. Amelung, T. H. Dixon, S. Baker, and S.-H. Hong (2010), Stratovolcano growth by co-eruptive intrusion: the 2008 eruption of Tungurahua Ecuador, *Geophysical Research Letters*, *37*, L21,302. 1.2, 3.5

Biggs, J., I. D. Bastow, D. Keir, and E. Lewi (2011), Pulses of deformation reveal frequently recurring shallow magmatic activity beneath the Main Ethiopian Rift, *Geochemistry, Geophysics, Geosystems*, *12*, Q0AB10, doi:10.1029/2011GC003662. 1.3

Bolge, L., M. Carr, K. Milidakis, F. Lindsay, and M. Feigenson (2009), Correlating geochemistry, tectonics, and volcanic volume along the Central American volcanic front, *Geochemistry Geophysics Geosystems*, *10*(12), Q12S18. 3.5.1

Borgia, A. (1983), Dynamics of lava flow fronts, Arenal Volcano, Costa Rica, *Journal of Volcanology and Geothermal Research*, *19*, 303–329, doi:10.1016/0377-0273(83)90116-6. 5.3.4

Borgia, A., and B. van Wyk de Vries (2003a), The volcano-tectonic evolution of Concepción, Nicaragua, *Bulletin of Volcanology*, *65*, 248–266, doi:10.1007/s00445-002-0256-8. 1.6

Borgia, A., and B. van Wyk de Vries (2003b), The volcano-tectonic evolution of Concepción, Nicaragua, *Bulletin of Volcanology*, *65*, 248–266, doi:10.1007/s00445-002-0256-8. 4.3

Borgia, A., C. Poore, M. J. Carr, W. G. Melson, and G. E. Alvarado (1988), Structural, stratigraphic, and petrologic aspects of the Arenal-Chato volcanic system, Costa Rica: Evolution of a young stratovolcanic complex, *Bulletin of Volcanology*, *50*, 86–105, doi:10.1007/BF01275171. 4.3.3

Borgia, A., L. Ferrari, and G. Pasquarè (1992), Importance of gravitational spreading in the tectonic and volcanic evolution of Mount Etna, *Nature*, *357*, 231–235, doi:10.1038/357231a0. 6.2

Borgia, A., P. T. Delaney, and R. P. Denlinger (2000), Spreading Volcanoes, *Annual Review of Earth and Planetary Sciences*, *28*, 539–570, doi:10.1146/annurev.earth.28.1.539. 4.3.3, 6.2

Borgia, A., P. Tizzani, G. Solaro, M. Manzo, F. Casu, G. Luongo, A. Pepe, P. Berardino, G. Fornaro, E. Sansosti, G. P. Ricciardi, N. Fusi, G. Di Donna, and R. Lanari (2005), Volcanic spreading of Vesuvius, a new paradigm for interpreting its volcanic activity, *Geophysical Research Letters*, *32*, 3303, doi:10.1029/2004GL022155. 4.3

Boyce, J. W., and R. L. Hervig (2009), Apatite as a monitor of late-stage magmatic processes at Volcán Irazú, Costa Rica, *Computer*, *157*, 135–145, doi:10.1007/s00410-008-0325-x. 1.7

Briole, P., D. Massonnet, and C. Delacourt (1997), Post-eruptive deformation associated with the 1986-87 and 1989 lava flows of Etna detected by radar interferometry, *Geophysical Research Letters*, *24*, 37–40, doi:10.1029/96GL03705. 5.2

Bürgmann, R., P. A. Rosen, and E. J. Fielding (2000), Synthetic Aperture Radar Interferometry to Measure Earth's Surface Topography and Its Deformation, *Annual Review of Earth and Planetary Sciences*, *28*, 169–209, doi:10.1146/annurev.earth.28.1.169. 1.2, 3.1

Burkart, B., and S. Self (1985), Extension and rotation of crustal blocks in northern Central America and effect on the volcanic arc, *Geology*, *13*, 22, doi:10.1130/0091-7613(1985)13<22:EAROCB>2.0.CO;2. 1.4, 1.4.2, 3.5.1

Burton, M. R., C. Oppenheimer, L. A. Horrocks, and P. W. Francis (2000), Remote sensing of CO_2 and H_2O emission rates from Masaya volcano, Nicaragua, *Geology*, *28*, 915–+, doi:10.1130/0091-7613(2000)28<915:RSOCAH>2.0.CO;2. 1.2, 1.6

Calvari, S. (2003), Effusion rate estimations during the 1999 summit eruption on Mount Etna, and growth of two distinct lava flow fields, *Journal of Volcanology and Geothermal Research*, *119*, 107–123, doi:10.1016/S0377-0273(02)00308-6. 5.1.1

Calvari, S., L. Lodato, A. Steffke, A. Cristaldi, A. J. L. Harris, L. Spampinato, and E. Boschi (2010), The 2007 Stromboli eruption: Event chronology and effusion rates using thermal infrared data, *Journal of Geophysical Research (Solid Earth)*, *115*, B04,201, doi:10.1029/2009JB006478. 5.1.1

Caravantes, G., J. Zurek, S. K. Ebmeier, H. Rymer, and C. Locke (in prep), Structures controlling volcanic activity within Masaya Caldera, *Bulletin of Volcanology.* 3.1, 3.3, 3.2, 3.5

Carr, M. (1981a), Evolution of a young parasitic cone towards a mature central vent; Izalco and Santa Ana volcanoes in El Salvador, Central America, *Journal of Volcanology and Geothermal Research*, *11*, 277–292, doi:10.1016/0377-0273(81)90027-5. 1.4.1, 1.5, 3.3

Carr, M. (1981b), Relation of lava compositions to volcano size and structure in El Salvador, *Journal of Volcanology and Geothermal Research*, *10*, 35–48, doi:10.1016/0377-0273(81)90053-6. 3.5.1

Carr, M. (1981c), Relation of lava compositions to volcano size and structure in El Salvador, *Journal of Volcanology and Geothermal Research*, *10*, 35–48, doi:10.1016/0377-0273(81)90053-6. 1.4.1, 1.5

Carr, M. (1981d), Evolution of a young parasitic cone towards a mature central vent; Izalco and Santa Ana volcanoes in El Salvador, Central America, *Journal of Volcanology and Geothermal Research*, *11*, 277–292, doi:10.1016/0377-0273(81)90027-5. 1.4.1

Carr, M. (1984), Symmetrical and segmented variation of physical and geochemical characteristics of the central american volcanic front, *Journal of Volcanology and Geothermal Research*, *20*, 231–252, doi:10.1016/0377-0273(84)90041-6. 1.4, 1.4.1, 3.5.1

Carr, M. (1987), Intra-eruption changes in composition of some mafic to intermediate tephras in Central America, *Journal of Volcanology and Geothermal Research*, *33*, 147–159, doi:10.1016/0377-0273(87)90058-8. 1.6

Carr, M. J., M. D. Feigenson, L. C. Patino, and A. Walker, J (2003), Volcanism and geochemistry in Central America: Progress and problems, *Geophysical Monograph*, *138*, 153–174. 1.4, 1.5, 1.6, 1.7, 3.5.1

Cervelli, P., P. Segall, F. Amelung, H. Garbeil, C. Meertens, S. Owen, A. Miklius, and M. Lisowski (2002), The 12 September 1999 Upper East Rift Zone dike intrusion at Kilauea Volcano, Hawaii, *Journal of Geophysical Research (Solid Earth)*, *107*, 2150, doi:10.1029/2001JB000602. 1.1

Chaussard, E., and F. Amelung (2011), Tectonic control of magma ascent in volcanic arcs: Space-geodetic evidence from the westsunda arc, indonesia, in *FRINGE 2011 Workshop, Frascati*, European Space Agency. 1.1, 1.2, 3.5, 3.5

Chesner, C., and W. Rose (1984), Geochemistry and evolution of the Fuego volcanic complex, Guatemala, *Journal of Volcanology and Geothermal Research*, *21*, 25–44, doi:10.1016/0377-0273(84)90014-3. 1.4

Chesner, C. A., C. R. Pullinger, and C. D. Escobar (2004), Physical and chemical evolution of San Miguel volcano, El Salvador, *Geological Society of America Special Papers*, *375*, 213–226, doi:10.1130/0-8137-2375-2.213. 1.5

Clark, S. K., M. K. Reagan, and T. Plank (1998), Trace element and U-series systematics for 1963-1965 tephras from Irazú Volcano, Costa Rica: implications for magma generation processes and transit times, *Geochimica et Cosmochimica Acta*, *62*, 2689–2699, doi:10.1016/S0016-7037(98)00179-3. 1.7

Colclough, S. (2006), Investigations of Nyamuragira and Nyiragongo Volcanoes (Democratic Republic of the Congo) Using InSAR, in *Fringe 2005 Workshop*, *ESA Special Publication*, vol. 610. 5.2

Conway, F. M., J. F. Diehl, and O. Matías (1992), Paleomagnetic constraints on eruption patterns at the Pacaya composite volcano, Guatemala, *Bulletin of Volcanology*, *55*, 25–32, doi:10.1007/BF00301117. 1.4

Coppola, D., M. R. James, T. Staudacher, and C. Cigolini (2010), A comparison of field- and satellite-derived thermal flux at Piton de la Fournaise: implications for the calculation of lava discharge rate, *Bulletin of Volcanology*, *72*, 341–356, doi:10.1007/s00445-009-0320-8. 5.1.1

Correa-Mora, F., C. DeMets, D. Alvarado, H. L. Turner, G. Mattioli, D. Hernandez, C. Pullinger, M. Rodriguez, and C. Tenorio (2009), GPS-derived coupling estimates for the Central America subduction zone and volcanic arc faults: El Salvador, Honduras and Nicaragua, *Geophysical Journal International*, *179*(3), 1279–1291, doi:10.1111/j.1365-246X.2009.04371.x. 1.4.2, 3.5.1

Corti, G., E. Carminati, F. Mazzarini, and M. Oziel Garcia (2005), Active strike-slip faulting in El Salvador, Central America, *Geology*, *33*, 989, doi:10.1130/G21992.1. 1.4.2

Davis, P. M. (1986), Surface deformation due to inflation of an arbitrarily oriented triaxial ellipsoidal cavity in an elastic half-space, with reference to Kilauea Volcano, Hawaii, *Journal of Geophysical Research*, *91*, 7429–7438, doi:10.1029/JB091iB07p07429. 1.1

de Zeeuw-van Dalfsen, E., R. Pedersen, F. Sigmundsson, and C. Pagli (2004), Satellite Radar Interferometry 1993–1999 suggests deep accumulation of magma near the crust-mantle boundary at the Krafla volcanic system, Iceland, *Geophysical Research Letters*, *31*(13), L13,611. 1.2

de Zeeuw-van Dalfsen, E., R. Pedersen, A. Hooper, and F. Sigmundsson (2012), Subsidence of Askja caldera 2000–2009: Modelling of deformation processes at an extensional plate boundary, constrained by time series InSAR analysis, *Journal of Volcanology and Geothermal Research*, *213–214*(0), 72 – 82, doi:10.1016/j.jvolgeores.2011.11.004. 1.2

Delaney, P. T., and R. P. Denlinger (1999), Stabilization of volcanic flanks by dike intrusion: an example from Kilauea, *Bulletin of Volcanology*, *61*, 356–362, doi:10.1007/s004450050278. 4.3

DeMets, C. (2001), A new estimate for present-day Cocos-Caribbean plate motion: Implications for slip along the Central American volcanic arc, *Geophysical Research Letters*, *28*, 4043–4046, doi:10.1029/2001GL013518. 1.4.2, 1.4, 1.6

Dieterich, J. H., and R. W. Decker (1975), Finite element modeling of surface deformation associated with volcanism, *Journal of Geophysical Research*, *80*, 4094–4102, doi:10.1029/JB080i029p04094. 1.1

Duffield, W., L. Stieltjes, and J. Varet (1982), Huge landslide blocks in the growth of piton de la fournaise, La réunion, and Kilauea volcano, Hawaii, *Journal of Volcanology and Geothermal Research*, *12*, 147–160, doi:10.1016/0377-0273(82)90009-9. 4.3.3

Durst, K. S. (2006), Analysis of Eruption Rates at Santiaguito, Guatemala Using ASTER and Aerial Derived Digital Elevation Models. 5.3.2

Durst, K. S. (2008), Erupted Magma Volume Estimates at Santiaguito and Pacaya Volcanoes, Guatemala using Digital Elevation Models, Master's thesis, Michigan Technological University. 3.4

Dvorak, J. J., and D. Dzurisin (1997), Volcano geodesy: The search for magma reservoirs and the formation of eruptive vents, *Reviews of Geophysics*, *35*, 343–384, doi:10.1029/97RG00070. 1.1, 1.3

Dzurisin, D. (2003), A comprehensive approach to monitoring volcano deformation as a window on the eruption cycle, *Reviews of Geophysics*, *41*, 1001, doi:10.1029/2001RG000107. 1, 1.1, 3.2.1

Dzurisin, D., M. Lisowski, C. W. Wicks, M. P. Poland, and E. T. Endo (2006), Geodetic observations and modeling of magmatic inflation at the Three Sisters volcanic center, central Oregon Cascade Range, USA, *Journal of Volcanology and Geothermal Research*, *150*, 35–54, doi:10.1016/j.jvolgeores.2005.07.011. 1.2, 3.5

Ebmeier, S. K., J. Biggs, T. A. Mather, G. Wadge, and F. Amelung (2010), Steady downslope movement on the western flank of Arenal volcano, Costa Rica, *Geochemistry, Geophysics, Geosystems*, *11*, Q12,004 14PP, doi:10.1029/2010GC003263. 1.3, 1.5, 2, 3.1, 3.3, 3.2, 3.5

Ebmeier, S. K., J. Biggs, T. A. Mather, J. R. Elliott, G. Wadge, and F. Amelung (2012), Measuring large topographic change with InSAR: Lava thicknesses, extrusion rate and subsidence rate at Santiaguito volcano, Guatemala, *Earth and Planetary Science Letters*, *335-336*, 216–225, doi:10.1016/j.epsl.2012.04.027. 1.3, 1.5, 2.2, 3.1, 3.3, 3.2, 3.5

Ebmeier, S. K., J. Biggs, T. A. Mather, and F. Amelung (in press), Applicability of InSAR to tropical volcanoes: insights from Central America, *Geological Society of London Special Publication*. 1.5

Eggers, A. (1983), Temporal gravity and elevation changes at Pacaya volcano, Guatemala, *Journal of Volcanology and Geothermal Research*, *19*, 223–237, doi:10.1016/0377-0273(83)90111-7. 1.4, 3.3

Elderfield, H., and A. Schultz (1996), Mid-Ocean Ridge Hydrothermal Fluxes and the Chemical Composition of the Ocean, *Annual Review of Earth and Planetary Sciences*, *24*, 191–224, doi:10.1146/annurev.earth.24.1.191. 1

Elsworth, D., and B. Voight (1995), Dike intrusion as a trigger for large earthquakes and the failure of volcano flanks, *Journal of Geophysical Research*, *100*, 6005–6024, doi:10.1029/94JB02884. 4.4

Escobar, R., O. Matias, and W. I. Rose (2008), Santiaguito Dome Geologic Map 2006. 5.1, 5.3.1, 5.3, 5.5

Fairbrothers, G. E., M. J. Carr, and D. G. Mayfield (1978), Temporal magmatic variation at Boqueron volcano, El Salvador, *Computer*, *67*, 1–9, doi:10.1007/BF00371627. 1.5

Fedotov, S. A., A. M. Chirkov, N. A. Gusev, G. N. Kovalev, and Y. B. Slezin (1980), The large fissure eruption in the region of Plosky Tolbachik volcano in Kamchatka, 1975 1976, *Bulletin of Volcanology*, *43*, 47–60, doi:10.1007/BF02597610. 5.2

Feigl, K. L., J. Gasperi, F. Sigmundsson, and A. Rigo (2000), Crustal deformation near Hengill volcano, Iceland 1993-1998: Coupling between magmatic activity and faulting inferred from elastic modeling of satellite radar interferograms, *Journal of Geophysical Research*, *105*, 25,655–25,670, doi:10.1029/2000JB900209. 1.2

Ferretti, A., C. Prati, and F. Rocca (1999), Multibaseline insar dem reconstruction: the wavelet approach, *Geoscience and Remote Sensing, IEEE Transactions on*, *37*(2), 705 –715, doi:10.1109/36.752187. 5.2

Fialko, Y., Y. Khazan, and M. Simons (2001a), Deformation due to a pressurized horizontal circular crack in an elastic half-space, with applications to volcano geodesy, *Geophysical Journal International*, *146*, 181–190, doi:10.1046/j.1365-246X.2001.00452.x. 1.1

Fialko, Y., M. Simons, and D. Agnew (2001b), The complete (3-D) surface displacement field in the epicentral area of the 1999 M_w 7.1 Hector Mine earthquake, California, from space geodetic observations, *Geophysical Research Letters*, *28*, 3063–3066, doi:10.1029/2001GL013174. 4.2.3

Finnegan, N. J., and M. E. Pritchard (2009), Magnitude and duration of surface uplift above the Socorro magma body, *Geology*, *37(3)*, 231–234, doi:10.1130/G25132A.1. 1.2

Fisher, R. A. (1922), On the Interpretation of χ^2 from Contingency Tables, and the Calculation of P., *Journal of the Royal Statistical Society*, *85*, 87–94, doi:10.2307/2340521. 3.5

Fornaciai, A., B. Behncke, M. Favalli, M. Neri, S. Tarquini, and E. Boschi (2010), Detecting short-term evolution of Etnean scoria cones: a LIDAR-based approach, *Bulletin of Volcanology*, *72*, 1209–1222, doi:10.1007/s00445-010-0394-3. 1.1

Foster, J., B. Brooks, T. Cherubini, C. Shacat, S. Businger, and C. L. Werner (2006), Mitigating atmospheric noise for InSAR using a high resolution weather model, *Geophysical Research Letters*, *33*, 16,304, doi:10.1029/2006GL026781. 2.1.4

Fournier, N., H. Rymer, G. Williams-Jones, and J. Brenes (2004), High-resolution gravity survey: Investigation of subsurface structures at Poás volcano, Costa Rica, *Geophysical Research Letters*, *31*, 15,602, doi:10.1029/2004GL020563. 1.7

Fournier, T., M. E. Pritchard, and N. Finnegan (2011a), Accounting for Atmospheric Delays in InSAR Data in a Search for Long-Wavelength Deformation in South America, *IEEE Transactions on Geoscience and Remote Sensing, vol. 49, issue 10, pp. 3856-3867*, *49*, 3856–3867, doi:10.1109/TGRS.2011.2139217. 2, 4.2.1

Fournier, T., M. E. Pritchard, and N. Finnegan (2011b), Accounting for Atmospheric Delays in InSAR Data in a Search for Long-Wavelength Deformation in South America, *IEEE Transactions on Geoscience and Remote Sensing*, *49*, 3856–3867, doi:10.1109/TGRS.2011.2139217. 2.1.4

Fournier, T. J., M. E. Pritchard, and S. N. Riddick (2010), Duration, magnitude, and frequency of subaerial volcano deformation events: New results from Latin America using InSAR and a global synthesis, *Geochemistry, Geophysics, Geosystems*, *11*, 1003, doi:10.1029/2009GC002558. 1.3, 1.1, 1.3, 1.2, 1.3, 2, 2.3, 3.1, 3.2, 3.3, 3.5, 3.5, 5.2

Francis, P., C. Oppenheimer, and D. Stevenson (1993), Endogenous growth of persistently active volcanoes, *Nature*, *366*, 554–557, doi:10.1038/366554a0. 3.4.2, 3.4.2

Fransson, J. E. S., G. Smith, and J. Askne (2001), Stem volume estimation in boreal forests using ERS-1/2 coherence and SPOT XS optical data, *International Journal of Remote Sensing*, *22*, 2777–2791, doi:10.1080/01431160010006872. 2.4.3

Frische, M., K. Garofalo, T. H. Hansteen, and R. Borchers (2006), Fluxes and origin of halogenated organic trace gases from Momotombo volcano (Nicaragua), *Geochemistry, Geophysics, Geosystems*, *7*, 5020, doi:10.1029/2005GC001162. 1.6

Froger, J., D. Remy, S. Bonvalot, and D. Legrand (2007), Two scales of inflation at Lastarria-Cordon del Azufre volcanic complex, central Andes, revealed from ASAR-ENVISAT interferometric data, *Earth and Planetary Science Letters*, *255*, 148–163, doi:10.1016/j.epsl.2006.12.012. 1.2, 3.5

Froger, J.-L., O. Merle, and P. Briole (2001), Active spreading and regional extension at Mount Etna imaged by SAR interferometry, *Earth and Planetary Science Letters*, *187*, 245–258, doi:10.1016/S0012-821X(01)00290-4. 1.3, 6.2

Froger, J.-L., Y. Fukushima, P. Briole, T. Staudacher, T. Souriot, and N. Villeneuve (2004), The deformation field of the August 2003 eruption at Piton de la Fournaise, Reunion Island, mapped by ASAR interferometry, *Geophysical Research Letters*, *31*, L14601, doi:10.1029/2004GL020479. 1.1

Garrison, J. M., M. K. Reagan, and K. W. W. Sims (2012), Dacite formation at ilopango caldera, el salvador: U-series disequilibrium and implications for petrogenetic processes and magma storage time, *Geochemistry, Geophysics, Geosystems*, *13*(Q06018), 20pp, doi:10.1029/2012GC004107. 1.5

Garvin, J. B. (1996), Topographic characterization and monitoring of volcanoes via airborne laser altimetry, *Geological Society, London, Special Publications*, *110*(1), 137–152, doi:10.1144/GSL.SP.1996.110.01.11. 5.1.1

Gemmell, J. (1987), Geochemistry of metallic trace elements in fumarolic condensates from Nicaraguan and Costa Rican volcanoes, *Journal of Volcanology and Geothermal Research*, *33*, 161–181, doi:10.1016/0377-0273(87)90059-X. 1.6

Genco, R., and M. Ripepe (2010), Inflation-deflation cycles revealed by tilt and seismic records at stromboli volcano, *Geophys. Res. Lett*, *37*(12), L12,302. 3.4.1

Goldstein, R. M., H. A. Zebker, and C. L. Werner (1988), Satellite radar interferometry - Two-dimensional phase unwrapping, *Radio Science*, *23*, 713–720, doi:10.1029/RS023i004p00713. 2.4.2, 3.2

Gomez, R. O. M. (2009), Map of the 1961-2009 eruption of Pacaya Volcano, Guatemala. 1.2

Grapenthin, R., B. Ófeigsson, F. Sigmundsson, E. Sturkell, and A. Hooper (2010), Pressure sources versus surface loads: Analyzing volcano deformation signal composition with an application to hekla volcano, iceland, *Geophysical Research Letters*, *37*(20), L20,310. 1.3

Halsor, S. P., and W. I. Rose (1988), Common characteristics of paired volcanoes in northern Central America, *Journal of Geophysical Research*, *93*, 4467–4476, doi:10.1029/JB093iB05p04467. 1.4

Hanssen, R. F. (2001), Radar interferometry data interpretation and error analysis, *Kluwer Academic Publishers*. 1.2, 2.1.1, 2.1.4, 2.4, 2.4.1, 2.4.2, 5.3

Harris, A. (2000), Effusion rate trends at Etna and Krafla and their implications for eruptive mechanisms, *Journal of Volcanology and Geothermal Research*, *102*, 237–269, doi:10.1016/S0377-0273(00)00190-6. 5.1

Harris, A., W. Rose, and L. Flynn (2003), Temporal trends in lava dome extrusion at Santiaguito 1922-2000, *Bulletin of Volcanology*, *65*, 77–89, doi:10.1007/s00445-002-0243-0. 5.1.2, 5.3.2, 5.3.3

Harris, A. J. L., L. P. Flynn, L. Keszthelyi, P. J. Mouginis-Mark, S. K. Rowland, and J. A. Resing (1998), Calculation of lava effusion rates from Landsat TM data, *Bulletin of Volcanology*, *60*, 52–71, doi:10.1007/s004450050216. 5.1.1

Harris, A. J. L., L. P. Flynn, D. A. Rothery, C. Oppenheimer, and S. B. Sherman (1999), Mass flux measurements at active lava lakes: Implications for magma recycling, *Journal of Geophysical Research*, *104*, 7117–7136, doi:10.1029/98JB02731. 3.4.2

Harris, A. J. L., L. P. Flynn, O. Matias, W. I. Rose, and J. Cornejo (2004), The evolution of an active silicic lava flow field: an ETM+ perspective, *Journal of Volcanology and Geothermal Research*, *135*, 147–168, doi:10.1016/j.jvolgeores.2003.12.011. 1.4, 5.1.2, 5.3.3

Harris, A. J. L., J. Dehn, and S. Calvari (2007), Lava effusion rate definition and measurement: a review, *Bulletin of Volcanology*, *70*, 1–22, doi:10.1007/s00445-007-0120-y. 5.1, 5.1.1, 5.1

Harris, A. J. L., A. Steffke, S. Calvari, and L. Spampinato (2011), Thirty years of satellite-dervied lava discharge rates at Etna: Implications for steady volume output, *Journal of Geophysical Research*, *116*, B08,204. 5.1.1

Harris, D. M., and A. T. Anderson (1984), Volatiles H_2O, CO_2, and Cl in a subduction related basalt, *Computer*, *87*, 120–128, doi:10.1007/BF00376218. 1.4

Hautmann, S., J. Gottsmann, R. S. J. Sparks, A. Costa, O. Melnik, and B. Voight (2009), Modelling ground deformation caused by oscillating overpressure in a dyke conduit at Soufrière Hills Volcano, Montserrat, *Tectonophysics*, *471*, 87–95, doi:10.1016/j.tecto.2008.10.021. 1.1

Hazlett, R. (1987), Geology of the San Cristobal volcanic complex, Nicaragua, *Journal of Volcanology and Geothermal Research*, *33*, 223–230, doi:10.1016/0377-0273(87)90064-3. 1.6

Heleno, S. I. N., C. Frischknecht, N. d'Oreye, J. N. P. Lima, B. Faria, R. Wall, and F. Kervyn (2010), Seasonal tropospheric influence on SAR interferograms near the ITCZ - The case of Fogo Volcano and Mount Cameroon, *Journal of African Earth Sciences*, *58*, 833–856, doi:10.1016/j.jafrearsci.2009.07.013. 2.1.1, 2.1, 2.1.2, 3.1

Hole, J. K., C. J. Bromley, N. F. Stevens, and G. Wadge (2007), Subsidence in the geothermal fields of the Taupo Volcanic Zone, New Zealand from 1996 to 2005 measured by InSAR, *Journal of Volcanology and Geothermal Research*, *166*, 125–146, doi:10.1016/j.jvolgeores.2007.07.013. 1.2

Hooper, A., H. Zebker, P. Segall, and B. Kampes (2004), A new method for measuring deformation on volcanoes and other natural terrains using InSAR persistent scatterers, *Geophysical Research Letters*, *31*, 23,611, doi:10.1029/2004GL021737. 4.2.2

Hooper, A., P. Segall, and H. Zebker (2007), Persistent scatterer interferometric synthetic aperture radar for crustal deformation analysis, with application to Volcan Alcedo, Galapagos, *Journal of Geophysical Research (Solid Earth)*, *112*, B07407, doi:10.1029/2006JB004763. 1.2

Hooper, A., B. Ófeigsson, F. Sigmundsson, B. Lund, P. Einarsson, H. Geirsson, and E. Sturkell (2011), Increased capture of magma in the crust promoted by ice-cap retreat in iceland, *Nature Geoscience*, *4*(11), 783–786. 1.3, 1.2

Husen, S., R. Quintero, E. Kissling, and B. Hacker (2003), Subduction-zone structure and magmatic processes beneath Costa Rica constrained by local earthquake tomography and petrological modelling, *Geophysical Journal International*, *155*, 11–32, doi:10.1046/j.1365-246X.2003.01984.x. 1.7

Jakobsdóttir, S. S., M. J. Roberts, G. B. Gudmundsson, H. Geirsson, and R. Slunga (2009), Earthquake swarms at Upptyppingar, north-east Iceland: A sign of magma intrusion?, *Studia Geophysica et Geodaetica*, *52*, 513–528, doi:10.1007/s11200-008-0035-x. 1.3

Johnson, D. J., F. Sigmundsson, and P. T. Delaney (2000), Comment on "Volume of magma accumulation or withdrawal estimated from surface uplift or subsidence, with application to the 1960 collapse of Kilauea volcano" by P. T. Delaney and D. F. McTigue, *Bulletin of Volcanology*, *61*, 491–493, 10.1007/s004450050006. 3.5.1

Jolivet, R., R. Grandin, C. Lasserre, M.-P. Doin, and G. Peltzer (2011), Systematic InSAR tropospheric phase delay corrections from global meteorological reanalysis data, *Geophysical Research Letters*, *38*, L17311, doi:10.1029/2011GL048757. 2.1.4

Jonsson, S., H. Zebker, and P. Segall (2002), Fault Slip Distribution of the 1999 Mw 7.1 Hector Mine, California, Earthquake, Estimated from Satellite Radar and GPS Measurements, *The Bulletin of the Seismological Society of America*, *92*, 1377–1389, doi:10.1785/0120000922. 5.4.1

Kazahaya, K., H. Shinohara, and G. Saito (1994), Excessive degassing of Izu-Oshima volcano: magma convection in a conduit, *Bulletin of Volcanology*, *56*, 207–216, doi:10.1007/BF00279605. 3.4.2

Kempter, K. (1996), Rincón de la Vieja volcano, Guanacaste province, Costa Rica: geology of the southwestern flank and hazards implications, *Journal of Volcanology and Geothermal Research*, *71*, 109–127, doi:10.1016/0377-0273(95)00072-0. 1.7

Kempter, K. (2000), Leakage of Active Crater lake brine through the north flank at Rincón de la Vieja volcano, northwest Costa Rica, and implications for crater collapse, *Journal of Volcanology and Geothermal Research*, *97*, 143–159, doi:10.1016/S0377-0273(99)00181-X. 1.7

Kutterolf, S., A. Freundt, U. Schacht, D. Bürk, R. Harders, T. Mörz, and W. Peréz (2008), Pacific offshore record of plinian arc volcanism in Central America: 3. Application to forearc geology, *Geochemistry, Geophysics, Geosystems*, *9*, Q02S03, doi:10.1029/2007GC001826. 1.5

Kwoun, O.-I., Z. Lu, C. Neal, and C. Wicks, Jr. (2006), Quiescent deformation of the Aniakchak Caldera, Alaska, mapped by InSAR, *Geology*, *34*, 5, doi:10.1130/G22015.1. 1.2

La Femina, P. C., T. H. Dixon, and W. Strauch (2002), Bookshelf faulting in Nicaragua, *Geology*, *30*, 751–754, doi:10.1130/0091-7613(2002)030<0751:BFIN> 2.0.CO;2. 1.4.2

La Femina, P. C., C. B. Connor, B. E. Hill, W. Strauch, and J. A. Saballos (2004), Magma-tectonic interactions in Nicaragua: the 1999 seismic swarm and eruption of Cerro Negro volcano, *Journal of Volcanology and Geothermal Research*, *137*, 187–199, doi:10.1016/j.jvolgeores.2004.05.006. 1.4.1, 1.6, 3.3

LaFemina, P., T. H. Dixon, R. Govers, E. Norabuena, H. Turner, A. Saballos, G. Mattioli, M. Protti, and W. Strauch (2009), Fore-arc motion and Cocos Ridge collision in Central America, *Geochemistry, Geophysics, Geosystems*, *10*, Q05S14, doi:10.1029/2008GC002181. 1.4.2, 1.6, 1.4.2, 3.5.1

Lagmay, A. M. F., B. van Wyk de Vries, N. Kerle, and D. M. Pyle (2000), Volcano instability induced by strike-slip faulting, *Bulletin of Volcanology*, *62*, 331–346, doi:10.1007/s004450000103. 4.3, 4.4, 6.2

Lanari, R., G. De Natale, P. Berardino, E. Sansosti, G. P. Ricciardi, S. Borgstrom, P. Capuano, F. Pingue, and C. Troise (2002), Evidence for a peculiar style of ground deformation inferred at Vesuvius volcano, *Geophysical Research Letters*, *29*, 1292, doi:10.1029/2001GL014571. 1.3, 1.3, 3.5

Laske, G., G. Masters, and C. Reif (), Crust2.0: A new global crustal model at 2 x 2 degrees, available at: http://igppweb.ucsd.edu/ gabi/crust2.html. 1.4, 1.5, 1.6, 1.7

Lesage, P., M. M. Mora, G. E. Alvarado, J. Pacheco, and J. Métaxian (2006), Complex behavior and source model of the tremor at Arenal volcano, Costa Rica, *Journal of Volcanology and Geothermal Research*, *157*, 49–59, doi:10.1016/j.jvolgeores.2006.03.047. 1.7, 4.3.1

Lewis, J. C., A. C. Boozer, A. López, and W. Montero (2008), Collision versus sliver transport in the hanging wall at the Middle America subduction zone: Constraints from background seismicity in central Costa Rica, *Geochemistry, Geophysics, Geosystems*, *9*, Q07S06, doi:10.1029/2007GC001711. 1.4.2

Li, Z., J. Muller, P. Cross, and E. J. Fielding (2005), Interferometric synthetic aperture radar (InSAR) atmospheric correction: GPS, Moderate Resolution Imaging Spectroradiometer (MODIS), and InSAR integration, *Journal of Geophysical Research (Solid Earth)*, *110*, B9 –3410, doi:10.1029/2004JB003446. 2.1.4

Li, Z., J.-P. Muller, P. Cross, P. Albert, J. Fischer, and R. Bennartz (2006), Assessment of the potential of MERIS near-infrared water vapour products to correct ASAR interferometric measurements, *International Journal of Remote Sensing*, *27*, 349–365, doi:10.1080/01431160500307342. 2.1.4

Lin, Y.-n. N., M. Simons, E. A. Hetland, P. Muse, and C. DiCaprio (2010), A multiscale approach to estimating topographically correlated propagation delays in radar interferograms, *Geochemistry, Geophysics, Geosystems*, *11*, Q09002, doi:10.1029/2010GC003228. 2.1.4

Liu, G., J. Li, Z. Xu, J. Wu, Q. Chen, H. Zhang, R. Zhang, H. Jia, and X. Luo (2010), Surface deformation associated with the 2008 Ms8.0 Wenchuan earthquake from ALOS L-band SAR interferometry, *International Journal of Applied Earth Observation and Geoinformation*, *12*, 496–505. 2.4.3

Liu, J. G., A. Black, H. Lee, H. Hanaizumi, and J. M. Moore (2001), Land surface change detection in a desert area in Algeria using multi-temporal ERS SAR coherence images, *International Journal of Remote Sensing*, *22*, 2463–2477, doi:10.1080/01431160152497673. 2.4.3

Locke, C. A., H. Rymer, and J. Cassidy (2003), Magma transfer processes at persistently active volcanoes: insights from gravity observations, *Journal of Volcanology and Geothermal Research*, *127*, 73–86, doi:10.1016/S0377-0273(03)00179-3. 1.6, 3.4.2, 3.4.2, 3.4.2

Lohman, R. B., and M. Simons (2005), Some thoughts on the use of InSAR data to constrain models of surface deformation: Noise structure and data downsampling, *Geochemistry, Geophysics, Geosystems*, *6*, 1007, doi:10.1029/2004GC000841. 2.1.1, 5.4.1

Lu, Z. (2007), InSAR Imaging of Volcanic Deformation over Cloud-prone Areas - Aleutian Islands, *Photogrammetric Enginieering and Remote Sensing*, *73*, 245–257. 1.2, 3.5

Lu, Z., and D. Dzurisin (2010a), Ground surface deformation patterns, magma supply, and magma storage at Okmok volcano, Alaska, from InSAR analysis: 2. Coeruptive deflation, July-August 2008, *Journal of Geophysical Research (Solid Earth)*, *115*, B14–B00B03, doi:10.1029/2009JB006970. 3.5

Lu, Z., and D. Dzurisin (2010b), Ground surface deformation patterns, magma supply, and magma storage at Okmok volcano, Alaska, from InSAR analysis: 2. Coeruptive deflation, July-August 2008, *Journal of Geophysical Research (Solid Earth)*, *115*(B14), 0–+, doi:10.1029/2009JB006970. 1.1, 1.3, 1.3

Lu, Z., and J. T. Freymueller (1998), Synthetic aperture radar interferometry coherence analysis over Katmai volcano group, Alaska, *Journal of Geophysical Research*, *103*, 29,887–29,894, doi:10.1029/98JB02410. 3.5, 4.2.1

Lu, Z., R. Fatland, M. Wyss, S. Li, J. Eichelberger, K. Dean, and J. Freymueller (1997), Deformation of New Trident volcano measured by ERS-1 SAR interferometry, Katmai National Park, Alaska, *Geophysical Research Letters*, *24*, 695–698, doi:10.1029/97GL00539. 1.2

Lu, Z., C. Wicks, D. Dzurisin, W. Thatcher, J. T. Freymueller, S. R. McNutt, and D. Mann (2000), Aseismic inflation of Westdahl volcano, Alaska, revealed by satellite radar interferometry, *Geophysical Research Letters*, *27*, 1567, doi:10.1029/1999GL011283. 1.2

Lu, Z., T. Masterlark, J. Power, D. Dzurisin, and C. Wicks (2002a), Subsidence at Kiska Volcano, Western Aleutians, detected by satellite radar interferometry, *Geophysical Research Letters*, *29*(18), 1855, doi:10.1029/2002GL014948. 1.3, 1.2, 3.5

Lu, Z., J. A. Power, V. S. McConnell, C. Wicks, and D. Dzurisin (2002b), Preeruptive inflation and surface interferometric coherence characteristics revealed by satellite radar interferometry at Makushin Volcano, Alaska: 1993-2000, *Journal of Geophysical Research (Solid Earth)*, *107*, 2266, doi:10.1029/2001JB000970. 1.1, 1.2

Lu, Z., E. Fielding, M. R. Patrick, and C. M. Trautwein (2003a), Estimating lava volume by precision combination of multiple baseline spaceborne and airborne interferometric synthetic aperture radar: the 1997 eruption of okmok volcano, alaska, *IEEE Transactions on Geoscience and Remote Sensing*, *41*, 1428–1436, doi:10.1109/TGRS.2003.811553. 5.1.1

Lu, Z., D. Wicks, D. Dzurisin, J. Power, W. Tatcher, and T. Masterlark (2003b), Interferometric synthetic aperture radar studies of Alaska volcanoes, *Earth Obs. Mag.*, *12*, 8–18. 3.5

Lu, Z., C. Wicks, O. Kwoun, J. A. Power, and D. Dzurisin (2004), Surface deformation associated with the March 1996 earthquake swarm at Akutan Island, Alaska, revealed by C-band ERS and L-band JERS radar interferometry, *AGU Fall Meeting Abstracts*, p. A66. 1.2

Lu, Z., T. Masterlark, and D. Dzurisin (2005a), Interferometric synthetic aperture radar study of Okmok volcano, Alaska, 1992-2003: Magma supply dynamics and postemplacement lava flow deformation, *Journal of Geophysical Research (Solid Earth)*, *110*, B02,403, doi:10.1029/2004JB003148. 1.1, 5.2, 5.3.4

Lu, Z., T. Masterlark, and D. Dzurisin (2005b), Interferometric synthetic aperture radar study of Okmok volcano, Alaska, 1992-2003: Magma supply dynamics and postemplacement lava flow deformation, *Journal of Geophysical Research (Solid Earth)*, *110*, B02,403, doi:10.1029/2004JB003148. 5.3.4

Lu, Z., T. Masterlark, and D. Dzurisin (2005c), Interferometric synthetic aperture radar study of Okmok volcano, Alaska, 1992-2003: Magma supply dynamics and postemplacement lava flow deformation, *Journal of Geophysical Research (Solid Earth)*, *110*, doi:10.1029/2004JB003148. 4.3, 4.3.2

Lundgren, P., and Z. Lu (2006), Inflation model of Uzon caldera, Kamchatka, constrained by satellite radar interferometry observations, *Geophysical Research Letters*, *33*, L06301, doi:10.1029/2005GL025181. 1.2, 3.5

Lundgren, P., S. Usai, E. Sansosti, R. Lanari, M. Tesauro, G. Fornaro, and P. Berardino (2001), Modeling surface deformation observed with synthetic aperture radar interferometry at Campi Flegrei caldera, *Journal of Geophysical Research*, *106*, 19,355–19,366, doi:10.1029/2001JB000194. 1.2, 2.1.2, 2.1.3, 3.2, 3.5, 6.2.1

Lundgren, P., P. Berardino, M. Coltelli, G. Fornaro, R. Lanari, G. Puglisi, E. Sansosti, and M. Tesauro (2003), Coupled magma chamber inflation and sector collapse slip observed with synthetic aperture radar interferometry on Mt. Etna volcano, *Journal of Geophysical Research (Solid Earth)*, *108*, 2247, doi:10.1029/2001JB000657. 1.1

Lundgren, P., F. Casu, M. Manzo, A. Pepe, P. Berardino, E. Sansosti, and R. Lanari (2004), Gravity and magma induced spreading of Mount Etna volcano revealed by satellite radar interferometry, *Geophysical Research Letters*, *31*, L04602, doi:10.1029/2003GL018736. 4, 4.3, 4.3, 4.3.3, 6.2.1

Lyons, J. J., G. P. Waite, W. I. Rose, and G. Chigna (2009), Patterns in open vent, strombolian behavior at Fuego volcano, Guatemala, 2005-2007, *Bulletin of Volcanology*, p. 37, doi:10.1007/s00445-009-0305-7. 1.4

Lyons, J. J., G. P. Waite, M. Ichihara, and J. M. Lees (2012), Tilt prior to explosions and the effect of topography on ultra-long-period seismic records at Fuego volcano, Guatemala, *Geophysical Research Letters*, pp. L08,305, 6 PP., doi:10.1029/2012GL051184. 1.3, 3.3, 3.4.1

Macfarlane, D. G., G. Wadge, D. A. Robertson, M. R. James, and H. Pinkerton (2006), Use of a portable topographic mapping millimetre wave radar at an active lava flow, *Geophysical Research Letters*, *330*, L03,301, doi:10.1029/2005GL025005. 5.1.1

Manconi, A., M. A. Longpre, T. R. Walter, V. R. Troll, and T. H. Hansteen (2009), The effects of flank collapses on volcano plumbing systems, *Geology*, *37*, 1099–1102, doi:10.1130/G30104A.1. 4.4

Mann, D., and J. Freymueller (2003), Volcanic and tectonic deformation on Unimak Island in the Aleutian Arc, Alaska, *Journal of Geophysical Research (Solid Earth)*, *108*, 2108, doi:10.1029/2002JB001925. 1.2

Martin, D. (1981), Behavioral patterns of Fuego volcano, Guatemala, *Journal of Volcanology and Geothermal Research*, *10*, 67–81, doi:10.1016/0377-0273(81)90055-X. 1.4.1, 1.4

Martini, F., F. Tassi, O. Vaselli, R. D. Potro, M. Martinez, R. V. del Laat, and E. Fernandez (2010), Geophysical, geochemical and geodetical signals of reawakening at turrialba volcano (costa rica) after almost 150 years of quiescence, *Journal of Volcanology and Geothermal Research*, *198*(3-4), 416 – 432, doi:10.1016/j.jvolgeores.2010.09.021. 1.7, 2.4.1, 3.3

Massonnet, D., and K. L. Feigl (1995), Discrimination of geophysical phenomena in satellite radar interferograms, *Geophysical Research Letters*, *22*, 1537–1540, doi:10.1029/95GL00711. 1.1, 2.1.2, 3.2

Massonnet, D., and K. L. Feigl (1998), Radar interferometry and its application to changes in the earth's surface, *Reviews of Geophysics*, *36*, 441–500, doi:10.1029/97RG03139. 1.2, 3.1, 5.2

Massonnet, D., P. Briole, and A. Arnaud (1995), Deflation of Mount Etna monitored by spaceborne radar interferometry, *Nature*, *375*, 567–570, doi:10.1038/375567a0. 2.1.1

Masterlark, T. (2007), Magma intrusion and deformation predictions: Sensitivities to the Mogi assumptions, *Journal of Geophysical Research (Solid Earth)*, *112*, B06419, doi:10.1029/2006JB004860. 1.1

Masterlark, T., and Z. Lu (2004), Transient volcano deformation sources imaged with interferometric synthetic aperture radar: Application to Seguam Island, Alaska, *Journal of Geophysical Research (Solid Earth)*, *109*(B18), B01401, doi:10.1029/2003JB002568. 1.1, 1.3

Mastin, L. G., E. Roeloffs, N. M. Beeler, and J. E. Quick (2008), Constraints on the size, overpressure, and volatile content of the Mount St Helen's magma system from geodetic and dome-growth measurements during the 2004-2006+ eruption, *USGS Proffesional Paper*, *1750*, 461–488. 1.3, 3.5.1

Mastin, L. G., M. Lisowski, E. Roeloffs, and N. Beeler (2009), Improved constraints on the estimated size and volatile content of the Mount St. Helens magma system from the 2004-2008 history of dome growth and deformation, *Geophysical Research Letters*, *36*, L20304, doi:10.1029/2009GL039863. 3.5.1

Mather, T. A., D. M. Pyle, V. I. Tsanev, A. J. S. McGonigle, C. Oppenheimer, and A. G. Allen (2006), A reassessment of current volcanic emissions from the Central American arc with specific examples from Nicaragua, *Journal of Volcanology and Geothermal Research*, *149*, 297–311, doi:10.1016/j.jvolgeores.2005.07.021. 3.4, 3.4.2, 3.4.2

Matthews, J. P., H. Kamata, S. Okuyama, Y. Yusa, and H. Shimizu (2003), Surface height adjustments in pyroclastic-flow deposits observed at Unzen volcano by JERS-1 SAR interferometry, *Journal of Volcanology and Geothermal Research*, *125*, 247–270, doi:10.1016/S0377-0273(03)00112-4. 1.3, 1.3

McKnight, S. B., and S. N. Williams (1997), Old cinder cone or young composite volcano?: The nature of Cerro Negro, Nicaragua, *Geology*, *25*, 339, doi:10.1130/0091-7613(1997)025<0339:OCCOYC>2.3.CO;2. 1.6

McNutt, S. R., and D. H. Harlow (1983), Seismicity at Fuego, Pacaya, Izalco, and San Cristobal Volcanoes, Central America, 1973-1974, *Bulletin of Volcanology*, *46*, 283–297, doi:10.1007/BF02597563. 1.6

Merle, O., and A. Borgia (1996), Scaled experiments of volcanic spreading, *Journal of Geophysical Research*, *101*, 13,805–13,818, doi:10.1029/95JB03736. 4.3.3

Métaxian, J., P. Lesage, and J. Dorel (1997), Permanent tremor of Masaya Volcano, Nicaragua: Wave field analysis and source location, *Journal of Geophysical Research*, *102*, 22,529–22,546, doi:10.1029/97JB01141. 1.6

Metzger, S., S. Jónsson, G. Danielsen, S. Hreinsdóttir, F. Jouanne, D. Giardini, and T. Villemin (2012), Present kinematics of the tjörnes fracture zone, north iceland, from campaign and continuous gps measurements, *Geophysical Journal International*. 1.2

Michael Conway, F. (1992), Cerro Quemado, Guatemala: the volcanic history and hazards of an exogenous volcanic dome complex, *Journal of Volcanology and Geothermal Research*, *52*, 303–308, doi:10.1016/0377-0273(92)90051-E. 1.4

Mogi, K. (1958), Relations between the Eruptions of Various Volcanoes and the Deformations of the Ground Surfaces around them, *Bulletin of the Earthquke Research Institute*, *36*, 99–134. 1.1, 4.3.1

Moran, S. C., O. Kwoun, T. Masterlark, and Z. Lu (2006), On the absence of InSAR-detected volcano deformation spanning the 1995 1996 and 1999 eruptions of Shishaldin Volcano, Alaska, *Journal of Volcanology and Geothermal Research*, *150*, 119–131, doi:10.1016/j.jvolgeores.2005.07.013. 3.3, 3.5

Morrell, K. D., E. Kirby, D. M. Fisher, and M. van Soest (2012), Geomorphic and exhumational response of the Central American Volcanic Arc to Cocos Ridge subduction, *Journal of Geophysical Research*, *117*, B04,409, 22pp, doi:10.1029/2011JB008969. 1.4.2, 1.4.2

Mothes, P., J. Biggs, S. Baker, S. Hong, F. Amelung, and T. Dixon (2008), Survey of Volcanic Activity in Ecuador using L-band SAR. 1.2, 1.3, 3.5, 5.2

Murray, L. K., J.and Wooller (2002), Persistent summit subsidence at Volcán de Colima, México, 1982 1999: strong evidence against Mogi deflation, *Journal of Volcanology and Geothermal Research*, *117*, 69–78, doi:10.1016/S0377-0273(02)00236-6. 4.3

Naranjo, J. A., R. S. J. Sparks, M. V. Stasiuk, H. Moreno, and G. J. Ablay (1992), Morphological, structura and textural variations in the 1988-1990 andesite lava of Lonquimay Volcano, Chile, *Geological Magazine*, *49129*, 657–678, doi:10.1017/S0016756800008426. 5.2

Navarro-Ochoa, C., J. C. Gavilanes-Ruíz, and A. Cortés-Cortés (2002), Movement and emplacement of lava flows at Volcan de Colima, Mexico: November 1998 February 1999, *Journal of Volcanology and Geothermal Research*, *117*(1-2), 155 – 167, doi:10.1016/S0377-0273(02)00242-1. 5.2

Newhall, C. (1987), Geology of the Lake Atitlán Region, Western Guatemala, *Journal of Volcanology and Geothermal Research*, *33*, 23–55, doi:10.1016/0377-0273(87)90053-9. 1.4

Ofeigsson, B., A. Hooper, F. Sigmundsson, E. Sturkell, and R. Grapenthin (2011), Deep magma storage at hekla volcano, iceland, revealed by insar time series analysis, *Journal of Geophysical Research*, *116*(B5), B05,401. 1.1, 1.2

Okada, Y. (1985), Surface deformation due to shear and tensile faults in a half-space, *Bulletin of the Seismological Society of America*, *75*, 1135–1154. 1.1

Oppenheimer, C. (1992), Sulphur eruptions at Volcán Poás, Costa Rica, *Journal of Volcanology and Geothermal Research*, *49*, 1–21, doi:10.1016/0377-0273(92)90002-U. 1.7

Oppenheimer, C. (1993), Thermal distributions at fumarole fields: implications for infrared remote sensing of active volcanoes, *Journal of Volcanology and Geothermal Research*, *55*, 97–115, doi:10.1016/0377-0273(93)90092-6. 1.6

Owen, S., P. Segall, M. Lisowski, A. Miklius, R. Denlinger, and M. Sako (2000), Rapid deformation of Kilauea Volcano: Global Positioning System measurements between 1990 and 1996, *Journal of Geophysical Research*, *105*, 18,983–18,998, doi:10.1029/2000JB900109. 1.1

Pagli, C., F. Sigmundsson, R. Pedersen, P. Einarsson, T. Árnadóttir, and K. L. Feigl (2007), Crustal deformation associated with the 1996 Gjálp subglacial eruption, Iceland: InSAR studies in affected areas adjacent to the Vatnajökull ice cap, *Earth and Planetary Science Letters*, *259*, 24–33, doi:10.1016/j.epsl.2007.04.019. 1.1

Papageorgiou, E., M. Foumelis, and I. Parcharidis (2012), Long-and short-term deformation monitoring of santorini volcano: Unrest evidence by dinsar analysis, *Selected Topics in Applied Earth Observations and Remote Sensing, IEEE Journal of*, *PP*(99), 1 –7, doi:10.1109/JSTARS.2012.2198871. 1.2, 3.5

Parks, M., J. Biggs, T. Mather, D. Pyle, F. Amelung, M. Monsalve, and L. N. Medina (2011), Co-eruptive subsidence at Galeras identified during an InSAR survey of Colombian volcanoes (2006-2009), *Journal of Volcanology and Geothermal Research*, *202*(3-4), 228 – 240, doi:10.1016/j.jvolgeores.2011.02.007. 1.1, 2, 3.5

Patino, L. C., M. J. Carr, and M. D. Feigenson (2000), Local and regional variations in Central American arc lavas controlled by variations in subducted sediment input, *Computer*, *138*, 265–283, doi:10.1007/s004100050562. 3.5.1

Pavez, A., D. Remy, S. Bonvalot, M. Diament, G. Gabalda, J.-L. Froger, P. Julien, D. Legrand, and D. Moisset (2006), Insight into ground deformations at Lascar volcano (Chile) from SAR interferometry, photogrammetry and GPS data: Implications on volcano dynamics and future space monitoring, *Remote Sensing of Environment*, *100*(3), 307 – 320, doi:10.1016/j.rse.2005.10.013. 1.1, 2.1.1, 2.1.4, 3.4.1, 3.5

Peck, D. L. (1978), Cooling and vesiculation of Alae lava lake, Hawaii, *U.S. Geol. Surv., Prof. Paper*, *935*. 4.3.2, 5.3.4

Pedersen, R., and F. Sigmundsson (2004), InSAR based sill model links spatially offset areas of deformation and seismicity for the 1994 unrest episode at Eyjafjallajökull volcano, Iceland, *Geophysical Research Letters*, *31*, L14610, doi:10.1029/2004GL020368. 1.3

Pedersen, R., and F. Sigmundsson (2006), Temporal development of the 1999 intrusive episode in the Eyjafjallajökull volcano, Iceland, derived from InSAR images, *Bulletin of Volcanology*, *68*, 377–393, doi:10.1007/s00445-005-0020-y. 1.3

Perlock, P. A., P. J. González, K. F. Tiampo, G. Rodríguez-Velasco, S. Samsonov, and J. Fernández (2008), Time Evolution of Deformation Using Time Series of Differential Interferograms: Application to La Palma Island (Canary Islands), *Pure and Applied Geophysics*, *165*, 1531–1554, doi:10.1007/s00024-004-0388-7. 1.2

Pertermann, M., and C. C. Lundstrom (2006), Phase equilibrium experiments at 0.5 GPa and 1100 1300 °C on a basaltic andesite from Arenal volcano, Costa Rica, *Journal of Volcanology and Geothermal Research*, *157*, 222–235, doi:10.1016/j.jvolgeores.2006.03.043. 3.3

Philibosian, B., and M. Simons (2011), A survey of volcanic deformation on Java using ALOS PALSAR interferometric time series, *Geochemistry, Geophysics, Geosystems*, *12*, Q11004, doi:10.1029/2011GC003775. 1.3, 1.1, 1.2, 2, 2.5, 3.1, 3.4.1, 3.3, 3.5, 3.5

Phipps Morgan, J., C. R. Ranero, and P. Vannucchi (2008), Intra-arc extension in Central America: Links between plate motions, tectonics, volcanism, and geochemistry, *Earth and Planetary Science Letters*, *272*, 365–371, doi:10.1016/j.epsl.2008.05.004. 1.4.2

Pinel, V., A. Hooper, S. de La Cruz-Reyna, G. Reyes-Davila, M. P. Doin, and P. Bascou (2011), The challenging retrieval of the displacement field from InSAR data for andesitic stratovolcanoes: Case study of Popocatepetl and Colima Volcano, Mexico, *Journal of Volcanology and Geothermal Research*, *200*, 49–61, doi:10.1016/j.jvolgeores.2010.12.002. 1.1, 2, 2.1, 3.4.1, 3.5, 5.2

Pinkerton, H., and L. Wilson (1994), Factors controlling the lengths of channel-fed lava flows, *Bulletin of Volcanology*, *56*, 108–120, doi:10.1007/BF00304106. 5.1

Plank, T., and C. H. Langmuir (1993), Tracing trace elements from sediment input to volcanic output at subduction zones, *Nature*, *362*, 739–743, doi:10.1038/362739a0. 1

Poland, M., G. Bawden, M. Lisowski, and D. Dzurisin (). 3.5

Poland, M., R. Bürgmann, D. Dzurisin, M. Lisowski, T. Masterlark, S. Owen, and J. Fink (2006), Constraints on the mechanism of long-term, steady subsidence at Medicine Lake volcano, northern California, from GPS, leveling, and InSAR, *Journal of Volcanology and Geothermal Research*, *150*, 55–78, doi:10.1016/j.jvolgeores.2005.07.007. 1.2, 3.5

Pritchard, M. E. (2006), InSAR, a tool for measuring Earth's surface deformation, *Physics Today*, pp. 68–69. 1.2

Pritchard, M. E., and M. Simons (2004a), An InSAR-based survey of volcanic deformation in the central Andes, *Geochemistry, Geophysics, Geosystems*, *5*, 2002, doi:10.1029/2003GC000610. 1.3, 1.2, 1.3, 2.1.1, 2.1, 3.1, 3.2, 3.3, 3.5, 4.2.4, 4.3.1, 4.3.2

Pritchard, M. E., and M. Simons (2004b), An InSAR-based survey of volcanic deformation in the southern Andes, *Geophysical Research Letters*, *31*, L15,610, doi:10.1029/2004GL020545. 1.2, 3.5

Pritchard, M. E., and M. Simons (2004c), Surveying Volcanic Arcs with Satellite Radar Interferometry: The Central Andes, Kamchatka, and Beyond, *GSA Today*, *14*, 4–11, doi:10.1130/1052-5173(2004)014¡4:SVAWSR¿2.0.CO;2. 3.3, 5.2

Prosser, J., and M. Carr (1987), Poás volcano, Costa Rica: Geology of the summit region and spatial and temporal variations among the most recent lavas, *Journal of Volcanology and Geothermal Research*, *33*, 131–146, doi:10.1016/0377-0273(87)90057-6. 1.7

Protti, M., F. Gündel, and K. McNally (1994), The geometry of the Wadati-Benioff zone under southern Central America and its tectonic significance: results from a high-resolution local seismographic network, *Physics of the Earth and Planetary Interiors*, *84*, 271–287, doi:10.1016/0031-9201(94)90046-9. 4.4

Quisefit, J. P., J. P. Toutain, G. Bergametti, M. Javoy, B. Cheynet, and A. Person (1989), Evolution versus cooling of gaseous volcanic emissions from Momotombo Volcano, Nicaragua: Thermochemical model and observations, *Geochimica et Cosmochimica Acta*, *53*, 2591–2608, doi:10.1016/0016-7037(89)90131-2. 1.6

Reagan, M., E. Duarte, G. J. Soto, and E. Fernndez (2006), The eruptive history of Turrialba volcano, Costa Rica, and potential hazards from future eruptions, *Geological Society of America Special Papers*, *412*, 235–257, doi:10.1130/2006.2412(13). 1.7

Reagan, M. K., J. B. Gill, E. Malavassi, and M. O. Garcia (1987), Changes in magma composition at Arenal volcano, Costa Rica, 1968 1985: Real-time monitoring of open-system differentiation, *Bulletin of Volcanology*, *49*, 415–434, doi:10.1007/BF01046634. 1.7, 4.3.1, 6.2.1

Remy, D., S. Bonvalot, P. Briole, and M. Murakami (2003), Accurate measurements of tropospheric effects in volcanic areas from SAR interferometry data: application to Sakurajima volcano (Japan), *Earth and Planetary Science Letters*, *213*, 299–310, doi:10.1016/S0012-821X(03)00331-5. 2.1.1, 2.1, 2.1.4

Reuter, H., A. Nelson, P. Strobl, W. Mehl, and A. Jarvis (2009), A first assessment of aster gdem tiles for absolute accuracy, relative accuracy and terrain parameters, in *Geoscience and Remote Sensing Symposium,2009 IEEE International,IGARSS 2009*, vol. 5, pp. 240–243, doi:10.1109/IGARSS.2009.5417688. 2.2

Richer, M., C. P. Mann, and J. Stix (2004), Mafic magma injection triggers eruption at ilopango caldera, el salvador, central america, *Geological Society of America Special Papers*, *375*, 175–190, doi:10.1130/0-8137-2375-2.175. 1.5

Riddick, S. N., M. E. Pritchard, W. D. Barnhart, and R. B. Lohman (2008), Comparing C and L band InSAR observations of volcanic deformation in South America, *American Geophysical Union, Fall Meeting 2008*. 1.2

Roche, O., B. Vanwykdevries, and T. Druitt (2001), Sub-surface structures and collapse mechanisms of summit pit craters, *Journal of Volcanology and Geothermal Research*, *105*, 1–18, doi:10.1016/S0377-0273(00)00248-1. 1.6, 3.5.1

Rodriguez, E., and J. M. Martin (1992), Theory and design of interferometric synthetic aperture radars, *IEE Proceedings F: Radar and Signal Processing*, *139*, 147–159. 2.2, 5.2

Rodriguez, E., C. S. Morris, and J. E. Belz (2006), A Global Assessment of the SRTM Performance, *J. Am. Soc. Photogrammetr. Remote Sens.*, *72*, 249–260. 2.2, 4.2.2

Rodríguez, L. A., I. M. Watson, W. I. Rose, Y. K. Branan, G. J. S. Bluth, G. Chigna, O. Matías, D. Escobar, S. A. Carn, and T. P. Fischer (2004), SO_2 emissions to the atmosphere from active volcanoes in Guatemala and El Salvador, 1999 2002, *Journal of Volcanology and Geothermal Research*, *138*, 325–344, doi:10.1016/j.jvolgeores.2004.07.008. 1.4, 1.5

Roggensack, K. (2001), Unraveling the 1974 eruption of Fuego volcano (Guatemala) with small crystals and their young melt inclusions, *Geology*, *29*, 911, doi:10.1130/0091-7613(2001)029<0911:UTEOFV>2.0.CO;2. 1.4

Roggensack, K., R. L. Hervig, S. B. McKnight, and S. N. Williams (1997), Explosive Basaltic Volcanism from Cerro Negro Volcano: Influence of Volatiles on Eruptive Style, *Science*, *277*(5332), 1639–1642, doi:10.1126/science.277.5332.1639. 1.6

Rose, W. I. (1972a), Santiaguito Volcanic Dome, Guatemala, *Geological Society of America Bulletin*, *83*, 1413–1434, doi:10.1130/0016-7606(1972)83[1413:SVDG]2.0.CO;2. 5.1

Rose, W. I. (1972b), Notes on the 1902 eruption of Santa María volcano, Guatemala, *Bulletin of Volcanology*, *36*, 29–45, doi:10.1007/BF02596981. 1.4, 3.3

Rose, W. I. (1987), *The Emplacement of Silicic Domes and Lava Flows*, vol. 212, pp. 17–27, Geological Society of America Special Paper -Volcanic activity at Santiaguito Volcano, 1976-1984. 5.1

Rose, W. I., S. Bonis, R. E. Stoiber, M. Keller, and T. Bickford (1973), Studies of volcanic ash from two recent Central American eruptions, *Bulletin of Volcanology*, *37*, 338–364, doi:10.1007/BF02597633. 1.6

Rosen, P., S. Hensley, E. Gurrola, F. Rogez, S. Chan, J. Martin, and E. Rodriguez (2001), Srtm c-band topographic data: quality assessments and calibration activities, in *Geoscience and Remote Sensing Symposium, 2001. IGARSS '01. IEEE 2001 International*, vol. 2, pp. 739 –741 vol.2, doi:10.1109/IGARSS.2001.976620. 2.2, 4.2.2, 5.3, 5.4.1

Rosen, P. A., S. Hensley, H. A. Zebker, F. H. Webb, and E. J. Fielding (1996), Surface deformation and coherence measurements of Kilauea Volcano, Hawaii, from SIR C radar interferometry, *Journal of Geophysical Research*, *101*, 23,109–23,126, doi:10.1029/96JE01459. 2.4.3, 2.5

Rosen, P. A., S. Hensley, G. Peltzer, and M. Simons (2004), Updated repeat orbit interferometry package released, *Eos Transactions, AGU*, *85(5)*, 47, doi:10.1029/2004EO050004. 3.2, 5.3

Rowland, S. K., and G. P. Walker (1990), Pahoehoe and aa in Hawaii: volumetric flow rate controls the lava structure, *Bulletin of Volcanology*, *52*, 615–628, doi:10.1007/BF00301212. 5.1

Ryan, G. A., S. C. Loughlin, M. R. James, L. D. Jones, E. S. Calder, T. Christopher, M. H. Strutt, and G. Wadge (2010), Growth of the lava dome and extrusion rates at Soufrière Hills Volcano, Montserrat, West Indies: 2005-2008, *Geophysical Research Letters*, *370*, L00E08, doi:10.1029/2009GL041477. 5.1.1

Ryder, C. H., J. B. Gill, F. Tepley, F. Ramos, and M. Reagan (2006), Closed- to open-system differentiation at Arenal volcano (1968 2003), *Journal of Volcanology and Geothermal Research*, *157*, 75–93, doi:10.1016/j.jvolgeores.2006.03.046. 1.7, 4.3.1

Rymer, H. (2000), Geophysical studies of the recent 15-year eruptive cycle at Poás Volcano, Costa Rica, *Journal of Volcanology and Geothermal Research*, *97*, 425–442, doi:10.1016/S0377-0273(99)00166-3. 1.7

Rymer, H., and G. C. Brown (1987), Causes of microgravity change at Poás volcano, Costa Rica: an active but non-erupting system, *Bulletin of Volcanology*, *49*, 389–398, doi:10.1007/BF01046632. 1.7

Rymer, H., J. Cassidy, C. A. Locke, and J. B. Murray (1995), Magma movements in Etna volcano associated with the major 1991 1993 lava eruption: evidence from gravity and deformation, *Bulletin of Volcanology*, *57*, 451–461, doi:10.1007/BF00300989. 3.4.2

Rymer, H., B. van Wyk de Vries, J. Stix, and G. Williams-Jones (1998), Pit crater structure and processes governing persistent activity at Masaya Volcano, Nicaragua, *Bulletin of Volcanology*, *59*, 345–355, doi:10.1007/s004450050196. 1.6

Sadofsky, S. J., M. Portnyagin, K. Hoernle, and P. van den Bogaard (2008), Subduction cycling of volatiles and trace elements through the Central American volcanic arc: evidence from melt inclusions, *Computer*, *155*, 433–456, doi:10.1007/s00410-007-0251-3. 3.4, 3.4.2, 3.5.1

Samsonov, S., M. van der Kooij, and K. Tiampo (2011), A simultaneous inversion for deformation rates and topographic errors of dinsar data utilizing linear least square inversion technique, *Computers and Geosciences*, *37*(8), 1083 – 1091, doi:10.1016/j.cageo.2011.01.007. 5.1

Sanderson, R., J. Johnson, and J. Lees (2010), Ultra-long period seismic signals and cyclic deflation coincident with eruptions at santiaguito volcano, guatemala, *Journal of Volcanology and Geothermal Research*, *198*(1), 35–44. 3.3, 3.4.1

Santoro, M., J. Askne, G. Smith, and J. E. S. Fransson (2002), Stem volume retrieval in boreal forests from ERS-1/2 interferometry, *Remote Sensing of Environment*, *81*(1), 19 – 35, doi:10.1016/S0034-4257(01)00329-7. 2.4.1

Schirzaei, M., T. R. Walter, H. R. Nankali, and E. P. Holohan (2011), Gravity-driven deformation of Damavand volcano, Iran, detected through InSAR time series, *Geology*, *39*, 251–254, doi:10.1130/G31779.1. 1.3, 1.3

Schmidt, D. A., and R. Bürgmann (2003), Time-dependent land uplift and subsidence in the Santa Clara valley, California, from a large interferometric synthetic aperture radar data set, *Journal of Geophysical Research (Solid Earth)*, *108*, 2416, doi:10.1029/2002JB002267. 2.1.3, 4.2.4

Segall, P. (2010), *Earthquake and Volcano Deformation*, Princeton University Press. 3.6

Self, S., M. R. Rampino, and M. J. Carr (1989), A reappraisal of the 1835 eruption of Cosigüina and its atmospheric impact, *Bulletin of Volcanology*, *52*, 57–65, doi:10.1007/BF00641387. 1.6

Seymour, M., and I. Cumming (1994), in *Geoscience and Remote Sensing Symposium, 1994. IGARSS '94. Surface and Atmospheric Remote Sensing: Technologies, Data Analysis and Interpretation., International, title=Maximum likelihood estimation for SAR interferometry*, vol. 4, pp. 2272 –2275, doi:10.1109/IGARSS.1994.399711. 2.4

Shirzaei, M., and R. Bürgmann (2012), Topography correlated atmospheric delay correction in radar interferometry using wavelet transforms, *Geophysical Research Letters*, *39*, L01305, doi:10.1029/2011GL049971. 2.1.4

Sigmundsson, F., H. Vadon, and D. Massonnet (1997), Readjustment of the Krafla spreading segment to crustal rifting measured by satellite radar interferometry, *Geophysical Research Letters*, *24*, 1843–1846, doi:10.1029/97GL01934. 1.3, 5.2

Sigmundsson, F., P. Durand, and D. Massonnet (1999), Opening of an eruptive fissure and seaward displacement at Piton de la Fournaise volcano measured by RADARSAT satellite radar interferometry, *Geophysical Research Letters*, *26*, 533–536, doi:10.1029/1999GL900055. 1.1, 3.3

Sigmundsson, F., S. Hreinsdóttir, A. Hooper, T. Árnadóttir, R. Pedersen, M. J. Roberts, N. Óskarsson, A. Auriac, J. Decriem, P. Einarsson, H. Geirsson, M. Hensch, B. G. Ófeigsson, E. Sturkell, H. Sveinbjörnsson, and K. L. Feigl (2010), Intrusion triggering of the 2010 Eyjafjallajökull explosive eruption, *Nature*, *468*, 426–430, doi:10.1038/nature09558. 1.1, 1.3, 1.2

Simons, M., and P. A. Rosen (2007), Interferometric Synthetic Aperture Radar Geodesy, *Treatise on Geophysics*, *3*, 391–446. 1.2

Siswowidjoyo, S., I. Suryo, and I. Yokoyama (1995), Magma eruption rates of Merapi volcano, Central Java, Indonesia during one century (1890–1992), *Bulletin of Volcanology*, *57*, 111–116, doi:10.1007/BF00301401. 5.1

Small, C., and T. Naumann (2001), The global distribution of human population and recent volcanism, *Global Environmental Change Part B: Environmental Hazards*, *3*(3–4), 93 – 109, doi:10.1016/S1464-2867(02)00002-5. 1, 1.4, 1.2

Smithsonian Institution (1993a), Poàs, *Bulletin of the Global Volcanism Network*, *18*. 3.3

Smithsonian Institution (1993b), Irazù, *Bulletin of the Global Volcanism Network*, *18*. 3.3

Smithsonian Institution (2000), Poàs, *Bulletin of the Global Volcanism Network*, *25*. 3.3

Smithsonian Institution (2008a), Turrialba, *Bulletin of the Global Volcanism Network*, *33*. 3.3

Smithsonian Institution (2008b), Poàs, *Bulletin of the Global Volcanism Network*, *18*. 3.3

Smithsonian Institution (2009), Masaya, *Bulletin of the Global Volcanism Network*, *34*. 3.4.1

Sparks, R. S. J., S. R. Young, J. Barclay, E. S. Calder, P. Cole, B. Darroux, M. A. Davies, T. H. Druitt, C. Harford, R. Herd, M. James, A. M. Lejeune, S. Loughlin, G. Norton, G. Skerrit, M. V. Stasiuk, N. S. Stevens, J. Toothill, G. Wadge, and R. Watts (1998), Magma production and growth of the lava dome of the Soufriere Hills Volcano, Montserrat, West Indies: November 1995 to December 1997, *Geophysical Research Letters*, *25*, 3421–3424, doi:10.1029/98GL00639. 5.1.1

Sparks, R. S. J., C. B. Folkes, M. C. Humphreys, D. N. Barfod, J. Clavero, M. C. Sunagua, S. R. McNutt, and M. E. Pritchard (2008), Uturuncu volcano, Bolivia: Volcanic unrest due to mid-crustal magma intrusion, *Am J Sci*, *308*(6), 727–769, doi:10.2475/06.2008.01. 3.5

Sparks, R. S. J., J. Biggs, and J. W. Neuberg (2012), Monitoring volcanoes, *Science*, *335*(6074), 1310–1311, doi:10.1126/science.1219485. 1, 1.1

Stevens, N., G. Wadge, and J. Murray (1999), Lava flow volume and morphology from digitised contour maps: a case study at Mount Etna, Sicily, *Geomorphology*, *28*(3-4), 251 – 261, doi:10.1016/S0169-555X(98)00115-9. 5.2

Stevens, N. F., and G. Wadge (2004), Towards operational repeat-pass SAR interferometry at active volcanoes, *Natural Hazards*, *33(1)*, 47–76, doi:10.1023/B:NHAZ.0000035005.45346.2b. 2

Stevens, N. F., G. Wadge, and C. A. Williams (2001a), Post-emplacement lava subsidence and the accuracy of ERS InSAR digital elevation models of volcanoes, *International Journal of Remote Sensing*, *22*, 819–828, doi:10.1080/01431160051060246. 1.3, 1.3, 4, 4.3, 4.3.2, 5.1.1, 5.3.4

Stevens, N. F., G. Wadge, C. A. Williams, J. G. Morley, J. Muller, J. B. Murray, and M. Upton (2001b), Surface movements of emplaced lava flows measured by synthetic aperture radar interferometry, *Journal of Geophysical Research*, *106*, 11,293–11,314, doi:10.1029/2000JB900425. 4.3.2

Stoiber, R. E., and M. J. Carr (1973), Quaternary volcanic and tectonic segmentation of Central America, *Bulletin of Volcanology*, *37*, 304–325, doi:10.1007/BF02597631. 1.4

Stoiber, R. E., S. N. Williams, and B. J. Huebert (1986), Sulfur and halogen gases at Masaya Caldera complex, Nicaragua: total flux and variations with time, *Journal of Geophysical Research*, *91*, 12,215–12,232, doi:10.1029/JB091iB12p12215. 3.4, 3.4.2

Streck, M. J., M. A. Dungan, F. Bussy, and E. Malavassi (2005), Mineral inventory of continuously erupting basaltic andesites at Arenal volcano, Costa Rica: implications for interpreting monotonous, crystal-rich, mafic arc stratigraphies, *Journal of Volcanology and Geothermal Research*, *140*, 133–155, doi:10.1016/j.jvolgeores.2004.07.018. 1.7, 4.3.1, 6.2.1

Sykioti, O., C. C. Kontoes, P. Elias, P. Briole, M. Sachpazi, D. Paradissis, and I. Kotsis (2003), Ground deformation at Nisyros volcano (Greece) detected by ERS-2 SAR differential interferometry, *International Journal of Remote Sensing*, *24*, 183–188, doi:10.1080/01431160305000. 1.2, 3.5

Syracuse, E. M., and G. A. Abers (2006), Global compilation of variations in slab depth beneath arc volcanoes and implications, *Geochemistry, Geophysics, Geosystems*, *7*, Q05,017, doi:10.1029/2005GC001045. 1.4, 1.4.2

Syracuse, E. M., P. E. van Keken, and G. A. Abers (2010), The global range of subduction zone thermal models, *Physics of the Earth and Planetary Interiors*, *183*, 73–90, doi:10.1016/j.pepi.2010.02.004. 3.7

Tassi, F., O. Vaselli, B. Capaccioni, C. Giolito, E. Duarte, E. Fernandez, A. Minissale, and G. Magro (2005), The hydrothermal-volcanic system of Rincon de la Vieja volcano (Costa Rica): A combined (inorganic and organic) geochemical approach to understanding the origin of the fluid discharges and its possible application to volcanic surveillance, *Journal of Volcanology and Geothermal Research*, *148*, 315–333, doi:10.1016/j.jvolgeores.2005.05.001. 1.7

Tassi, F., O. Vaselli, V. Barboza, E. Fernandez, and E. Duarte (2009), Fluid geochemistry and seismic activityin the period 1998-2002 at Turrialba Volcano (Costa Rica), *Annals of Geophysics*, *47*(4). 1.7

Thorpe, R. S., C. A. Locke, G. C. Brown, P. W. Francis, and M. Randal (1981), Magma chamber below Poas volcano, Costa Rica, *Journal of the Geological Society*, *138*(3), 367–373, doi:10.1144/gsjgs.138.3.0367. 1.7

Turner, H. L., P. LaFemina, A. Saballos, G. S. Mattioli, P. E. Jansma, and T. Dixon (2007), Kinematics of the Nicaraguan forearc from GPS geodesy, *Geophysical Research Letters*, *34*, L02302, doi:10.1029/2006GL027586. 1.4.2

van Keken, P. E., B. R. Hacker, E. M. Syracuse, and G. A. Abers (2011), Subduction factory: 4. Depth-dependent flux of H_2O from subducting slabs worldwide, *Journal of Geophysical Research (Solid Earth)*, *116*, B01401, doi:10.1029/2010JB007922. 3.7

van Wyk de Vries, B., and P. Francis (1997), Catastrophic collapse at stratovolcanoes induced by gradual volcano spreading, *Nature*, *387*, 387–390. 4.3, 4.3.3, 4.4, 6.2

Voight, B. (2000), Structural stability of andesite volcanoes and lava domes, in *Astronomy, Physics and Chemistry of* H_3^+, *Royal Society of London Philosophical Transactions Series A*, vol. 358, p. 1663. 4.3.3, 4.4, 6.2

Voight, B., R. Sparks, A. Miller, R. Stewart, R. Hoblitt, A. Clarke, J. Ewart, W. Aspinall, B. Baptie, E. Calder, et al. (1999), Magma flow instability and cyclic activity at soufrière hills volcano, montserrat, british west indies, *Science*, *283*(5405), 1138–1142. 3.4.1

Wade, J. A., T. Plank, W. G. Melson, G. J. Soto, and E. H. Hauri (2006), The volatile content of magmas from Arenal volcano, Costa Rica, *Journal of Volcanology and Geothermal Research*, *157*, 94–120, doi:10.1016/j.jvolgeores.2006.03.045. 1.3, 1.7, 5.1.1

Wadge, G. (1981), The variation of magma discharge during basaltic eruptions, *Journal of Volcanology and Geothermal Research*, *11*, 139–168. 5.1

Wadge, G. (1983), The magma budget of Volcan Arenal, Costa Rica from 1968 to 1980, *Journal of Volcanology and Geothermal Research*, *19*, 281–302, doi:10.1016/0377-0273(83)90115-4. 4.3.3

Wadge, G., P. W. Webley, I. N. James, R. Bingley, A. Dodson, S. Waugh, T. Veneboer, G. Puglisi, M. Mattia, D. Baker, S. C. Edwards, S. J. Edwards, and P. J. Clarke (2002), Atmospheric models, GPS and InSAR measurements of the tropospheric water vapour field over Mount Etna, *Geophysical Research Letters*, *29*(19), 190,000–1, doi:10.1029/2002GL015159. 2.1, 2.1.4, 4.2.2

Wadge, G., D. G. Macfarlane, D. A. Robertson, A. J. Hale, H. Pinkerton, R. V. Burrell, G. E. Norton, and M. R. James (2005), AVTIS: A novel millimetre-wave ground based instrument for volcano remote sensing, *Journal of Volcanology and Geothermal Research*, *146*, 307–318, doi:10.1016/j.jvolgeores.2005.03.003. 1.1

Wadge, G., G. S. Mattioli, and R. A. Herd (2006), Ground deformation at Soufrière Hills Volcano, Montserrat during 1998–2000 measured by radar interferometry and GPS, *Journal of Volcanology and Geothermal Research*, *152*, 157–173, doi:10.1016/j.jvolgeores.2005.11.007. 1.1, 1.3, 2.1.1, 2.1, 2.1.4, 4.1, 4.1, 4.2.2, 4.4, 4.5, 4.3.3

Wadge, G., M. Zhu, R. J. Holley, I. N. James, P. A. Clark, C. Wang, and M. J. Woodage (2010), Correction of atmospheric delay effects in radar interferometry using a nested mesoscale atmospheric model, *Journal of Applied Geophysics*, *72*, 141–149. 2.1, 2.1.4

Walker, J., S. Williams, R. Kalamarides, and M. Feigenson (1993), Shallow open-system evolution of basaltic magma beneath a subduction zone volcano: the masaya caldera complex, nicaragua, *Journal of volcanology and geothermal research*, *56*(4), 379–400. 3.5.1

Walker, J. A., K. Roggensack, L. C. Patino, B. I. Cameron, and O. Matías (2003), The water and trace element contents of melt inclusions across an active subduction zone, *Computer*, *146*, 62–77, doi:10.1007/s00410-003-0482-x. 3.4, 3.4.2

Wallace, P. J. (2005), Volatiles in subduction zone magmas: concentrations and fluxes based on melt inclusion and volcanic gas data, *Journal of Volcanology and Geothermal Research*, *140*, 217–240, doi:10.1016/j.jvolgeores.2004.07.023. 3.4, 3.5.1

Ward, S. N., and S. Day (2003), Ritter Island Volcano-lateral collapse and the tsunami of 1888, *Geophysical Journal International*, *154*, 891–902, doi:10.1046/j.1365-246X.2003.02016.x. 4, 4.3.3, 6.2

Watson, I., C. Oppenhiemer, B. Voight, P. W. Francis, A. Clarke, J. Stix, and Miller (2000), The relationship between degassing and ground deformation at Soufriere Hills Volcano, Montserrat, *Journal of Volcanology and Geothermal Research*, *98*, 117–126, doi:10.1016/S0377-0273(99)00187-0. 3.2.1

Watt, S. F. L., D. M. Pyle, J. A. Naranjo, and T. A. Mather (2009), Landslide and tsunami hazard at Yate volcano, Chile as an example of edifice destruction on strike-slip fault zones, *Bulletin of Volcanology*, *71*, 559–574, doi:10.1007/s00445-008-0242-x. 6.2

Wauthier, C., W. Cayol, F. Kervyn, and N. d'Oreye (2009), The January 2002 eruption of Nyiragongo volcano (DRC) captured by InSAR, in *Geoscience and Remote Sensing Symposium,2009 IEEE International,IGARSS 2009*, vol. 2, pp. II–416 –II–419, doi:10.1109/IGARSS.2009.5418103. 1.3, 1.1

Wauthier, C., V. Cayol, F. Kervyn, and N. d'Oreye (2012), Magma sources involved in the 2002 Nyiragongo eruption, as inferred from an InSAR analysis, *Journal of Geophysical Research*, *117*, B05,411, doi:10.1029/2011JB008257. 1.1

Webley, P. W., G. Wadge, and I. N. James (2004), Determining radio wave delay by non-hydrostatic atmospheric modelling of water vapour over mountains, *Physics and Chemistry of the Earth*, *29*, 139–148, doi:10.1016/j.pce.2004.01.013. 2.1.1, 2.1.4

Whelley, P., J. Jay, E. Calder, M. Pritchard, N. Cassidy, S. Alcaraz, and A. Pavez (2012), Post-depositional fracturing and subsidence of pumice flow deposits: Lascar Volcano, Chile, *Bulletin of Volcanology*, *74*, 511–531, 10.1007/s00445-011-0545-1. 1.3, 1.3

Wicks, C. W., D. Dzurisin, S. Ingebritsen, W. Thatcher, Z. Lu, and J. Iverson (2002), Magmatic activity beneath the quiescent Three Sisters volcanic center, central Oregon Cascade Range, USA, *Geophysical Research Letters*, *29*(7), 070,000–1, doi:10.1029/2001GL014205. 2.1.4

Wicks, C. W., W. Thatcher, D. Dzurisin, and J. Svarc (2006), Uplift, thermal unrest and magma intrusion at Yellowstone caldera, *Nature*, *440*, 72–75, doi:10.1038/nature04507. 1.2

Wicks, C. W., R. White, H. Patia, C. Collins, W. Johnson, and H. Yarai (2007), Surface Deformation from ALOS Interferometry Related to the July 2006 Seismic Crisis and Dike Intrusion on Central New Britain Island, Papua New Guinea, in *Fall Meeting 2007*, American Geophysical Union. 1.2

Williams-Jones, G. (2001), A model of degassing and seismicity at Arenal Volcano, Costa Rica, *Journal of Volcanology and Geothermal Research*, *108*, 121–139, doi:10.1016/S0377-0273(00)00281-X. 4.4

Williams-Jones, G. (2003), Gravity changes and passive SO_2 degassing at the Masaya caldera complex, Nicaragua, *Journal of Volcanology and Geothermal Research*, *123*, 137–160, doi:10.1016/S0377-0273(03)00033-7. 1.6, 3.3, 3.4.1, 3.4.2

Witter, M., H. Geirsson, P. La Femina, D. Roman, M. Rodgers, A. Muñoz, A. Morales, V. Tenorio, D. Chavarria, M. Feineman, et al. (2011), May 2011 eruption of telica volcano, nicaragua: Multidisciplinary observations, in *AGU Fall Meeting Abstracts*, vol. 1, p. 2670. 3.4.1

Wonnacott, R. J., T. H. Wonnacott (1990), *Introductory Statistics, Fifth Edition*, John Wiley and sons. 5.3.1

Wood, R. (1974), Microearthquakes at Central American volcanoes, *Bulletin of the Seismological Society of America*, *64*(1), 275–277. 1.6

Woodruff, L., W. I. Rose, and W. Rigot (1979), Contrasting fractionation patterns for sequential magmas from two calc-alkaline volcanoes in Central America, *Journal of Volcanology and Geothermal Research*, *6*, 217–240, doi:10.1016/0377-0273(79)90003-9. 1.4

Wooster, M. J., and T. Kaneko (1998), Satellite thermal analyses of lava dome effusion rates at Unzen Volcano, Japan, *Journal of Geophysical Research*, *103*, 20,935–20,948, doi:10.1029/97JB03392. 5.1.1

Wright, R., S. Blake, A. J. L. Harris, and D. A. Rothery (2001), A simple explanation for the space-based calculation of lava eruption rates, *Earth and Planetary Science Letters*, *192*, 223–233, doi:10.1016/S0012-821X(01)00443-5. 5.1.1

Wright, T. J., B. E. Parsons, and Z. Lu (2004), Toward mapping surface deformation in three dimensions using InSAR, *Geophysical Research Letters*, *31*, 1607, doi:10.1029/2003GL018827. 4.2.3, 5.3

Wright, T. J., C. Ebinger, J. Biggs, A. Ayele, G. Yirgu, D. Keir, and A. Stork (2006), Magma-maintained rift segmentation at continental rupture in the 2005 Afar dyking episode, *Nature*, *442*, 291–294, doi:10.1038/nature04978. 1.2

Yang, X.-M., P. M. Davis, and J. H. Dieterich (1988), Deformation from inflation of a dipping finite prolate spheroid in an elastic half-space as a model for volcanic stressing, *Journal of Geophysical Research*, *93*, 4249–4257. 1.1, 3.6, 3.5.1

Zebker, H. A., and J. Villasensor (1992), Decorrelation in interferometric radar echoes, *IEEE Transactions on Geoscience and Remote Sensing*, *30*, 950–959, doi:10.1109/36.175330. 2.2, 2.4, 2.4.1, 2.4.2, 5.2

Zebker, H. A., P. A. Rosen, and S. Hensley (1997), Atmospheric effects in interferometric synthetic aperature radar surface deformation and topographic maps, *Journal of Geophysical Research*, *102*, 7547–7564, doi:10.1029/96JB03804. 2.1.1

Zebker, H. A., F. Amelung, and S. Jonsson (2000), Remote sensing of volcano surface and internal processes using radar interferometry, *Geophysical Monograph*, *116*, 179–205. 2, 3.2, 3.3

Zellmer, G. F. (2008), *Some first order observations on magma transfer from mantle wedge to upper crust at arc volcanoes*, vol. 304, Geological Society, London, Special Publications, doi:10.1144/SP304.1. 3.7

Zobin, V. (2002), Overview of the 1997 2000 activity of Volcán de Colima, México, *Journal of Volcanology and Geothermal Research*, *117*, 1–19, doi:10.1016/S0377-0273(02)00232-9. 5.2